PROBABILISTIC FINITE ELEMENT MODEL UPDATING AND DAMAGE DETECTION OF STRUCTURES BY USING BAYESIAN STATISTICS

A Thesis Submitted to
the Graduate School of Engineering and Sciences of
İzmir Institute of Technology
in Partial Fulfillment of the Requirements for the Degree of

DOCTOR OF PHILOSOPHY

in Civil Engineering

by
Hasan CEYLAN

December 2022
İZMİR

ACKNOWLEDGEMENTS

First, I would like to express my eternal grateful to my supervisor, Assoc. Prof. Dr. Gürsoy TURAN, for his motivation, patience, continuous support and spending his precious time to help for the studies done in this thesis. He always behaved like a father to me during this long journey and I felt like a son to him. I would like to thank and give my best regards to him for his such fatherly hospitable attitude and senior guidance during my graduate education.

Second, I would like to send my special gratitude to doctoral committee members, Prof. Dr. Engin AKTAŞ and Assoc. Prof. Dr. Ufuk YAZGAN, for their gentle comments and pinpointed recommendations on the core parts of the thesis. Their significant contributions bring the main objectives of this study to light. I also thank the examining committee members, Prof. Dr. Özgür ÖZÇELİK and Assoc. Prof. Dr. Emre ERCAN, for contributing to my defense seminar with their worthwhile comments.

I appreciate Assoc. Prof. Dr. Çağlayan HIZAL who encouraged me to study on the finite element model updating and damage detection in a probabilistic way by using Bayesian statistics. I would also thank to him for his help and collaboration to derive the formulations for the two-stage Bayesian model updating procedure which is presented in Chapter 3. I would like to thank to my colleague and roommate, MSc. Derya KARAKAYA, for her kind support and calming advices.

I would also like to give my most sincere and deepest regards to my parents who raised me and brought me to this educational level. I would like to thank my beloved sister who always supported me during this period.

Finally, headliners come out last, I wish to give my heartfelt and deepest appreciation to my love, my wife, Selcan CEYLAN, for her endless patience and support during my PhD education. She always tried to reduce my stress and helped to plan this period. Without her, this thesis may not be possible to be written in a well-organized way. I cannot put into words the support she gave me. I love you so much my love, you are the meaning of my entire life.

ABSTRACT

PROBABILISTIC FINITE ELEMENT MODEL UPDATING AND DAMAGE DETECTION OF STRUCTURES BY USING BAYESIAN STATISTICS

Finite element (FE) model updating is extensively employed in many applications of various engineering branches for damage detection purposes. An FE model is expected to reflect the properties of actual structures. However, it is almost impossible for an FE model to carry the properties of the real-life structure. As a result, differences exist between analytical models and actual structures. The aim of model updating is to minimize these differences as much as possible. In model updating procedures, there are inevitable uncertainties due to inevitable measurement noise and modelling errors. Therefore, model updating and damage detection process should be performed in a probabilistic way instead of a deterministic one. To this end, Bayesian model updating methods have gained much attention in the literature to account for the uncertainties of the parameters to be updated. Among these methods, those that use the concept of system modes have gained much more attention since it enables researchers to account for modelling error uncertainties and to avoid mode matching problem. For those methods, discrepancies between system modes and measured modes are considered and system modes are updated to obtain those that best fit the measured modes. Further, system modes are connected to the FE model via eigenvalue equations. In this study, a two-stage Bayesian model updating method which utilizes the concept of system modes has been firstly reformulated to compare three different assumptions on the modelling error variance of eigenvalue equations. Results reveal that the Bayesian model updating formulations that use the system modes concept give unreasonably too small posterior uncertainties for the updated parameters. This makes the probabilistic approach questionable since getting such small uncertainties may almost be equivalent to a deterministic approach. To increase the posterior uncertainty levels to more reasonable levels, a two-stage sensitivity-based Bayesian model updating methodology is proposed in this study. The results show that the proposed method successfully improves the updating results and increases the posterior uncertainties to more realistic levels.

ÖZET

YAPILARIN BAYESYAN İSTATİSTİKLERİ İLE OLASILIKSAL SONLU ELEMANLAR MODEL GÜNCELLEMESİ VE HASAR TESPİTİ

Sonlu elemanlar model güncelleme yöntemi, mühendisliğin çeşitli alanlarında hasar tespit çalışmaları için yaygın bir biçimde kullanılmaktadır. Bir sonlu elemanlar modelinin fiziksel yapının davranışını yansıtması beklenir. Fakat, bir modelin gerçek yapı davranışlarını bütünüyle karşılaması neredeyse imkansızdır. Fiziksel yapı ile bu yapının analitik modeli arasında her zaman bir fark vardır. Model güncellemenin amacı bu farkları mümkün olabildiğince düşürmektir. Model güncelleme yöntemlerinde, ölçüm gürültüsü ve modelleme hatalarından kaynaklı belirsizlikler de kaçınılmazdır. Bu nedenle, model güncelleme ve hasar tespiti konularında deterministik çalışmak yerine olasılıksal çalışmak daha uygundur. Bu doğrultuda, güncellenen parametrelerin belirsizliklerini de hesaba katabilmek adına Bayesyan model güncelleme teknikleri literatürde oldukça sık kullanılmaktadır. Bu teknikler arasında, sistem modlarını kullanan Bayesyan teknikleri modelleme hatasını hesaba katabilme ve mod eşleştirme sorununu önleme olanağı tanıdığı için, araştırmacıların oldukça dikkatini çekmiştir. Sistem modları, optimizasyon sürecinin bağımsız değişkenleri olup sonlu elemanlar modeline özdeğer denklemleriyle bağlanırlar. Bu çalışmada ilk olarak, sistem modları kavramını kullanan iki aşamalı bir Bayesyan model güncelleme yöntemi yeniden formüle edilmiştir. Buradaki amaç, literatürde geçen özdeğer denklemlerinin modelleme hatası varyansları üzerindeki farklı üç ayrı varsayımını kıyaslamaktır. Elde edilen sonuçlara göre, sistem modlarını kullanan Bayesyan model güncelleme tekniklerinin makul olmayan çok küçük değerlere sahip sonsal belirsizlikler verdiği gözlenmiştir. Bu sonuç, olasılıksal yaklaşımı sorgulanabilir hale getirmektedir, çünkü bu kadar küçük belirsizlik değerleri deterministik bir yaklaşıma eşdeğer sayılabilir. Bahsedilen sonsal belirsizlik seviyelerini makul düzeye çıkarabilmek adına, bu çalışmada, iki aşamalı hassasiyet tabanlı bir Bayesyan model güncelleme yöntemi önerilmiştir. Elde edilen sonuçlara göre, önerilen yöntemin güncelleme sonuçlarını başarılı bir şekilde iyileştirip sonsal belirsizlik seviyelerini daha gerçekçi düzeylere yükselttiği görülmüştür.

TABLE OF CONTENTS

LIST OF FIGURES

Figure **Page**

Figure **Page**

Figure **Page**

LIST OF TABLES

Table **Page**

Table **Page**

Table **Page**

CHAPTER 1

INTRODUCTION

Structural damage is described as variations in properties of material, geometry and boundary conditions which affects its operating functionality (Khoshnoudian and Esfandiari, 2011). Damage generally results in loss of stiffness in a structure. Local cracks in a structure, plasticity formation due to overcapacity loadings or slipping of reinforcing bars in a reinforced concrete structure can be given as structural damage examples. Structural damage can increase with time such as fatigue or environmental damages, or it is caused due to sudden loadings such as blast and earthquakes. As damage increases, structures cannot maintain their integrity and structural failure occurs. If the propagation of damage causes an unexpected and sudden failure, it is inevitable to adversely affect the human life and economic value. Therefore, damage detection topics have gained much attention for lots of area such as mechanical, civil and aerospace engineering because of its importance on monitoring structural health (Perera et al., 2013).

1.1. Introduction to Finite Element Model Updating

Many implementations of different engineering branches extensively employ the finite element (FE) method, and an FE model is expected to reflect the properties of actual real-life structures. However, it is almost impossible for an FE model to carry the properties of the real-life structure as George E. P. Box expressed this fact by a beautiful idiom “All models are wrong, but some are useful”. As a result, differences exist between analytical models and actual structures. Than Soe (2013) indicated the reasons of these differences as

- modelling errors caused by using nominal geometrical properties due to imperfections in actual geometry
- modelling errors due to the uncertainties in modelling the exact connection details between the structural members

- errors in model order caused by discretization of FE models
- errors in structural parameters such as using nominal material properties due to the obscurity of exact material properties, defining poorly known boundary conditions, etc.

Sufficiently accurate FE models of structures are required to estimate the dynamic behaviors and to work on the scenarios that may affect the actual structures. To this end, extensive studies have been conducted on model updating for decades and researchers have developed effective FE model updating methods to decrease discrepancies between analytical models and actual structures. Further, FE model updating is effectively employed for damage identification purposes. Damage in a structure is traced by using model updating methods in such a way that FE model of the structure is firstly calibrated to reach the finest FE model reflecting undamaged structural behavior. When damage occurs in the structure, discrepancies appear between the created model and the damaged physical structure (Alkayem et al., 2018). These discrepancies are represented by deviations in structural parameters which are selected as possible damaged parameters. Then, FE model is adjusted by minimizing the deviations, and parameters are updated to be compatible with those of the damaged state. Final state of the FE model indicates the damage. A literature review of the existing model updating methods has been provided in the following section.

1.1.1. A General Literature Review on the Model Updating Methods

The model updating methods are classified by Mottershead and Friswell (1993) in accordance with the type of measurement and parameters which are updated. Measured response can be analyzed in frequency domain or modal parameters can be extracted to work in modal domain with modal frequencies and mode shapes. On the other hand, updating parameters can be selected as physical parameters, damping or stiffness matrices, whole mass matrix or individual element matrices, etc. Further, model updating methods can be grouped as non-iterative, iterative, sensitivity-based, probabilistic and statistical methods (Alkayem et al., 2018).

In non-iterative methods, mass and stiffness matrices are directly reconstructed with just one step (Caesar and Peter, 1987). According to Abdullah et al. (2015), these

methods give convenient results and the model parameters well match with those obtained from the measured data. Further, incomplete model data can be employed without using any model reduction and model expansion methods (Carvalho et al., 2007). However, studies in the literature state that direct methods are not practical. These methods require measurement data from full degrees of freedom (DOF) of structures (Than Soe, 2013). If the full measurement of all DOFs is available, model updating can be performed non-iteratively. However, measuring all DOFs of a structure is not possible and measured data is generally incomplete in practice. Therefore, direct methods have very limited applications in practice and the updated parameters may not carry the characteristics of the physical structure. Due to this reason, size of the measurement data and FE model should be equal to each other. On the contrary, these techniques impair the structural connectivity and updated structural properties may not reflect a physical meaning (Abdullah et al., 2015).

In iterative methods, an objective function of selected updating parameters is used to update the parameters. Optimization procedures which require eigen solutions or FRF data provide a wider opportunity to select updating parameters (Chen and Bicanic, 2010). Therefore, selected optimization techniques, structural updating parameters, selected objective functions and constraints determine the effectiveness of the updating process. For example, Modak et al. (2002) select an objective function that defines the discrepancies between the modal parameters which are measured and those obtained from the analytical model. However, according to Zapico-Valle et al. (2012), selection of the structural updating parameters is not an easy task and requires a significant physical judgement of the actual structure. For example, selecting updating parameters for connections of structural elements are problematic due to the complex behaviors in actual connections.

Mottershead et al. (2011) have characterized the sensitivity-based FE model updating methods as most outstanding one in model updating among the iterative methods. It is developed from the Taylor series expansion. The discrepancy between FE model and the measured data is described as

$$\varepsilon = \mathrm{R}_e - \mathbf{R}_a \tag{1.1}$$

where $\mathbf{R}_e$ and $\mathbf{R}_a$ the structural responses obtained from experimental data and analytical models, respectively. This structural response can be considered as FRF, modal

parameters or acceleration responses, etc. The residual in the i^{th} iteration is described as $\triangle R = \mathbf{R}_e - \mathbf{R}_{ai}$. Sensitivity matrix is then be defined as

$$\mathbf{S}_{ij} = \frac{\partial \mathbf{R}_{ai}}{\partial \mathbf{P}_j} \tag{1.2}$$

where $\mathbf{P}_j$ is the selected structural parameter. $\mathbf{S}$ is calculated for present value of the parameter $\mathbf{P}$ which is $\mathbf{P}_i$. Here, $\mathbf{P}$ and $\mathbf{P}_i$ are the measured parameter and model parameter, respectively. Equation (1.2) is solved for the parameter $\mathbf{P}$ at each iteration, as its residuals;

$$\Delta \mathbf{P} = \mathbf{P} - \mathbf{P}_i \tag{1.3}$$

and model is updated to the next iteration until consecutive results of $\mathbf{P}_i$ is converged to each other.

Sensitivity-based FE model updating methods are investigated by many researchers for damage detection. Farhat and Hemez (1993) applied an element-by-element sensitivity method on four simple structures. Bakir et al. (2007) implemented a sensitivity-based constraint optimization algorithm on a reinforced concrete frame to update its FE model and detect the inflicted damage. However, it is reached in the literature that the sensitivity-based methods have some drawbacks. A sensitivity matrix has to be constructed for all updating parameters, which makes the method computationally extensive. They also may not be applied on structures with significant damage (Jung and Kim, 2013).

Mthembu (2012) states in her thesis that decision of the number of the uncertain parameters is another important criterion for model updating process since the parameters of the FE model should have a certain minimum number to capture the dynamic characteristics of the actual system. She also stated that every structure and their FE model is unique and therefore designing a generalized model updating procedure that conforms every updating problem is a challenging issue. To overcome these problems, she proposed an automated procedure to detect and select the most uncertain parameters in any FE model. Therefore, several FE models (multi-model

framework approach) of one actual system have been constructed and selected the best model by updating each model simultaneously.

1.2. Research Motivation

Since almost everything is uncertain in real life, it is inevitable to have a certain discrepancy between the physical structure and its FE model. Measurement data obtained from actual systems have inevitable measurement noise by nature. Further, FE models cannot reflect the exact properties of the actual systems, no matter how detailed the physical systems are modeled. Therefore, statistics and probability theory come into the picture to deal with these uncertainties. Many researchers have employed probabilistic approaches to FE model updating and damage identification fields for several decades. Therefore, statistics-based and probabilistic FE model updating methods are widely utilized in the literature. Marwala and Sibisi (2005) use a Bayesian probabilistic approach to calibrate the beams. Mustafa and Matsumoto (2017) have developed a Bayesian model updating technique by using element-level parameterization since the different parts of structures experience different level of damage. They applied their methodologies on an existing truss structure by using an incomplete measurement data. They concluded that their method is capable of updating large-scale structures with incomplete measurements. However, local damage detection performed by the proposed method has been only possible for significant local damage.

For the model updating procedures, matching the modes of the analytical model to the measured counterparts is a fundamental problem since the initial model may not reflect the dynamic properties of the real-life structure. Initial FE model is generally constructed by measuring the undamaged structure and the calibrated model is used to identify damage on the structure in a future time. Damaged structure may have different dynamic characteristics from its undamaged state, and this may result in the mode matching problem between the model of undamaged state and the damaged structure. To overcome the mode matching problem, Vanik et al. (2000) have introduced new variables to the Bayesian model updating literature. These variables are named as system modes, and they are independent form both FE model modes and measured modes. This independence solves the mode matching problem in the probabilistic model updating literature. System modes have been connected to the FE model by using

eigenvalue equations which brings out the modelling error term. By doing so, this concept also enables researchers to analyze modelling error uncertainties. After them, many researchers have used the concept of system modes for decades. Detailed literature is reviewed in the following chapters of this thesis.

Motivation of the research done in this thesis is based on the inevitable uncertainties that exist in the model updating procedures. Therefore, the models should be updated in a probabilistic manner instead of deterministic approaches. Uncertainty quantification by using probabilistic approaches enables researchers to see how confident the model updating and damage identification procedure.

1.3. Research Objective

Numerous studies have been performed on the probabilistic FE model updating and damage identification in the literature. Among them, probabilistic approaches that use Bayesian statistics have gained much attention in recent years since Bayesian theory can define complete probability distributions of the updating and damage parameters. Besides, less data are employed in Bayesian model updating techniques compared to the frequentist statistics-based methods which need a large number of samples to define probability distributions. Due to these reasons, in this thesis, Bayesian model updating and damage identification techniques have been investigated in detail.

Some problems that are found in the Bayesian model updating literature originate the main research objectives of the studies that is covered in this thesis and these problems are presented as follows

- Model updating that is performed by using a single objective function needs weighting factors to weight each term of the objective function. It is investigated in the literature that there is almost no rational way to determine these factors. Some researchers solve this problem by using Bayesian inference. However, it is seen that these Bayesian approaches require multiple data sets which is encountered for the frequentist approach.
- The resulting posterior uncertainties of the parameters that are updated using Bayesian model updating are found to have unrealistically too small values. This result suggests that the updated parameters are very close to their

deterministic counterparts and therefore there might be no need to use a probabilistic approach for the updating process. To this end, the Bayesian model updating strategies that result in such small posterior uncertainties have been revisited and reformulated to compare and discuss their results.

- In the literature, parameters are updated and updating results are presented with their posterior uncertainties as a conclusion. Most of the research do not address the physical meaning of the updating results such as displacements, internal forces and stresses developing in structural members. These properties are essential to estimate the safety and remaining life of structures.

1.4. Outlines

The main research objectives are investigated under four chapters as follows

- Chapter 2 revisits the FE model updating procedures that uses a single objective function and multi-objective functions. The problem of assigning weighting factors in a single objective optimization is addressed and a Bayesian method that already exists in the literature is investigated to get optimal prediction of the weighting factors. Then this method is compared with the analysis results of a frequentist approach.
- In Chapter 3, a two-stage Bayesian model updating approach that utilizes the concept of system modes is reformulated by considering that modelling error variances are different for each mode. The results are compared with the other assumptions on the modelling error variances in the literature.
- In Chapter 4, a sensitivity-based Bayesian model updating procedure is proposed based on the results obtained in Chapter 3, and the results are compared with the results obtained in Chapter 3.
- Chapter 5 introduces the probabilistic damage detection topic. The Bayesian model updating methods presented in Chapter 3 and 4 are applied on the IASC-ASCE benchmark problem.

CHAPTER 2

OPTIMALLY WEIGHTED SENSITIVITY-BASED MODEL UPDATING BY USING PREDICTION ERROR VARIANCES

2.1. Introduction

The assessment of structural condition involves damage identification by using measured responses. System identification techniques use these responses to determine the characteristics of structures and model updating method is used to assess the change in these characteristics. In this context, system identification can be performed by using the static or dynamic responses. When the static responses are used, damage detection is limited to local identification due to the sensitivity of static measurements near the sensors. On the other hand, when the dynamic responses are employed, global identification is possible due to their nature to reflect the global behavior. (Perera et al., 2013). In vibration-based model updating, structural vibrations are measured to extract dynamic characteristics from the measured data. Structural properties which principally reflect the behavior of the structure are chosen as the updating parameters. The model parameters which minimize the discrepancies between the measured properties and those calculated from the model are obtained as the best parameters that carry the properties of actual structural behavior. Estimations of these parameters are sensitive to uncertainties that arise due to the restrictions in FE modeling of actual structures, inevitable existence of noise in the measured data and errors encountered during the modal parameter identification stage (Christodoulou et al., 2008).

2.2. Problem of Parameter Estimation

In this section, parameter estimation problem in FE model updating procedures is investigated for the optimization problems that use single and multi-objective functions.

2.2.1. Problem of Parameter Estimation based on Modal Residual Functions

In dynamic-based model updating procedures, the objective functions that optimize the selected structural parameters are generally formed as the residual functions between the measured and model modal parameters.

Let a structure be measured N times. From each measurement, one can obtain a modal data set with N_m number of modes. Let $\mathbf{D}$ be the cluster that has the measured modal properties, $\{\hat{f}_n^r, \hat{\phi}_n^r\}$, in which n=1, …, N_m and r=1, …, N. Here, $\hat{f}_n^r$ and $\hat{\phi}_n^r$ denote the measured eigenfrequency and eigenvector of the n^{th} mode in the r^{th} modal data set, respectively. Let $\boldsymbol{\theta}$ be the vector of selected model parameters to model the dynamic behavior of the actual structure. Then, let $f_n(\boldsymbol{\theta})$ and $\phi_n(\boldsymbol{\theta})$ be the eigenfrequency and eigenvector of the n^{th} mode, respectively, extracted from the FE model for a specific value of $\boldsymbol{\theta}$. $f_n(\boldsymbol{\theta})$ and $\phi_n(\boldsymbol{\theta})$ are evaluated by the eigenvalue analysis of the mass and stiffness matrix of the model, which is parameterized as $\mathbf{K}(\boldsymbol{\theta}) = \sum_i^{N_\theta} \theta_i K_i$. Here, K_i is the non-parametric part of the stiffness matrix. The aim here is to estimate the optimal value of the parameter set $\boldsymbol{\theta}$ that will ensure $f_n(\boldsymbol{\theta})$ and $\phi_n(\boldsymbol{\theta})$ to best match the measured modal data in the cluster $\mathbf{D}$. Therefore, an error function is formed for each modal parameter in the least-squares manner as

$$J_{f_n}(\boldsymbol{\theta}) = \frac{1}{N}\sum_{r=1}^{N}\frac{[\,f_n(\boldsymbol{\theta}) - \hat{f}_n^r\,]^2}{(\hat{f}_n^r)^2} \tag{2.1}$$

$$J_{\phi_n}(\boldsymbol{\theta}) = \frac{1}{N}\sum_{r=1}^{N}\frac{\| \mathbf{L}_0\phi_n(\boldsymbol{\theta}) - \hat{\phi}_n^r \|^2}{\| \hat{\phi}_n^r \|^2} \tag{2.2}$$

where ||.|| represents the Euclidian norm and $\mathbf{L}_0$ is an observation matrix consisting of 0's and 1's that interrelates the measured DOFs and FE model DOFs (Christodoulou and Papadimitriou, 2007). The functions in equations (2.1) and (2.2) are called error functions because there exists always a discrepancy between the measured and model modal properties due to the uncertainties mentioned before.

There are numerous optimization methods in the literature to deal with the inverse parameter estimation problem. In conventional model updating optimization

methods, parameter estimation is performed by employing a single objective function. If the dynamic responses are measured, the objective function is generally considered in the form of weighted sum of the error functions of modal properties that correspond to each mode of the structure. The prediction error of an individual modal characteristic is generally obtained by using the least-squares approach.

2.2.2. Formulation of Model Updating Procedures by Using Single-objective Function

In the most general form, the model updating is performed by optimizing the following objective function as a weighted least-squares approach;

$$\arg_{\theta} min \quad J(\boldsymbol{\theta}) = \sum_{n=1}^{N_m} w_n J_{f_n}(\boldsymbol{\theta}) + \sum_{n=1}^{N_m} \bar{w}_n J_{\phi_n}(\boldsymbol{\theta}) \tag{2.3}$$

where $J_{f_n}(\boldsymbol{\theta})$ and $J_{\phi_n}(\boldsymbol{\theta})$ are the error functions of an individual modal characteristic of the n^{th} mode which are defined in equations (2.1) and (2.2). w_n and $\bar{w}_n$ are the weighting factors of the error functions $J_{f_n}(\boldsymbol{\theta})$ and $J_{\phi_n}(\boldsymbol{\theta})$, respectively, satisfying $w_n \geq 0$ and $\bar{w}_n \geq 0$, and $\sum_{n=0}^{N_m} w_n + \sum_{n=0}^{N_m} \bar{w}_n = 1$. $J(\boldsymbol{\theta})$ represents the fitness function (or the objective function) between the measured characteristics and those predicted from the FE model. Here, relative importance in prediction errors is determined by the values of these weighting factors. Estimation of the optimum values of the model parameters in the vector $\boldsymbol{\theta}$ directly depends on the choice of the weighting factors. There will be a different set of optimum structural parameters for each different value. This means that the weighting factors which have different values will yield a different optimum structural model. Berman (1995) also states this issue emphasizing that the inverse problem of model updating is not unique. Therefore, the main question in the literature is that 'which values should be assigned to the weighting factors that results in the optimum structural model which best represents the actual structural behavior?'

There are many studies in the literature to deal with the estimation of the weighting factors. According to Haralampidis et al. (2005) and Christodoulou and Papadimitriou (2007), weighting factors should be determined according to the

sufficiency of the constructed FE model to represent the structural behavior and the quality of the measurements. However, quantification of the modelling error and uncertainties in the measured modal properties is not possible and such uncertainties always exist in real life applications. Therefore, they deduce that the selection of the values of the weightings is generally arbitrary and they are determined with the experience of users or trial and error procedure. Oh et al. (2015) also address that there are no studies that can determine the weighting values of each mode of the structure by using a methodology based on a general and logical basis and it is usually problem dependent.

2.2.3. Formulation of the Parameter Estimation Problem by Using Multi-objective Function

The problems and limitations encountered in determination of weighting factors have forced researchers to search for the methods that will not require the weighting factors, and the approaches with the multi-objective functions have come into the picture. In multi-objective optimization methods, several objective functions are minimized simultaneously and a set of optimal parameters that may represent the actual structure is obtained. The resulting parameters form the Pareto optimal solutions. The idea behind the Pareto optimality is that the optimal solution is not unique, but there are alternative solutions that do not dominate each other when all objective functions are considered. Therefore, these solutions have a trade-off and each can be considered as the best solution with respect to at least one of the objectives.

In fact, each error function in equations (2.1) and (2.2) forms an objective function that gives in a total number of $T=2N_m$ objectives. Therefore, the problem can be investigated as a multi-objective optimization. It can be formulated as

$$Min \quad (J_{f_1}(\boldsymbol{\theta}),,....,J_{f_{N_m}}(\boldsymbol{\theta}),J_{\phi_1}(\boldsymbol{\theta}),.....,J_{\phi_{N_m}}(\boldsymbol{\theta})) \tag{2.4}$$

Equation (2.4) is minimized to get a set of Pareto optimal solutions, which is known as Pareto optimal front. Let $\boldsymbol{\theta}$ be a parameter vector in the parameter space $\boldsymbol{\Theta}$. Here, $\boldsymbol{\theta}$ is considered as non-dominated to other solutions if and only if no parameter vector in $\boldsymbol{\Theta}$

exists that dominates $\boldsymbol{\theta}$. Mathematically, $\boldsymbol{\theta}'$ is dominated by a vector $\boldsymbol{\theta}$ if the following condition is satisfied (Christodoulou et al., 2008);

$$J_i(\boldsymbol{\theta}) \leq J_i(\boldsymbol{\theta}')\ \forall i \in \{1,....,T\} \quad and \quad J_j(\boldsymbol{\theta}) < J_j(\boldsymbol{\theta}')\ \exists j \in \{1,....,T\} \tag{2.5}$$

A representative pareto optimal front of a two-objective function is representatively shown in Figure 2.1. As Jin et al. (2014) have explained, for the solution C, the objective function F_1 is decreased with no change in the objective function F_2 by considering the solution A instead of the solution C. Similarly, the objective function F_2 is decreased with no change in the the objective function F_1 by considering the solution B instead of the solution C. Then, solutions A and B dominate the solution C and therefore, C is not on the pareto optimal front. However, the solution A and the solution B are non-dominated to each other since there is no chance for both solutions to decrease one of the objective functions without increasing the other. It should be noted that the ideal solution is at a point in which both objectives have a value of zero and there will be no pareto solutions in an ideal case. However, pareto optimal solutions are always encountered due to the uncertainties.

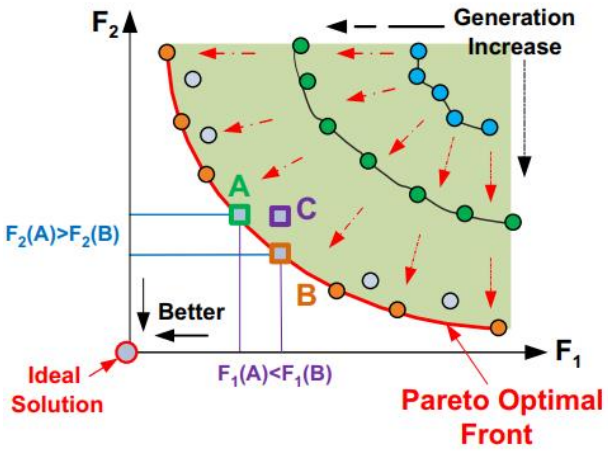

Figure 2.1. Pareto optimal front of a two-objective function

(Source: Jin et al., 2014)

2.2.4. Comparison between Single and Multi-objective Optimization

In single-objective optimization, optimal structural model is obtained by changing the weighting factors. It requires the user's preference and trial-and-error procedure. Therefore, the chosen structural model directly depends on the selected weighting factors. On the contrary, multi-objective optimization does not require any weighting factors and results in all possible structural models in a single run. The number of Pareto solutions depends on the number of objective functions. As a conclusion of this, multi-objective optimization techniques also require a decision-making strategy to select one of the alternative solutions. The relation between single and multi-objective optimization is that each optimal structural model in the Pareto front corresponds to the optimal structural model resulted from the single-objective optimization that is performed for a particular value of the weighting factors (Christodoulou and Papadimitriou, 2007). In other words, optimal Pareto structural models can be obtained by changing the values of the weightings from 0 to 1. However, Kim and de Weck (2005) state that no solutions can be obtained in the concave region of the Pareto optimal front by conventional weighted least-squares approach. Therefore, the single-objective optimization with weighted sums will miss the alternative solutions of a problem having a concave Pareto front region.

In the present study, the problems with convex Pareto front have been considered to relate the single and multi-objective approaches. The aim is to focus on the problem of deciding one of the alternatives among the Pareto optimal solutions, which best represent the actual structure. This is equivalent to the selection of the optimum values of the weighting factors in a single-optimization problem.

2.3. Estimating the Weighting Factors Using Bayesian Inference

In this section, the studies performed by Christodoulou and Papadimitriou (2007) and Christodoulou et al. (2008) are followed to investigate the optimal selection of weighting factors in a single objective function by using the Bayesian inference which is a probabilistic approach. Thus, the presented theoretical background in this section is not novel but usefully to deal with the problem of estimating the weighting factors in a rational basis. The presented study is then applied on two numerical studies

to discuss this problem. The first study comprises a two-story shear frame and the second one is a ten-story shear frame.

2.3.1. Probability Distribution of Model Parameters Using Modal Data

The Bayes' theorem is a convenient method to predict the parameters of a structural model enabling the use of probability distributions to have an idea about the uncertainty amount in the parameters. Let **θ** and **D** be the set of structural model parameters and cluster of the measured modal data, respectively, with reference to section 2.1. In addition, let *M* be the modelling assumptions and **c** be the set of prediction error parameters that denotes the coefficient of variation (c.o.v). Then, the posterior probability distribution, $p(\boldsymbol{\theta} \mid \mathbf{D}, M, \mathbf{c})$ is written as (Christodoulou and Papadimitriou, 2007);

$$p(\boldsymbol{\theta} \mid \mathbf{D}, M, \mathbf{c}) = \kappa \, p(\mathbf{D} \mid \boldsymbol{\theta}, M, \mathbf{c}) \, p(\boldsymbol{\theta} \mid M, \mathbf{c}) \tag{2.6}$$

where κ is a normalizing constant to ensure that the integral $p(\boldsymbol{\theta} \mid \mathbf{D}, M, \mathbf{c})$ is one, $p(\mathbf{D} \mid \boldsymbol{\theta}, M, \mathbf{c})$ denotes the probability of measuring the data from a model with parameters **θ**. Here, $p(\boldsymbol{\theta} \mid M, \mathbf{c})$ represents the prior probability distribution of the model. Error term **c** includes the parameters to account for the modelling assumptions. Therefore, *M* can be taken out of the formulation for simplicity.

The error vector, $\varepsilon^r = [\varepsilon_1^r, \varepsilon_2^r, \ldots, \varepsilon_{N_m}^r]$ shows the modal property discrepancies between those of measured and FE model for each mode. The errors for eigenfrequencies and eigenvectors are defined as

$$\varepsilon_{f_n}^r = \hat{f}_n^r - f_n(\boldsymbol{\theta}) \tag{2.7}$$

$$\varepsilon_{\phi_n}^r = \hat{\boldsymbol{\phi}}_n^r - \mathbf{L}_0 \boldsymbol{\phi}_n(\boldsymbol{\theta}) \tag{2.8}$$

The prediction errors in equations (2.7) and (2.8) are modelled as zero-mean Gaussian vectors to be used in the Bayes' theorem. For example, the prediction error for the n^{th} eigenfrequency is modelled to be $\varepsilon_{f_n}^r \sim N(0, c_{f_n}^2 f_n^{r2})$. The term $c_{f_n}^2 f_n^{r2}$ corresponds to the variance and $c_{f_n} f_n^r$ corresponds to the standard deviation of the error term. Similarly,

prediction error of the n^{th} eigenvector is modelled to be $\varepsilon_{\phi_n}^r \sim N(0, C_n^r)$. The term C_n^r is the covariance matrix that has the diagonal elements of $c_{\phi_n}^2 \|\phi_n^r\|^2$. Here, the parameter **c** includes the set of c.o.v values of these prediction error vectors.

The prediction errors in ε^r are assumed to be independent and choosing that the prediction errors follow a multi-variate Gaussian probability distribution, $p(\mathbf{D} \mid \boldsymbol{\theta}, \mathbf{c})$ is obtained as (Christodoulou and Papadimitriou, 2007)

$$p(\mathbf{D} \mid \boldsymbol{\theta}, \mathbf{c}) = \frac{1}{v(2\pi)^{\frac{NN_D}{2}} \rho(\mathbf{c})} \exp\left[-\frac{NN_D}{2} J(\boldsymbol{\theta}, \mathbf{c}) \right] \tag{2.9}$$

where $J(\boldsymbol{\theta}, \mathbf{c})$ is the objective function and defined as

$$J(\boldsymbol{\theta}, \mathbf{c}) = \sum_{n=1}^{N_m} \frac{\alpha_{f_n}}{c_{f_n}^2} J_{f_n}(\boldsymbol{\theta}) + \sum_{n=1}^{N_m} \frac{\alpha_{\phi_n}}{c_{\phi_n}^2} J_{\phi_n}(\boldsymbol{\theta}) \tag{2.10}$$

and $\rho(\mathbf{c})$ denotes the covariance matrix of the prediction error parameters in the parameter vector **c**.

Then, the probability distribution function of the prediction error parameters is defined as

$$\eta(\mathbf{c}) = \prod_{n=1}^{N_m} (c_{f_n})^{\alpha_{f_n} NN_D} (c_{\phi_n})^{\alpha_{\phi_n} NN_D} \tag{2.11}$$

v is a constant which has a value of

$$v = \prod_{n=1}^{N_m} \prod_{r=1}^{N} \hat{f}_n^r \left(\| \phi_n^r \| \right) \tag{2.12}$$

In the above equations, N denotes the number of modal data sets and N_D represents the number of measured modal data in a modal data set. Coefficients α_{f_n} and α_{ϕ_n}

corresponds to the number of modal parameters in the sub-objective functions $J_{f_n}(\boldsymbol{\theta})$ and $J_{\phi_n}(\boldsymbol{\theta})$, respectively.

If the parameters **c** are known, the optimal structural model parameters are obtained by maximizing the posterior probability density function (PDF) $p(\boldsymbol{\theta} \mid \mathbf{D}, M, \mathbf{c})$ in equation (2.6). However, the prediction errors are uncertain parameters of the updating process. Therefore, assuming an initial probability distribution, $p(\boldsymbol{\theta} \mid M, \mathbf{c})$ to be $q_\theta(\boldsymbol{\theta})$, the optimal value of the structural parameters can be evaluated just by minimizing $J(\boldsymbol{\theta}, \boldsymbol{\sigma})$ in equation (2.10). By doing so, optimal model parameters will directly depend on the assumption of the probability distribution of the prediction error parameters **c**.

2.3.2. Estimation of Weighting Factors by Using the Prediction Error Parameters

The objective function in equation (2.10) is constructed with a weighted least-squares approach, which is very similar to the objective function in equation (2.3). Therefore, Christodoulou and Papadimitriou (2007) have compared $J(\boldsymbol{\theta}, \mathbf{c})$ and $J(\boldsymbol{\theta})$, and concluded that the values of the weighting factors can be defined as

$$w_{f_n} = \frac{\alpha_{f_n}}{c_{f_n}^2} \quad and \quad w_{\phi_n} = \frac{\alpha_{\phi_n}}{c_{\phi_n}^2} \tag{2.13}$$

Therefore, they have also concluded that estimation of the weighting factors is exactly the same with the estimation of the prediction errors.

Now, the problem has turned into estimating the optimal values of **c** from the measured modal data. Since the measured data include measurement errors and the FE model has modelling errors, this case is similar to evaluating the optimum values of the model parameters discussed in the previous section. Probability distributions are again employed to have an idea about the amount of uncertainty in the prediction error parameters. The updated probability distribution of the prediction error parameters, ***c***, conditioned on the modal data is defined as

$$p(\mathbf{c} \mid \mathbf{D}) = \frac{p(\mathbf{D} \mid \mathbf{c}) q_c(\mathbf{c})}{h} \tag{2.14}$$

where $p(\mathbf{D} \mid \mathbf{c})$ denotes the probability of measuring modal parameters under the conditions of prediction error parameters **c**, it is defined as

$$p(\mathbf{D} \mid \mathbf{c}) = \int_{\boldsymbol{\Theta}} p(\mathbf{D} \mid \boldsymbol{\theta}, \mathbf{c}) q(\boldsymbol{\theta}) d\boldsymbol{\theta} \tag{2.15}$$

$q_c(\mathbf{c})$ is the prior probability distribution of the prediction error parameters, h is a normalizing constant to guarantee that the integral of $p(\mathbf{c} \mid \mathbf{D})$ results in unity.

In equation (2.15), the initial probability distribution $p(\boldsymbol{\theta} \mid \mathbf{c})$ of the structural model parameters conditioned on the prediction error parameters **c**, is assumed to be independent from **c** such that $p(\boldsymbol{\theta} \mid \mathbf{c}) = q(\boldsymbol{\theta})$.

Substituting $p(\mathbf{D} \mid \boldsymbol{\theta}, \mathbf{c})$ from equation (2.9) into equation (2.15), the following expression is obtained by Christodoulou and Papadimitriou (2007) as;

$$p(\mathbf{c} \mid \mathbf{D}) = \frac{1}{h v (2\pi)^{\frac{NN_D}{2}}} \frac{q_c(\mathbf{c})}{\rho(\mathbf{c})} \int_{\boldsymbol{\Theta}} q(\boldsymbol{\theta}) \exp\left[-\frac{NN_D}{2} J(\boldsymbol{\theta}, \mathbf{c}) \right] d\boldsymbol{\theta} \tag{2.16}$$

The most probable prediction error parameters, conditioned on the measured data set **D**, are obtained by maximizing equation (2.16). However, it is not an easy task to overcome the integral term of this function over the parameter space **Θ**.

Differentiating equation (2.16) with respect to each parameter in **c** and solving the resulting equation, the optimal parameters $\hat{\mathbf{c}}$ is obtained as

$$\left. \frac{\partial p(\mathbf{c} \mid \mathbf{D})}{\partial c_{f_n}} \right|_{\mathbf{c}=\hat{\mathbf{c}}} = 0 \quad \textit{and} \quad \left. \frac{\partial p(\mathbf{c} \mid \mathbf{D})}{\partial c_{\phi_n}} \right|_{\mathbf{c}=\hat{\mathbf{c}}} = 0 \tag{2.17}$$

where n=1, …, N_m. Substituting $p(\mathbf{D} \mid \mathbf{c})$ from equation (2.15) into equation (2.14), and then substituting the final expression into equation (2.17) by assuming a constant initial distribution of $q_c(c)$, the equation (2.17) can be written as

$$\left[\int_{\boldsymbol{\Theta}} \frac{\partial p(\mathbf{D}\,|\,\boldsymbol{\theta},\mathbf{c})}{\partial c_{f_n}} q(\boldsymbol{\theta})\,d\boldsymbol{\theta}\right]_{\mathbf{c}=\hat{\mathbf{c}}} = 0 \;\; and \;\; \left[\int_{\boldsymbol{\Theta}} \frac{\partial p(\mathbf{D}\,|\,\boldsymbol{\theta},\mathbf{c})}{\partial c_{\phi_n}} q(\boldsymbol{\theta})\,d\boldsymbol{\theta}\right]_{\mathbf{c}=\hat{\mathbf{c}}} = 0 \qquad (2.18)$$

Then, taking the first derivative of $p(\mathbf{D} \mid \boldsymbol{\theta}, \mathbf{c})$ in equation (2.9) with respect to each parameter in the set of $\mathbf{c}$, they have obtained the following relation for the optimal parameters $\hat{\mathbf{c}}$.

$$\int_{\boldsymbol{\Theta}} \exp\left[-\frac{NN_D}{2} J(\boldsymbol{\theta},\hat{\mathbf{c}})\right] d\boldsymbol{\theta} = \frac{1}{\hat{c}_{f_n}^2} \int_{\boldsymbol{\Theta}} J_{f_n}(\boldsymbol{\theta}) \exp\left[-\frac{NN_D}{2} J(\boldsymbol{\theta},\hat{\mathbf{c}})\right] d\boldsymbol{\theta} \qquad (2.19)$$

They have defined an asymptotic approximation for the Laplace-type integrations to calculate the integral in equation (2.19). The Laplace-type integration has been asymptotically approximated as

$$\int_{\Theta} f(\mathbf{x}) \exp\left[-k^2 g(\mathbf{x})\right] d\mathbf{x} \approx (2\pi)^{N_x} \frac{f(\hat{\mathbf{x}}) \exp\left[-k^2 g(\hat{\mathbf{x}})\right]}{\sqrt{\det[H(\hat{\mathbf{x}})]}} \quad for \;\; k \to \infty \qquad (2.20)$$

where $\hat{\mathbf{x}}$ is the optimum value of $\mathbf{x}$, which minimizes the function $g(\mathbf{x})$. Here, $H(\mathbf{x})$ is the Hessian of the function $k^2 g(\mathbf{x})$.

Comparing the integral on the left-side of the equation (2.19) with equation (2.20), it can be deduced that $f(\mathbf{x})=1$, $g(\mathbf{x})= J(\boldsymbol{\theta}, \hat{\mathbf{c}})$ and $k^2=0.5\mathrm{NN_D}$. Similarly, the right-side of the equation (19) reveals that $f(\mathbf{x})= J_{f_n}(\boldsymbol{\theta})$ or $f(\mathbf{x})= J_{\phi_n}(\boldsymbol{\theta})$, $g(\mathbf{x})= J(\boldsymbol{\theta}, \hat{\mathbf{c}})$ and $k^2=0.5\mathrm{NN_D}$. It is clear that both integrations account for the same optimum value $\widehat{\boldsymbol{\theta}}(\mathbf{c})$ which is the optimum value of the structural parameters conditioned on $\boldsymbol{\sigma}$, and for the same Hessian $H_D(\widehat{\boldsymbol{\theta}}(\mathbf{c}), \mathbf{c})$. Therefore, the exponential terms and the Hessian determinant terms cancel each other. As a conclusion, equation (2.19) is reduced to the following relations

$$c_{f_n} = J_{f_n}(\hat{\boldsymbol{\theta}}(\mathbf{c}))^{0.5} \quad and \quad c_{\phi_n} = J_{\phi_n}(\hat{\boldsymbol{\theta}}(\mathbf{c}))^{0.5} \qquad (2.21)$$

This relation implies that the optimal prediction error c.o.v values, $\hat{c}_{f_n}$ and $\hat{c}_{\Phi_n}$ of the n^{th} mode is equal to the square root of the optimal value of the error function that is calculated between the measured modal data of the n^{th} mode and that estimated by using optimum structural model which has the optimum parameter set of $\widehat{\boldsymbol{\theta}} = \widehat{\boldsymbol{\theta}}(\hat{\mathbf{c}})$. Since the assumption of a constant initial distribution of $q_c(c)$ is considered during the derivation of this relation, Christodoulou and Papadimitriou (2007) have questioned the generality of this deduction and showed that the Bayesian approach already generalizes the relation for non-uniform initial distributions.

Since estimating the optimum values of the prediction error parameters directly related depends on estimating the optimal weighting factors, it has been also solved by the relation in equation (2.21). Therefore, by substituting equation (2.21) with the optimum values $\hat{c}_{f_n}$ and $\hat{c}_{\Phi_n}$ into the equation (2.13), the optimal weighting factors for n^{th} mode can be expressed as

$$\hat{w}_{f_n} = \frac{\alpha_{f_n}}{J_{f_n}(\hat{\boldsymbol{\theta}})} \quad and \quad \hat{w}_{\phi_n} = \frac{\alpha_{\phi_n}}{J_{\phi_n}(\hat{\boldsymbol{\theta}})} \tag{2.22}$$

Here, the optimal value $\widehat{\boldsymbol{\theta}} = \widehat{\boldsymbol{\theta}}(\hat{\mathbf{c}})$ minimizes $J(\boldsymbol{\theta}, \mathbf{c})$ in equation (2.10). This is equivalent to the minimization of $J(\boldsymbol{\theta}, \mathbf{w})$ in equation (2.3) for $\mathbf{w}=\hat{\mathbf{w}}$. The single objective function is minimized by importing the optimal weighting factors such that $\widehat{\boldsymbol{\theta}} = \widehat{\boldsymbol{\theta}}(\hat{\mathbf{w}})$. This solution corresponds to the Pareto optimal parameters in multi-objective optimization.

However, optimal structural model parameters $\widehat{\boldsymbol{\theta}}$ cannot be determined before assigning the optimal weighting factors. Since the optimal model parameters are not known, the denominator of equation (2.22) cannot be evaluated to obtain the optimum weighting factors. Therefore, the optimum values of $\hat{\mathbf{w}}$ and $\widehat{\boldsymbol{\theta}} = \widehat{\boldsymbol{\theta}}(\hat{\mathbf{w}})$ are calculated by simultaneously solving the equations in (2.22) for n=1, …, N_m and equation (2.3).

2.4. Numerical Studies

- ***Implementation on a two-DOF model***

In the first numerical study, the numerical example of a two-DOF model developed by Christodoulou and Papadimitriou (2007) has been simulated and analyzed. They have considered a simple two-DOF spring-mass model that represents a two-story shear frame. The nominal values of mass and stiffness are assumed to be uniformly distributed over stories such that $m_1=m_2=m$ and $k_1=k_2=k$, respectively. The values of k and m are prescribed for the first eigenfrequency value to be 1 Hz. To this end, k is set as 1013 N/m and m is set as 9.8 kg. The eigenvalue analysis results in the eigenfrequencies of f_1=1.000 Hz and f_2=2.618 Hz.

The updating procedure is performed by using the eigenfrequencies only for demonstration purposes. To simulate the measurement data, Gaussian noise is included to the nominal values of the natural frequencies to deal with the measurement noise and modelling error. For the n^{th} eigenfrequency, noise is added from the Gaussian distribution of $N(\mu_{f_n}, \varepsilon_{f_n}^2 f_n^2)$. Thus, the uncertainties are controlled by the mean value μ and c.o.v ε of the associated parameters. To this end, measured modal data are simulated to have the uncertainty levels of μ_{f_1}= 0% and ε_{f_1}= 1% for the first mode. For the second mode, two values of μ_{f_2}= 0% and μ_{f_2} = 5%, and five values of ε_{f_2} = 0.05%, 0.5%, 1%, 3% and 5% have been used. Such high uncertainty level of μ_{f_2} = 5% relative to that of the first mode is selected on purpose so that both modes do not simultaneously match the measured modes.

The mass is considered to be well-known as usual in the model updating literature. Stiffness values of the structure are parameterized as $k_1=k_2=\theta k$. In other words, a single model parameter θ is selected to be updated as the scaling coefficient of the stiffness values of both stories. Thus, the uniform distribution of the stiffness over the structure will be preserved after the updating process.

This updating problem includes two sub-objectives which are the error functions $J_{f_n}(\theta)$ in equation (2.1) defined for n=1, 2. The single objective function is set as a weighted least squares of sub-objectives as in equation (2.3). The optimal values of weighting factors w_{f_n} and the parameter θ have been obtained by simultaneously

solving the objective function $J(\theta,w)$ in equation (2.3) and equations in (2.22) for n=1, 2. As Christodoulou et al. (2008) stated, this is a nested optimization process since the estimation of the weighting factors requires estimation of the optimal model parameter $\hat{\theta}$. Therefore, this optimization is performed iteratively. Initial values of the weighting factors are taken to be inversely proportional to the c.o.v of the measured modal frequencies. Further, the initial value of the model parameter θ is considered as 1.00. Unconstrained nonlinear optimization tool '*fminsearch*' which is a built-in function in Matlab program is employed for the minimization of $J(\theta,w)$. In each iteration, the value of each weighting factor, w_{f_n} in equation (2.22) is updated by employing the optimal value of its corresponding error function $J_{f_n}(\hat{\theta})$. A tolerance value of 1E-5 is set for the error function calculated between the weightings in the current and previous iteration to stop the optimization process.

The optimal values of $\hat{\theta}$ and $\hat{\mathbf{c}}$, and the weighting factors $\hat{\mathbf{w}}$ are given in Table 2.1 for various values of the initially introduced uncertainties μ_{f_2} and ε_{f_2}. The optimal values of **c** for each mode are equal to the square-root of the optimal value that corresponds the error function from equation (2.21).

For the uncertainty level of μ_{f_2}= 0%, there are three optimal model parameters having the $\hat{\theta}$ values of 1.02, 1.00 and 1.01. The model with $\hat{\theta}$ = 1.02, which corresponds to ε_{f_2}=3% and 5%, provides a small prediction error of 9E-4 % for the first mode and relatively high prediction error for the second mode. This result is due to the higher initial uncertainty in the second mode than that in the first mode (ε_{f_2}=3% and 5% > ε_{f_1}=1%).

As a consequence of this, the error function corresponding to the first mode is optimally weighted with much higher value. Similarly, the model with $\hat{\theta}$ = 1.00, which corresponds to ε_{f_2} = 0.05% and 0.5%, provides a very small prediction errors of 4E-4 % - 7E-4 % for the second mode and relatively high prediction error for the first mode due to the higher initial uncertainty in the first mode (ε_{f_2} = 0.05% and 0.5% < ε_{f_1} = 1%). Therefore, the error function corresponding to the second mode is optimally weighted with much higher value. Further, the model with $\hat{\theta}$ = 1.01, which corresponds to ε_{f_2} = 1%, provides equal prediction errors of 0.31% for both modes since they have equal initial uncertainties (ε_{f_1} = ε_{f_2} = 1%). Thus, the error functions of both modes are almost equally weighted.

For the uncertainty level of μ_{f_2} = 5%, there are two optimal model parameters having the $\hat{\theta}$ values of 1.02 and 1.10. The model with $\hat{\theta}$ = 1.02, which corresponds to ε_{f_2} = 1%, 3% and 5%, provides relatively small prediction errors of 0.005 - 9E-4 % for the first mode because of the higher initial uncertainty in the second mode ($\varepsilon_{f_2} \geq \varepsilon_{f_1}$=1% with μ_{f_2}=5%). The model with $\hat{\theta}$ = 1.10, which corresponds to ε_{f_2}=0.05% and 0.5%, provides relatively small prediction errors of 0.001% for the second mode because of the higher initial uncertainty in the first mode (ε_{f_2}=0.05% and 0.5% < ε_{f_1}=1% with μ_{f_2}=5%).

Table 2.1**.** Optimal structural parameters with the corresponding prediction errors (by using a single set of modal data)

Optimally weighted									**Equally weighted** $w_1 = w_2 = 0.5$		
Initial errors (%)				**Optimal str. param.**	**Optimal prediction errors**		**Optimal weights**		**Optimal str. param.**	**Optimal prediction errors**	
μ_{f_1}	ε_{f_1}	μ_{f_2}	ε_{f_2}	$\hat{\theta}$	$\hat{c}_1$(%)	$\hat{c}_2$(%)	$\hat{w}_1$	$\hat{w}_2$	$\hat{\theta}$	$\hat{c}_1$(%)	$\hat{c}_2$(%)
0	1	0	0.05	1.00	0.97	4E-4	2E-7	1.00	1.01	0.49	0.49
			0.5	1.00	0.80	7E-4	8E-7	1.00	1.01	0.40	0.40
			1	1.01	0.31	0.31	0.51	0.49	1.01	0.31	0.31
			3	1.02	9E-4	0.14	1.00	4E-5	1.02	0.07	0.07
			5	1.02	9E-4	0.89	1.00	1E-6	1.03	0.45	0.45
		5	0.05	1.10	3.98	0.001	1E-6	1.00	1.06	1.91	1.99
			0.5	1.10	4.15	0.001	1E-7	1.00	1.06	1.99	2.07
			1	1.02	9E-4	4.15	1.00	5E-8	1.06	2.08	2.17
			3	1.02	9E-4	4.84	1.00	3E-8	1.07	2.42	2.54
			5	1.02	0.005	5.52	1.00	1E-6	1.07	2.76	2.92

For comparison purposes, optimal model parameters are evaluated by minimizing the equally weighted error functions. The values of the optimal model parameters $\hat{\theta}$ increase with the increase in the initial uncertainties. For the uncertainty level of μ_{f_2}=0%, the optimal prediction errors are equal for both modes while the initial uncertainty in each mode is in fact different. Therefore, the optimal prediction errors do not give any reasonable information about the uncertainties in the modes. For the

uncertainty level of μ_{f_2}=5%, the optimal prediction errors are almost equal for both modes as in the case of μ_{f_2}=0%. It can be realized that the optimal prediction errors are slightly greater for the second mode when compared to those of the first mode. This may be due to the uncertainty level of μ_{f_2}=5% of the second mode. However, this does not give any reasonable information about the increase in the uncertainties ε_{f_2}. Equally considering the modes that have different uncertainty levels results in the biased estimation of the parameters with unrealistic prediction errors.

The optimal weighting values are inversely proportional to the optimal values of the error functions. Since the resulting error values are too small numbers for the best fitted modes, there exist a considerable difference between the weighting values of best fitted and poorly fitted modes. In fact, the weighting factors for the best fitted ones have very large values relative to the poorly fitted ones. However, normalization of the weighting values to satisfy $\sum_{i=0}^{n} w_i = 1$ causes them to have either a value that is very close to 1 or that very close to 0.

- ***Implementation on a numerical model of an existing ten-story laboratory shear frame***

The updating methodology is implemented on a numerical model of an existing 10-story laboratory frame. The structural model is set with shear frame assumptions since its stiffness is significantly higher than the other direction and no torsional behaviour is expected. The detailed physical properties of the laboratory model can be found in the paper published by Ceylan et al. (2020). The laboratory model and its analytical model are illustrated in Figure 2.2. The stiffness of each story is also shown on the figure.

Modal damping ratios of the first six modes are extracted from experimental impulse response data by an exponential decaying function. Damping ratios of the higher modes are considered to be the same as that of sixth mode. The damping ratios are evaluated as less than 0.2%.

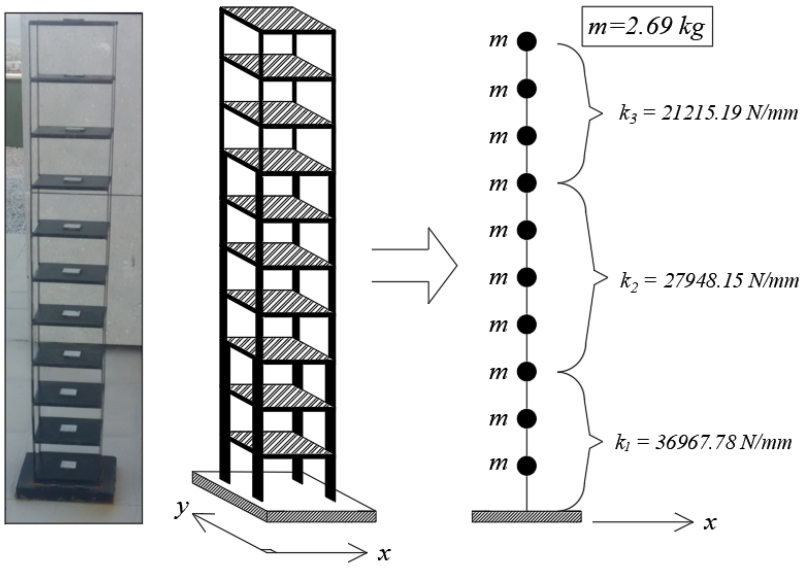

Figure 2.2. 10-story shear frame model

The analytical model is excited by generating a Gaussian white noise excitation signal with a duration of 30 seconds having a sampling frequency of 10 kHz to extract acceleration measurements. The Newmark-β simulation is employed with the constant average acceleration approach. In addition, two different levels of random noise are put into each acceleration response to introduce different noise levels. The aim is to obtain two different modal sets for comparison purposes. Noise is added into each response to get an RMS of 50% and 300% of the RMS of the response itself. The relatively high noise level of 300% is selected on purpose to simulate poor quality data. Acceleration response measurements are created having a duration of 30 seconds and a sampling frequency of 10 kHz. The response data are resampled to a lower sampling frequency of 100 Hz to decrease the sample size of the generated signals.

Modal frequencies, f_n the FE model and experimental damping ratios ξ_n are provided in Table 2.2. Modal parameters, $\hat{f}_n$ and $\hat{\phi}_n$ of the numerical model have been extracted by using the covariance-based stochastic subspace identification technique (SSI-COV) for the simulations with noise levels of 50% and 300%.

Modal shapes, ϕ_n of the FE model and those predicted from the acceleration data with the noise levels of 50% and 300% have been provided in Figure 2.3. In the figure, some of the modal shapes identified from signal with the noise level of 300% are relatively ill-conditioned.

Table 2.2. Modal frequencies (Hz) and damping ratios of the analytical model

# Mode, n	f_n	$\hat{f}_n$ %50	$\hat{f}_n$ %300	ξ_n
1	2.569	2.569	2.555	0.0019
2	7.166	7.171	7.164	0.0018
3	11.592	11.591	11.588	0.0018
4	16.019	16.022	16.021	0.0018
5	19.820	19.812	19.804	0.0017
6	23.627	23.641	23.611	0.0017
7	26.008	26.015	26.050	-
8	28.342	28.330	28.294	-
9	31.070	31.087	31.061	-
10	34.633	34.640	34.668	-

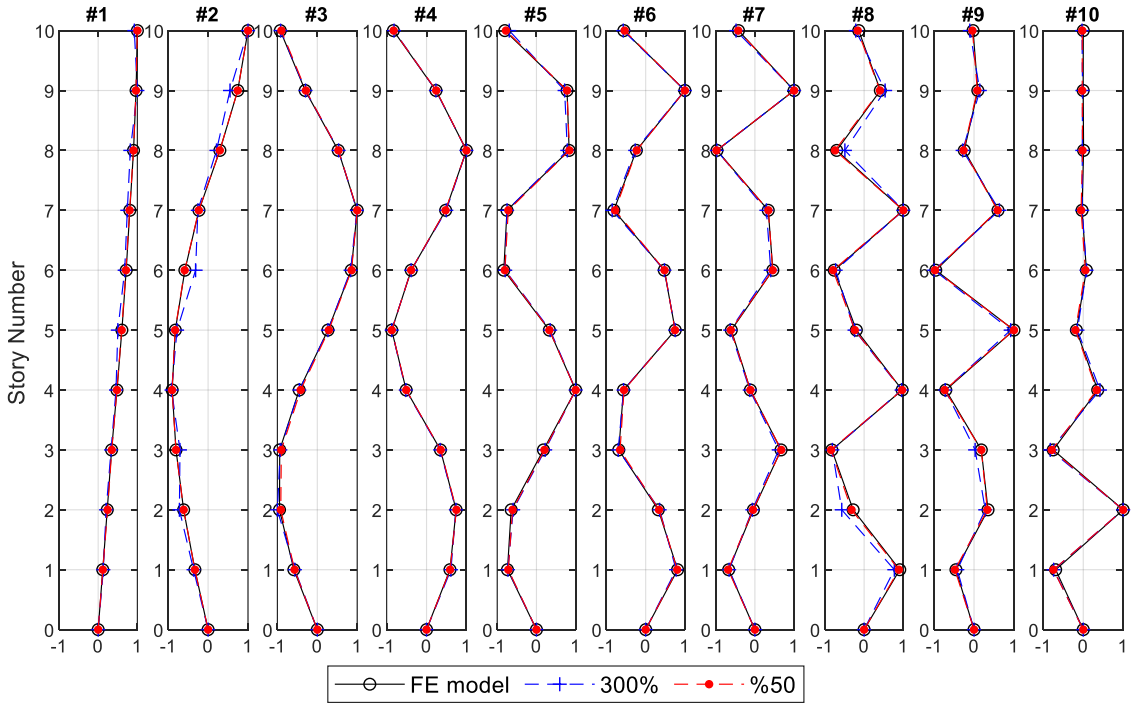

Figure 2.3. Mode shapes identified from the eigenvalue analysis of FE model and those obtained from the noisy signals

For the model updating procedure, the mass of the structure is assumed to be well-known and the model parameter vector $\boldsymbol{\theta}$ is selected to include the stiffness

parameters k_1, k_2 and k_3 to be updated. This updating problem includes 20 sub-objectives which are the error functions $J_{f_n}(\boldsymbol{\theta})$ in equation (2.1) for each modal frequency and $J_{\phi_n}(\boldsymbol{\theta})$ in equation (2.2) for each modal vector defined for n=1,..,10. The single objective function is constructed as a weighted sum of these sub-objectives as in equation (2.3). The optimum values of weighting factors and the parameter $\boldsymbol{\theta}$ have been obtained by simultaneously solving $J(\theta,w)$ in equation (2.3) and the set of equations in (2.22) for i=1, 20. Initial value of each weighting factor is taken to be 0.05. Further, the initial value of the model parameters θ is taken as k_1 = 35000 N/mm, k_2 = 27000 N/mm and k_3 = 20000 N/mm. The optimization problem is solved by the same process discussed in previous two-DOF example. The optimal values of the model parameters $\hat{\theta}_{opt}$ and the weighting factors $\hat{w}$ are provided in Table 2.3.

Equally weighted sums of the error functions are minimized, and the results are also provided for comparison purposes. According to the results, the error functions corresponding to the seventh and tenth modal frequencies are optimally weighted with relatively high value in the analysis with the noise level of 50%. On the contrary, the error function of the sixth modal frequency is optimally weighted with a value of very close to unity in the analysis with the noise level of 300%. Further, smaller weighting values are obtained for the error functions that correspond to the mode shapes. The reason of this is that modal vectors are more sensitive to uncertainty levels.

The optimal prediction error values are also provided in Figure 2.4. The optimal prediction errors of the mode shapes are significantly higher than those of the modal frequencies. By comparing the optimal prediction errors obtained by optimally and equally weighted error functions, it is obvious that the prediction errors obtained by the equally weighted ones have much higher values. This results in the FE models having the optimal model parameters provided in Table 2.3. Errors of the parameters are evaluated as the fractional error between model parameters of the initially constructed FE model and the updated ones. The errors obtained by using the equally weighted error functions are much higher than those of the optimally weighted ones.

Table 2.3. Values of the optimal model parameters and weighting factors

	% 50				**%300**			
	$\widehat{\boldsymbol{\theta}}_{\boldsymbol{opt}}$							
	Optimally weighted	***Error (%)***	***Equally weighted***	***Error (%)***	***Optimally weighted***	***Error (%)***	***Equally weighted***	***Error (%)***
$\hat{k}_1$(N/mm)	37007	0.12	36583	1.05	36715	0.68	35120	5.00
$\hat{k}_2$(N/mm)	27925	0.08	27461	1.74	28017	0.25	27211	2.64
$\hat{k}_3$(N/mm)	21232	0.08	21967	3.54	21195	0.10	23012	8.47
	Optimal weights				***Optimal weights***			
$\widehat{W}_1$	5.70E-8				2.22E-12			
$\widehat{W}_2$	4.16E-20				6.03E-11			
$\widehat{W}_3$	1.95E-19				9.90E-9			
$\widehat{W}_4$	1.15E-18				5.55E-10			
$\widehat{W}_5$	2.90E-20				9.38E-10			
$\widehat{W}_6$	4.20E-20				1.00			
$\widehat{W}_7$	0.9948				8.52E-12			
$\widehat{W}_8$	3.63E-20				2.01E-11			
$\widehat{W}_9$	1.28E-20				4.74E-11			
$\widehat{W}_{10}$	0.0052				3.20E-12			
$\widehat{W}_{11}$	2.28E-22				1.21E-14			
$\widehat{W}_{12}$	8.40E-22				1.53E-15			
$\widehat{W}_{13}$	1.30E-23				5.85E-14			
$\widehat{W}_{14}$	1.83E-22				1.73E-13			
$\widehat{W}_{15}$	1.40E-23				1.53E-15			
$\widehat{W}_{16}$	1.91E-23				3.10E-14			
$\widehat{W}_{17}$	8.05E-23				1.11E-14			
$\widehat{W}_{18}$	6.40E-24				1.28E-15			
$\widehat{W}_{19}$	1.34E-23				2.93E-15			
$\widehat{W}_{20}$	3.03E-24				1.24E-14			

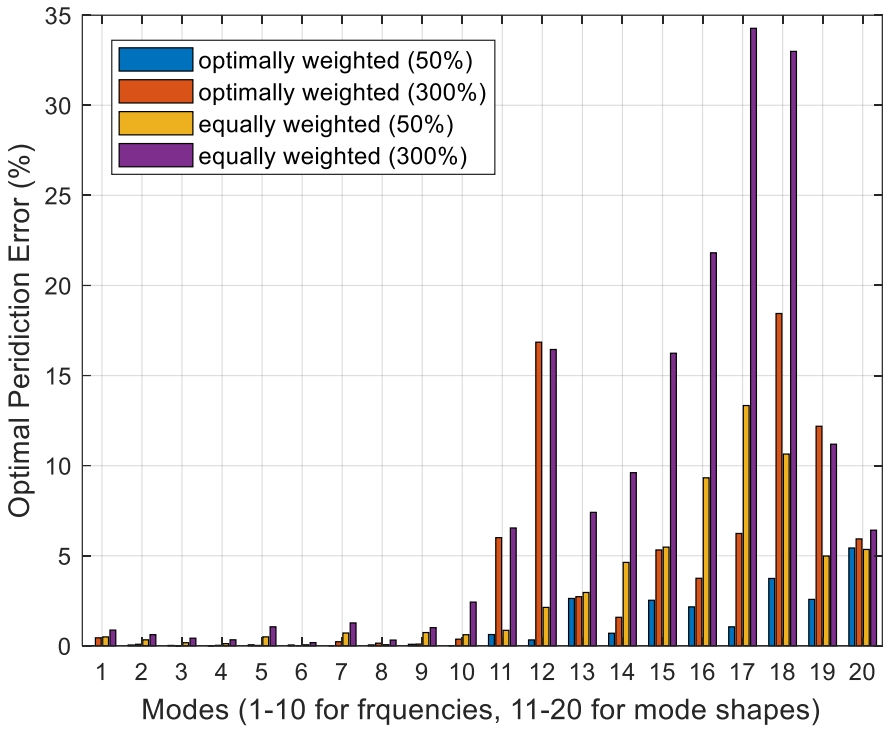

Figure 2.4. Optimal prediction errors for eqaully and optimally weighted analysis

Here, an important conclusion is that although the optimal weighting values of most of the error functions seem nearly zero and seem as if they do not reflect the behavior of the corresponding modal property on the structure, they contribute to the optimization process due to relatively high values of the corresponding error function. This enables the contribution of the corresponding modal property with the high prediction error. The mode shapes of the FE models updated by using optimal weights for the noise levels of 50% and 300% are presented in Figure 2.5. Even though the mode shapes identified for the case of 300% are relatively ill-conditioned, those of the updated ones fit best with those of the initial FE model.

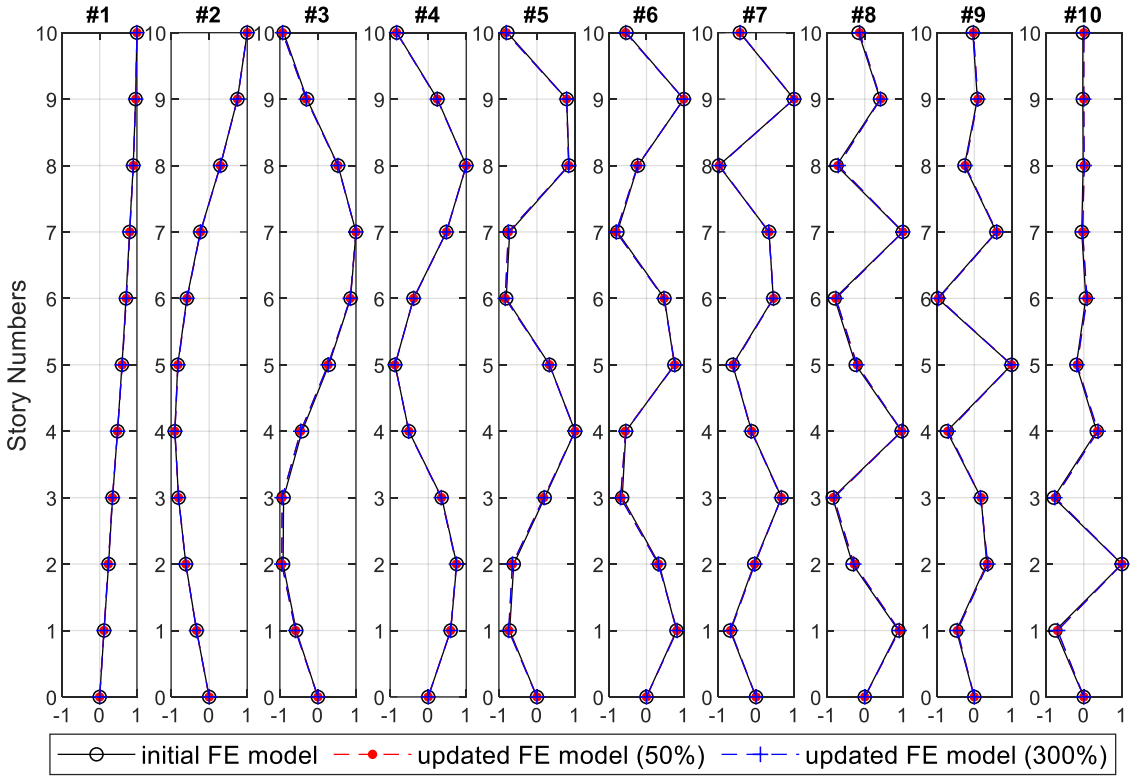

Figure 2.5. Mode shapes of the updated FE models by using optimal weights

Another analysis is carried out on the numerical model to see the difference between the frequentist and the Bayesian approach on the weighting and prediction error values. To this end, 1000 different simulations of the numerical model are performed by introducing different noise levels. This is done to imitate the different excitation levels of various measurement periods as can be encountered in real applications. Then, the modal properties are extracted from each simulation and thus, 1000 different modal data sets are obtained. Afterwards, 10, 100 and 500 samples from these modal data sets are randomly selected, and the sample variance of each modal property has been evaluated for 10, 100, 500 and 1000 samples. In accordance with equations (2.21) and (2.22), these variance values are used to obtain the weighting of the corresponding modal property. The single objective function has been obtained by using the weighted error functions. Calculated weights for the considered samples are presented in Figure 2.6. The optimal prediction errors obtained for the samples are also presented in Figure 2.7. According to this figure, it is obvious that prediction errors obtained for 10 samples are much higher than the other sample sizes. As seen in Figure

2.6, the reason may be the assignment of the relatively high weighting values on the first and fourth eigenfrequency modes for 10 samples because of the insufficient data to obtain the reasonable variance of samples. This causes the inadequate distribution of the weighting values on the modal properties. In addition, it is realized that the prediction error of the modal properties decreases when the sample size is increased. This reveals that the quality of the updating procedure improved with the increase in the number of acquired modal data sets. However, taking such a large number of measurements may not be practical in real applications. The more the sample size is, the results of the frequentist approach get closer to those of a probability distribution defined for the Bayesian approach. This shows the adequacy of the probabilistic approaches to use in the FE model updating procedures.

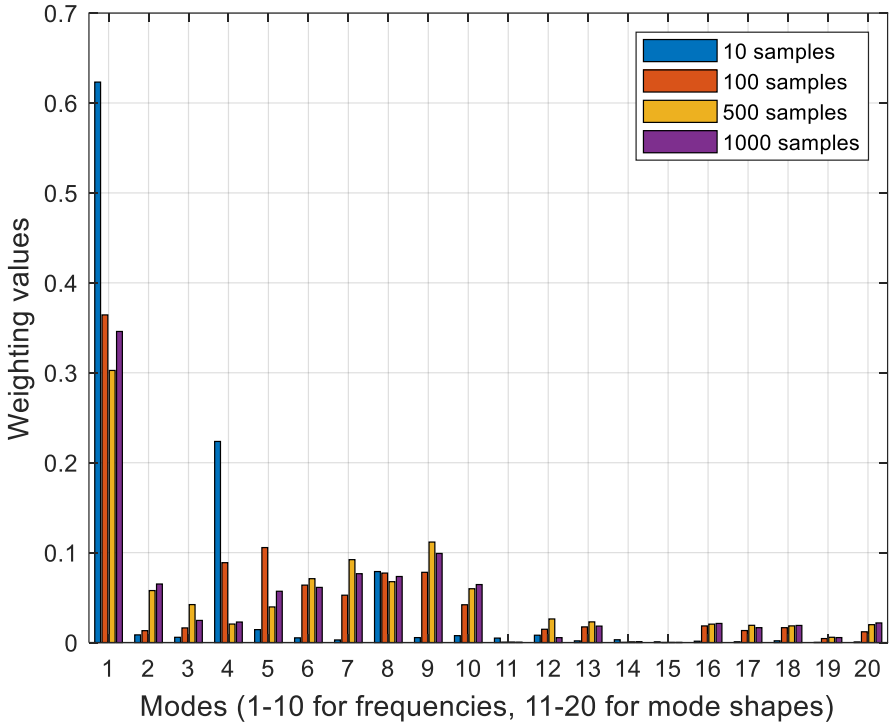

Figure 2.6. Weighting values assigned for 10, 100, 500 and 1000 samples

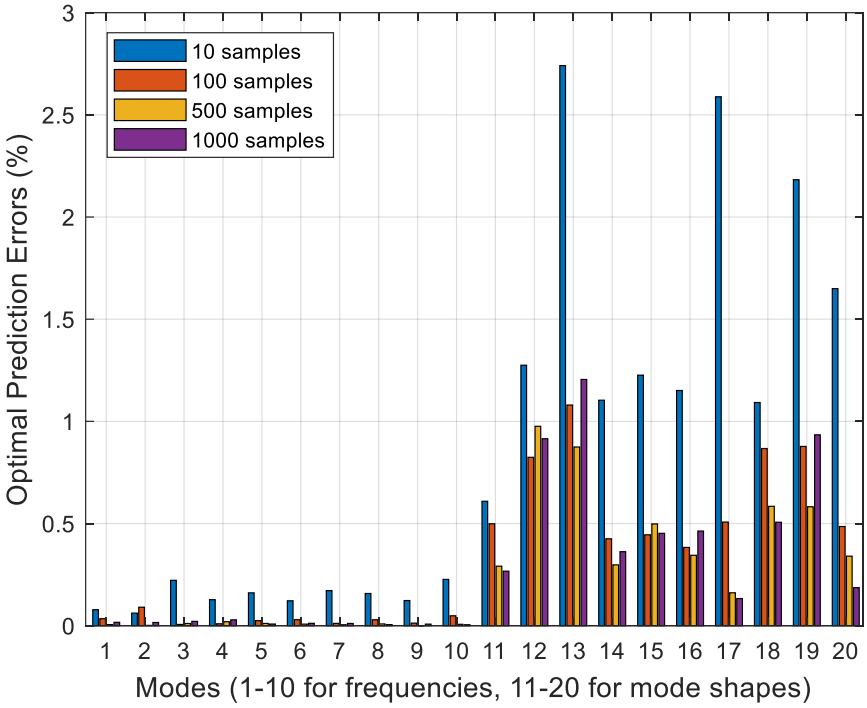

Figure 2.7. Optimal prediction errors obtained for 10, 100, 500 and 1000 samples

2.5. Conclusions

In this chapter, the problems encountered in the FE model updating are addressed when the single objective function is set as the weighted sums of the error functions. It is observed by the performed numerical studies that the equally weighted-least squares approach is problematic as already emphasized in the literature since it does not account for the uncertainties in the updating process. Thus, behavior of the updated structure is inevitably affected by these uncertainties. Further, each mode has different contributions to dynamic behavior of structures and equally weighted-least squares does not account for this, either. In the investigated study, weighting factors are optimally selected to be inversely proportional to the prediction error of each mode. The numerical investigations show that optimal selection of the weights gives reasonable updating results. However, it can be realized that the values of the weightings become too large if the corresponding prediction error is too small. This may result a specific mode to be considered redundantly dominant on the others. Considering the results of two-DOF example, a slight difference between the initial prediction errors of two modes causes the normalized weighting values to be very close to zero or one. The same

situation is encountered in the results of the ten-DOF example. There is no weighting value resulting in the mid-range of zero and one unless the uncertainties are equal. Further, it is shown in the last numerical study that a large amount of measurement data is needed to approach to the adequate probabilistic distributions. In the assumptions during the derivations of the performed procedure, the approximation of the integral in equation (2.20) is valid for β goes to infinity, which corresponds to the number of available data. The numerical results in the first two example is encountered due to the limited amount of generated modal data, which violates this assumption. Therefore, investigated methodology also requires large number of data sets to give reasonable results. This is similar to the situation in frequentist approach as shown by the last numerical example.

The researchers in the literature state that there is still no rational way to assign the weighting factors, but the procedure is problem dependent. As an alternative to using single objectives, many researchers have suggested to use multi-objective functions which do not require any assignment of weighting factors. However, multi-objective optimization results in Pareto solutions, which again requires a decision-making strategy to select the best Pareto optimal parameter. This is almost equivalent to the selection of optimal weights in a single objective problem. Further, Oh et al., (2015) touch on the arbitrariness of the weighting values and propose using the modal participation factors to determine the weighting values with respect to the contribution of the modes on the dynamic characteristics of structures. However, this is also a problem dependent approach.

CHAPTER 3

A TWO-STAGE BAYESIAN MODEL UPDATING METHOD UTILIZING THE CONCEPT OF SYSTEM MODES

3.1. Introduction

Damage detection has a crucial importance among many engineering communities. FE model updating is effectively used by many researchers for structural damage identification purposes. An FE model of a structure is expected to represent the properties of real-life structures. However, it is almost impossible for an FE model to carry all properties of the actual structure. There are various uncertainties that need to be considered during FE model updating. In dynamic-based FE model updating, structural vibrations are measured to extract dynamic characteristics from the measured data. Structural uncertain properties that principally reflect the behavior of the structure are selected as the parameters to be updated. Parameters which minimize the difference between the measured characteristics and those calculated from the FE model are obtained as the best parameters which represent the actual structural behavior. The estimations of these parameters are sensitive to uncertainties that arise because of the limitations in FE modeling of actual structures (referred as modelling error), inevitable existence of measurement noise in the acquired data (referred as measurement error), and inherent variability in structural characteristics because of variations in environmental conditions such as temperature and humidity (Behmanesh and Moaveni, 2015, 2016; Song et al., 2020).

In most of the modal-based FE model updating procedures, a single objective function is set by considering the discrepancies between the modal frequencies and mode shapes which are obtained from the FE model, and their measured counterparts. The following equation is an example of such kind of objective function.

$$J = \sum_{n=1}^{N_m} w_n \left[f_n - \hat{f}_n \right]^2 + \sum_{n=1}^{N_m} \bar{w}_n \left\| \boldsymbol{\phi}_n - \hat{\boldsymbol{\phi}}_n \right\|^2 \tag{3.1}$$

Here, f_n and $\hat{f}_n$ are modal frequency and its measured counterpart for the n^{th} mode, respectively. Similarly, $\boldsymbol{\phi}_n$ and $\hat{\boldsymbol{\phi}}_n$ are the mode shape and its measured counterpart for the n^{th} mode, respectively. w_n and $\bar{w}_n$ are the weighting factors for the corresponding discrepancy term, and N_m is the total number of observed modes. In most of the model updating literature, weighting factors are not determined in a rational way and no uncertainty information is included in such functions as discussed in the previous chapter. It should be noted that there are some published papers in the literature which associate the uncertainty level of each discrepancy term with its corresponding weighting factor to account for the uncertainties such as the studies conducted by Christodoulou et al. (2008), Christodoulou and Papadimitriou (2007) and, Kim and Weck (2005). Christodoulou and Papadimitriou (2007) have used a conventional Bayesian model updating to estimate optimal weighting factors and this study has been investigated by the author in detail in the previous chapter. On the other hand, the most important issue for this type of objective functions is mode matching problem between the modes of the model and measured ones. The model mode corresponding to its measured counterpart must be exactly known to write the objective function in equation (3.1). However, this is difficult for real-life applications. In general, the following problems may be encountered.

- Measured modal data obtained from structures are incomplete with respect to their FE models since some modes of the structures may not be obtained during dynamic tests. For example, some lower or intermediate modes such as torsional ones may not be excited and identified due to the excitation conditions.
- The initial FE model may result in some modes which do not exist for the measured structure, or the order of the modes might be different due to modelling assumptions.
- Some modes may be more affected by local damage compared to other modes and such damage cases may change the order of the modes of the structure. (Yuen, 2010; page:194).

These problems limit the usage of the objective function in equation (3.1) for real-life applications. The concept of "system modes" is introduced in the literature to overcome the mode matching problem. System modes are included in the updating process as additional parameters to be updated. This concept will be further discussed in detail in the following sections.

There are various stochastic model updating (SMU) methods in the literature that account for the uncertainties. In conventional SMU techniques, uncertainties are considered by the statistic-based modelling of the uncertain parameters and the corresponding statistical moments such as their mean and variance are obtained by employing Monte Carlo Simulation methods. However, multiple sets of measured data are needed for such methods and numerous iterations should be performed to evaluate statistical moments and distributions. Dealing with large structures and models makes the computational effort significantly high (Fang et al., 2012; Govers and Link, 2010). Among SMU methods, Bayesian model updating (BMU) approach is widely used in the literature to deal with the uncertainties in a probabilistic manner. The main idea behind BMU is to define the posterior (updated) probability of uncertain parameters by updating prior distributions of the parameters by using measured data. Here, the uncertainties that belong to measured data, FE modelling assumptions and uncertain parameters are modelled to follow a certain probability distribution. This approach also requires the calculation of statistical properties of the measured data which again requires simulations such as Monte Carlo employing multiple sets of data. In the literature, therefore, two-stage BMU framework has gained more attention by researchers. In this framework, the uncertainties of measured data are obtained by using Bayesian Modal Operational Analysis (BAYOMA) in the first stage (Katafygiotis and Yuen, 2001; Yuen and Katafygiotis, 2003, 2001). Thereafter, these uncertainties are employed in the Bayesian model updating process. Hence, need for multiple sets of measured data and statistical simulations are avoided and computational cost is considerably reduced. In these approaches, the concept of rigid constraints and soft constraints is also introduced for the uncertain parameters. When the uncertainty of a parameter is prescribed and is not updated during the updating process, it is considered as rigid constraint for that parameter. On the contrary, if the uncertainty of the parameter is also updated with an initial guess, it is considered as soft constraint. Yuen et al. (2006) have proposed a BMU method which considers the modelling error in the eigenvalue equations. Their procedure requires the uncertainty quantification of the

measured modal data and thus it is a kind of two-stage BMU. They consider a prescribed modeling error uncertainty that is equal for all modes as a rigid constraint and take the mass values as known and not included as a parameter to be updated. Hızal and Turan (2020) have a similar two-stage approach for multiple setups of measurements. Differently from Yuen et al. (2006), they consider the modelling error that is equal for all modes as soft constraint and take the mass values into account as uncertain parameters with small variances. Their study reveals that considering modelling error as soft constraint significantly reduces the computational time and posterior uncertainties in model parameters. Yan and Katafygiotis (2015) used another similar two-stage BMU for multiple setup measurements. They consider the modelling error uncertainty to be different for each mode and update it as soft constraint. In their approach, only the uncertainties of the measured mode shapes are considered and measured eigenvalues are assumed to be well-estimated. Yuen et al. (2006), and Hızal and Turan (2020), however, considered the uncertainties of both measured eigenvalues and mode shapes. The correlation between the measured eigenvalues and mode shapes may induce problems in two-stage BMU because of mode shape scaling (Au and Zhang, 2016; Hızal and Turan, 2020). Therefore, calculation of the correlation between measured eigenvalues and mode shapes are avoided in the literature. Yuen et al. (2006) do not consider this fact and include this correlation in their formulation. However, they use a diagonal posterior covariance matrix for the measured modal data which correspond to uncorrelated measured eigenvalues and mode shapes in all their applications. Yan and Katafygiotis (2015) avoid this fact by assuming measured eigenvalues with zero uncertainties. Hızal and Turan (2020) have introduced a modification into the Bayesian Fast Fourier Transform Approach (BFFTA) proposed by Au (2011) and they derived that measured eigenvalues and mode shapes are uncorrelated by defining norm constraints for mode shapes in the modal identification stage.

This part of the thesis focuses on the two-stage Bayesian Model Updating formulations derived by Çağlayan Hızal in Chapter 5 of his dissertation (Hızal, 2019) and in the published work by Hızal and Turan (2020). Therefore, this study can be considered as a follow-up work. First, their formulations are reformulated for a single setup case assuming that mass values are known with a sufficient accuracy and are not taken as parameters to be updated as Yuen et al. (2006) do. Second, the modelling error uncertainty of eigenvalue equations are considered to be different for each mode and

updated in each iteration as Yan and Katafygiotis (2015) do in their study. In this regard, the study presented in this chapter can be considered as a compilation of these three related studies with minor modifications. Besides, the main objective of this chapter is to compare three different assumptions on modelling error variances considered in the literature. These are investigated under three different cases as follows:

- Case 1: Modelling error variances of eigenvalue equations are considered to be different for each mode and updated in each iteration as soft constraints. Thus, an independent modelling error variance is defined for each mode. This study mainly focuses on this assumption.
- Case 2: Modelling error variances of eigenvalue equations are considered to be the same for each mode and updated in each iteration as a soft constraint. Thus, a single modelling error variance is defined as a soft constraint. This case corresponds to a similar study performed by Hızal and Turan (2020).
- Case 3: Modelling error variance has a prescribed value which is the same for all modes. It is not updated during the updating process and kept as a rigid constraint. This case corresponds to a similar study performed by Yuen (2010).

A comparative numerical application is performed to investigate the influence of the three different assumptions on the Bayesian model updating procedure. Modal identification stage is performed by the proposed method by Hızal (2019) to avoid the calculation of the correlation between the measured eigenvalues and mode shapes. Numerical studies are performed on a numerical twelve-story shear frame model by employing complete and incomplete measured modal data.

3.2. Two-Stage Bayesian Model Updating Utilizing the Concept of System Modes

In this section, a two-stage Bayesian model updating procedure that utilizes the concept of system modes is reformulated by assuming that the modelling error variances of eigenvalue equations are different for each mode and updated in each iteration as soft constraints.

3.2.1. Modal Identification Stage

In two stage approaches, the modal identification phase which takes place as the initial step has a critical role to estimate a reliable probabilistic model for observed modal parameters. In this context, the use of BAYOMA techniques make a successful contribution for better representing the modal parameter distribution. Considering this aspect, BFFTA which has been first proposed by Au (2011) is adopted in this study. Implementing the BFFTA theory in the modal identification phase significantly reduces the computation effort since the likelihood function for the modal parameters of the measured structure can be well estimated. Here, as shown by Hızal (2019), another prominent merit of BFFTA can be considered the fact that it can provide a block diagonal posterior covariance matrix by inclusion of mode shape norm constraints. In this context, a negative log-likelihood function for posterior PDF of modal parameters based on the measured FFT data is defined as below (Au, 2011).

$$L_n(\boldsymbol{\Xi}_n) = -\ln\left\{ p\left(\boldsymbol{\Xi}_n \middle| D\right)\right\} = NN_{f,n}\ln\pi + N_{f,n}(N-1)\ln S_{e,n} + \sum_k \ln(\bar{S}_n D_{k,n} + S_{e,n}) + S_{e,n}^{-1}\kappa_n - \boldsymbol{\psi}_n^T \boldsymbol{\Delta}_n \boldsymbol{\psi}_n \tag{3.2}$$

where $p(\boldsymbol{\Xi}_n \mid D)$ is the posterior probability distribution of modal parameter set, $\boldsymbol{\Xi}_n = \{\lambda_n, \xi_n, \bar{S}_n, S_{e,n}, \boldsymbol{\psi}_n\}$, based on the measurement data D. Here, λ_n is the eigenvalue, ξ_n is the damping ratio, $S_{e,n}$ is the spectral density of the error function, $\bar{S}_n$ is the spectral density of the modal excitation. These are defined as spectrum parameters. $\boldsymbol{\psi}_n$ is the modal shape vector, which has a unit norm for the n^{th} mode. N is the number of measured DOFs and $N_{f,n}$ is the number of data points in the frequency band selected by the user. In addition, following variables are defined by Hızal and Turan (2020) as

$$\kappa_n = \sum_k \mathbf{F}_k^* \mathbf{F}_k$$

$$\boldsymbol{\Delta}_n = \sum_k \frac{\bar{S}_n D_{k,n} S_{e,n}^{-1}}{\bar{S}_n D_{k,n} + S_{e,n}} \mathrm{Re}(\mathbf{F}_k^* \mathbf{F}_k) \tag{3.3}$$

$$D_{k,n} = \frac{1}{(1-\beta_{k,n})^2 + (4\xi_n^2 \beta_{k,n})} \quad ; \quad \beta_{k,n} = \frac{\omega_n^2}{\omega_k^2} \quad ; \quad \omega_k = 2\pi f_k$$

where $\mathbf{F}_k$ represents the Fast Fourier Transform (FFT) vector of the measured acceleration data and f_k is the excitation frequency.

Optimal values of the modal parameters can be estimated by minimizing the objective function in equation (3.2) by defining an extra norm constraint term for $\boldsymbol{\psi}_n$ to ensure the norm of the mode shapes to be unity. Then, the posterior probability distribution of modal parameters is assumed to follow a Gaussian distribution to obtain the most probable values (MPVs) and posterior uncertainties of the optimal modal parameters as

$$p(\boldsymbol{\Xi}_n \,|\mathbf{Z}_k) = \exp\left[-\frac{1}{2}(\boldsymbol{\Xi}_n - \hat{\boldsymbol{\Xi}}_n)^T \mathbf{H}_{\hat{\boldsymbol{\Xi}}_n} (\boldsymbol{\Xi}_n - \hat{\boldsymbol{\Xi}}_n)\right] \tag{3.4}$$

where $\hat{\boldsymbol{\Xi}}_n$ is the set of MPVs of the modal parameters and $\mathbf{Z}_k$ is the augmented FFT vector of measured acceleration data, which includes real and imaginary parts of the FFT vector of $\mathbf{F}_k$. Here, $\mathbf{H}_{\hat{\boldsymbol{\Xi}}_n}$ is the Hessian matrix of the objective function, which is obtained by second order derivatives of $L_n(\boldsymbol{\Xi}_n)$ at MPV subjecting a norm constraint term for $\boldsymbol{\psi}_n$. Hızal (2019) has shown that no correlation exists between the spectrum parameters of $\boldsymbol{\Xi}_{s,n} = \{\lambda_n, \xi_n, \bar{S}_n, S_{e,n}\}$ and $\boldsymbol{\psi}_n$ by the help of defined norm constraint term for $\boldsymbol{\psi}_n$. This results in a block diagonal Hessian $\mathbf{H}_{\hat{\boldsymbol{\Xi}}_n}$ matrix, which enables that the spectrum parameters can be separated from the mode shapes. Thus, the Hessian matrix $\mathbf{H}_{\hat{\boldsymbol{\Xi}}_n}$ is written as (Hızal, 2019; Hızal and Turan, 2020)

$$\mathbf{H}_{\hat{\boldsymbol{\Xi}}_n} = \begin{bmatrix} \mathbf{H}_{\hat{\boldsymbol{\Xi}}_{s,n}} & \mathbf{0} \\ \mathbf{0} & \mathbf{H}_{\hat{\boldsymbol{\psi}}_n} \end{bmatrix} \tag{3.5}$$

where $\mathbf{H}_{\hat{\boldsymbol{\Xi}}_{s,n}}$ is the Hessian matrix of the measured spectrum parameters, which is obtained from the second order derivatives of $L_n(\boldsymbol{\Xi}_n)$, and $\mathbf{H}_{\hat{\boldsymbol{\Psi}}_n}$ is the Hessian matrix of the measured mode shapes, which is obtained from the second order derivatives of the objective function, which is constructed by using $L_n(\boldsymbol{\Xi}_n)$ and the norm constraint term for $\boldsymbol{\psi}_n$. Hızal (2019) shows and proves that $\hat{\boldsymbol{\psi}}_n$ is the eigenvector of $\mathbf{H}_{\hat{\boldsymbol{\Psi}}_n}$ which

corresponds to its zero eigenvalue. Thus, he also proves that $\widehat{\boldsymbol{\psi}}_n$ is the null vector of $\mathbf{H}_{\widehat{\boldsymbol{\psi}}_n}$.

3.2.2. Model Updating Stage

In this section, posterior probability distributions of the modal parameters that are obtained in the modal identification stage are employed as the prior probability distributions of prediction errors between the measured and system modes.

3.2.2.1. Concept of System Modes

Extra variables, referred as "system modes" in the literature (Vanik et al., 2000), are employed in model updating procedure to solve the mode matching problem. System modes are considered to reflect the actual eigenvalues and mode shapes of the measured structure independent from the modes of its FE model. There may be high discrepancies between the modes of the model and measured modes due to mathematical modelling assumptions (Beck et al., 2001; Yan and Katafygiotis, 2015; Yuen, 2010). In this context, there are three different mode definitions in this chapter which are measured modes, modes obtained from the FE model and the system modes. For the model updating procedures that use this concept, discrepancies between system modes and measured modes are considered and system modes are updated to obtain those that best fit the measured modes. Further, system modes are connected to the FE model and model parameters via eigenvalue equations. It will be seen later that modes obtained from the eigenvalue decomposition of the FE model are never used in the procedure, which solves the mode matching issue. Here, the system mode shapes are obtained to cover all DOFs of the FE model even though spatially incomplete mode shapes are measured from the actual structure. Thus, modal expansion techniques are not required to identify the unmeasured components of the measured mode shapes.

3.2.2.2. Structural Model and Parametrization of Stiffness Matrix

Let a linear structural model $\mathcal{M}$ be assumed for a convenient parametrization of the stiffness matrix with N_d DOFs. The model is parameterized by defining the

parametric stiffness matrix, $\mathbf{K}(\boldsymbol{\theta})$ with a size of $N_d \times N_d$, in terms of a linear combination of substructure stiffness matrices, $\mathbf{K}_i$ as;

$$\mathbf{K}(\boldsymbol{\theta}) = \mathbf{K}_0 + \sum_{i=1}^{N_\theta} \theta_i \mathbf{K}_i \tag{3.6}$$

where $\mathbf{K}_0$ is the portion of the stiffness matrix which is not affected by the updating procedure. The substructure stiffness matrix, $\mathbf{K}_i$, is the elementwise nominal stiffness matrix extended to the size of $N_d \times N_d$. Thus, they represent the contributions of a part of the structure to the system stiffness matrix. $\boldsymbol{\theta} = [\ \theta_1\ \ \theta_2\ \ \theta_3 \ldots \theta_{N_\theta}]^T$ is the vector of stiffness scaling factors $\theta_i \in R^{N_\theta}$ which are required to be updated to modify $\mathbf{K}_i$ so that the FE model can represent the actual structural conditions. Here, N_θ represents the total number of stiffness scaling factors. In the literature, there is another definition for θ_i and $\mathbf{K}_i$ in the literature. θ_i can be employed as a stiffness parameter (stiffness value) instead of considering it as a scaling factor. In this case, θ_i is the i^{th} stiffness parameter and $\mathbf{K}_i$ are the corresponding non-parametric and constant matrices which include just the geometrical information of a specific portion of the structure. In this chapter, θ_i is taken as the stiffness parameter and $\mathbf{K}_i$ is considered as the corresponding non-parametric and constant matrix.

Beck et al. (1999) states that expressing the stiffness matrix as the linear parametrization that is given in equation (3.6) is convenient for the optimization process and sufficient to identify the presence and location of damage.

For the framework presented above, parametrization of stiffness matrix is performed in element-level since practical experiences show that particular parts of a structure prone to varying levels of damage. Real-world examples show that the change in mass induced by local damage is significantly less than the variance in local stiffness. Further, it is well-known that mass matrix can be obtained with sufficient accuracy and corresponding uncertainties can be considered as negligible. Therefore, in most studies, the variation in mass is not considered and the stiffness parameters are updated only. To this end, mass matrix is assumed to be well-known and it is not considered as a parameter to be updated in this chapter.

3.2.2.3. Probability Model for the Stiffness Parameters

The prior probability distribution of $\boldsymbol{\theta}$ is considered to follow multivariate truncated Gaussian distribution which truncates the negative values of $\boldsymbol{\theta}$ since the negative values are physically meaningless for the stiffness parameters.

The prior PDF of $\boldsymbol{\theta}$ with mean value of $\hat{\boldsymbol{\theta}}_0$ and with covariance matrix of $\boldsymbol{\Sigma}_{\boldsymbol{\theta}}$ can be defined, assuming each stiffness parameter θ_i to be linearly independent, as

$$p(\boldsymbol{\theta}) = \begin{cases} \dfrac{1}{\sqrt{(2\pi)^{N\theta}\left|\boldsymbol{\Sigma}_{\boldsymbol{\theta}}\right|}} \exp\left[-\dfrac{1}{2}\left(\boldsymbol{\theta}-\hat{\boldsymbol{\theta}}_0\right)^T \boldsymbol{\Sigma}_{\boldsymbol{\theta}}^{-1}\left(\boldsymbol{\theta}-\hat{\boldsymbol{\theta}}_0\right)\right], & for\,each\ \theta_i > 0 \\ 0, & for\,any\ \theta_i < 0 \end{cases} \tag{3.7}$$

Here, $\hat{\boldsymbol{\theta}}_0$ is the vector of prior MPVs of the stiffness parameters and it should be selected as the nominal parameters that represent the nominal FE model. $\boldsymbol{\Sigma}_{\boldsymbol{\theta}}$ is the prior covariance matrix of the stiffness parameters and it represents the uncertainty in the nominal FE model before the model updating procedure. Since each θ_i is assumed linearly independent, $\boldsymbol{\Sigma}_{\boldsymbol{\theta}}$ is a diagonal matrix whose diagonal elements consist of the prior variance of each stiffness parameter.

3.2.2.4. Probability Model for the Eigenvalue-equation Errors

The standard eigenvalue equation for a dynamic system is written as;

$$\mathbf{K}(\boldsymbol{\theta})\bar{\boldsymbol{\phi}}_n = \bar{\lambda}_n \mathbf{M}\bar{\boldsymbol{\phi}}_n \tag{3.8}$$

where $\bar{\lambda}_n$ and $\bar{\boldsymbol{\phi}}_n$ are the eigenvalues and mode shapes for the n^{th} mode, respectively, which are obtained from the eigenvalue decomposition of the FE model. $\mathbf{M}$ denotes the mass matrix with a size of $N_d \times N_d$ and it is assumed to be sufficiently known. However, the n^{th} mode of the measured structure may not correspond to the n^{th} mode of the FE model because of the mode matching problems explained in the introduction part. Therefore, eigenvalues and mode shapes of the FE model are replaced by the system eigenvalues and system mode shapes to construct the eigenvalue equations. This operation inevitably introduces an uncertainty in the eigenvalue equation. To this end,

an error vector is included to account for the discrepancies between the system modes and FE model as

$$\mathbf{K}(\boldsymbol{\theta})\boldsymbol{\phi}_n = \lambda_n \mathbf{M}\boldsymbol{\phi}_n + \boldsymbol{\varepsilon}_n \tag{3.9}$$

Rearranging equation (3.9), following error vector is obtained as

$$\boldsymbol{\varepsilon}_n = \left[\mathbf{K}(\boldsymbol{\theta}) - \lambda_n \mathbf{M}\right]\boldsymbol{\phi}_n \tag{3.10}$$

where $\boldsymbol{\varepsilon}_n$ is the modelling error vector for the n^{th} mode and it is modelled as the independent Gaussian variables with a zero-mean value and the covariance matrix of $\boldsymbol{\Sigma}_{eq,n}$ as;

$$\boldsymbol{\varepsilon}_n \sim N(0, \boldsymbol{\Sigma}_{eq,n}) \tag{3.11}$$

Thus, system modes are mathematically connected with the FE model by introducing an error definition in-between.

The prior PDF for the system eigenvalue and system mode shape of the n^{th} mode is defined by selecting a Gaussian distribution as a probability model;

$$p(\lambda_n, \boldsymbol{\phi}_n, \boldsymbol{\Sigma}_{eq,n} \mid \boldsymbol{\theta}) = \frac{1}{\sqrt{(2\pi)^{N_d} \left|\boldsymbol{\Sigma}_{eq,n}\right|}} \exp\left[-\frac{1}{2}\boldsymbol{\varepsilon}_n{}^T \boldsymbol{\Sigma}_{eq,n}^{-1} \boldsymbol{\varepsilon}_n\right] \tag{3.12}$$

where, $\boldsymbol{\Sigma}_{eq,n}$ is the prior covariance matrix for the eigenvalue-equation errors. The uncertainty in these equations for a specific mode n is assumed to be independent and identically distributed. Therefore, it is defined for the n^{th} mode as

$$\boldsymbol{\Sigma}_{eq,n} = S_{eq,n}\mathbf{I}_{N_d} \tag{3.13}$$

Where $\mathbf{I}_{N_d}$ denotes $N_d \times N_d$ identity matrix and $S_{eq,n}$ represents the prior variance of modelling error for the n^{th} mode.

By assuming that modelling error is also independent for different modes of the selected structural model and defining

$$\boldsymbol{\Gamma}_n = \mathbf{K}(\boldsymbol{\theta}) - \lambda_n \mathbf{M} \tag{3.14}$$

one can define the following prior PDF;

$$\begin{aligned} p(\boldsymbol{\lambda}, \boldsymbol{\Phi}, \boldsymbol{\Sigma}_{eq} \,|\, \boldsymbol{\theta}) &= \prod_{n=1}^{N_m} p(\lambda_n, \boldsymbol{\phi}_n, \boldsymbol{\Sigma}_{eq,n} \,|\, \boldsymbol{\theta}) \\ &= \prod_{n=1}^{N_m} \left[2\pi S_{eq,n} \right]^{-\frac{N_d}{2}} \exp\left[-\frac{1}{2} \boldsymbol{\varepsilon}_n{}^T S_{eq,n}^{-1} \mathbf{I}_{N_d} \boldsymbol{\varepsilon}_n \right] \\ &= \prod_{n=1}^{N_m} \left[2\pi S_{eq,n} \right]^{-\frac{N_d}{2}} \exp\left[-\frac{1}{2} \boldsymbol{\phi}_n^T \boldsymbol{\Gamma}_n^T S_{eq,n}^{-1} \mathbf{I}_{N_d} \boldsymbol{\phi}_n \boldsymbol{\Gamma}_n \right] \end{aligned} \tag{3.15}$$

where $\boldsymbol{\lambda} = [\lambda_1 \;\; \lambda_2 \;\; \lambda_3 \ldots \lambda_{N_m}]$ is the vector of system eigenvalues, $\boldsymbol{\Phi} = [\boldsymbol{\phi}_1 \;\; \boldsymbol{\phi}_2 \;\; \boldsymbol{\phi}_3 \ldots \boldsymbol{\phi}_{Nm}]$ is the matrix of system mode shapes, $\boldsymbol{\Sigma}_{eq}$ represents the covariance matrix whose diagonal elements consist of the set $\{\boldsymbol{\Sigma}_{eq,1}, \boldsymbol{\Sigma}_{eq,2}, \boldsymbol{\Sigma}_{eq,3}, \ldots, \boldsymbol{\Sigma}_{eq,N_m}\}$. For simplicity in the later formulations, prior variances of the modelling error are collected in the set of $\mathbf{S_{eq}} = \{S_{eq,1}, S_{eq,2}, S_{eq,3}, \ldots, S_{eq,N_m}\}$.

3.2.2.5. Probability Model for the Discrepancy between Eigenvalues

Measured eigenvalues can be related to the system eigenvalues by assuming a prediction error in-between as

$$\hat{\lambda}_n = \lambda_n + \varepsilon_{\hat{\lambda}_n} \tag{3.16}$$

where $\hat{\lambda}_n$ is the measured eigenvalue for the n^{th} mode and the error term $\varepsilon_{\hat{\lambda}_n}$ is modeled to follow a Gaussian distribution that has a zero-mean and the variance of $S_{\hat{\lambda}_n}$ as;

$$\varepsilon_{\hat{\lambda}_n} \sim N(0, S_{\hat{\lambda}_n}) \tag{3.17}$$

Prior probability distribution for the discrepancy between system eigenvalues, λ_n and measured eigenvalues, $\hat{\lambda}_n$ of the n^{th} mode can be defined by assuming a Gaussian probability model. Since the MPVs and prior uncertainties of the measured eigenvalues are already known from the modal identification process, this prior PDF is written as a likelihood function as follows;

$$p(\hat{\lambda}_n, S_{\hat{\lambda}_n} \mid \lambda_n) = \frac{1}{\sqrt{2\pi S_{\hat{\lambda}_n}}} \exp\left[-\frac{\left(\hat{\lambda}_n - \lambda_n\right)^2}{2 S_{\hat{\lambda}_n}} \right] \tag{3.18}$$

where $S_{\hat{\lambda}_n}$ denotes the prior variance for the measured eigenvalues of $\hat{\lambda}_n$ and it is obtained in the Bayesian modal identification process.

The prediction error is assumed to be independent for different modes of the selected structural model and one can define the following prior PDF;

$$\begin{aligned} p(\hat{\boldsymbol{\lambda}}, \boldsymbol{\Sigma}_{\hat{\boldsymbol{\lambda}}} \mid \boldsymbol{\lambda}) &= \prod_{n=1}^{N_m} p(\hat{\lambda}_n, S_{\hat{\lambda}_n} \mid \lambda_n) \\ &= \prod_{n=1}^{N_m} \frac{1}{\sqrt{2\pi S_{\hat{\lambda}_n}}} \exp\left[-\frac{\left(\hat{\lambda}_n - \lambda_n\right)^2}{2 S_{\hat{\lambda}_n}} \right] \end{aligned} \tag{3.19}$$

where $\hat{\boldsymbol{\lambda}} = [\hat{\lambda}_1 \;\; \hat{\lambda}_2 \;\; \hat{\lambda}_3 \; \ldots \; \hat{\lambda}_{N_m}]$ is the vector of measured eigenvalues and $\boldsymbol{\Sigma}_{\hat{\boldsymbol{\lambda}}}$ represents the prior covariance matrix whose diagonal elements consist of the set $\{S_{\hat{\lambda}_1}, S_{\hat{\lambda}_2}, S_{\hat{\lambda}_3}, \ldots, S_{\hat{\lambda}_{N_m}}\}$

3.2.2.6. Probability Model for the Discrepancy between Mode Shapes

In this study, structures are assumed to be measured with a single setup to obtain the required vibration data. However, in most real-life applications, measured DOFs of structures are smaller than those of their FE model. Mode shape components of the model should be matched with their spatially incomplete measured counterparts. Since direct usage of FE model mode shapes is avoided in this study to overcome mode

matching problem, components of the system mode shapes have been matched with their measured counterparts. To this end, following relation can be written

$$\tilde{\boldsymbol{\phi}}_n = \mathbf{L}_0 \boldsymbol{\phi}_n \tag{3.20}$$

where $\mathbf{L}_0$ is the selection matrix consisting of 1's and 0's to pick the components of the system mode shape, $\boldsymbol{\phi}_n$, which correspond to measured DOFs only, and $\tilde{\boldsymbol{\phi}}_n$ is the vector including the corresponding components of $\boldsymbol{\phi}_n$. Then, measured mode shapes $\hat{\boldsymbol{\psi}}_n$ can be related to $\tilde{\boldsymbol{\phi}}_n$ for the n^{th} mode by including a prediction error as

$$\begin{aligned} \hat{\boldsymbol{\psi}}_n &= \tilde{\boldsymbol{\phi}}_n + \boldsymbol{\varepsilon}_{\hat{\boldsymbol{\psi}}_n} \\ &= \mathbf{L}_0 \boldsymbol{\phi}_n + \boldsymbol{\varepsilon}_{\hat{\boldsymbol{\psi}}_n} \end{aligned} \tag{3.21}$$

where $\boldsymbol{\varepsilon}_{\hat{\boldsymbol{\psi}}_n}$ is the prediction-error vector consisting of the error term for each mode shape component and it is modelled as Gaussian variables with zero-means and the covariance matrix of $\boldsymbol{\Sigma}_{\hat{\psi}_n}$ as;

$$\boldsymbol{\varepsilon}_{\hat{\boldsymbol{\psi}}_n} \sim N(0, \boldsymbol{\Sigma}_{\hat{\boldsymbol{\psi}}_n}) \tag{3.22}$$

Discrepancy between $\tilde{\boldsymbol{\phi}}_n$ and $\hat{\boldsymbol{\psi}}_n$ should be considered to construct the probability model. Here, the measured mode shapes are normalized to have a unit norm. Therefore, $\tilde{\boldsymbol{\phi}}_n$ should also have unit norm so that the discrepancy in equation (3.21) can be defined. Therefore, discrepancy between $\frac{\tilde{\boldsymbol{\phi}}_n}{\|\tilde{\boldsymbol{\phi}}_n\|}$ and $\hat{\boldsymbol{\psi}}_n$ should be considered instead of $\tilde{\boldsymbol{\phi}}_n$ and $\hat{\boldsymbol{\psi}}_n$. Note that the resulting vector $\frac{\tilde{\boldsymbol{\phi}}_n}{\|\tilde{\boldsymbol{\phi}}_n\|}$ is constrained to have unit norm.

Here, $\boldsymbol{\Sigma}_{\hat{\psi}_n}$ is the prior covariance matrix that is used to define the uncertainties in the prediction error vector $\boldsymbol{\varepsilon}_{\hat{\boldsymbol{\psi}}_n}$ and it is also the posterior covariance matrix for $\hat{\boldsymbol{\psi}}_n$ obtained in Bayesian modal identification process. However, it should be kept in mind that $\boldsymbol{\Sigma}_{\hat{\psi}_n}$ cannot be obtained explicitly since the Bayesian modal identification process does not output an invertible Hessian matrix, $\mathbf{H}_{\hat{\psi}_n}$, of the measured mode shapes.

Prior probability distribution for the discrepancy between $\frac{\tilde{\boldsymbol{\phi}}_n}{\|\tilde{\boldsymbol{\phi}}_n\|}$ and measured mode shapes, $\hat{\boldsymbol{\psi}}_n$ of the n^{th} mode can be defined by assuming a Gaussian probability model. Since the MPVs and prior uncertainties of the measured mode shapes are already known from the modal identification process, this prior PDF is written as a likelihood function as follows;

$$p(\hat{\boldsymbol{\psi}}_n, \mathbf{H}_{\hat{\boldsymbol{\psi}}_n} \mid \tilde{\boldsymbol{\phi}}_n) \approx \exp\left[-\frac{1}{2}\left(\frac{\tilde{\boldsymbol{\phi}}_n}{\|\tilde{\boldsymbol{\phi}}_n\|} - \hat{\boldsymbol{\psi}}_n \right)^T \mathbf{H}_{\hat{\boldsymbol{\psi}}_n} \left(\frac{\tilde{\boldsymbol{\phi}}_n}{\|\tilde{\boldsymbol{\phi}}_n\|} - \hat{\boldsymbol{\psi}}_n \right) \right] \tag{3.23}$$

Substituting equation (3.20) into equation (3.23), one can obtain the following PDF

$$p(\hat{\boldsymbol{\psi}}_n, \mathbf{H}_{\hat{\boldsymbol{\psi}}_n} \mid \boldsymbol{\phi}_n) = \exp\left[-\frac{1}{2}\left(\frac{\mathbf{L}_0 \boldsymbol{\phi}_n}{\|\mathbf{L}_0 \boldsymbol{\phi}_n\|} - \hat{\boldsymbol{\psi}}_n \right)^T \mathbf{H}_{\hat{\boldsymbol{\psi}}_n} \left(\frac{\mathbf{L}_0 \boldsymbol{\phi}_n}{\|\mathbf{L}_0 \boldsymbol{\phi}_n\|} - \hat{\boldsymbol{\psi}}_n \right) \right] \tag{3.24}$$

It should be noticed that the Hessian matrix $\mathbf{H}_{\hat{\psi}_n}$ is introduced in equations (3.23) and (3.24) since $\boldsymbol{\Sigma}_{\hat{\psi}_n}$ cannot be obtained.

By assuming that the prediction error vectors are also independent for different modes of the selected structural model, one can define the following prior PDF;

$$\begin{aligned} p(\hat{\boldsymbol{\psi}}, \mathbf{H}_{\hat{\boldsymbol{\psi}}} \mid \boldsymbol{\Phi}) &= \prod_{n=1}^{N_m} p(\hat{\boldsymbol{\psi}}_n, \mathbf{H}_{\hat{\boldsymbol{\psi}}_n} \mid \boldsymbol{\phi}_n) \\ &= \prod_{n=1}^{N_m} \exp\left[-\frac{1}{2}\left(\frac{\mathbf{L}_0 \boldsymbol{\phi}_n}{\|\mathbf{L}_0 \boldsymbol{\phi}_n\|} - \hat{\boldsymbol{\psi}}_n \right)^T \mathbf{H}_{\hat{\boldsymbol{\psi}}_n} \left(\frac{\mathbf{L}_0 \boldsymbol{\phi}_n}{\|\mathbf{L}_0 \boldsymbol{\phi}_n\|} - \hat{\boldsymbol{\psi}}_n \right) \right] \end{aligned} \tag{3.25}$$

where $\hat{\boldsymbol{\psi}} = [\hat{\boldsymbol{\psi}}_1 \ \hat{\boldsymbol{\psi}}_2 \ \hat{\boldsymbol{\psi}}_3 \ \ldots \ \hat{\boldsymbol{\psi}}_{Nm}]$ denotes the vector of measured mode shapes and $\mathbf{H}_{\hat{\psi}}$ represents the block diagonal Hessian matrix whose diagonal elements consist of the set $\{\mathbf{H}_{\hat{\psi}_1}, \mathbf{H}_{\hat{\psi}_2}, \mathbf{H}_{\hat{\psi}_3}, \ldots, \mathbf{H}_{\hat{\psi}_{Nm}}\}$.

3.2.2.7. Posterior (updated) Probability Model for the Parameters to be Updated

Defining the set of all parameters to be updated as $\boldsymbol{\Theta} = \{\boldsymbol{\theta}, \boldsymbol{\lambda}, \boldsymbol{\Phi}, \mathbf{S_{eq}}\}$ and the set of all measured modal data as $\hat{\boldsymbol{\Omega}} = \{\hat{\boldsymbol{\lambda}}, \hat{\boldsymbol{\psi}}, \boldsymbol{\Sigma}_{\hat{\boldsymbol{\lambda}}}, \mathbf{H}_{\hat{\boldsymbol{\psi}}}\}$, and by using the Bayes' Theorem, posterior probability of the parameters $\boldsymbol{\Theta}$ conditioned on the measured modal data $\hat{\boldsymbol{\Omega}}$ is written as

$$p(\boldsymbol{\Theta} \,|\, \hat{\boldsymbol{\Omega}}) = c_0\, p(\hat{\boldsymbol{\Omega}} \,|\, \boldsymbol{\Theta})\, p(\boldsymbol{\Theta}) \tag{3.26}$$

where $c_0 = 1 / p(\hat{\boldsymbol{\Omega}})$. Since it does not depend on the parameters of $\boldsymbol{\Theta}$, it services as a normalizing constant so that the posterior probability function $p(\boldsymbol{\Theta} \mid \hat{\boldsymbol{\Omega}})$ integrates to 1. Here, the likelihood function $p(\hat{\boldsymbol{\Omega}} \mid \boldsymbol{\Theta})$ is defined as

$$\begin{aligned} p(\hat{\boldsymbol{\Omega}} \,|\, \boldsymbol{\Theta}) &= p(\hat{\boldsymbol{\lambda}}, \hat{\boldsymbol{\psi}}, \boldsymbol{\Sigma}_{\hat{\boldsymbol{\lambda}}}, \mathbf{H}_{\hat{\boldsymbol{\psi}}}) \\ &= p(\hat{\boldsymbol{\lambda}}, \boldsymbol{\Sigma}_{\hat{\boldsymbol{\lambda}}} \,|\, \boldsymbol{\lambda})\, p(\hat{\boldsymbol{\psi}}, \mathbf{H}_{\hat{\boldsymbol{\psi}}} \,|\, \boldsymbol{\Phi}) \end{aligned} \tag{3.27}$$

and prior PDF, $p(\boldsymbol{\Theta})$, of the parameters to be updated are defined as

$$\begin{aligned} p(\boldsymbol{\Theta}) &= p(\boldsymbol{\theta}, \boldsymbol{\lambda}, \boldsymbol{\Phi}, \boldsymbol{\Sigma}_{eq}) \\ &= p(\boldsymbol{\lambda}, \boldsymbol{\Phi}, \boldsymbol{\Sigma}_{eq} \,|\, \boldsymbol{\theta})\, p(\boldsymbol{\theta}) \end{aligned} \tag{3.28}$$

Substituting equations (3.27) and (3.28) into equation (3.26), posterior PDF of $\boldsymbol{\Theta}$ conditioned on $\hat{\boldsymbol{\Omega}}$ can be written as follows

$$p(\boldsymbol{\Theta} \,|\, \hat{\boldsymbol{\Omega}}) = c_0\, p(\hat{\boldsymbol{\lambda}}, \boldsymbol{\Sigma}_{\hat{\boldsymbol{\lambda}}} \,|\, \boldsymbol{\lambda})\, p(\hat{\boldsymbol{\psi}}, \mathbf{H}_{\hat{\boldsymbol{\psi}}} \,|\, \boldsymbol{\Phi})\, p(\boldsymbol{\lambda}, \boldsymbol{\Phi}, \boldsymbol{\Sigma}_{eq} \,|\, \boldsymbol{\theta})\, p(\boldsymbol{\theta}) \tag{3.29}$$

MPVs of the parameters, $\boldsymbol{\Theta}$, conditioned on the measured modal data can be obtained by maximizing the posterior PDF given in equation (3.29). It is known in the literature

that more convenient strategy to solve such optimization problem is to minimize the negative log-likelihood function of the posterior PDF.

3.2.2.8. Negative Log-likelihood Function of the Posterior Distribution

Negative log-likelihood function of the posterior PDF which is given in equation (3.29) can be written as

$$\begin{aligned} L(\boldsymbol{\Theta}) = -\ln c_0 - \ln\left[p(\hat{\boldsymbol{\lambda}}, \boldsymbol{\Sigma}_{\hat{\boldsymbol{\lambda}}} | \boldsymbol{\lambda}) \right] - \ln\left[p(\hat{\boldsymbol{\psi}}, \mathbf{H}_{\hat{\boldsymbol{\psi}}} | \boldsymbol{\Phi}) \right] \\ - \ln\left[p(\boldsymbol{\lambda}, \boldsymbol{\Phi}, \boldsymbol{\Sigma}_{eq} | \boldsymbol{\theta}) \right] - \ln\left[p(\boldsymbol{\theta}) \right] \end{aligned} \tag{3.30}$$

Calculating the negative natural logarithm of each term, one can obtain the following negative log-likelihood function

$$\begin{aligned} L(\boldsymbol{\Theta}) = & \sum_{n=1}^{N_m} \frac{\left(\hat{\lambda}_n - \lambda_n \right)^2}{2 S_{\hat{\lambda}_n}} + \frac{1}{2} \sum_{n=1}^{N_m} \left(\frac{\mathbf{L}_0 \boldsymbol{\phi}_n}{\left\| \mathbf{L}_0 \boldsymbol{\phi}_n \right\|} - \hat{\boldsymbol{\psi}}_n \right)^T \mathbf{H}_{\hat{\boldsymbol{\psi}}_n} \left(\frac{\mathbf{L}_0 \boldsymbol{\phi}_n}{\left\| \mathbf{L}_0 \boldsymbol{\phi}_n \right\|} - \hat{\boldsymbol{\psi}}_n \right) \\ & + \frac{1}{2} \sum_{n=1}^{N_m} N_d \ln(S_{eq,n}) + \frac{1}{2} \sum_{n=1}^{N_m} \boldsymbol{\phi}_n^T \boldsymbol{\Gamma}_n^T S_{eq,n}^{-1} \mathbf{I}_{N_d} \boldsymbol{\phi}_n \boldsymbol{\Gamma}_n \\ & + \frac{1}{2} \left(\boldsymbol{\theta} - \hat{\boldsymbol{\theta}}_0 \right)^T \boldsymbol{\Sigma}_{\boldsymbol{\theta}}^{-1} \left(\boldsymbol{\theta} - \hat{\boldsymbol{\theta}}_0 \right) \end{aligned} \tag{3.31}$$

It should be noted that constant terms are neglected while writing equation (3.31) since they have no effect on the optimization of the parameters. This function needs to be minimized with respect to each parameter to obtain most probable values. However, it is not quadratic for $\boldsymbol{\phi}_n$ due to the norm term of $\|\mathbf{L}_0 \boldsymbol{\phi}_n\|$ and therefore explicit expressions cannot be obtained for the MPVs of the parameters. Computationally challenging numerical optimization methods need to be applied to solve for the most probable values. Instead of using such type of numerical optimization methods and to obtain the explicit expressions for the most probable values, a new independent variable is assigned for the norm term. Thus, negative log-likelihood function turns into a complete quadratic form. Introducing the new variable as

$$\eta_n = \left\| \mathbf{L}_0 \boldsymbol{\phi}_n \right\| \tag{3.32}$$

Negative log-likelihood function in equation (3.31) is rewritten by substituting equation (3.32) as

$$\begin{aligned} L(\boldsymbol{\Theta}) = & \sum_{n=1}^{N_m} \frac{\left(\hat{\lambda}_n - \lambda_n \right)^2}{2 S_{\hat{\lambda}_n}} + \frac{1}{2} \sum_{n=1}^{N_m} \left(\eta_n^{-1} \mathbf{L}_0 \boldsymbol{\phi}_n - \hat{\boldsymbol{\psi}}_n \right)^T \mathbf{H}_{\hat{\boldsymbol{\psi}}_n} \left(\eta_n^{-1} \mathbf{L}_0 \boldsymbol{\phi}_n - \hat{\boldsymbol{\psi}}_n \right) \\ & + \frac{1}{2} \sum_{n=1}^{N_m} N_d \ln(S_{eq,n}) + \frac{1}{2} \sum_{n=1}^{N_m} \boldsymbol{\phi}_n^T \boldsymbol{\Gamma}_n^T S_{eq,n}^{-1} \mathbf{I}_{N_d} \boldsymbol{\Gamma}_n \boldsymbol{\phi}_n \\ & + \frac{1}{2} \left(\boldsymbol{\theta} - \hat{\boldsymbol{\theta}}_0 \right)^T \boldsymbol{\Sigma}_{\boldsymbol{\theta}}^{-1} \left(\boldsymbol{\theta} - \hat{\boldsymbol{\theta}}_0 \right) \end{aligned} \tag{3.33}$$

As a result, negative log-likelihood function in equation (3.33) is in a completely quadratic form and its minimization with respect to each parameter can be easily performed. However, introducing η_n as an independent variable removes the norm constraint on $\mathbf{L}_0 \boldsymbol{\phi}_n$. Therefore, a norm constraint should be extrinsically added to the negative log-likelihood function to enforce $\mathbf{L}_0 \boldsymbol{\phi}_n$ to have a unit norm. Besides, a norm constraint should also be added for $\boldsymbol{\phi}_n$ to have a unit norm. The reason for this is that, as it will be shown later, measured mode shapes do not contribute to the optimization process of parameters and the mode shape information is gathered by just the posterior Hessian matrix of $\mathbf{H}_{\hat{\psi}_n}$. Therefore, $\boldsymbol{\phi}_n$ should have the same norm for each iteration to comply with $\mathbf{H}_{\hat{\psi}_n}$. Otherwise, incompatible results can be obtained in each iteration due to the dependence of minimization process on the norm of the $\boldsymbol{\phi}_n$ and the optimization process can end up with a minimum value which is unreasonable. Then, the final objective function to minimize is formed by using the Lagrange multiplier method as

$$J(\boldsymbol{\Theta}, \boldsymbol{\alpha}, \boldsymbol{\beta}) = L(\boldsymbol{\Theta}) + \sum_{n=1}^{N_m} \alpha_n \left(\boldsymbol{\phi}_n^T \mathbf{L}_0^T \mathbf{L}_0 \boldsymbol{\phi}_n - \eta_n^2 \right) + \sum_{n=1}^{N_m} \beta_n \left(1 - \boldsymbol{\phi}_n^T \boldsymbol{\phi}_n \right) \tag{3.34}$$

where $\boldsymbol{\alpha} = [\alpha_1 \quad \alpha_2 \quad \alpha_3 \ . \ . \ . \ \alpha_{Nm}]$ and $\boldsymbol{\beta} = [\beta_1 \quad \beta_2 \quad \beta_3 \ . \ . \ . \ \beta_{Nm}]$ are the vectors of corresponding Lagrange multipliers.

3.2.3. Optimization Problem

The objective function in equation (3.34) should be minimized with respect to each parameter in the set of $\boldsymbol{\Theta} = \{\boldsymbol{\theta}, \boldsymbol{\lambda}, \boldsymbol{\Phi}, \mathbf{S_{eq}}\}$ to obtain the optimum values of each parameter. As can be realized, this function is not quadratic for these parameters at the same time to minimize. However, it becomes quadratic when any other three of them are fixed and considered as being constant at their optimal values (Yuen and Kuok, 2011). Therefore, this optimization problem is solved in an iterative manner as a series of optimizations which are;

$$\begin{aligned}
\boldsymbol{\Phi}^* &= \arg\min_{\boldsymbol{\Phi}} J(\boldsymbol{\theta}^*, \boldsymbol{\lambda}^*, \boldsymbol{\Phi}, \mathbf{S}_{\mathbf{eq}}^*) \\
\boldsymbol{\lambda}^* &= \arg\min_{\boldsymbol{\lambda}} J(\boldsymbol{\theta}^*, \boldsymbol{\lambda}, \boldsymbol{\Phi}^*, \mathbf{S}_{\mathbf{eq}}^*) \\
\boldsymbol{\theta}^* &= \arg\min_{\boldsymbol{\theta}} J(\boldsymbol{\theta}, \boldsymbol{\lambda}^*, \boldsymbol{\Phi}^*, \mathbf{S}_{\mathbf{eq}}^*) \\
\mathbf{S}_{\mathbf{eq}}^* &= \arg\min_{\mathbf{S_{eq}}} J(\boldsymbol{\theta}^*, \boldsymbol{\lambda}^*, \boldsymbol{\Phi}^*, \mathbf{S}_{\mathbf{eq}})
\end{aligned} \tag{3.35}$$

The iterative process is ended when prescribed convergence criteria are satisfied for the updated parameters. Each optimization problem in equation (3.35) is explained in detail in the following sections.

3.2.3.1. Minimization of *J* with respect to System Mode Shapes

Minimization of the objective function *J* with respect to mode shapes is performed for each mode separately. Thus, the optimal value of the system mode shape for the n^{th} mode is obtained by minimizing *J* with respect to $\boldsymbol{\phi}_n$ as

$$\frac{\partial J}{\partial \boldsymbol{\phi}_n} = \left[\boldsymbol{\Gamma}_n^T S_{eq,n}^{-1} \boldsymbol{\Gamma}_n + \eta_n^{-2} \mathbf{L}_0^T \mathbf{H}_{\hat{\boldsymbol{\psi}}_n} \mathbf{L}_0 + 2\alpha_n \mathbf{L}_0^T \mathbf{L}_0 \right] \boldsymbol{\phi}_n - \eta_n^{-1} \mathbf{L}_0^T \mathbf{H}_{\hat{\boldsymbol{\psi}}_n} \hat{\boldsymbol{\psi}}_n - 2\beta_n \boldsymbol{\phi}_n \tag{3.36}$$

By fixing the rest of parameters at their optimum values and equating the first derivative obtained in equation (3.36) to zero, one can obtain the following equation;

$$\left.\frac{\partial J}{\partial \boldsymbol{\phi}_n}\right|_{\boldsymbol{\phi}_n=\boldsymbol{\phi}_n^*} = 0$$
$$\Rightarrow \underbrace{\left[\frac{1}{2}\boldsymbol{\Gamma}_n^{*T} S_{eq,n}^{*-1}\boldsymbol{\Gamma}_n^* + \frac{1}{2}\eta_n^{*-2}\mathbf{L}_0^T\mathbf{H}_{\hat{\boldsymbol{\psi}}_n}\mathbf{L}_0 + \alpha_n^*\mathbf{L}_0^T\mathbf{L}_0\right]}_{\mathbf{A}_n^*}\boldsymbol{\phi}_n^* - \eta_n^{*-1}\mathbf{L}_0^T\mathbf{H}_{\hat{\boldsymbol{\psi}}_n}\hat{\boldsymbol{\psi}}_n = \beta_n^*\boldsymbol{\phi}_n^* \tag{3.37}$$

where

$$\boldsymbol{\Gamma}_n^* = \mathbf{K}(\boldsymbol{\theta}^*) - \lambda_n^*\mathbf{M} \tag{3.38}$$

and

$$\mathbf{A}_n^* = \frac{1}{2}\boldsymbol{\Gamma}_n^{*T} S_{eq,n}^{*-1}\boldsymbol{\Gamma}_n^* + \frac{1}{2}\eta_n^{*-2}\mathbf{L}_0^T\mathbf{H}_{\hat{\boldsymbol{\psi}}_n}\mathbf{L}_0 + \alpha_n^*\mathbf{L}_0^T\mathbf{L}_0 \tag{3.39}$$

Hızal and Turan (2020) have proved that measured mode shape $\hat{\boldsymbol{\psi}}_n$ is a null vector of its corresponding posterior Hessian matrix $\mathbf{H}_{\hat{\psi}_n}$ for the n^{th} mode.

$$\begin{aligned}&\mathbf{H}_{\hat{\boldsymbol{\psi}}_n}\hat{\boldsymbol{\psi}}_n = \mathbf{0}\\ &\Rightarrow\ \eta_n^{*-1}\mathbf{L}_0^T\mathbf{H}_{\hat{\boldsymbol{\psi}}_n}\hat{\boldsymbol{\psi}}_n = \mathbf{0}\end{aligned} \tag{3.40}$$

By eliminating the term in equation (3.40) from equation (3.37), since it is a vector of zeros, one can obtain the following standard eigenvalue problem.

$$\mathbf{A}_n^*\boldsymbol{\phi}_n^* = \beta_n^*\boldsymbol{\phi}_n^* \tag{3.41}$$

Optimal value for the Lagrange multiplier, β_n^* can be evaluated as the minimum eigenvalue of the matrix $\mathbf{A}_n^*$. Besides, optimal value of the system mode shape for the n^{th} mode, $\boldsymbol{\phi}_n^*$, is then obtained as the eigenvector which corresponds to this minimum eigenvalue. However, the optimal values of $\boldsymbol{\theta}^*$, λ_n^*, $S_{eq,n}^*$, $\eta_n^*$and α_n^* must be defined to

obtain the matrix $\mathbf{A}_n^*$. Therefore, an initial guess for each of these parameters is needed to start iterations.

- Initial value for the optimum stiffness parameter vector, $\boldsymbol{\theta}^*$, can be taken as the nominal stiffness parameter vector of the nominal FE model as $\boldsymbol{\theta}^* = \widehat{\boldsymbol{\theta}}_0$.
- Optimal value of η_n^* can be calculated by using its definition as

$$\eta_n^* = \left\| \mathbf{L}_0 \boldsymbol{\phi}_n^* \right\| \tag{3.42}$$

- Optimal value of α_n^* can be evaluated by minimizing the objective function J with respect to η_n as;

$$\begin{aligned} &\frac{\partial J}{\partial \eta_n} = -\eta_n^{-3} \boldsymbol{\phi}_n^T \mathbf{L}_0^T \mathbf{H}_{\hat{\boldsymbol{\phi}}_n} \mathbf{L}_0 \boldsymbol{\phi}_n - 2\alpha_n \eta_n \\ &\left. \frac{\partial J}{\partial \eta_n} \right|_{\eta_n = \eta_n^*, \alpha_n = \alpha_n^*} = 0 \quad \Rightarrow -\eta_n^{*-3} \boldsymbol{\phi}_n^{*T} \mathbf{L}_0^T \mathbf{H}_{\hat{\boldsymbol{\phi}}_n} \mathbf{L}_0 \boldsymbol{\phi}_n^* - 2\alpha_n^* \eta_n^* = 0 \end{aligned} \tag{3.43}$$

Optimal value of α_n^* is calculated as;

$$\alpha_n^* = -\frac{1}{2} \eta_n^{*-4} \boldsymbol{\phi}_n^{*T} \mathbf{L}_0^T \mathbf{H}_{\hat{\boldsymbol{\phi}}_n} \mathbf{L}_0 \boldsymbol{\phi}_n^* \tag{3.44}$$

Since the values of α_n^* and η_n^* depend on the optimal value of the system mode shape of $\boldsymbol{\phi}_n^*$, an initial guess for $\boldsymbol{\phi}_n^*$ is necessary to start iterations. The measured mode shapes cannot be considered as the initial guess for $\boldsymbol{\phi}_n^*$ due to the fact that they are generally spatially incomplete.

- Initial guess for $\boldsymbol{\phi}_n^*$ can be calculated by assuming that the modelling error, in eigen-equations for the n^{th} mode, goes to infinity ($S_{eq,n} \rightarrow \infty$) so that the initial guess values are not affected by the nominal FE model. Then, the following matrix is obtained as

$$\mathbf{A}_n^0 = \bar{\eta}_n^{-2}\mathbf{L}_0^T\mathbf{H}_{\hat{\psi}_n}\mathbf{L}_0 + \bar{\alpha}_n\mathbf{L}_0^T\mathbf{L}_0 \tag{3.45}$$

Initial guess value for $\boldsymbol{\phi}_n^*$ is obtained as the eigenvector of the matrix $\mathbf{A}_n^0$ which corresponds to its minimum eigenvalue. Here, $\bar{\eta}_n$ and $\bar{\alpha}_n$ are the initial values for η_n and α_n, respectively. They are employed only for the calculation of the initial value of $\boldsymbol{\phi}_n^*$. Any positive number may be assumed as the initial value, since the order of the eigenvalues of $\mathbf{A}_n^0$ and scaling of its eigenvectors are not affected. For simplicity, they can be taken as $\bar{\eta}_n$ = 1 and $\bar{\alpha}_n$ = 1.

The optimal values for $\eta_n^*$and α_n^* can be calculated using equations (3.42) and (3.44), respectively, by substituting the initial guess of $\boldsymbol{\phi}_n^*$. To calculate the optimum value for $\boldsymbol{\phi}_n^*$ in the first iteration by using equation (3.39), the initial guess values for λ_n^* and $S_{eq,n}^*$ are required which will be explained in the next sections.

3.2.3.2. Minimization of *J* with respect to System Eigenvalues

Minimization of the objective function *J* with respect to system eigenvalues is performed for each mode separately. Thus, the optimal value of the system eigenvalue for the n^{th} mode is obtained by minimizing *J* with respect to λ_n as

$$\frac{\partial J}{\partial \lambda_n} = -S_{eq,n}^{-1}\boldsymbol{\phi}_n^T\mathbf{K}(\boldsymbol{\theta})^T\mathbf{M}\boldsymbol{\phi}_n + S_{eq,n}^{-1}\boldsymbol{\phi}_n^T\mathbf{M}^T\mathbf{M}\boldsymbol{\phi}_n\lambda_n - S_{\hat{\lambda}_n}^{-1}\hat{\lambda}_n + S_{\hat{\lambda}_n}^{-1}\lambda_n \tag{3.46}$$

By fixing the rest of the parameters at their optimum values and equating the first derivative obtained in equation (3.46) to zero, one can obtain the following equation;

$$\left.\frac{\partial J}{\partial \lambda_n}\right|_{\lambda_n=\lambda_n^*} = 0$$
$$\Rightarrow \quad \lambda_n^* = \frac{S_{eq,n}^{*-1}\boldsymbol{\phi}_n^{*T}\mathbf{K}(\boldsymbol{\theta}^*)^T\mathbf{M}\boldsymbol{\phi}_n^* + S_{\hat{\lambda}_n}^{-1}\hat{\lambda}_n}{S_{eq,n}^{*-1}\boldsymbol{\phi}_n^{*T}\mathbf{M}^T\mathbf{M}\boldsymbol{\phi}_n^* + S_{\hat{\lambda}_n}^{-1}} \tag{3.47}$$

In order to simplify this expression for future usage, the following terms are replaced by their scalar values as

$$\begin{aligned} G_{\lambda_n} &= \boldsymbol{\phi}_n^{*T}\mathbf{M}^T\mathbf{M}\boldsymbol{\phi}_n^* \\ g_{\lambda_n} &= \boldsymbol{\phi}_n^{*T}\mathbf{K}(\boldsymbol{\theta}^*)^T\mathbf{M}\boldsymbol{\phi}_n^* \end{aligned} \tag{3.48}$$

Substituting equation (3.48) into equation (3.47), the optimal value of the system eigenvalue for the n^{th} mode can be expressed as

$$\lambda_n^* = \frac{S_{eq,n}^{*-1} g_{\lambda_n} + S_{\hat{\lambda}_n}^{-1}\hat{\lambda}_n}{S_{eq,n}^{*-1} G_{\lambda_n} + S_{\hat{\lambda}_n}^{-1}} \tag{3.49}$$

Initial guess for λ_n^* can be calculated by assuming that the modelling error in eigen-equations for the n^{th} mode goes to infinity ($S_{eq,n} \rightarrow \infty$) so that the initial guess values are not affected by the nominal FE model. Thus, equation (3.49) is reduced to the following equality;

$$\lambda_n^* = \hat{\lambda}_n \tag{3.50}$$

which means measured eigenvalues can be used as the initial guess for the system eigenvalues.

3.2.3.3. Minimization of *J* with respect to Stiffness Parameters

Optimal values of the stiffness parameters $\boldsymbol{\theta}^*$ can be obtained by searching for the minimum value of J with respect to $\boldsymbol{\theta}$ if a zero slope exists in the search domain.

$$\begin{aligned} \frac{\partial J}{\partial \boldsymbol{\theta}} = \Sigma_{\boldsymbol{\theta}}^{-1}\boldsymbol{\theta} + \sum_{n=1}^{N_m}\sum_{i=1}^{N_\theta} S_{eq,n}^{-1}\boldsymbol{\phi}_n^T\mathbf{K}_i^T\theta_i\Big(\sum_{i=1}^{N_\theta}\mathbf{K}_i\Big)\boldsymbol{\phi}_n - \Sigma_{\boldsymbol{\theta}}^{-1}\hat{\boldsymbol{\theta}}_0 \\ - \sum_{n=1}^{N_m}\sum_{i=1}^{N_\theta} S_{eq,n}^{-1}\boldsymbol{\phi}_n^T\mathbf{K}_i^T(\lambda_n\mathbf{M} - \mathbf{K}_0)\boldsymbol{\phi}_n \end{aligned} \tag{3.51}$$

For simplicity in the notations, following variables are defined;

$$\mathbf{G}_{K_n} = \left[\mathbf{K}_1\boldsymbol{\phi}_n^* \;\; \mathbf{K}_2\boldsymbol{\phi}_n^* \;\; . \;\; . \;\; . \;\; K_{N_\theta}\boldsymbol{\phi}_n^* \right]_{N_d \times N_\theta}$$
$$\mathbf{g}_{K_n} = \left[(\lambda_n^*\mathbf{M} - \mathbf{K}_0)\boldsymbol{\phi}_n^* \right]_{N_d \times 1} \tag{3.52}$$

By fixing the rest of the parameters at their optimum values, and equating the first derivative to zero, one can obtain the following equation;

$$\left.\frac{\partial J}{\partial \boldsymbol{\theta}}\right|_{\boldsymbol{\theta}=\boldsymbol{\theta}^*} = \Sigma_{\boldsymbol{\theta}}^{-1}\boldsymbol{\theta}^* + \sum_{n=1}^{N_m} \mathbf{S}_{eq,n}^{*-1}\mathbf{G}_{K_n}^T\mathbf{G}_{K_n}\boldsymbol{\theta}^* - \Sigma_{\boldsymbol{\theta}}^{-1}\hat{\boldsymbol{\theta}}_0 - \sum_{n=1}^{N_m} \mathbf{S}_{eq,n}^{*-1}\mathbf{G}_{K_n}^T\mathbf{g}_{K_n} = 0$$
$$\Rightarrow \quad \left[\Sigma_{\boldsymbol{\theta}}^{-1} + \sum_{n=1}^{N_m} S_{eq,n}^{*-1}\mathbf{G}_{K_n}^T\mathbf{G}_{K_n} \right]\boldsymbol{\theta}^* = \Sigma_{\boldsymbol{\theta}}^{-1}\hat{\boldsymbol{\theta}}_0 + \sum_{n=1}^{N_m} S_{eq,n}^{*-1}\mathbf{G}_{K_n}^T\mathbf{g}_{K_n} \tag{3.53}$$

Then, optimal values of the stiffness parameters can be expressed as

$$\boldsymbol{\theta}^* = \left[\Sigma_{\boldsymbol{\theta}}^{-1} + \sum_{n=1}^{N_m} S_{eq,n}^{*-1}\mathbf{G}_{K_n}^T\mathbf{G}_{K_n} \right]^{-1} \left[\Sigma_{\boldsymbol{\theta}}^{-1}\hat{\boldsymbol{\theta}}_0 + \sum_{n=1}^{Nm} S_{eq,n}^{*-1}\mathbf{G}_{K_n}^T\mathbf{g}_{K_n} \right] \tag{3.54}$$

3.2.3.4. Minimization of *J* with respect to Modelling Error Variances

Minimization of the objective function *J* with respect to modelling error variances can be performed for each mode separately. Thus, the optimal value of modelling error variance for the n^{th} mode is obtained by searching the minimum value of *J* with respect to $S_{eq,n}$ in the parameter space.

$$\frac{\partial J}{\partial S_{eq,n}} = \frac{1}{2}N_d S_{eq,n}^{-1} - \frac{1}{2}S_{eq,n}^{-2}\boldsymbol{\phi}_n^T\boldsymbol{\Gamma}_n^T\boldsymbol{\Gamma}_n\boldsymbol{\phi}_n \tag{3.55}$$

By fixing the rest of the parameters at their optimum values, and equating the first derivative to zero, one can obtain the following equation

$$\left.\frac{\partial J}{\partial S_{eq,n}}\right|_{S_{eq,n}=S_{eq,n}^{*}} = \frac{1}{2} N_d S_{eq,n}^{*-1} - \frac{1}{2} S_{eq,n}^{*-2} \boldsymbol{\phi}_n^T \boldsymbol{\Gamma}_n^T \boldsymbol{\Gamma}_n \boldsymbol{\phi}_n = 0 \tag{3.56}$$

The optimum value of the modelling error variance for the n^{th} mode can be obtained as the non-trivial solution as follows

$$S_{eq,n}^{*} = \frac{\left\| \boldsymbol{\Gamma}_n^{*} \boldsymbol{\phi}_n^{*} \right\|^2}{N_d} \tag{3.57}$$

The trivial solution leads to $S_{eq,n} = \infty$. Initial guess for $S_{eq,n}$ can be calculated for the first iteration by substituting the initial values of λ_n^*, $\boldsymbol{\theta}^*$ and $\boldsymbol{\phi}_n^*$ into equation (3.57).

3.2.4. Posterior Uncertainty for the Updated Parameters

Posterior PDF of the parameters in set $\boldsymbol{\Theta} = \{\boldsymbol{\theta}, \boldsymbol{\lambda}, \boldsymbol{\Phi}, \mathbf{S_{eq}}\}$ can be modelled as a Gaussian distribution evaluated at the optimum parameters with their posterior covariance matrix. Thus, optimal parameters can be considered as the MPVs of the parameters with the uncertainties in the posterior covariance matrix. The posterior covariance matrix is evaluated as the inverse of the Hessian matrix which is calculated at the optimum parameter values. Then, the posterior variance of each parameter can be extracted from the posterior covariance matrix. However, the resulting Hessian matrix is a singular matrix because of the norm constraints induced for modal shapes. To this end, pseudo inverse of the following Hessian matrix should be evaluated to calculate the posterior covariance matrix. To this end, the Hessian matrix is calculated as

$$\mathbf{H}(\boldsymbol{\Theta}^*) = \begin{bmatrix} \mathbf{J}^{(\boldsymbol{\lambda},\boldsymbol{\lambda})} & \mathbf{J}^{(\boldsymbol{\lambda},\boldsymbol{\Phi})} & \mathbf{J}^{(\boldsymbol{\lambda},\boldsymbol{\theta})} & \mathbf{J}^{(\boldsymbol{\lambda},\mathbf{S_{eq}})} \\ \mathbf{J}^{(\boldsymbol{\Phi},\boldsymbol{\lambda})} & \mathbf{J}^{(\boldsymbol{\Phi},\boldsymbol{\Phi})} & \mathbf{J}^{(\boldsymbol{\Phi},\boldsymbol{\theta})} & \mathbf{J}^{(\boldsymbol{\Phi},\mathbf{S_{eq}})} \\ \mathbf{J}^{(\boldsymbol{\theta},\boldsymbol{\lambda})} & \mathbf{J}^{(\boldsymbol{\theta},\boldsymbol{\Phi})} & \mathbf{J}^{(\boldsymbol{\theta},\boldsymbol{\theta})} & \mathbf{J}^{(\boldsymbol{\theta},\mathbf{S_{eq}})} \\ \mathbf{J}^{(\mathbf{S_{eq}},\boldsymbol{\lambda})} & \mathbf{J}^{(\mathbf{S_{eq}},\boldsymbol{\Phi})} & \mathbf{J}^{(\mathbf{S_{eq}},\boldsymbol{\theta})} & \mathbf{J}^{(\mathbf{S_{eq}},\mathbf{S_{eq}})} \end{bmatrix}_{N_h \times N_h} \tag{3.58}$$

where $N_h = 2N_m+N_dN_m+N_\theta$ and the elements represent the derivatives of the objective function of J ($\boldsymbol{\theta}$, $\boldsymbol{\alpha}$, $\boldsymbol{\beta}$). For example, $\mathbf{J}^{(\boldsymbol{\lambda},\boldsymbol{\Phi})}$ represents the differentiation of J with respect to $\boldsymbol{\lambda}$ and $\boldsymbol{\Phi}$, respectively. The Hessian matrix, $\mathbf{H}(\boldsymbol{\Theta}^*)$ is a symmetric matrix and the elements in the lower triangle are the transpose of the corresponding elements in the upper triangle. (i.e., $\mathbf{J}^{(\boldsymbol{\theta},\boldsymbol{\lambda})} = \left[\mathbf{J}^{(\boldsymbol{\lambda},\boldsymbol{\theta})}\right]^T$). Therefore, one of these corresponding elements and all diagonal elements are derived and each derivation has been provided in Appendix A.

3.2.5. Iterative Procedure and Computational Issues

In the presented two-stage Bayesian model updating procedure, the system modes, stiffness parameters and modelling error variance of each mode are updated by employing the measured modal data in an iterative manner by utilizing the presented formulations in Section 3.2.3. The flow chart of the overall process is presented in Figure 3.1 The optimization process is performed as a series of optimization problems defined in equation (3.35) as follows:

Modal identification stage:

- *Step 1*: By using the BFFTA, estimate the MPVs of the measured eigenvalues $\hat{\boldsymbol{\lambda}}$ and corresponding posterior covariance matrix $\boldsymbol{\Sigma}_{\hat{\boldsymbol{\lambda}}}$. It should be noticed that there is no need to estimate the MPVs of the measured mode shapes. Instead, estimate $\mathbf{H}_{\hat{\psi}}$ which is used in the formulations.

Model updating stage:

- *Step 2*: Take the initial values of the stiffness parameters as $\boldsymbol{\theta}^* = \hat{\boldsymbol{\theta}}_0$, and initial values of system eigenvalues as $\boldsymbol{\lambda}^* = \hat{\boldsymbol{\lambda}}$. Calculate initial value of $\mathbf{K}^* = \mathbf{K}(\boldsymbol{\theta}^*)$.

- *Step 3*: Calculate the initial guess for the system mode shape $\boldsymbol{\phi}_n^*$ by using equation (3.45). Here, $\mathbf{A}_n^0$ is a positive semi-definite matrix. Therefore, $\boldsymbol{\phi}_n^*$ is the eigenvector of $\mathbf{A}_n^0$, which corresponds to its minimum positive eigenvalue.
- *Step 4*: Calculate $S_{eq,n}^*$ by using equation (3.57).
- *Step 5*: Calculate η_n^* and α_n^* by using equations (3.42) and (3.43), respectively.
- *Step 6*: Calculate the system mode shapes $\boldsymbol{\phi}_n^*$ by using equation (3.41).
- *Step 7*: Calculate the system eigenvalues λ_n^* by using equation (3.49).
- *Step 8*: Calculate the stiffness parameters $\boldsymbol{\theta}^*$ by using equation (3.54)
- *Step 9*: Calculate $\mathbf{K}^* = \mathbf{K}(\boldsymbol{\theta}^*)$ by using calculated stiffness parameters in Step 8.
- Iterate over *Steps 4 to 9* until the calculated stiffness parameters $\boldsymbol{\theta}^*$ satisfy a prescribed convergence criterion.
- *Step 10*: Calculate the posterior covariance matrix of the updated parameters. The posterior covariance matrix is calculated by the pseudo-inverse of equation (3.58) and diagonal elements result in the posterior variance of the parameters.

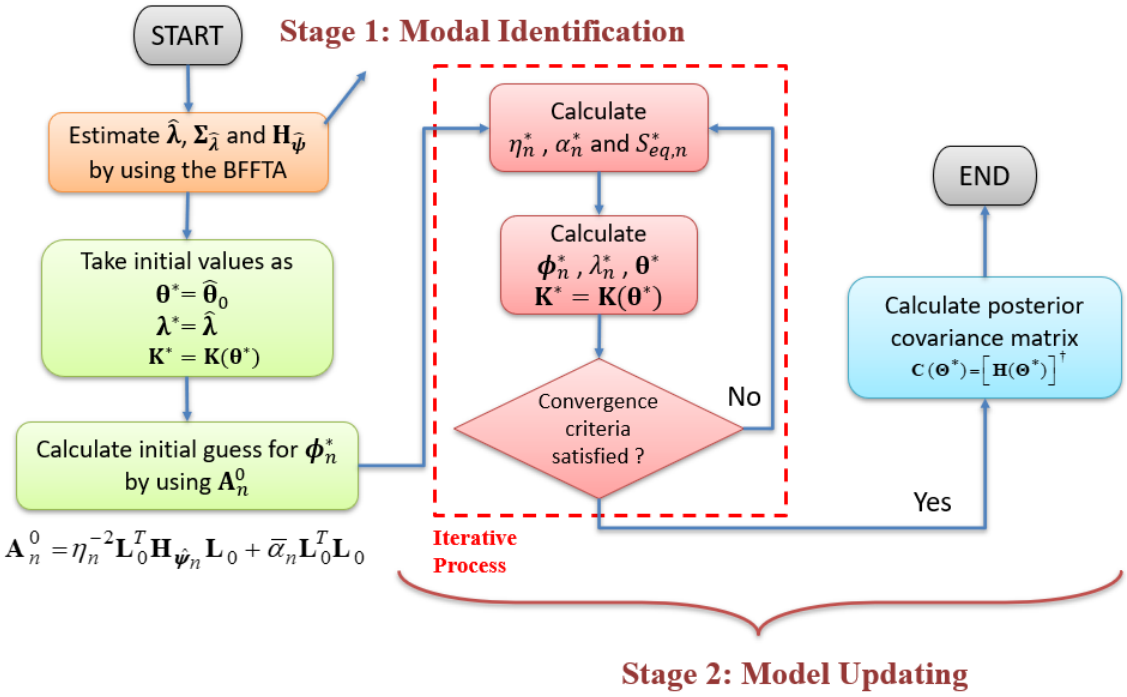

Figure 3.1. Flow chart of the presented two-stage Bayesian model updating procedure

3.2.6. Numerical Studies

The presented methodology is implemented on a numerical twelve-story shear frame structure to reveal the accuracy of the formulated algorithms. This numerical model has been proposed by Yuen (2010, page: 202) to validate his proposed methodology. The same numerical model is intentionally investigated in this study to compare the model updating results. To this end, the mass of each story is considered to be M = 100 tons and stiffness value of each story is selected to be $K = 202.767 \times 10^3$ kN/m. This structure is considered as the actual structure. For numerical simulations, modal damping ratio is taken as 0.1% for each mode. The structure is excited at story levels by independent Gaussian white noise. The simulations are carried out by the Newmark-beta method with the constant average acceleration for 500 seconds and a time step of 0.005 seconds. Acceleration measurements are obtained from all story levels in a single setup. Each acceleration response is contaminated with Gaussian white noise to mimic the measurement noise. To this end, the noise level is set to have an RMS of 50% of the RMS of the noise-free response. Modal identification of the numerical model is performed by using Fast Bayesian FFT method (Au, 2011) and the posterior uncertainties of modal parameters have been obtained by using the alternative method proposed by Hızal (2019) in Chapter 2 of his dissertation.

Stiffness value of each story is selected as an updating parameter, which results in a total of 12 stiffness parameters to be updated (N_θ = 12). Therefore, a non-parametric and constant elementwise stiffness matrix is defined, for the first story, as

$$\mathbf{K}_1 = \begin{bmatrix} 1 & \mathbf{0}_{1\times 11} \\ \mathbf{0}_{11\times 1} & \mathbf{0}_{11\times 11} \end{bmatrix}_{12\times 12} \tag{3.59}$$

and, for the remaining stories, as

$$\mathbf{K}_i = \begin{bmatrix} \mathbf{0}_{(i-2)\times(i-2)} & \mathbf{0}_{(i-2)\times 1} & \mathbf{0}_{(i-2)\times 1} & \mathbf{0}_{(i-2)\times(12-i)} \\ \mathbf{0}_{1\times(i-2)} & 1 & -1 & \mathbf{0}_{1\times(12-i)} \\ \mathbf{0}_{1\times(i-2)} & -1 & 1 & \mathbf{0}_{1\times(12-i)} \\ \mathbf{0}_{(12-i)\times(i-2)} & \mathbf{0}_{(12-i)\times 1} & \mathbf{0}_{(12-i)\times 1} & \mathbf{0}_{(12-i)\times(12-i)} \end{bmatrix}_{12\times 12} \tag{3.60}$$

where $i = 2, 3, \ldots, 12$. Since all elements are affected by the updating process,

$$\mathbf{K}_0 = \mathbf{0}_{12\times 12} \tag{3.61}$$

To construct the initial (nominal) model of the structure, nominal stiffness value of each story is chosen from a uniform distribution which is defined between $2K$ and $3K$. Thus, the nominal values are overestimated with 100% and 200% of the actual stiffness values. To start iteration process of the updating procedure, initial value of the stiffness parameters, $\widehat{\boldsymbol{\theta}}_0$, are assigned as the vector of nominal stiffness parameters. Besides, a large prior variance is selected for each stiffness parameter to have a non-informative prior stiffness distribution. In this context, variance of each stiffness parameter is assigned as the square of its stiffness value. The prior covariance matrix of the stiffness parameters, $\boldsymbol{\Sigma}_{\boldsymbol{\theta}}$, is constructed as a diagonal matrix and each diagonal element is the calculated variance value.

In this numerical study, three different cases are investigated. In Case 1, modelling error variance of each mode is considered to be different, and each is updated with the system eigenvalues, mode shapes and stiffness parameters as soft constraints. Accordingly, Case 1 corresponds to the results of present study. In Case 2, the identical modelling error variance is used for all modes and it is updated with the system eigenvalues, mode shapes and stiffness parameters as soft constraint. This case corresponds to a similar study done by Hızal and Turan (2020). In Case 3, modelling error variance is considered as rigid constraint and its value is prescribed before the updating procedure and it is not updated. This case corresponds to a similar study done by Yuen (2010).

As the first application for the validation purpose, it is considered that all modes and DOFs of the structure are available and the structure is updated by the complete modal data. MPVs of the updated system frequencies with their posterior c.o.v are presented for each case in Table 3.1. Besides, updated modelling error variances are provided for Case 1 and 2. For Case 3, a prescribed value of 1 is used for the modelling error variance. For all three cases, updated system frequencies agree very well with the actual natural frequencies even if the initial values are not close to the actual ones. One can notice that posterior uncertainties are completely same for Case 2 and 3. This is

reasonable because posterior uncertainties of measured eigenfrequencies are considerably small when compared to the values of modelling errors obtained in these cases. Thus, posterior uncertainties of system frequencies converge to the posterior uncertainties of the measured ones. However, for Case 1, different modelling error variances are obtained for each mode and considerably small values are obtained for the first two modes. This significantly reduces the posterior uncertainties of the system frequencies.

Table 3.1. Updated system frequencies and modelling error variances with complete modal data

	Case 1 Presented Study			**Case 2**			**Case 3**		
Actual (Hz)	Upd. (Hz)	c.o.v	Upd. $S_{eq,n}$	Upd. (Hz)	c.o.v ($\times 10^{-4}$)	Upd. S_{eq}	Upd. (Hz)	c.o.v ($\times 10^{-4}$)	S_{eq}
0.90	0.90	3.19×10^{-8}	8.38×10^{-6}	0.90	4.70		0.90	4.70	
2.69	2.69	1.23×10^{-10}	2.87×10^{-4}	2.69	3.46		2.69	3.46	
4.43	4.43	6.11×10^{-19}	0.022	4.43	2.47		4.43	2.47	
6.10	6.11	8.92×10^{-19}	0.123	6.11	2.68		6.11	2.68	
7.68	7.68	4.99×10^{-19}	0.207	7.68	2.05		7.68	2.05	
9.14	9.14	2.82×10^{-18}	0.040	9.14	1.84	0.0083	9.14	1.84	1
10.45	10.45	3.04×10^{-19}	0.851	10.45	1.90		10.45	1.90	
11.60	11.60	2.17×10^{-19}	0.257	11.60	2.02		11.60	2.02	
12.56	12.56	2.55×10^{-19}	0.559	12.56	1.54		12.56	1.54	
13.33	13.33	1.26×10^{-20}	16.192	13.33	1.58		13.33	1.58	
13.88	13.88	1.52×10^{-20}	21.996	13.88	1.67		13.88	1.67	
14.22	14.23	7.84×10^{-21}	25.245	14.23	1.98		14.23	1.98	

MPVs of the updated stiffness parameters are provided with their posterior uncertainties for each case in Table 3.2. All the updated stiffness values agree well with their actual values despite the high initial values. One can see that Case 2 has slightly better convergence of all the parameters to their actual values. The posterior c.o.v values for all cases appear to be in the same order of magnitude. However, Case 1 results in the relatively lowest values for the posterior c.o.v values of the stiffness parameters. Here, for Case 3, stiffness parameter values do not converge to their actual ones for prescribed values of modelling error variance smaller than 1 since selections of different values affect all updating procedure. Selecting a small value for modelling error variance does not mean that it is small at the beginning of iterations. Therefore, this fact should be kept in mind while comparing the level of uncertainty results of Case 3 with Case 1 and 2. However, the values of posterior c.o.v for Case 1 are relatively smaller than those of Case 2 and Case 3.

Table 3.2. Updated stiffness parameters with complete modal data ($\times 10^3$ kN/m)

			Case 1 Presented Study		**Case 2**		**Case 3**	
Param.	Actual	Initial	Updated	c.o.v ($\times\mathbf{10^{-11}}$)	Updated	c.o.v ($\times\mathbf{10^{-11}}$)	Updated	c.o.v ($\times\mathbf{10^{-11}}$)
θ_1	202.767	517.2	201.7	6.18	203.4	36.83	205.5	131.24
θ_2	202.767	549.1	205.3	15.73	202.8	217.47	202.0	416.93
θ_3	202.767	464.5	202.8	1.79	202.7	400.58	202.9	292.15
θ_4	202.767	509.1	202.1	5.33	203.0	487.38	203.2	145.62
θ_5	202.767	586.6	202.2	8.48	202.9	430.31	202.8	90.07
θ_6	202.767	587.3	204.3	10.43	202.9	235.75	203.2	122.18
θ_7	202.767	431.0	202.5	3.66	202.8	121.20	203.0	17.66
θ_8	202.767	447.5	202.9	2.95	202.5	332.10	201.5	62.62
θ_9	202.767	415.9	202.8	2.92	203.0	444.54	203.2	27.68
θ_{10}	202.767	494.9	203.9	4.00	203.1	417.37	203.7	167.97
θ_{11}	202.767	411.6	202.1	3.85	202.9	270	202.8	185.36
θ_{12}	202.767	498.2	202.7	0.35	202.6	94.29	202.5	54.77

Most probable system mode shapes are presented for each case in Figure 3.2. Their modal assurance criterion (MAC) values and posterior c.o.v values of the modal shapes are provided in Table 3.3. In this study, MAC values are calculated between the updated system mode shapes and actual mode shapes of the numerical model. Referring to Figure 3.2 and MAC values, all updated mode shapes are acceptable when compared to mode shapes of the actual numerical structure. Besides, Case 2 performs very well with all MAC values of 100%. For Case 1, relatively smaller MAC values and slightly larger posterior c.o.v values are obtained for the last three modes. Case 1 results in relatively higher modelling error variances for these modes, which may explain the low MAC values larger c.o.v values. Since the modelling error variances for the higher modes are obtained higher as expected and mode shapes are sensitive to the modelling error, this result may be considered to be more realistic when compared with the results of Case 2 and 3.

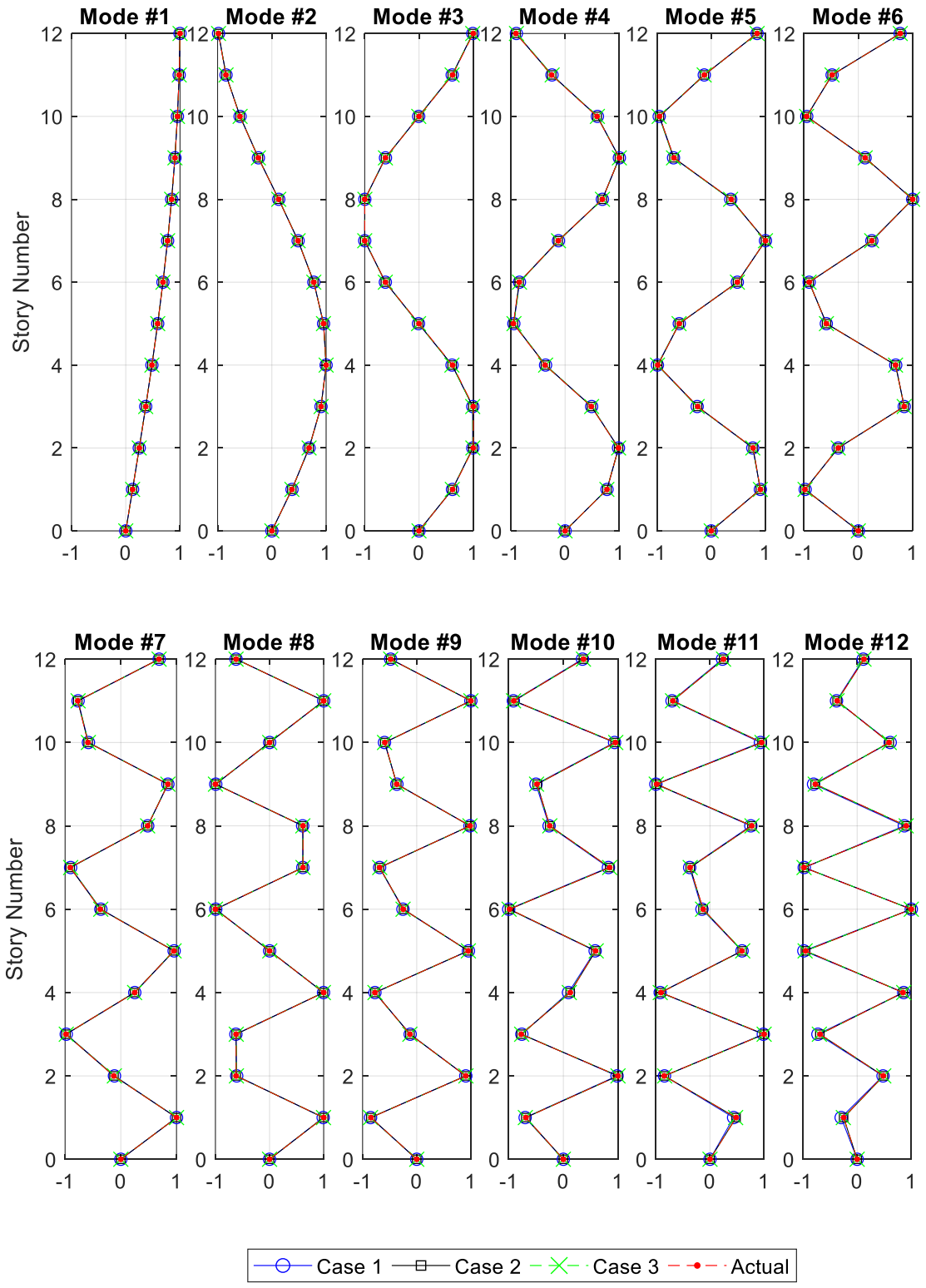

Figure 3.2. Updated system mode shapes with complete modal data for each case

Table 3.3. MAC values and posterior c.o.v of the updated system mode shapes with complete modal data

# Mode	**Case 1 Presented Study**		**Case 2**		**Case 3**	
	MAC (%)	c.o.v ($\times\mathbf{10^{-3}}$)	MAC (%)	c.o.v ($\times\mathbf{10^{-3}}$)	MAC (%)	c.o.v ($\times\mathbf{10^{-3}}$)
1	100.00	0.12	100.00	0.81	100.00	1.28
2	100.00	0.64	100.00	1.38	100.00	2.57
3	100.00	1.97	100.00	1.62	100.00	3.16
4	99.99	3.53	100.00	1.75	99.99	4.61
5	99.99	3.93	100.00	1.58	99.99	4.77
6	100.00	2.84	100.00	1.53	100.00	5.78
7	99.99	6.76	100.00	1.54	100.00	6.92
8	100.00	6.20	100.00	1.63	100.00	8.38
9	100.00	7.73	100.00	1.81	100.00	8.58
10	99.94	15.09	100.00	2.19	99.99	10.44
11	99.92	22.14	100.00	2.90	99.99	13.55
12	99.89	37.07	100.00	2.68	99.99	18.84

Further, Case 1 is investigated for incomplete modal data. First, different numbers of measured modes are considered with spatially complete measured mode shapes. For this investigation, it is considered as if the first two, four, seven or ten modes only are measured from the structure and model updating is performed by using these modes only. MPVs of the updated stiffness parameters are provided in Table 3.4. Further, results are illustratively presented in Figure 3.3.

Table 3.4. Updated stiffness parameters using different number of modes ($\times 10^3$ kN/m)

Parameter	**Number of considered measured modes**							
	2		**4**		**7**		**10**	
	Updated	c.o.v ($\times\mathbf{10^{-15}}$)	Updated	c.o.v ($\times\mathbf{10^{-14}}$)	Updated	c.o.v ($\times\mathbf{10^{-12}}$)	Updated	c.o.v ($\times\mathbf{10^{-11}}$)
θ_1	201.7	1.94	201.8	4.61	201.8	7.34	201.6	6.04
θ_2	206.4	4.49	206.4	7.28	206.3	12.42	205.4	14.61
θ_3	203.8	1.60	203.8	1.55	203.4	1.27	202.9	1.29
θ_4	202.0	0.52	201.8	3.13	202.1	3.12	202.1	4.59
θ_5	201.8	0.51	201.8	2.03	202.1	9.75	202.1	7.93
θ_6	205.2	0.83	204.9	5.71	204.5	11.57	204.2	9.35
θ_7	203.3	1.06	202.8	2.12	202.8	5.02	202.5	3.78
θ_8	203.6	1.97	203.3	2.14	202.9	7.08	202.9	3.01
θ_9	202.9	0.14	203.1	0.11	202.9	4.42	202.9	2.52
θ_{10}	203.8	2.69	203.9	0.13	203.7	3.32	203.9	3.30
θ_{11}	199.8	1.64	201.4	3.90	201.9	3.53	202.1	3.31
θ_{12}	207.8	1.40	203.2	0.99	202.4	0.67	202.6	3.30

Updated values are not as good as the ones obtained for the complete modal data. Since the model is updated with respect to the considered modes only and the available information is reduced, this is an expected result. Even so, the values of the updated stiffness parameters are in a good agreement with the actual ones. According to Figure 3.3, the presented study has slightly more convergence problems than the other cases. For example, for θ_{12}, the convergence quality is poor when the number of considered modes is very limited.

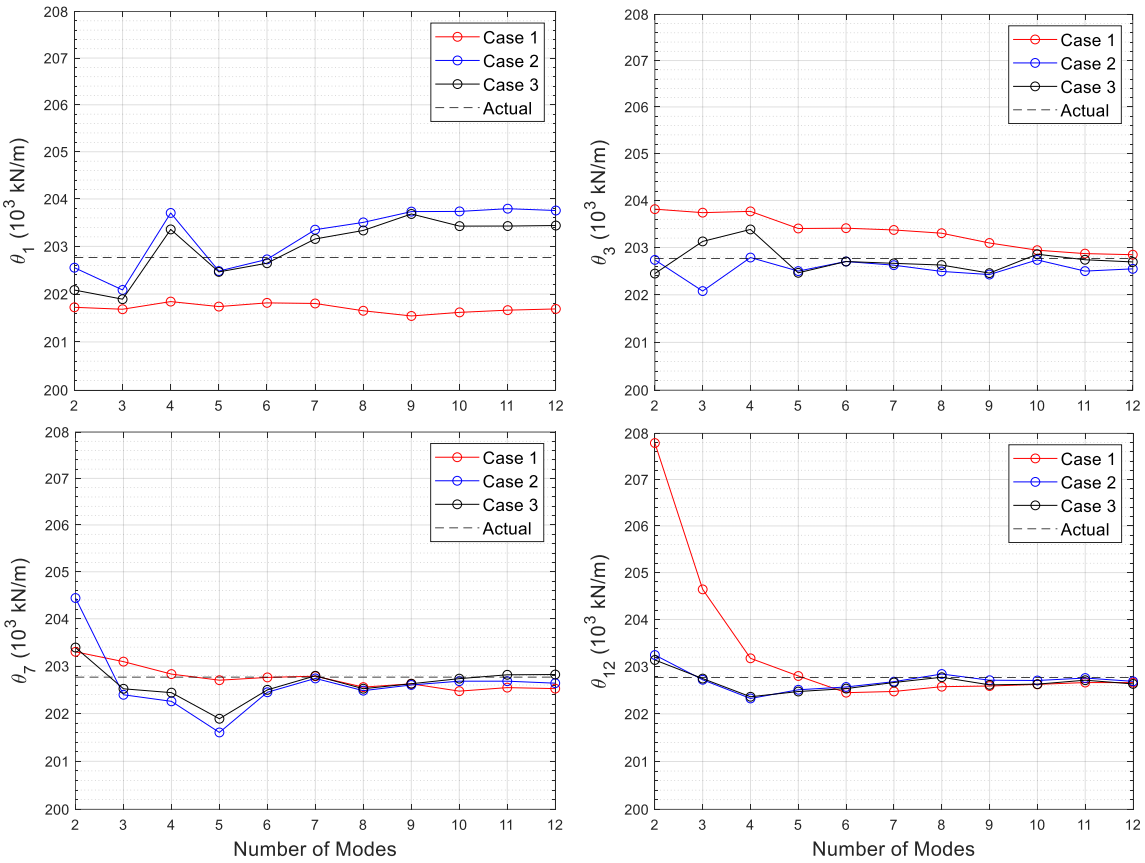

Figure 3.3. Convergence of some stiffness parameters with the number of considered modes

Figure 3.4 shows the graphical representation of the change in the posterior c.o.v values with the number of modes considered in the analysis. According to results presented in Table 3.4 and Figure 3.4, posterior c.o.v of the stiffness parameters increase with the increased number of considered measured modes. It is known that the updating process is performed to obtain the updating parameters which best fit the measured modes. When the considered number of modes increases, it may become

harder to obtain the parameters which best-fit all the considered modes. Besides, modelling error is generally high for higher modes of structures. Due to these facts, uncertainty in the updated parameters increases with the increase in considered measured modes. However, this result is exactly the opposite of that presented in the literature. Figure 3.5 provides the change in posterior c.ov. levels with the considered number of modes presented by Yuen (2010) for the same numerical example. Since the available information increases with the increase in mode number, it is found in the literature that uncertainties should decrease with the increase in the number of considered measured modes.

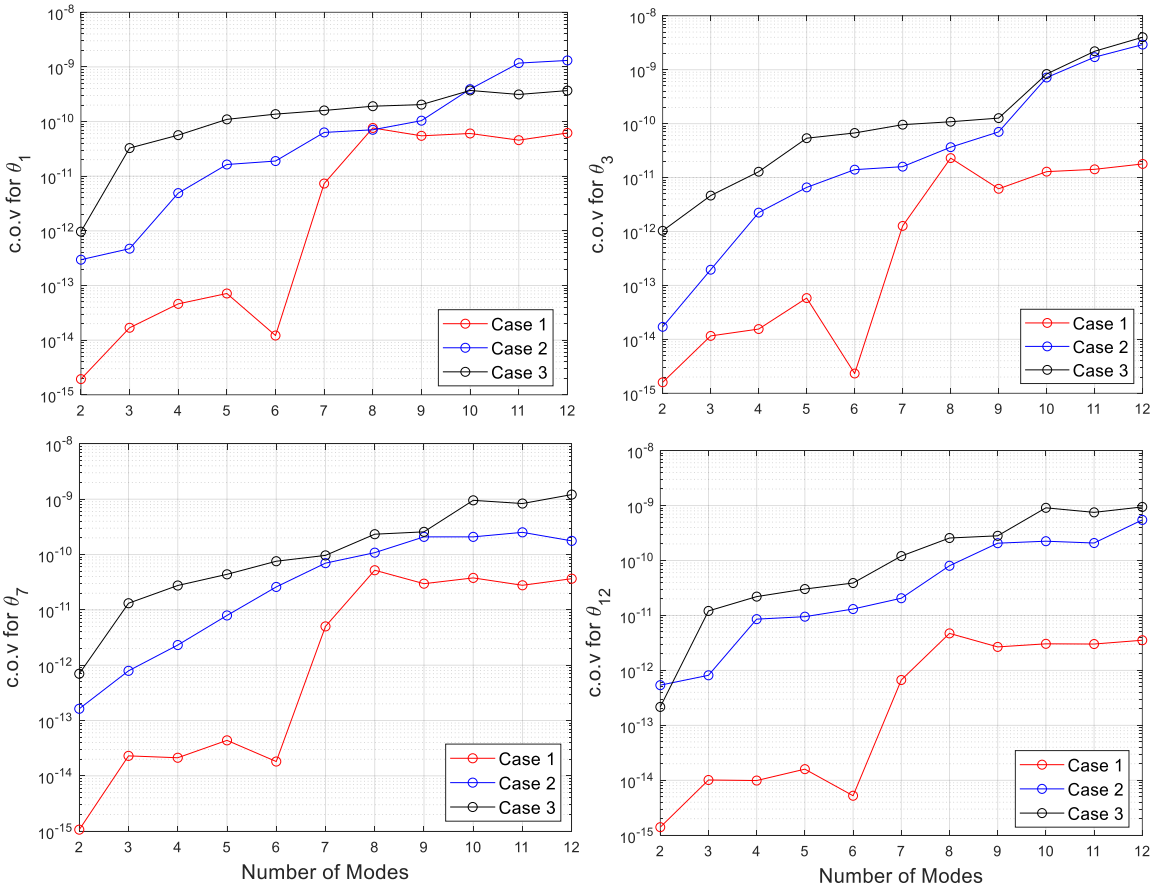

Figure 3.4. Change in posterior c.o.v values with the considered number of modes for Case 1, 2 and 3

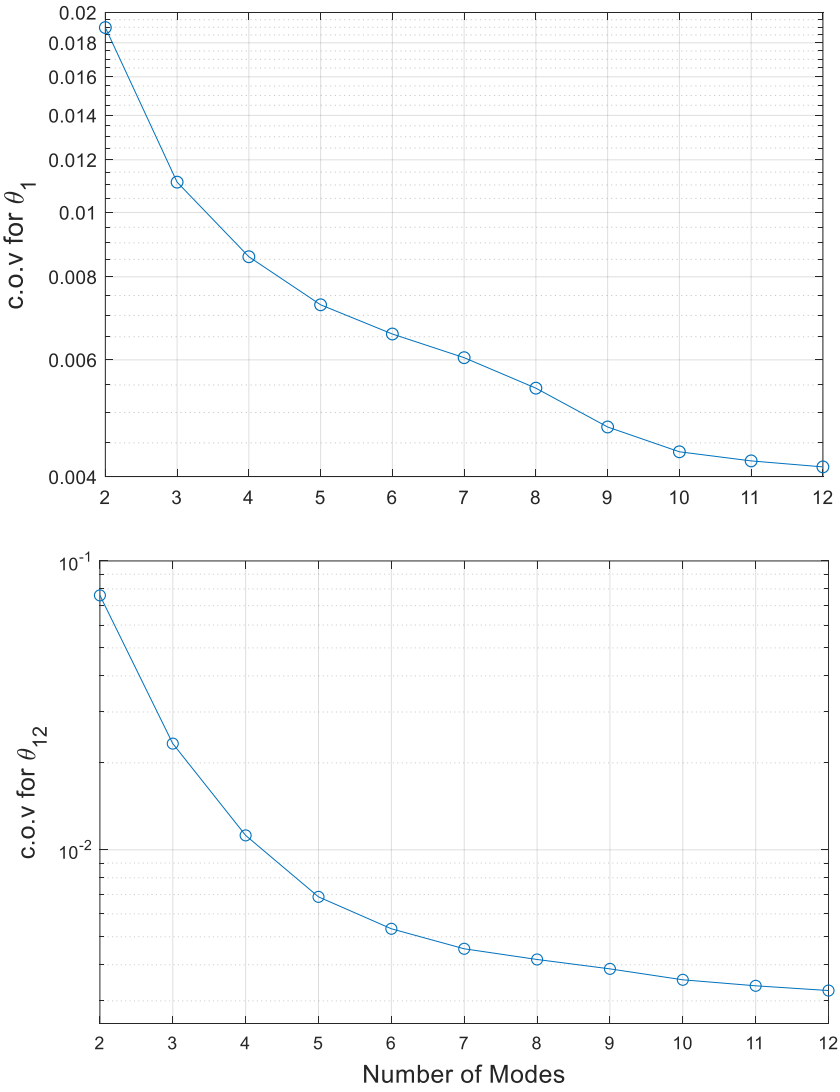

Figure 3.5. Change in posterior c.o.v values with the considered number of modes presented by Yuen (2010) for the same numerical example

Second, the performance of Case 1, 2 and 3 is investigated in case of using incomplete measured modal data and spatially incomplete mode shapes. To this end, two different incompleteness scenarios are investigated, and measurement scheme of each scenario is shown in Table 3.5. It is worth to note that the influence of change in number of modes on the updating process is already analyzed by keeping the number of measured DOFs unchanged. Therefore, here, both the number of modes and measured DOFs are increased while considering Scenario 2.

Table 3.5. Measurement schemes for Scenario 1 and Scenario 2

Scenario 1		**Scenario 2**	
Measured Modes	Measured DOFs	Measured Modes	Measured DOFs
1, 2, 3	1, 2, 6, 8, 11, 12	1, 2, 3, 4, 5, 6, 7, 8	1, 2, 4, 5, 7, 8, 9, 10, 12

3.2.6.1. Results of Scenario 1:

MPVs of the updated system frequencies with their posterior c.o.v values are provided in Table 3.6 for each case. Modelling error variances are also given in the table. Updated system frequencies are found to be compatible with the actual values for each case. Further, Case 1 significantly reduces the posterior c.o.v of the updated system frequencies since the modelling error variance is accounted for each mode.

Table 3.6. Updated system frequencies for Scenario 1

	Case 1 Presented Study			**Case 2**			**Case 3**		
Actual (Hz)	Upd. (Hz)	c.o.v	Updated $S_{eq,n}$	Upd. (Hz)	c.o.v	Upd. S_{eq}	Upd. (Hz)	c.o.v	S_{eq}
0.90	0.90	2.26×10^{-17}	9.08×10^{-15}	0.90	4.66×10^{-4}		0.90	4.66×10^{-4}	
2.69	2.69	5.28×10^{-52}	0.09	2.69	3.43×10^{-4}	0.006	2.69	3.43×10^{-4}	1
4.43	4.43	2.39×10^{-52}	1.61	4.43	2.48×10^{-4}		4.43	2.48×10^{-4}	

Updating results for the stiffness parameters are provided in Table 3.7 for each case. According to the results, most of the updated stiffness parameters in each case are biased from their actual values when compared to the results obtained with spatially complete mode shape data. Since half of the DOFs are not measured, at least one of the incomplete mode shapes may not reflect the dynamic behavior of the actual structure as good as the complete ones. Further, increment in the number of measured modes does not improve the biased results, it even causes the worse updating results. It is reasonable since increasing the number of modes introduces higher uncertainties in the identification of stiffness parameters. On the other hand, Case 1 results in considerably

lower posterior c.o.v values, which proves that the reliability of model updating with Case 1 is significantly higher with spatially incomplete mode shape data.

Table 3.7. Updated stiffness parameters for Scenario 1 ($\times 10^3$ kN/m)

			Case 1 Present Study		**Case 2**		**Case 3**	
Param.	Actual	Initial	Updated	c.o.v ($\times\mathbf{10^{-24}}$)	Updated	c.o.v ($\times\mathbf{10^{-12}}$)	Updated	c.o.v ($\times\mathbf{10^{-11}}$)
θ_1	202.767	517.2	202.8	5.60	200.2	8.58	202.2	20.47
θ_2	202.767	549.1	206.5	30.14	199.6	13.67	202.9	6.28
θ_3	202.767	464.5	183.5	9.15	195.5	50.79	196.7	103.76
θ_4	202.767	509.1	192.5	1.03	189.9	28.48	194.7	34.64
θ_5	202.767	586.6	221.1	7.35	204.4	7.49	202.8	15.87
θ_6	202.767	587.3	233.0	9.98	207.7	22.12	202.2	85.12
θ_7	202.767	431.0	195.7	8.28	189.8	29.68	189.8	15.39
θ_8	202.767	447.5	215.4	6.58	218.7	3.44	218.6	4.07
θ_9	202.767	415.9	197.0	2.51	190.4	49.66	185.2	132.98
θ_{10}	202.767	494.9	228.4	2.85	229.2	4.74	230.0	11.91
θ_{11}	202.767	411.6	184.4	6.28	192.5	31.28	197.2	59.22
θ_{12}	202.767	498.2	207.1	5.72	205.9	9.18	202.8	11.12

To account for the convergence speed, the same convergence criterion is applied for each case and iteration histories are presented in Figure 3.6. As the convergence criterion, relative error between the updated stiffness parameters which are obtained in two consecutive iterations are calculated and iterations are stopped if the relative error is smaller than 10^{-3}. As seen from the figure, Case 1 has the highest convergence speed with a total of 7 iterations.

Most probable system mode shapes are presented in Figure 3.7 for each case, and their MAC values and posterior c.o.v values are provided in Table 3.8. Referring to Figure 3.7 and the MAC values, all updated mode shapes are in an acceptable agreement with the first three mode shapes of the actual numerical model. However, the third system mode shape is slightly distorted for Case 1 and its MAC value is lower than that of the other modes. Further, Case 1 gives significantly lower posterior c.o.v values for the first and second mode, and relatively large value for the third mode. The updated modelling error variance is also higher for the third mode. This may explain the relatively low MAC value and larger c.o.v for this mode. The components of the updated system mode shapes, which correspond to the incomplete components of the

measured mode shapes, are identified in good agreement with the actual values of the missing components for all three cases.

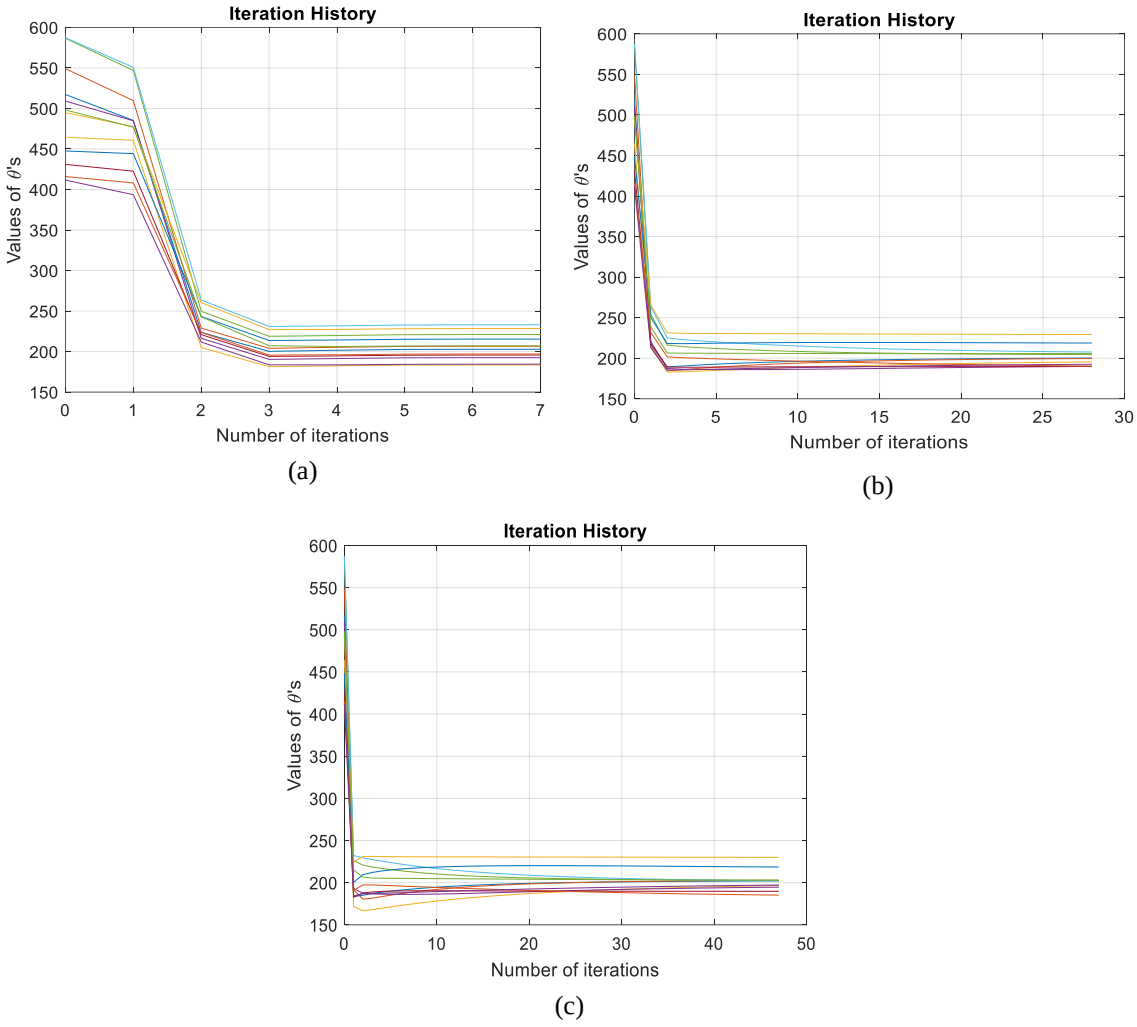

Figure 3.6. Iteration histories of Scenario 1 for (a) Case 1 (b) Case 2 and (c) Case 3

Table 3.8. MAC values and posterior c.o.v of the updated system mode shapes for Scenario 1

	Case 1 Presented Study		**Case 2**		**Case 3**	
# Mode	MAC (%)	c.o.v	MAC (%)	c.o.v	MAC (%)	c.o.v
1	99.99	1.87×10^{-7}	100.00	0.87×10^{-3}	100.00	6.31×10^{-3}
2	99.98	0.92×10^{-7}	99.98	1.15×10^{-3}	99.97	4.80×10^{-3}
3	99.68	2.97×10^{-3}	99.92	1.49×10^{-3}	99.94	7.26×10^{-3}

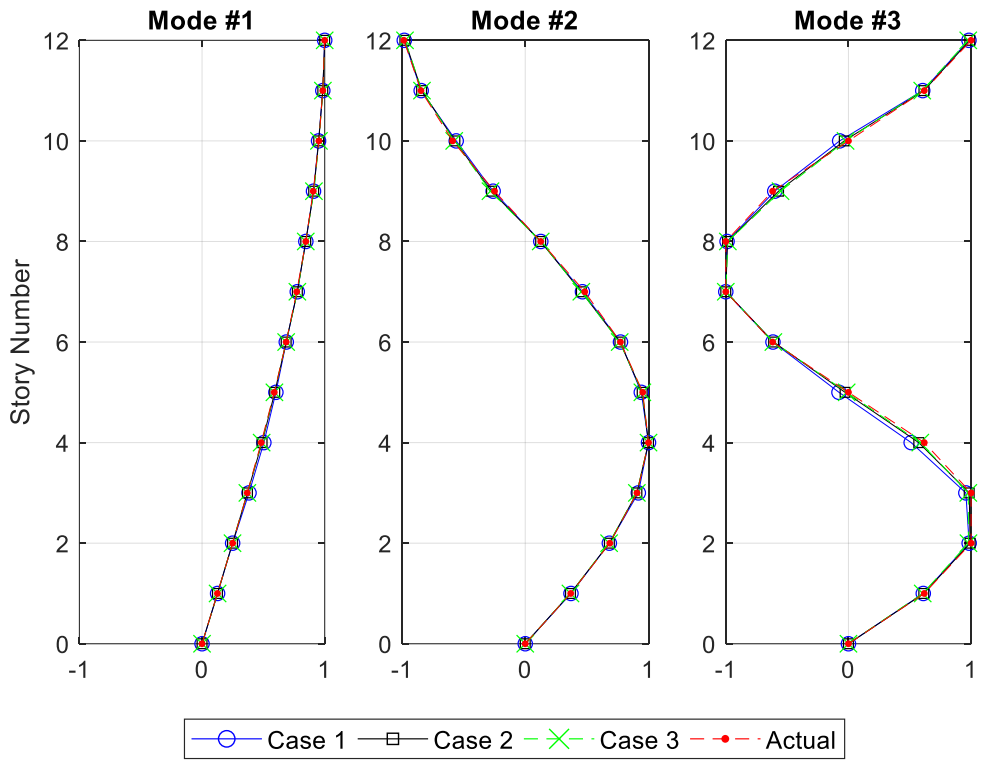

Figure 3.7. Updated system mode shapes for Scenario 1

3.2.6.2. Results of Scenario 2:

Since the updated stiffness parameters are unsatisfactory for all three cases in scenario 1, another analysis needs to be performed as “Scenario 2” by increasing the number of measured modes and measured DOFs. MPVs of the updated system frequencies with their posterior c.ov values are provided in Table 3.9 for each case. Modelling error variances are also given in the table. Updated system frequencies are compatible with the actual values for each case. As previously obtained, Case 1 significantly reduces the posterior c.o.v of the updated system frequencies. The results in Table 3.9 are compared with those provided in Table 3.1 and Table 3.6, which correspond to the complete modal data and Scenario 1, respectively. It can be clearly seen that system frequencies are updated very well for all cases and scenarios. Besides, the values of posterior c.o.v of the updated system frequencies, which are obtained by Case 2 and Case 3, are not affected from incomplete measured modal data. In contrast, those obtained by Case 1 show variations with the change in the incompleteness condition of the measured modal data. According to Table 3.1, Table 3.6 and Table 3.9,

it can be concluded that the values of the posterior c.o.v of the system frequencies show a decreasing trend with the decrease in the number of measured modal data.

Table 3.9. Updated system frequencies for Scenario 2

	Case 1 Presented Study			**Case 2**			**Case 3**		
Actual (Hz)	Upd. (Hz)	c.o.v	Updated $S_{eq,n}$	Upd. (Hz)	c.o.v	Upd. S_{eq}	Upd. (Hz)	c.o.v	S_{eq}
0.90	0.90	1.05×10^{-13}	2.49×10^{-8}	0.90	4.68		0.90	4.68×10^{-4}	
2.69	2.69	1.14×10^{-23}	0.018	2.69	3.44×10^{-4}		2.69	3.44×10^{-4}	
4.43	4.43	1.23×10^{-23}	0.35	4.43	2.50×10^{-4}		4.43	2.50×10^{-4}	
6.10	6.11	1.24×10^{-23}	0.89	6.11	2.69×10^{-4}	0.01	6.11	2.69×10^{-4}	1
7.68	7.68	6.74×10^{-24}	8.10	7.68	2.06×10^{-4}		7.68	2.06×10^{-4}	
9.14	9.14	4.55×10^{-24}	8.66	9.14	1.85×10^{-4}		9.14	1.85×10^{-4}	
10.45	10.46	3.61×10^{-24}	47.22	10.46	1.95×10^{-4}		10.46	1.95×10^{-4}	
11.60	11.60	3.02×10^{-24}	22.71	11.60	2.01×10^{-4}		11.60	2.01×10^{-4}	

MPVs of the stiffness parameters are provided in Table 3.10 and their iteration history for each case is presented in Figure 3.8. According to these results, updated stiffness parameters by using Case 2 and 3 agree well with the actual values whereas those obtained by Case 1 has some biased values similar to the results obtained for Scenario 1. These results can also be visually observed by investigating the iteration history plots in Figure 3.8. Increasing the modal information (number of considered modes and measured DOFs) corrects the updated results for Case 2 and 3. Since Case 1 accounts for modelling error for each mode, it implicitly gives less weights to the modes with high uncertainties. Therefore, updating process concentrates on some modes with lower uncertainties and by-pass the other modes. When the modal data is already incomplete, it may result in significantly less information for a successful updating process. The uncertainty results in Table 3.10 are compared with those provided in Table 3.2 and Table 3.7, which correspond to the results of complete modal data and Scenario 1, respectively. Posterior c.o.v values of the updated stiffness parameters are in a significantly decreasing trend with the decrease in measured modal data for Case 1. However, any significant change cannot be realized for Case 2 and 3.

Table 3.10. Updated stiffness parameters for Scenario 2 (× 10^3 kN/m)

Param.	Actual	Initial	**Case 1 Presented Study**		**Case 2**		**Case 3**	
			Updated	c.o.v ($\times$**10^{-19}**)	Updated	c.o.v ($\times$**10^{-10}**)	Updated	c.o.v ($\times$**10^{-10}**)
θ_1	202.767	517.2	201.6	1.45	204.1	1.74	203.4	1.56
θ_2	202.767	549.1	205.1	3.20	203.4	3.05	204.0	3.85
θ_3	202.767	464.5	194.5	4.00	199.1	1.45	202.2	7.83
θ_4	202.767	509.1	208.4	1.88	202.5	2.60	202.0	3.44
θ_5	202.767	586.6	207.3	1.43	207.6	1.86	203.2	3.17
θ_6	202.767	587.3	230.1	2.08	203.6	1.86	201.3	5.90
θ_7	202.767	431.0	183.5	8.65	200.1	2.82	202.9	6.25
θ_8	202.767	447.5	200.7	1.08	202.4	1.33	203.8	2.66
θ_9	202.767	415.9	202.1	1.01	203.4	2.24	203.3	2.07
θ_{10}	202.767	494.9	203.5	0.88	204.0	1.63	203.6	3.29
θ_{11}	202.767	411.6	193.5	3.31	202.7	0.94	202.1	9.05
θ_{12}	202.767	498.2	211.5	0.83	202.4	2.71	202.8	10.00

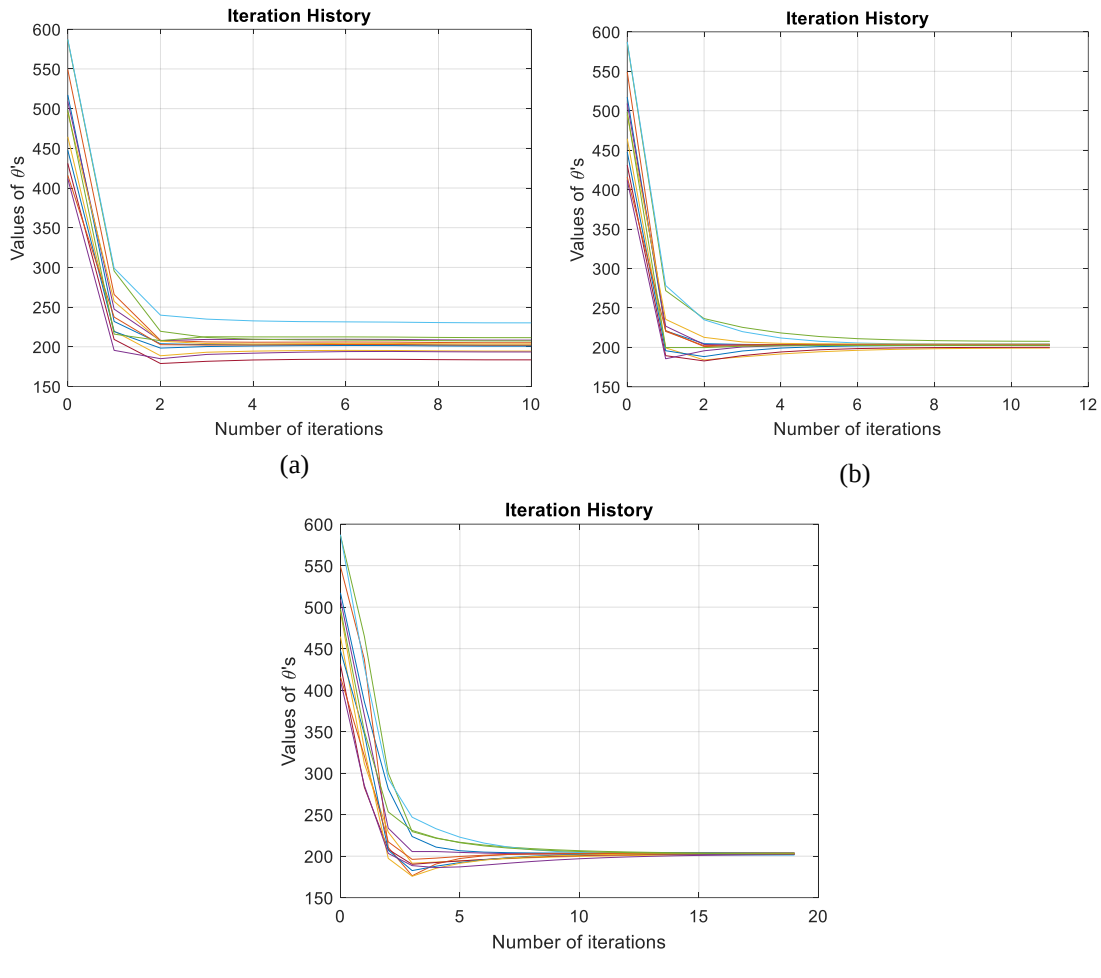

Figure 3.8. Iteration histories of Scenario 2 for (a) Case 1 (b) Case 2 and (c) Case 3

Most probable system mode shapes are presented in Figure 3.9 for each case, and their MAC values and posterior c.o.v values are provided in Table 3.11. According to the results, all updated mode shapes are in an acceptable agreement with the first eight mode shapes of the actual model. However, some distortions are visible for Case 1, which is proved by lower MAC values when compared with the results obtained for Case 2 and 3. Further, Case 1 gives lower posterior c.o.v values for the first and second mode, and relatively large values for higher modes. For higher modes, there is no considerable difference among posterior c.o.v obtained in different cases.

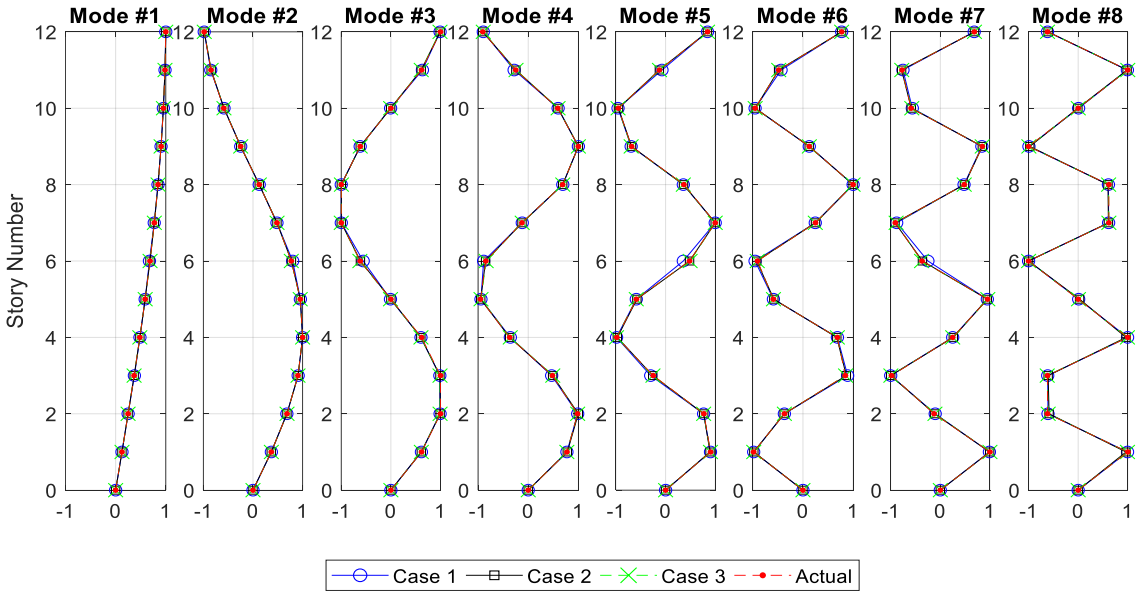

Figure 3.9. Updated system mode shapes for Scenario 2

Table 3.11. MAC values and posterior c.o.v of the updated system mode shapes for Scenario 2

# Mode	Case 1 Present Study		Case 2		Case 3	
	MAC (%)	c.o.v	MAC (%)	c.o.v	MAC (%)	c.o.v
1	100.00	6.52×10^{-6}	100.00	1.02×10^{-3}	100.00	3.16×10^{-3}
2	99.99	2.35×10^{-6}	100.00	1.70×10^{-3}	100.00	4.34×10^{-3}
3	99.94	2.57×10^{-3}	100.00	1.71×10^{-3}	99.99	4.12×10^{-3}
4	99.94	3.71×10^{-3}	100.00	2.17×10^{-3}	99.99	4.69×10^{-3}
5	99.66	6.19×10^{-3}	99.99	2.33×10^{-3}	99.99	6.38×10^{-3}
6	99.91	13.04×10^{-3}	99.99	1.80×10^{-3}	100.00	6.73×10^{-3}
7	99.76	14.11×10^{-3}	99.99	1.74×10^{-3}	99.98	6.59×10^{-3}
8	100.00	15.31×10^{-3}	99.99	1.99×10^{-3}	100.00	7.70×10^{-3}

3.3. Conclusions

In this section, remarkable findings and discussions on the results are briefly presented for the investigated two-stage Bayesian model updating methodology.

3.3.1. Concluding Remarks

This chapter is a follow-up study on the two-stage Bayesian FE model updating formulations derived by Çağlayan Hızal in Chapter 5 of his dissertation (Hızal, 2019) and in the published work by Hızal and Turan (2020). They consider the measurement error in the measured modal data and modelling error in the model updating stage. No correlation is assumed between the eigenvalues and eigenvectors and therefore, they could define prior distributions for eigenvalues and eigenvectors, separately. As previously proposed in the literature, the concept of system modes is also used to avoid the mode matching which is one of the main problems in the model updating literature. First, their derivations are reformulated for a single setup case assuming that mass values are known with a sufficient accuracy and are not taken as parameters to be updated. Hızal and Turan (2020) have considered the modelling error variances of eigenvalue equations to be the same for each mode. They have defined a single modelling error variance as a soft constraint. In the present study, however, reformulation is performed by considering the modelling error variances of eigenvalue equations to be different for each mode and updated in each iteration. Therefore, an independent modelling error variance is defined for each mode. Besides, there are some studies in the literature which consider the modelling error variance as a rigid constraint such as Yuen (2010). They assign a prescribed value for the modelling error variance and do not update it. The major objective of this chapter is to compare these three different assumptions on modelling error variances. To this end, a comparative numerical analysis is conducted to investigate the influences of these three assumptions on the Bayesian model updating procedure. The numerical study is performed on a twelve-story shear frame structure.

The results of numerical study reveal that considering modelling error variance to be different for each mode significantly reduces the posterior uncertainties of the updated system frequencies and stiffness parameters. By considering different

modelling error variances for each mode, less weight is assigned for the modes with higher uncertainties and this fact significantly reduces the posterior c.o.v values. Minimization process concentrates on some specific modes with lower uncertainties and by-pass the other modes. On the other hand, investigated assumption of modelling error variance does not significantly reduce the posterior uncertainties of the system mode shapes.

The influence of different modelling error assumptions is also investigated for incomplete modal data. It is found that the uncertainty in the updated parameters, for the modelling error assumptions which is the same for all modes and with a prescribed value, does not significantly change under different incomplete modal data conditions. Further, the posterior uncertainties of system frequencies are never affected by incomplete modal data. However, it is observed for the considered modelling error assumption that uncertainty in the updated parameters significantly increases with the increase in considered number of measured modes and measured DOFs. The reason can be explained as follows; the updating process is performed to obtain the parameters which best-fit all the measured modes. When the considered number of modes increases, it may become harder to optimize the parameters that best-fit all the considered modes. However, as discussed by referring to Figure 3.5, this result is the opposite of findings in the literature. According to the literature, uncertainties should decrease with the increase in the considered number of modes since the available information is increasing. Further, modelling error is generally high for higher modes of structures and the uncertainty in the updated parameters may increase by introducing higher modes in the updating process. On the contrary, with the increase in number of the measured modes, updated parameters better converge to the actual values while their posterior uncertainties are getting increased.

3.3.2. Discussions on the Conclusions

It can be concluded that considering modelling error variance to be different for each mode results in convergence problems for incomplete measured modal data even if it reduces the posterior uncertainties. Besides, using a rigid constraint for the modelling error is not realistic since the prescribed value may not represent the actual modelling errors. Taking the modelling error variance to be the same for each mode does not

account for the modelling errors of the eigen equations of each mode and therefore they are not weighted with a proper value which is also not realistic. Introducing the modelling error term in the updating procedure is needed to account for the modelling errors, however, it brings some other problems to be solved. There are studies in the literature which do not consider the modelling error. However, this inevitably increases the posterior uncertainties of the updated parameters (Yan and Katafygiotis, 2015). As a result, the underlying solution may be somehow removing the modelling error term. It may be removed from the formulations by combining Bayesian model updating framework with the sensitivity-based approaches which are employed by many researchers in the model updating field. By doing so, sensitivity equations which account for the changes in the parameters can be derived in the optimization process and thus, modelling error term will no longer be necessary to account for the discrepancies in the eigen equations. Thus, a robust model updating technique can be developed to solve the incomplete modal data problem.

CHAPTER 4

A TWO-STAGE SENSITIVITY-BASED BAYESIAN MODEL UPDATING METHOD UTILIZING THE FE MODEL MODES

4.1. Introduction

The previous chapter has focused on the two-stage Bayesian FE model updating formulations by utilizing the concept of system modes. In that study, concept of system modes is used to avoid the mode matching problem in model updating procedure. Using the system modes requires the definition of modelling error term which sets the relation between the system modes and the FE model via eigenvalue equations. Modelling error variance is updated separately for each mode differently from Hızal's (2019) research which assumes a single modelling error variance for all modes. For both studies, modelling error variance has been updated as a soft constraint. Besides, there are some studies in the literature which consider the modelling error variance as a rigid constraint, such as Yuen (2010). They assign a prescribed value for the modelling error variance and do not update it. The major objective of the previous chapter has been to compare three different assumptions on modelling error variances. Results of the previous study have revealed that the formulations with the three modelling error assumptions give unreasonably small posterior c.o.v values. Even if the updating results are not convergent to the actual values, too small posterior c.o.v values are obtained. This shows that the algorithm strictly relies on the divergent results, which is unreasonable.

Besides the modelling error term, formulation in the previous chapter requires a norm constraint term in the objective function for the normalization of the system mode shapes. The reason is that the system mode shapes are used as independent variables and therefore their norms may not remain same over iterations. To guarantee a constant norm over iterations for the mode shape vectors, a norm constraint term is added to the objective function. However, this results in an invertible Hessian matrix of the updated

parameters, which requires pseudo-inverse operation to obtain the posterior covariance matrix. It is realized in the literature that researchers who use a norm constraint term in the objective function generally face relatively small posterior uncertainties for the updated parameters (Yan and Katafygiotis, 2015; Hızal, 2019; Hızal and Turan, 2020).

According to the above discussions, it can be deduced that the underlying solution to avoid too small posterior uncertainties may be somehow removing the modelling error and/or the norm constraint terms from the formulations. However, Au (2012), and Yan and Katafygiotis (2015) state that removing modelling error term in classical formulations increases the posterior parameter uncertainties since the modelling error still exists in reality. If the concept of system modes is still used in the formulations, modelling error term should be considered to account for the corresponding uncertainties. Therefore, to remove the modelling error term, one should leave the concept of system modes. To this end, in this chapter, Bayesian model updating framework is combined with a deterministic sensitivity-based model updating approach. By doing so, modal properties of the FE model are directly employed instead of system modes. Thus, the eigenvalue equations are constructed by using FE model modes, which eliminates modelling error term from the objective function. Besides, using the FE modes automatically removes the need for the norm constraint for the mode shapes since they can be directly obtained from the eigenvalue analysis of the updated system. In this case, eigen frequencies and mode shapes should be considered in terms of updating stiffness parameters. This results in a closed-form non-linear objective function of updating parameters. Minimization of such an objective function requires numerical optimization algorithms such as the Newton method. Therefore, sensitivity equations which account for the changes in the parameters are derived in this chapter.

Derivations of the sensitivity equations are obtained by following the formulations proposed by Otsuki et al. (2021). All their derivations are performed from a deterministic point of view. Thus, in the present study differently from Otsuki et al. (2021), sensitivity derivations are performed in a probabilistic way by introducing the Bayesian model updating framework. It is shown that posterior covariance matrix of the updated parameters is the inverse of Hessian matrix of the objective function that is constructed as a non-linear function of stiffness and mass parameters. Therefore, posterior uncertainties of the updated parameters are obtained by using the posterior

covariance matrix. To this end, Hessian of the objective function is derived for the existing problem.

To solve the optimization problem, “SMU: MATLAB Package for Structural Model Updating” which is shared by Wang et. al. (2019) is used for the solution of the optimization problem. The existing SMU package is modified from a deterministic approach to the probabilistic one.

A comparative numerical study is performed to investigate the effects of the presented formulations on the MPVs and the posterior uncertainties of the updated parameters. To this end, numerical studies are performed on the same numerical twelve-story shear frame model that is used in the previous chapter by employing complete and incomplete measured modal data. Then, the proposed method is experimentally verified on a 10-story laboratory shear frame model.

4.2. A Two-stage Sensitivity-based Bayesian Model Updating Utilizing the FE Model Modes

The main difference from the formulations derived by Otsuki et al. (2021) is that the deterministic formulations are turned into probabilistic ones. Further, each term of the objective function is considered as a scalar value in this study instead of vectors. This considerably reduces the dimension of the analytical Jacobian when compared with their derivations.

4.2.1. Modal Identification Stage

In this stage, the modal identification is performed with the same Bayesian modal identification strategy that is introduced in Section 3.2.1.

4.2.2. Model Updating Stage

In this section, sensitivity-based formulations are introduced to develop a sensitivity-based Bayesian model updating methodology.

4.2.2.1. Structural Model and Parametrization of Stiffness and Mass Matrices

In Chapter 3, the stiffness matrix is parameterized only and mass is assumed to be known and it is not considered as a parameter to be updated. Differently from the parameterization that is discussed in Section 3.2.2.2, the mass of the structure is also considered as an updating variable in this chapter.

The model is parameterized by defining the parametric stiffness and mass matrices, $\mathbf{K}(\boldsymbol{\theta})$ and $\mathbf{M}(\boldsymbol{\rho})$, with a size of $N_d \times N_d$, in terms of a linear combination of substructure stiffness and mass matrices, $\mathbf{K}_i$ and $\mathbf{M}_j$, respectively, as;

$$\mathbf{K}(\boldsymbol{\theta}) = \mathbf{K}_0 + \sum_{i=1}^{N_\theta} \theta_i \mathbf{K}_i \qquad \mathbf{M}(\boldsymbol{\rho}) = \mathbf{M}_0 + \sum_{j=1}^{N_\rho} \rho_j \mathbf{M}_j \tag{4.1}$$

where $\mathbf{M}_0$ and $\mathbf{K}_0$ are the non-parametric portions of the mass and stiffness matrix which are not affected by the updating procedure, respectively. The substructure stiffness and mass matrices, $\mathbf{K}_i$ and $\mathbf{M}_j$, are the elementwise nominal stiffness and mass matrices extended to the size of $N_d \times N_d$, respectively. Thus, they represent the contributions of a part of the structure to the overall stiffness and mass matrix. $\boldsymbol{\theta} = [\ \theta_1\ \theta_2\ \theta_3 \ldots \theta_{N_\theta}]^{\mathrm{T}}$ is a vector that comprises stiffness scaling factors $\theta_i \in R^{N_\theta}$ and $\boldsymbol{\rho} = [\ \rho_1\ \rho_2\ \rho_3 \ldots \rho_{N_\rho}]^{\mathrm{T}}$ is a vector that comprises mass scaling factors $\rho_j \in R^{N_\rho}$. These factors are required to modify $\mathbf{K}_i$ and $\mathbf{M}_j$ so that the FE model can reasonably represent the actual structural conditions based on the measured modal data. Here, N_θ and N_ρ represent the total number of stiffness and mass scaling factors, respectively. The parameter vectors $\boldsymbol{\theta}$ and $\boldsymbol{\rho}$ are combined into a single vector for the clarity of further formulations as

$$\boldsymbol{\chi} = \begin{bmatrix} \boldsymbol{\theta} \\ \boldsymbol{\rho} \end{bmatrix} = \begin{bmatrix} \theta_1 & \theta_2 & \cdots & \theta_{N_\theta} & \rho_1 & \rho_2 & \cdots & \rho_{N_\rho} \end{bmatrix}^T \tag{4.2}$$

4.2.2.2. Posterior (updated) Probability Model for the Parameters to be Updated

After achieving the most probable parameter set, $\mathbf{D} = \{ \hat{\boldsymbol{\lambda}} , \hat{\boldsymbol{\phi}}, \boldsymbol{\Sigma}_{\hat{\lambda}} , \mathbf{H}_{\hat{\phi}} \}$ by making use of the BAYOMA, the conditional probability distribution for the set of stiffness and mass scaling parameters can be derived by employing well-known Bayes' theorem based on the identified modal data. Here, the corresponding posterior PDF for $\boldsymbol{\chi}$ given **D** can be defined as

$$p(\boldsymbol{\chi} \mid \mathbf{D}) = c_0 p(\mathbf{D} \mid \boldsymbol{\chi}) p(\boldsymbol{\theta}) p(\boldsymbol{\rho}) \tag{4.3}$$

where $c_0 = 1 / p(\mathbf{D})$ represents a normalizing factor so that the probability function $p(\boldsymbol{\chi} \mid \mathbf{D})$ integrates to 1. Here, the likelihood function $p(\mathbf{D} \mid \boldsymbol{\chi})$ is expanded as

$$p(\mathbf{D} \mid \boldsymbol{\chi}) = p(\hat{\boldsymbol{\lambda}}, \hat{\boldsymbol{\phi}}, \boldsymbol{\Sigma}_{\hat{\lambda}}, \mathbf{H}_{\hat{\phi}} \mid \boldsymbol{\chi}) = p(\hat{\boldsymbol{\lambda}}, \boldsymbol{\Sigma}_{\hat{\lambda}} \mid \boldsymbol{\chi}) \, p(\hat{\boldsymbol{\phi}}, \mathbf{H}_{\hat{\phi}} \mid \boldsymbol{\chi}) \tag{4.4}$$

Substituting equation (4.4) into equation (4.3), posterior PDF of the parameters $\boldsymbol{\chi}$ conditioned on the measured modal data **D** can be written as follows

$$p(\boldsymbol{\chi} \mid \mathbf{D}) = c_0 p(\hat{\boldsymbol{\lambda}}, \boldsymbol{\Sigma}_{\hat{\lambda}} \mid \boldsymbol{\chi}) \, p(\hat{\boldsymbol{\phi}}, \mathbf{H}_{\hat{\phi}} \mid \boldsymbol{\chi}) \, p(\boldsymbol{\theta}) \, p(\boldsymbol{\rho}) \tag{4.5}$$

MPVs of the parameters, $\boldsymbol{\chi}$ based on the measured modal data can be obtained by maximizing the posterior PDF given in equation (4.5). It is known in the literature that more convenient way to solve this optimization problem is to minimize the negative log-likelihood function of the posterior PDF.

4.2.2.3. Probability Model for the Stiffness and Mass Parameters

The prior probability distribution of $\boldsymbol{\theta}$ and $\boldsymbol{\rho}$ is taken as multivariate truncated Gaussian distribution which truncates the negative values since the negative values of the stiffness and mass parameters have no physical meaning.

The prior PDF of $\boldsymbol{\theta}$ with mean value of $\hat{\boldsymbol{\theta}}_0$ and with covariance matrix of $\boldsymbol{\Sigma}_{\boldsymbol{\theta}}$ can be defined as

$$p(\boldsymbol{\theta}) = \begin{cases} \dfrac{1}{\sqrt{(2\pi)^{N\theta}\left|\boldsymbol{\Sigma}_{\boldsymbol{\theta}}\right|}} \exp\left[-\dfrac{1}{2}\left(\boldsymbol{\theta}-\hat{\boldsymbol{\theta}}_0\right)^T \boldsymbol{\Sigma}_{\boldsymbol{\theta}}^{-1}\left(\boldsymbol{\theta}-\hat{\boldsymbol{\theta}}_0\right)\right], & for\ each\ \theta_i > 0 \\ 0, & for\ any\ \theta_i < 0 \end{cases} \tag{4.6}$$

Similarly, the prior PDF of $\boldsymbol{\rho}$ with mean value of $\hat{\boldsymbol{\rho}}_0$ and with covariance matrix of $\boldsymbol{\Sigma}_{\boldsymbol{\rho}}$ can be defined as

$$p(\boldsymbol{\rho}) = \begin{cases} \dfrac{1}{\sqrt{(2\pi)^{N\boldsymbol{\rho}}\left|\boldsymbol{\Sigma}_{\boldsymbol{\rho}}\right|}} \exp\left[-\dfrac{1}{2}\left(\boldsymbol{\rho}-\hat{\boldsymbol{\rho}}_0\right)^T \boldsymbol{\Sigma}_{\boldsymbol{\rho}}^{-1}\left(\boldsymbol{\rho}-\hat{\boldsymbol{\rho}}_0\right)\right], & for\ each\ \rho_j > 0 \\ 0, & for\ any\ \rho_j < 0 \end{cases} \tag{4.7}$$

In equations (4.6) and (4.7), $\hat{\boldsymbol{\theta}}_0$ and $\hat{\boldsymbol{\rho}}_0$ are the vectors of prior MPVs of the stiffness and mass parameters, respectively, and they should be selected as the nominal parameters that represent the nominal FE model. $\boldsymbol{\Sigma}_{\boldsymbol{\theta}}$ and $\boldsymbol{\Sigma}_{\boldsymbol{\rho}}$ are the prior covariance matrix of the stiffness and mass parameters, respectively. They represent the uncertainty in the nominal FE model before the model updating procedure. In this study, mass and stiffness parameters are considered to be linearly independent. This makes $\boldsymbol{\Sigma}_{\boldsymbol{\theta}}$ a diagonal matrix with diagonal elements that consist of the prior variance of each stiffness parameter. Similarly, $\boldsymbol{\Sigma}_{\boldsymbol{\rho}}$ is a diagonal matrix whose diagonal elements are the prior variance of each mass parameter.

4.2.2.4. Probability Model for the Discrepancy between Eigenvalues

This section and the rest of the following sections are newly introduced as part of this progress report. Differently from the previous study, eigenvalues of the FE model are employed instead of the system eigenvalues to remove the modelling error term from the objective function. Then, measured eigenvalues can be related to the FE model eigenvalues, $\lambda_n(\boldsymbol{\chi})$, by assuming a prediction error in-between as

$$\hat{\lambda}_n = \lambda_n(\boldsymbol{\chi}) + \varepsilon_{\hat{\lambda}_n}(\boldsymbol{\chi}) \tag{4.8}$$

where $\hat{\lambda}_n$ is the measured eigenvalue for the n^{th} mode and the error term $\varepsilon_{\hat{\lambda}_n}(\boldsymbol{\chi})$ is modelled as a Gaussian distribution with a zero-mean and the variance of $S_{\hat{\lambda}_n}$ as;

$$\varepsilon_{\hat{\lambda}_n} \sim N(0, S_{\hat{\lambda}_n}) \tag{4.9}$$

Prior probability distribution for the discrepancy between the FE model eigenvalues, $\lambda_n(\boldsymbol{\chi})$ and measured eigenvalues, $\hat{\lambda}_n$ of the n^{th} mode can be defined by assuming a Gaussian probability model. Since the MPVs and prior uncertainties of the measured eigenvalues are already known from the modal identification process, this prior PDF is written as a likelihood function as follows;

$$p(\hat{\lambda}_n, S_{\hat{\lambda}_n} \mid \boldsymbol{\chi}) = \frac{1}{\sqrt{2\pi S_{\hat{\lambda}_n}}} \exp\left(-\frac{\left[\hat{\lambda}_n - \lambda_n(\boldsymbol{\chi})\right]^2}{2 S_{\hat{\lambda}_n}} \right) \tag{4.10}$$

where $S_{\hat{\lambda}_n}$ denotes the prior variance for the measured eigenvalues of $\hat{\lambda}_n$ and it is obtained in the Bayesian modal identification process.

By assuming that the prediction error for each mode is independent, one can define the following prior PDF as;

$$p(\hat{\boldsymbol{\lambda}}, \boldsymbol{\Sigma}_{\hat{\boldsymbol{\lambda}}} | \boldsymbol{\chi}) = \prod_{n=1}^{N_m} p(\hat{\lambda}_n, S_{\hat{\lambda}_n} | \boldsymbol{\chi}) = \prod_{n=1}^{N_m} \frac{1}{\sqrt{2\pi S_{\hat{\lambda}_n}}} \exp\left(-\frac{\left[\hat{\lambda}_n - \lambda_n(\boldsymbol{\chi})\right]^2}{2 S_{\hat{\lambda}_n}} \right) \tag{4.11}$$

where $\hat{\boldsymbol{\lambda}} = [\hat{\lambda}_1 \;\; \hat{\lambda}_2 \;\; \hat{\lambda}_3 \; \ldots \; \hat{\lambda}_{N_m}]$ is the vector of measured eigenvalues and $\boldsymbol{\Sigma}_{\hat{\boldsymbol{\lambda}}}$ represents the prior covariance matrix whose diagonal elements consist of the set $\{S_{\hat{\lambda}_1}, S_{\hat{\lambda}_2}, S_{\hat{\lambda}_3}, \ldots, S_{\hat{\lambda}_{N_m}}\}$.

4.2.2.5. Probability Model for the Discrepancy between the Mode Shapes

In this study, it is assumed that a single setup of vibration data is available at hand for the model updating process. The data can be obtained by a complete measurement of a structure in a single setup, or a pre-identification data merging strategy can be employed to merge multiple setup data into a single setup data (Ceylan et al., 2020). In most real-life applications, measured DOFs of structures are, however, smaller than those of the FE model. Spatially incomplete measured mode shape vectors and mode shape components of the FE model should be matched. For this purpose, following relation is implemented

$$\bar{\boldsymbol{\phi}}_n(\boldsymbol{\chi}) = \mathbf{L}_0 \boldsymbol{\phi}_n(\boldsymbol{\chi}) \tag{4.12}$$

where $\mathbf{L}_0$ is the selection matrix consisting of 1's and 0's to pick the components of the mode shape of the FE model, $\boldsymbol{\phi}_n(\boldsymbol{\chi})$. Thus, $\bar{\boldsymbol{\phi}}_n(\boldsymbol{\chi})$ can be compared to the measured modal shapes.

Bayesian modal identification process uses a unit norm constraint for mode shape normalization. Therefore, MPV of the measured mode shape $\hat{\boldsymbol{\psi}}_n$ has a unit norm and $\mathbf{H}_{\hat{\psi}_n}$ is the Hessian of $\hat{\boldsymbol{\psi}}_n$. In the model updating procedure presented in this study, however, each measured mode shape is normalized as its coordinate (h_n^{th} coordinate) with the largest absolute value to be 1. This type of normalization is employed since it leads to a solution for the calculation of eigenvector derivatives. Let the measured mode

shape with the aforementioned normalization be defined as $\hat{\boldsymbol{\phi}}_n$, then $\hat{\boldsymbol{\psi}}_n$ can be substituted by the following relation

$$\hat{\boldsymbol{\psi}}_n = \frac{\hat{\boldsymbol{\phi}}_n}{\left\|\hat{\boldsymbol{\phi}}_n\right\|} \tag{4.13}$$

where || . || denotes 2-norm of a vector. Then, the partial modes shapes of the FE model, $\bar{\boldsymbol{\phi}}_n(\boldsymbol{\chi})$, which corresponds to the measured DOFs, are also normalized as its h_n^{th} coordinate to be 1.

Measured mode shape $\hat{\boldsymbol{\phi}}_n$ can be related to $\bar{\boldsymbol{\phi}}_n(\boldsymbol{\chi})$ for the n^{th} mode by including a prediction error as

$$\begin{aligned} \hat{\boldsymbol{\phi}}_n &= \bar{\boldsymbol{\phi}}_n(\boldsymbol{\chi}) + \boldsymbol{\varepsilon}_{\hat{\boldsymbol{\phi}}_n}(\boldsymbol{\chi}) \\ &= \mathbf{L}_0 \boldsymbol{\phi}_n(\boldsymbol{\chi}) + \boldsymbol{\varepsilon}_{\hat{\boldsymbol{\phi}}_n}(\boldsymbol{\chi}) \end{aligned} \tag{4.14}$$

where $\boldsymbol{\varepsilon}_{\hat{\boldsymbol{\phi}}_n}(\boldsymbol{\chi})$ is the prediction-error vector consisting of the error term for each mode shape component and it is modelled as Gaussian variables with zero-means and the covariance matrix of $\boldsymbol{\Sigma}_{\hat{\phi}_n}$ as;

$$\boldsymbol{\varepsilon}_{\hat{\boldsymbol{\phi}}_n} \sim N(0, \boldsymbol{\Sigma}_{\hat{\boldsymbol{\phi}}_n}) \tag{4.15}$$

Here, $\boldsymbol{\Sigma}_{\hat{\phi}_n}$ is the prior covariance matrix that is used to define the uncertainties in the prediction error vector $\boldsymbol{\varepsilon}_{\hat{\boldsymbol{\phi}}_n}(\boldsymbol{\chi})$.

Discrepancy between $\bar{\boldsymbol{\phi}}_n(\boldsymbol{\chi})$ and $\hat{\boldsymbol{\phi}}_n$ should be considered to construct the probability model. To this end, prior probability distribution for the discrepancy between $\bar{\boldsymbol{\phi}}_n(\boldsymbol{\chi})$ and measured mode shapes, $\hat{\boldsymbol{\phi}}_n$ of the n^{th} mode can be defined by assuming a Gaussian probability model. Since the MPVs and prior uncertainties of the measured mode shapes are already known from the modal identification process, this prior PDF is written as a likelihood function as follows;

$$p(\hat{\boldsymbol{\phi}}_n, \mathbf{H}_{\hat{\boldsymbol{\phi}}_n} \mid \boldsymbol{\chi}) = \exp\left(-\frac{1}{2}\left[\hat{\boldsymbol{\phi}}_n - \bar{\boldsymbol{\phi}}_n(\boldsymbol{\chi})\right]^T \mathbf{H}_{\hat{\boldsymbol{\phi}}_n} \left[\hat{\boldsymbol{\phi}}_n - \bar{\boldsymbol{\phi}}_n(\boldsymbol{\chi})\right] \right) \tag{4.16}$$

$\mathbf{H}_{\hat{\boldsymbol{\phi}}_n}$ is the Hessian matrix of $\hat{\boldsymbol{\phi}}_n$ and it is different from $\mathbf{H}_{\hat{\boldsymbol{\psi}}_n}$ which is the output of the Bayesian modal identification procedure. $\mathbf{H}_{\hat{\boldsymbol{\psi}}_n}$ represents the Hessian of the mode shape vector of $\hat{\boldsymbol{\psi}}_n$ which has a unit norm.

The PDF of the error term in equation (4.14) should not be affected by the normalization of the modal shape vector. Thus, the following equality should be satisfied

$$p(\hat{\boldsymbol{\psi}}_n, \mathbf{H}_{\hat{\boldsymbol{\psi}}_n} \mid \boldsymbol{\chi}) = p(\hat{\boldsymbol{\phi}}_n, \mathbf{H}_{\hat{\boldsymbol{\phi}}_n} \mid \boldsymbol{\chi}) \tag{4.17}$$

where

$$p(\hat{\boldsymbol{\psi}}_n, \mathbf{H}_{\hat{\boldsymbol{\psi}}_n} \mid \boldsymbol{\chi}) = \exp\left(-\frac{1}{2}\left[\hat{\boldsymbol{\psi}}_n - \bar{\bar{\boldsymbol{\phi}}}_n(\boldsymbol{\chi})\right]^T \mathbf{H}_{\hat{\boldsymbol{\psi}}_n} \left[\hat{\boldsymbol{\psi}}_n - \bar{\bar{\boldsymbol{\phi}}}_n(\boldsymbol{\chi})\right] \right) \tag{4.18}$$

and $\bar{\bar{\boldsymbol{\phi}}}_n(\boldsymbol{\chi})$ represents the measured counterpart of the mode shape of the FE model for the n^{th} mode, which has a unit norm.

By substituting equation (4.16) and (4.18) into equation (4.17), one can obtain the following expression;

$$\hat{\boldsymbol{\phi}}_n^T \mathbf{H}_{\hat{\boldsymbol{\phi}}_n} \hat{\boldsymbol{\phi}}_n = \hat{\boldsymbol{\psi}}_n^T \mathbf{H}_{\hat{\psi}_n} \hat{\boldsymbol{\psi}}_n \tag{4.19}$$

By substituting equation (4.13) into equation (4.19), one can obtain

$$\hat{\boldsymbol{\phi}}_n^T \mathbf{H}_{\hat{\boldsymbol{\phi}}_n} \hat{\boldsymbol{\phi}}_n = \frac{\hat{\boldsymbol{\phi}}_n^T}{\left\|\hat{\boldsymbol{\phi}}_n\right\|} \mathbf{H}_{\hat{\psi}_n} \frac{\hat{\boldsymbol{\phi}}_n}{\left\|\hat{\boldsymbol{\phi}}_n\right\|} = \hat{\boldsymbol{\phi}}_n^T \frac{\mathbf{H}_{\hat{\psi}_n}}{\left\|\hat{\boldsymbol{\phi}}_n\right\|^2} \hat{\boldsymbol{\phi}}_n \tag{4.20}$$

Equation (4.20) reveals the relation between $\mathbf{H}_{\hat{\boldsymbol{\psi}}_n}$ and $\mathbf{H}_{\hat{\boldsymbol{\phi}}_n}$ as;

$$\mathbf{H}_{\hat{\boldsymbol{\phi}}_n} = \frac{\mathbf{H}_{\hat{\psi}_n}}{\left\|\hat{\boldsymbol{\phi}}_n\right\|^2} \tag{4.21}$$

In equation (4.16), Hessian matrix is introduced instead of the covariance matrix. The reason is that it is not possible to obtain the exact $\boldsymbol{\Sigma}_{\hat{\psi}_n}$ since the Bayesian modal identification process does not output an invertible Hessian matrix, $\mathbf{H}_{\hat{\psi}_n}$, of the measured mode shapes. Pseudo-inverse of $\mathbf{H}_{\hat{\psi}_n}$ can be obtained instead (Hızal, 2019).

By assuming that the prediction error vectors are independent for different modes of the selected structural model, one can define the following prior PDF;

$$p(\hat{\boldsymbol{\phi}}, \mathbf{H}_{\hat{\boldsymbol{\phi}}} \,|\, \boldsymbol{\chi}) = \prod_{n=1}^{N_m} p(\hat{\boldsymbol{\phi}}_n, \mathbf{H}_{\hat{\boldsymbol{\phi}}_n} \,|\, \boldsymbol{\chi}) \tag{4.22}$$

where $\hat{\boldsymbol{\phi}} = [\hat{\boldsymbol{\phi}}_1 \;\; \hat{\boldsymbol{\phi}}_2 \;\; \hat{\boldsymbol{\phi}}_3 \;\; \ldots \;\; \hat{\boldsymbol{\phi}}_{Nm}]$ is the matrix of measured mode shapes and $\mathbf{H}_{\hat{\boldsymbol{\Phi}}}$ represents the block diagonal Hessian matrix whose diagonal elements consist of the set $\{\mathbf{H}_{\hat{\boldsymbol{\phi}}_1}, \mathbf{H}_{\hat{\boldsymbol{\phi}}_2}, \mathbf{H}_{\hat{\boldsymbol{\phi}}_3}, \ldots, \mathbf{H}_{\hat{\boldsymbol{\phi}}_{Nm}}\}$.

4.2.2.6. Negative Log-likelihood Function of the Posterior PDF

Substituting equations (4.6), (4.7), (4.11) and (4.22) into equation (4.5), and after some arrangements, a negative log-likelihood function for the posterior PDF is written as follows

$$\begin{aligned} L(\boldsymbol{\chi}) = {} & \frac{1}{2}\sum_{n=1}^{N_m} \frac{\left[\hat{\lambda}_n - \lambda_n(\boldsymbol{\chi})\right]^2}{S_{\hat{\lambda}_n}} \\ & + \frac{1}{2}\sum_{n=1}^{N_m} \left(\left[\hat{\boldsymbol{\phi}}_n - \mathbf{L}_0 \boldsymbol{\phi}_n(\boldsymbol{\chi})\right]^T \mathbf{H}_{\hat{\boldsymbol{\phi}}_n} \left[\hat{\boldsymbol{\phi}}_n - \mathbf{L}_0 \boldsymbol{\phi}_n(\boldsymbol{\chi})\right] \right) \\ & + \frac{1}{2}\left(\boldsymbol{\theta} - \hat{\boldsymbol{\theta}}_0\right)^T \boldsymbol{\Sigma}_{\boldsymbol{\theta}}^{-1} \left(\boldsymbol{\theta} - \hat{\boldsymbol{\theta}}_0\right) + \frac{1}{2}\left(\boldsymbol{\rho} - \hat{\boldsymbol{\rho}}_0\right)^T \boldsymbol{\Sigma}_{\boldsymbol{\rho}}^{-1} \left(\boldsymbol{\rho} - \hat{\boldsymbol{\rho}}_0\right) \end{aligned} \tag{4.23}$$

It should be noted that constant terms are neglected while writing equation (4.23) since they have no effect on the optimization of the parameters. The objective function in equation (4.23) needs to be minimized with respect to each parameter to obtain most probable value of $\boldsymbol{\chi}$ which consists of $\boldsymbol{\theta}$ and $\boldsymbol{\rho}$.

4.2.3. Optimization Problem

The objective function is a closed-form non-linear function of $\boldsymbol{\chi}$ and therefore minimization process requires a numerical optimization algorithm. To solve this optimization problem, "SMU: MATLAB Package for Structural Model Updating" which is shared by Wang et al. (2019) is used for the existing problem. The existing SMU package is modified by following the formulations derived by Otsuki et al. (2021). Wang et al. (2019) have used the *lsqnonlin* and *fmincon* solvers in MATLAB optimization toolbox. These solvers numerically solve the optimization problem in an iterative way and in each iteration, Jacobian of the objective function is needed. The solvers have built-in numerical gradient calculators. However, Otsuki et al. (2021) state that providing an analytical gradient of the objective function results in more accurate results while decreasing the computational time. Therefore, in this study, the analytical Jacobian matrix of the objective function is derived in a similar way proposed by Otsuki et al. (2021). They have derived sensitivity equations for two different objective functions which are constructed by a weighted least squares sense. Both use the discrepancies between eigenvalues and mode shape vectors. The difference is that one uses the modal assurance criterion (MAC) values of the mode shapes and the other one uses the direct difference between the mode shape vectors. In the present study, direct difference between the mode shape vectors is formulized in the objective function and therefore their derivations have been followed for the direct difference method. To this end, the objective function is rewritten in the following form

$$\begin{aligned} &\arg\min_{\boldsymbol{\chi}} L(\boldsymbol{\chi}) = \mathbf{r}(\boldsymbol{\chi})^T \mathbf{r}(\boldsymbol{\chi}) \\ &\textit{subjected to}\, \mathbf{L}_{\boldsymbol{\chi}} \le \boldsymbol{\chi} \le \mathbf{U}_{\boldsymbol{\chi}} \end{aligned} \tag{4.24}$$

where $\mathbf{r}(\boldsymbol{\chi})$ is a residual vector, and $\mathbf{L}_{\chi}$ and $\mathbf{U}_{\chi}$ are the vectors that include lower and upper bounds of each parameter, respectively.

Each term in equation (4.23) has a scalar value. Thus, this equation can be rewritten as follows

$$L(\boldsymbol{\chi}) = \frac{1}{2}\sum_{n=1}^{N_m}\frac{\left[\hat{\lambda}_n - \lambda_n(\boldsymbol{\chi})\right]^2}{S_{\hat{\lambda}_n}} + \sum_{n=1}^{N_m}\alpha_n(\boldsymbol{\chi}) + \beta(\boldsymbol{\theta}) + \gamma(\boldsymbol{\rho}) \tag{4.25}$$

where

$$\alpha_n(\boldsymbol{\chi}) = \frac{1}{2}\left[\hat{\boldsymbol{\phi}}_n - \mathbf{L}_0\boldsymbol{\phi}_n(\boldsymbol{\chi})\right]^T \mathbf{H}_{\hat{\boldsymbol{\phi}}_n}\left[\hat{\boldsymbol{\phi}}_n - \mathbf{L}_0\boldsymbol{\phi}_n(\boldsymbol{\chi})\right] \tag{4.26}$$

$$\beta(\boldsymbol{\theta}) = \frac{1}{2}\left(\boldsymbol{\theta} - \hat{\boldsymbol{\theta}}_0\right)^T \boldsymbol{\Sigma}_{\boldsymbol{\theta}}^{-1}\left(\boldsymbol{\theta} - \hat{\boldsymbol{\theta}}_0\right) \tag{4.27}$$

$$\gamma(\boldsymbol{\rho}) = \frac{1}{2}\left(\boldsymbol{\rho} - \hat{\boldsymbol{\rho}}_0\right)^T \boldsymbol{\Sigma}_{\boldsymbol{\rho}}^{-1}\left(\boldsymbol{\rho} - \hat{\boldsymbol{\rho}}_0\right) \tag{4.28}$$

where $\alpha_n(\boldsymbol{\chi})$, $\beta(\boldsymbol{\theta})$ and $\gamma(\boldsymbol{\rho})$ are scalar quantities.

As a result, the residual vector $\mathbf{r}(\boldsymbol{\chi})$ can be defined as

$$\mathbf{r}(\boldsymbol{\chi}) = \begin{bmatrix} \mathbf{r}_1(\boldsymbol{\chi}) \\ \mathbf{r}_2(\boldsymbol{\chi}) \\ \vdots \\ \mathbf{r}_{Nm}(\boldsymbol{\chi}) \\ r_{\beta}(\boldsymbol{\theta}) \\ r_{\gamma}(\boldsymbol{\rho}) \end{bmatrix} \tag{4.29}$$

where

$$\mathbf{r}_n(\boldsymbol{\chi}) = \begin{bmatrix} \frac{1}{\sqrt{2}} \cdot \frac{\hat{\lambda}_n - \lambda_n(\boldsymbol{\chi})}{\sigma_{\hat{\lambda}_n}} \\ \alpha_n(\boldsymbol{\chi})^{1/2} \end{bmatrix}_{2\times 1} \quad n = 1, 2, ..., N_m \tag{4.30}$$

$$r_{\beta}(\boldsymbol{\theta}) = \beta(\boldsymbol{\theta})^{1/2} \quad and \quad r_{\gamma}(\boldsymbol{\rho}) = \gamma(\boldsymbol{\rho})^{1/2} \tag{4.31}$$

Thus, the residual vector $\mathbf{r}(\boldsymbol{\chi})$ is a column vector with a size of $(2N_m+2) \times 1$. Otsuki et al. (2021) do not consider the mode shape term $\alpha_n(\boldsymbol{\chi})$ as a scalar term in their formulations, rather they use this term as a complete mode shape vector. By using their approach, $\mathbf{r}(\boldsymbol{\chi})$ should have a size of $(N_{md}N_m+N_\theta+N_\rho) \times 1$ which is quite large with respect to the proposed one in this study. Therefore, considering the mode shape term as a scalar one reduces the computational time significantly, especially for large systems.

4.2.3.1. Derivation of Jacobian of the Objective Function $L(\boldsymbol{\chi})$

Jacobian of the objective function $L(\boldsymbol{\chi})$ in equation (4.25) with respect to updating parameters $\boldsymbol{\chi}$ is performed by following the formulations derived by Otsuki et al. (2021). For the sake of clarity, $\mathbf{r}(\boldsymbol{\chi}) = \mathbf{r}$ is used in the following equations. Jacobian of $L(\boldsymbol{\chi})$ with respect to $\boldsymbol{\chi}$ can be defined by using the chain rule of derivative as;

$$\frac{\partial L(\boldsymbol{\chi})}{\partial \boldsymbol{\chi}} = \frac{\partial L(\boldsymbol{\chi})}{\partial \mathbf{r}} \cdot \frac{\partial \mathbf{r}}{\partial \boldsymbol{\chi}} \tag{4.32}$$

where $\partial L(\boldsymbol{\chi})/\partial \mathbf{r}$ can be obtained as

$$\frac{\partial L(\boldsymbol{\chi})}{\partial \mathbf{r}} = 2\mathbf{r}^T \tag{4.33}$$

and $\partial \mathbf{r}/\partial \boldsymbol{\chi}$ can be defined as

$$\frac{\partial \mathbf{r}}{\partial \boldsymbol{\chi}} = \begin{bmatrix} \frac{\partial \mathbf{r}_1}{\partial \boldsymbol{\chi}} \\ \frac{\partial \mathbf{r}_2}{\partial \boldsymbol{\chi}} \\ \vdots \\ \frac{\partial \mathbf{r}_{Nm}}{\partial \boldsymbol{\chi}} \\ \frac{\partial r_\beta}{\partial \boldsymbol{\chi}} \\ \frac{\partial r_\gamma}{\partial \boldsymbol{\chi}} \end{bmatrix} \tag{4.34}$$

Here, the Jacobian of the residual term for the n^{th} mode can be defined as

$$\frac{\partial \mathbf{r}_n}{\partial \boldsymbol{\chi}} = \left[\frac{\partial \mathbf{r}_n}{\partial \theta_1} \quad \cdots \quad \frac{\partial \mathbf{r}_n}{\partial \theta_{N\theta}} \quad \frac{\partial \mathbf{r}_n}{\partial \rho_1} \quad \cdots \quad \frac{\partial \mathbf{r}_n}{\partial \rho_{N\rho}} \right] \tag{4.35}$$

where the term, $\partial \mathbf{r}_n / \partial \theta_i$, can be obtained by the first order differentiation of $\mathbf{r}_n$ with respect to θ_i as;

$$\frac{\partial \mathbf{r}_n}{\partial \theta_i} = \begin{bmatrix} -\frac{1}{\sqrt{2}} \cdot \frac{\dfrac{\partial \lambda_n(\boldsymbol{\chi})}{\partial \theta_i}}{\sigma_{\hat{\lambda}_n}} \\ \frac{1}{2} \alpha_n(\boldsymbol{\chi})^{-1/2} \dfrac{\partial \alpha_n(\boldsymbol{\chi})}{\partial \theta_i} \end{bmatrix}_{2\times 1} \tag{4.36}$$

Here, $\partial \alpha_n(\boldsymbol{\theta}) / \partial \theta_i$ is derived as

$$\frac{\partial \alpha_n(\boldsymbol{\chi})}{\partial \theta_i} = \left[\mathbf{L}_0 \boldsymbol{\phi}_n(\boldsymbol{\chi}) - \hat{\boldsymbol{\phi}}_n \right]^T \mathbf{H}_{\hat{\boldsymbol{\phi}}_n} \mathbf{L}_0 \frac{\partial \boldsymbol{\phi}_n(\boldsymbol{\chi})}{\partial \theta_i} \tag{4.37}$$

The term, $\partial \mathbf{r}_n / \partial \rho_j$, in equation (4.35) can be obtained by the first order differentiation of $\mathbf{r}_n$ with respect to ρ_j as;

$$\frac{\partial \mathbf{r}_n}{\partial \rho_j} = \begin{bmatrix} -\frac{1}{\sqrt{2}} \cdot \frac{\dfrac{\partial \lambda_n(\boldsymbol{\chi})}{\partial \rho_j}}{\sigma_{\hat{\lambda}_n}} \\ \frac{1}{2} \alpha_n(\boldsymbol{\chi})^{-1/2} \dfrac{\partial \alpha_n(\boldsymbol{\chi})}{\partial \rho_j} \end{bmatrix}_{2\times 1} \tag{4.38}$$

where

$$\frac{\partial \alpha_n(\boldsymbol{\chi})}{\partial \rho_j} = \left[\mathbf{L}_0 \boldsymbol{\phi}_n(\boldsymbol{\chi}) - \hat{\boldsymbol{\phi}}_n \right]^T \mathbf{H}_{\hat{\boldsymbol{\phi}}_n} \mathbf{L}_0 \frac{\partial \boldsymbol{\phi}_n(\boldsymbol{\chi})}{\partial \rho_j} \tag{4.39}$$

The Jacobian of the residual term, r_β is calculated as

$$\frac{\partial r_\beta}{\partial \boldsymbol{\chi}} = \left[\frac{1}{2} \beta(\boldsymbol{\theta})^{-1/2} \frac{\partial \beta(\boldsymbol{\theta})}{\partial \boldsymbol{\theta}} \quad \mathbf{0}_{1\times N\rho} \right] \tag{4.40}$$

where

$$\frac{\partial \beta(\boldsymbol{\theta})}{\partial \boldsymbol{\theta}} = \left(\boldsymbol{\theta} - \hat{\boldsymbol{\theta}}_0 \right)^T \boldsymbol{\Sigma}_{\boldsymbol{\theta}}^{-1} \tag{4.41}$$

which is a row vector with a size of $1 \times N_\theta$. The Jacobian of the residual term, r_γ is calculated as

$$\frac{\partial r_\gamma}{\partial \boldsymbol{\chi}} = \left[\mathbf{0}_{1\times N\theta} \quad \frac{1}{2} \gamma(\boldsymbol{\rho})^{-1/2} \frac{\partial \gamma(\boldsymbol{\rho})}{\partial \boldsymbol{\rho}} \right] \tag{4.42}$$

where

$$\frac{\partial \gamma(\boldsymbol{\rho})}{\partial \boldsymbol{\rho}} = \left(\boldsymbol{\rho} - \hat{\boldsymbol{\rho}}_0 \right)^T \boldsymbol{\Sigma}_{\boldsymbol{\rho}}^{-1} \tag{4.43}$$

which is a row vector with a size of $1 \times N_\rho$.

$\partial \mathbf{r}_n / \partial \boldsymbol{\chi}$ is a matrix with a size of $2 \times (N_\theta + N_\rho)$ and $\partial \mathbf{r} / \partial \boldsymbol{\theta}$ is a matrix with a size of $(2N_m+2) \times (N_\theta + N_\rho)$. By using the original formulations derived by Otsuki et al. (2021), the Jacobian matrix should have a larger size of $(N_{md}N_m+N_\theta+N_\rho) \times (N_\theta + N_\rho)$. Considering the terms of the objective function $L(\boldsymbol{\theta})$ as scalars significantly reduces the dimension of the Jacobian, and thus the computational time for the optimization process.

To evaluate the Jacobian of the objective function $L(\boldsymbol{\theta})$, it is required to calculate the Jacobian of eigenvalues, $\partial \lambda_n(\boldsymbol{\chi}) / \partial \theta_i$ and $\partial \lambda_n(\boldsymbol{\chi}) / \partial \rho_j$ in equations (4.36) and (4.38), and the Jacobian of eigenvectors, $\partial \boldsymbol{\phi}_n(\boldsymbol{\chi}) / \partial \theta_i$ and $\partial \boldsymbol{\phi}_n(\boldsymbol{\chi}) / \partial \rho_j$ in equations (4.37) and (4.39), respectively.

4.2.3.2. Jacobian of Eigenvalues and Eigenvectors

Jacobian of the eigenvalues and eigenvectors of the n^{th} mode are formulated by following the derivations done by Otsuki et al. (2021).

Eigenvalue equation for the corresponding mode is defined as

$$\left[\mathbf{K}(\boldsymbol{\theta})-\lambda_n(\boldsymbol{\chi})\mathbf{M}(\boldsymbol{\rho})\right]\boldsymbol{\phi}_n(\boldsymbol{\chi})=\mathbf{0} \tag{4.44}$$

- **Differentiation with respect to the stiffness parameters**

Differentiating equation (4.44) with respect to θ_i gives the following equation;

$$\left[\mathbf{K}_i-\frac{\partial\lambda_n(\boldsymbol{\chi})}{\partial\theta_i}\mathbf{M}(\boldsymbol{\rho})\right]\boldsymbol{\phi}_n(\boldsymbol{\chi})+\left[\mathbf{K}(\boldsymbol{\theta})-\lambda_n(\boldsymbol{\chi})\mathbf{M}(\boldsymbol{\rho})\right]\frac{\partial\boldsymbol{\phi}_n(\boldsymbol{\chi})}{\partial\theta_i}=\mathbf{0} \tag{4.45}$$

Rearranging equation (4.45), one can obtain the following expression;

$$\left[\mathbf{K}(\boldsymbol{\theta})-\lambda_n(\boldsymbol{\chi})\mathbf{M}(\boldsymbol{\rho})\right]\frac{\partial\boldsymbol{\phi}_n(\boldsymbol{\chi})}{\partial\theta_i}=\frac{\partial\lambda_n(\boldsymbol{\chi})}{\partial\theta_i}\mathbf{M}(\boldsymbol{\rho})\boldsymbol{\phi}_n(\boldsymbol{\chi})-\mathbf{K}_i\boldsymbol{\phi}_n(\boldsymbol{\chi}) \tag{4.46}$$

Equation (4.46) is pre-multiplied by $\boldsymbol{\phi}_n^T(\boldsymbol{\chi})$

$$\begin{aligned}&\boldsymbol{\phi}_n^T(\boldsymbol{\chi})\left[\mathbf{K}(\boldsymbol{\theta})-\lambda_n(\boldsymbol{\chi})\mathbf{M}(\boldsymbol{\rho})\right]\frac{\partial\boldsymbol{\phi}_n(\boldsymbol{\chi})}{\partial\theta_i}\\&\quad=\frac{\partial\lambda_n(\boldsymbol{\chi})}{\partial\theta_i}\boldsymbol{\phi}_n^T(\boldsymbol{\chi})\mathbf{M}(\boldsymbol{\rho})\boldsymbol{\phi}_n(\boldsymbol{\chi})-\boldsymbol{\phi}_n^T(\boldsymbol{\chi})\mathbf{K}_i\boldsymbol{\phi}_n(\boldsymbol{\chi})\end{aligned} \tag{4.47}$$

Since $\boldsymbol{\phi}_n^T(\boldsymbol{\chi})$ is the left eigenvector of the matrix $\mathbf{K}(\boldsymbol{\theta})-\lambda_n(\boldsymbol{\chi})\mathbf{M}(\boldsymbol{\rho})$, left-hand side of equation (4.47) is zero. Then, $\partial\lambda_n(\boldsymbol{\chi})/\partial\theta_i$ can be obtained as

$$\frac{\partial \lambda_n(\mathbf{s})}{\partial \theta_i} = \frac{\boldsymbol{\phi}_n^T(\mathbf{s})\mathbf{K}_i\boldsymbol{\phi}_n(\mathbf{s})}{\boldsymbol{\phi}_n^T(\mathbf{s})\mathbf{M}(\boldsymbol{\rho})\boldsymbol{\phi}_n(\mathbf{s})} \tag{4.48}$$

Jacobian of mode shape vector of the n^{th} mode $\partial\boldsymbol{\phi}_n(\boldsymbol{\chi})/\partial\theta_i$ cannot be obtained by using equation (4.46) since the matrix $\mathbf{K}(\boldsymbol{\theta})-\lambda_n(\boldsymbol{\chi})\mathbf{M}(\boldsymbol{\rho})$ on the left-hand side is rank deficient. As a remedy, the fact that the measured mode shape is normalized as its coordinate (h_n^{th} coordinate) with the largest absolute value to be 1 has been used. The partial modes shapes of the FE model $\bar{\boldsymbol{\phi}}_n(\boldsymbol{\chi})$, which corresponds to the measured DOFs, are also normalized as its h_n^{th} coordinate to be 1. Thus, the value of the h_n^{th} coordinate for both mode shape vectors never changes over iterations and sensitivity of the h_n^{th} coordinate is zero, and it is defined as

$$\frac{\partial \bar{\boldsymbol{\phi}}_{h_n,n}(\boldsymbol{\chi})}{\partial \theta_i} = 0 \quad \text{and} \quad \frac{\partial \boldsymbol{\phi}_{a_n,n}(\boldsymbol{\chi})}{\partial \theta_i} = 0 \tag{4.49}$$

Note that h_n^{th} coordinate of $\bar{\boldsymbol{\phi}}_n(\boldsymbol{\chi})$ corresponds to a_n^{th} coordinate of the mode shape of the FE model, $\boldsymbol{\phi}_n(\boldsymbol{\theta})$ with complete DOFs of the model. Since the a_n^{th} coordinate of $\partial\boldsymbol{\phi}_n(\boldsymbol{\chi})/\partial\theta_i$ is always 0, it can be removed from equation (4.46) to solve the rank deficiency problem. For this purpose, a transformation for the modal shape vector is implemented as follows

$$\boldsymbol{\phi}_n(\boldsymbol{\chi}) = \mathbf{A}_n\,\bar{\boldsymbol{\phi}}_n(\boldsymbol{\chi}) + \tilde{\mathbf{1}} \tag{4.50}$$

where

$$\mathbf{A}_n = \begin{bmatrix} \mathbf{I}_{a_n-1} & \mathbf{0}_{(a_n-1)\times(N_d-a_n)} \\ \mathbf{0}_{1\times(a_n-1)} & \mathbf{0}_{1\times(N_d-a_n)} \\ \mathbf{0}_{(N_d-a_n)\times(a_n-1)} & \mathbf{I}_{N_d-a_n} \end{bmatrix}_{N_d\times(N_d-1)} \tag{4.51}$$

and $\boldsymbol{\phi}_n^-(\boldsymbol{\chi})$ denotes the reduced mode shape vector of the FE model for the n^{th} mode without the a_n^{th} coordinate, and $\widetilde{\mathbf{1}}$ is a zero-column vector with its a_n^{th} coordinate equal to 1.

Since the rank deficiency problem exists on the left-hand side of equation (4.46), the transformation in equation (4.50) is substituted in here. It should be noted that $\partial\widetilde{\mathbf{1}} \,/\, \partial\theta_i$ is a zero vector, and the following equation is obtained

$$\left[\mathbf{K}(\boldsymbol{\theta}) - \lambda_n(\boldsymbol{\chi})\mathbf{M}(\boldsymbol{\rho})\right]\mathbf{A}_n \frac{\partial \boldsymbol{\phi}_n^-(\boldsymbol{\chi})}{\partial \theta_i} = \frac{\partial \lambda_n(\boldsymbol{\chi})}{\partial \theta_i}\mathbf{M}(\boldsymbol{\rho})\boldsymbol{\phi}_n(\boldsymbol{\chi}) - \mathbf{K}_i\boldsymbol{\phi}_n(\boldsymbol{\chi}) \tag{4.52}$$

The matrix $\left[\mathbf{K}(\boldsymbol{\theta}) - \lambda_n(\boldsymbol{\chi})\mathbf{M}(\boldsymbol{\rho})\right]\mathbf{A}_n$ on the left-hand side of equation (4.52) has more rows than columns and therefore a pseudo-inverse operation is needed to solve the equation for $\partial\boldsymbol{\phi}_n^-(\boldsymbol{\chi})/\partial\theta_i$. A simpler solution can be obtained, however, by pre-multiplying equation (4.52) with $\mathbf{A}_n^T$ as

$$\begin{aligned}\mathbf{A}_n^T\left[\mathbf{K}(\boldsymbol{\theta}) - \lambda_n(\boldsymbol{\chi})\mathbf{M}(\boldsymbol{\rho})\right]\mathbf{A}_n \frac{\partial \boldsymbol{\phi}_n^-(\boldsymbol{\chi})}{\partial \theta_i} \\ = \mathbf{A}_n^T\left(\frac{\partial \lambda_n(\boldsymbol{\chi})}{\partial \theta_i}\mathbf{M}(\boldsymbol{\rho})\boldsymbol{\phi}_n(\boldsymbol{\chi}) - \mathbf{K}_i\boldsymbol{\phi}_n(\boldsymbol{\chi})\right)\end{aligned} \tag{4.53}$$

Then, $\partial\boldsymbol{\phi}_n^-(\boldsymbol{\chi})/\partial\theta_i$ can be obtained as

$$\frac{\partial \boldsymbol{\phi}_n^-(\boldsymbol{\chi})}{\partial \theta_i} = \left(\mathbf{A}_n^T\left[\mathbf{K}(\boldsymbol{\chi}) - \lambda_n(\boldsymbol{\chi})\mathbf{M}(\boldsymbol{\rho})\right]\mathbf{A}_n\right)^{-1}\mathbf{A}_n^T\left(\frac{\partial \lambda_n(\boldsymbol{\chi})}{\partial \theta_i}\mathbf{M}(\boldsymbol{\rho})\boldsymbol{\phi}_n(\boldsymbol{\chi}) - \mathbf{K}_i\boldsymbol{\phi}_n(\boldsymbol{\chi})\right) \tag{4.54}$$

The resulting Jacobian of the mode shape vector of the n^{th} mode $\partial\boldsymbol{\phi}_n(\boldsymbol{\chi})/\partial\theta_i$ can be obtained as

$$\frac{\partial \boldsymbol{\phi}_n(\boldsymbol{\chi})}{\partial \theta_i} = \mathbf{A}_n \frac{\partial \boldsymbol{\phi}_n^-(\boldsymbol{\chi})}{\partial \theta_i} \tag{4.55}$$

- **Differentiation with respect to the mass parameters**

By using similar steps, Jacobian of the eigenvalues and eigenvectors have been obtained with respect to the mass parameters.

Differentiating equation (4.44) with respect to ρ_j gives the following equation;

$$\left[-\lambda_n \mathbf{M}_j - \frac{\partial \lambda_n(\boldsymbol{\chi})}{\partial \rho_i}\mathbf{M}(\boldsymbol{\rho})\right]\boldsymbol{\phi}_n(\boldsymbol{\chi}) + \left[\mathbf{K}(\boldsymbol{\theta}) - \lambda_n(\boldsymbol{\theta})\mathbf{M}(\boldsymbol{\rho})\right]\frac{\partial \boldsymbol{\phi}_n(\boldsymbol{\chi})}{\partial \rho_j} = \mathbf{0} \tag{4.56}$$

Rearranging equation (4.56), one can obtain the following expression;

$$\left[\mathbf{K}(\boldsymbol{\theta}) - \lambda_n(\boldsymbol{\chi})\mathbf{M}(\boldsymbol{\rho})\right]\frac{\partial \boldsymbol{\phi}_n(\boldsymbol{\chi})}{\partial \rho_j} = \left[\lambda_n \mathbf{M}_j + \frac{\partial \lambda_n(\boldsymbol{\chi})}{\partial \rho_j}\mathbf{M}(\boldsymbol{\rho})\right]\boldsymbol{\phi}_n(\boldsymbol{\chi}) \tag{4.57}$$

Equation (4.57) is pre-multiplied by $\boldsymbol{\phi}_n^T(\boldsymbol{\chi})$

$$\begin{aligned}\boldsymbol{\phi}_n^T(\boldsymbol{\chi})&\left[\mathbf{K}(\boldsymbol{\theta}) - \lambda_n(\boldsymbol{\chi})\mathbf{M}(\boldsymbol{\rho})\right]\frac{\partial \boldsymbol{\phi}_n(\boldsymbol{\chi})}{\partial \rho_j} \\ &= \frac{\partial \lambda_n(\boldsymbol{\chi})}{\partial \rho_j}\boldsymbol{\phi}_n^T(\boldsymbol{\chi})\mathbf{M}(\boldsymbol{\rho})\boldsymbol{\phi}_n(\boldsymbol{\chi}) - \boldsymbol{\phi}_n^T(\boldsymbol{\chi})\mathbf{K}_i\boldsymbol{\phi}_n(\boldsymbol{\chi})\end{aligned} \tag{4.58}$$

Since $\boldsymbol{\phi}_n^T(\boldsymbol{\chi})$ is the left eigenvector of the matrix $\mathbf{K}(\boldsymbol{\theta}) - \lambda_n(\boldsymbol{\chi})\mathbf{M}(\boldsymbol{\rho})$, left-hand side of equation (4.58) is zero. Then, $\partial \lambda_n(\boldsymbol{\chi})/\partial \rho_j$ can be obtained as

$$\frac{\partial \lambda_n(\boldsymbol{\chi})}{\partial \rho_j} = \frac{-\lambda_n(\boldsymbol{\chi})\boldsymbol{\phi}_n^T(\boldsymbol{\chi})\mathbf{M}_j\boldsymbol{\phi}_n(\boldsymbol{\chi})}{\boldsymbol{\phi}_n^T(\boldsymbol{\chi})\mathbf{M}(\boldsymbol{\rho})\boldsymbol{\phi}_n(\boldsymbol{\chi})} \tag{4.59}$$

Jacobian of mode shape vector of the n^{th} mode $\partial \boldsymbol{\phi}_n(\boldsymbol{\chi})/\partial \rho_j$ cannot be obtained by using equation (4.57) since the matrix $\mathbf{K}(\boldsymbol{\theta}) - \lambda_n(\boldsymbol{\chi})\mathbf{M}(\boldsymbol{\rho})$ on the left-hand side is rank

deficient. As discussed under the previous title for the differentiation with respect to the stiffness parameters, the measured and FE model mode shapes are normalized as their coordinate (h_n^{th} coordinate) with the largest absolute value to be 1. Thus, the value of the h_n^{th} coordinate for both mode shape vectors never changes over iterations and sensitivity of the h_n^{th} coordinate is zero, and it is defined as

$$\frac{\partial \bar{\boldsymbol{\phi}}_{h_n,n}(\boldsymbol{\chi})}{\partial \rho_j} = 0 \quad \text{and} \quad \frac{\partial \boldsymbol{\phi}_{a_n,n}(\boldsymbol{\chi})}{\partial \rho_j} = 0 \tag{4.60}$$

h_n^{th} coordinate of $\bar{\boldsymbol{\phi}}_n(\boldsymbol{\chi})$ corresponds to a_n^{th} coordinate of the mode shape of the FE model, $\boldsymbol{\phi}_n(\boldsymbol{\theta})$ with complete DOFs of the model. Since the a_n^{th} coordinate of $\partial \boldsymbol{\phi}_n(\boldsymbol{\chi})/\partial \rho_j$ is always 0, it can be removed from equation (4.57) to solve the rank deficiency problem.

The same transformation for the modal shape vector is implemented as introduced in equation (4.50). To this end, equation (4.50) is substituted in equation (4.57) and the following equation is obtained

$$\left[\mathbf{K}(\boldsymbol{\theta}) - \lambda_n(\boldsymbol{\chi})\mathbf{M}(\boldsymbol{\rho})\right]\mathbf{A}_n \frac{\partial \boldsymbol{\phi}_n^-(\boldsymbol{\chi})}{\partial \rho_j} = \frac{\partial \lambda_n(\boldsymbol{\chi})}{\partial \rho_j}\mathbf{M}(\boldsymbol{\rho})\boldsymbol{\phi}_n(\boldsymbol{\chi}) + \lambda_n(\boldsymbol{\chi})\mathbf{M}_j\boldsymbol{\phi}_n(\boldsymbol{\chi}) \tag{4.61}$$

The matrix $\left[\mathbf{K}(\boldsymbol{\theta}) - \lambda_n(\boldsymbol{\chi})\mathbf{M}(\boldsymbol{\rho})\right]\mathbf{A}_n$ on the left-hand side of equation (4.61) has more rows than columns and therefore a pseudo-inverse operation is needed to solve the equation for $\partial \boldsymbol{\phi}_n^-(\boldsymbol{\chi})/\partial \rho_j$. A simpler solution can be obtained, however, by pre-multiplying equation (4.61) with $\mathbf{A}_n^T$ as

$$\begin{aligned}\mathbf{A}_n^T\left[\mathbf{K}(\boldsymbol{\theta}) - \lambda_n(\boldsymbol{\chi})\mathbf{M}(\boldsymbol{\rho})\right]\mathbf{A}_n \frac{\partial \boldsymbol{\phi}_n^-(\boldsymbol{\chi})}{\partial \rho_j} \\ = \mathbf{A}_n^T\left(\frac{\partial \lambda_n(\boldsymbol{\chi})}{\partial \rho_j}\mathbf{M}(\boldsymbol{\rho})\boldsymbol{\phi}_n(\boldsymbol{\chi}) - \mathbf{K}_i\boldsymbol{\phi}_n(\boldsymbol{\chi})\right)\end{aligned} \tag{4.62}$$

Then, $\partial \boldsymbol{\phi}_n^-(\boldsymbol{\chi})/\partial \rho_j$ can be obtained as

$$\frac{\partial \boldsymbol{\phi}_n^-(\boldsymbol{\chi})}{\partial \rho_j} = \left(\mathbf{A}_n^T \left[\mathbf{K}(\boldsymbol{\chi}) - \lambda_n(\boldsymbol{\chi}) \mathbf{M}(\boldsymbol{\rho}) \right] \mathbf{A}_n \right)^{-1} \mathbf{A}_n^T \left(\frac{\partial \lambda_n(\boldsymbol{\chi})}{\partial \rho_j} \mathbf{M}(\boldsymbol{\rho}) \boldsymbol{\phi}_n(\boldsymbol{\chi}) - \mathbf{K}_i \boldsymbol{\phi}_n(\boldsymbol{\chi}) \right) \quad (4.63)$$

The resulting Jacobian of the mode shape vector of the n^{th} mode $\partial \boldsymbol{\phi}_n(\boldsymbol{\chi})/\partial \rho_j$ can be obtained as

$$\frac{\partial \boldsymbol{\phi}_n(\boldsymbol{\chi})}{\partial \rho_j} = \mathbf{A}_n \frac{\partial \boldsymbol{\phi}_n^-(\boldsymbol{\chi})}{\partial \rho_j} \quad (4.64)$$

4.2.4. Posterior Uncertainty for the Updated Parameters

Let $\boldsymbol{\Theta}$ be a normally distributed (Gaussian) random vector with mean value of $\hat{\boldsymbol{\Theta}}_0$ and a covariance matrix of $\boldsymbol{\Sigma}_{\boldsymbol{\Theta}}$. Then, PDF of $\boldsymbol{\Theta}$ is written as

$$p(\boldsymbol{\Theta}) = \frac{1}{\sqrt{(2\pi)^{N_\Theta} \left| \boldsymbol{\Sigma}_{\boldsymbol{\Theta}} \right|}} \exp\left[-\frac{1}{2} \left(\boldsymbol{\Theta} - \hat{\boldsymbol{\Theta}}_0 \right)^T \boldsymbol{\Sigma}_{\boldsymbol{\Theta}}^{-1} \left(\boldsymbol{\Theta} - \hat{\boldsymbol{\Theta}}_0 \right) \right] \quad (4.65)$$

Objective function is defined as a negative logarithm function to deal with a minimization problem. Therefore, the negative logarithm of equation (4.65) is given as

$$L(\boldsymbol{\Theta}) = -\ln\left[p(\boldsymbol{\Theta}) \right] = \frac{1}{2} N_\Theta \ln(2\pi) + \frac{1}{2} \ln \left| \boldsymbol{\Sigma}_{\boldsymbol{\Theta}} \right| + \frac{1}{2} \left(\boldsymbol{\Theta} - \hat{\boldsymbol{\Theta}}_0 \right)^T \boldsymbol{\Sigma}_{\boldsymbol{\alpha}}^{-1} \left(\boldsymbol{\Theta} - \hat{\boldsymbol{\Theta}}_0 \right) \quad (4.66)$$

First derivative of $L(\boldsymbol{\Theta})$ with respect to the random variable vector, $\boldsymbol{\Theta}$ gives the Jacobian of the objective function as

$$\frac{\partial L(\boldsymbol{\Theta})}{\partial \boldsymbol{\Theta}} = \left(\boldsymbol{\Theta} - \hat{\boldsymbol{\Theta}}_0 \right)^T \boldsymbol{\Sigma}_{\boldsymbol{\Theta}}^{-1} \quad (4.67)$$

Then, second derivative of the objective function can be obtained by differentiating equation (4.67) with respect to $\boldsymbol{\Theta}$ and it gives the Hessian matrix of the objective function $L(\boldsymbol{\Theta})$ as

$$\mathbf{H}(\boldsymbol{\Theta}) = \frac{\partial^2 L(\boldsymbol{\Theta})}{\partial \boldsymbol{\Theta}^2} = \boldsymbol{\Sigma}_{\boldsymbol{\Theta}}^{-1} \tag{4.68}$$

Equation (4.68) reveals that inverse of the covariance matrix is equal to the Hessian matrix or inverse of the Hessian matrix is equal to the covariance matrix.

Now, Bayes' Theorem is revisited here and it is

$$p(\boldsymbol{\theta} \mid \mathbf{D}) = c_0 p(\mathbf{D} \mid \boldsymbol{\theta}) p(\boldsymbol{\theta}) \tag{4.69}$$

If the prior PDF of $p(\boldsymbol{\theta})$ is selected as a non-informative prior, then the posterior PDF of $p(\boldsymbol{\theta} \mid \mathbf{D})$ is considered to follow the distribution of the likelihood function $p(\mathbf{D} \mid \boldsymbol{\theta})$. Since the likelihood function is modeled to follow a Gaussian distribution in this study, then $p(\boldsymbol{\theta} \mid \mathbf{D})$ should also follow a Gaussian distribution. Therefore, posterior PDF of $p(\boldsymbol{\theta} \mid \mathbf{D})$ can be considered as

$$p(\boldsymbol{\theta} \mid \mathbf{D}) \sim p(\boldsymbol{\Theta}) \tag{4.70}$$

Then, by referring to equation (4.68), one can say that inverse of the Hessian of the objective function which is defined in equation (4.23) should give the covariance matrix of the updated parameters.

Hessian of the objective function can be calculated by differentiating equation (4.32) with respect to $\boldsymbol{\chi}$

$$\mathbf{H}_L(\boldsymbol{\chi}) = \frac{\partial^2 L}{\partial \boldsymbol{\chi}^2} = 2\left[\frac{\partial \mathbf{r}}{\partial \boldsymbol{\chi}}\right]^T \left[\frac{\partial \mathbf{r}}{\partial \boldsymbol{\chi}}\right] + 2\mathbf{r}^T \cdot \frac{\partial^2 \mathbf{r}}{\partial \boldsymbol{\chi}^2} \tag{4.71}$$

where $\partial^2 \mathbf{r} / \partial \boldsymbol{\chi}^2$ should be defined since it is the only undefined term to calculate the Hessian of the objective function. If both $\boldsymbol{\chi}$ and $\mathbf{r}$ are vectors, then $\partial^2 \mathbf{r} / \partial \boldsymbol{\chi}$ is a third-

order tensor. Therefore, the second term in equation (4.71) is modified to transform 3-D matrix problem into an equivalent 2-D matrix representation. To this end, $\partial^2\mathbf{r}/\partial\boldsymbol{\chi}^2$ can be considered as an array of Hessian matrices, one for each component of $\mathbf{r}$. In this study, it is defined for each mode instead of each component. However, it should be kept in mind that $\mathbf{r}$ that is provided in equation (4.29) includes r_β and r_γ which are defined only in terms of $\boldsymbol{\theta}$ and $\boldsymbol{\rho}$, respectively.

By defining $\partial^2\mathbf{r}_n/\partial\boldsymbol{\chi}^2$ for the n^{th} mode, $\partial^2 r_\beta/\partial\boldsymbol{\chi}^2$ and $\partial^2 r_\gamma/\partial\boldsymbol{\chi}^2$, equation (4.71) can be rewritten as

$$\mathbf{H}_L(\boldsymbol{\chi})=\frac{\partial^2 L}{\partial\boldsymbol{\chi}^2}=2\left[\frac{\partial\mathbf{r}}{\partial\boldsymbol{\chi}}\right]^T\left[\frac{\partial\mathbf{r}}{\partial\boldsymbol{\chi}}\right]+2\sum_{n=1}^{N_m}\bar{\mathbf{r}}_n^{\,T}\left[\frac{\partial^2\mathbf{r}_n}{\partial\boldsymbol{\chi}^2}\right]+2r_\beta\left[\frac{\partial^2 r_\beta}{\partial\boldsymbol{\chi}^2}\right]+2r_\gamma\left[\frac{\partial^2 r_\gamma}{\partial\boldsymbol{\chi}^2}\right] \tag{4.72}$$

where

$$\frac{\partial^2\mathbf{r}_n}{\partial\boldsymbol{\chi}^2}=\begin{bmatrix}
\frac{\partial^2\mathbf{r}_n}{\partial\theta_1\partial\theta_1} & \cdots & \frac{\partial^2\mathbf{r}_n}{\partial\theta_1\partial\theta_{N_\theta}} & \frac{\partial^2\mathbf{r}_n}{\partial\theta_1\partial\rho_1} & \cdots & \frac{\partial^2\mathbf{r}_n}{\partial\theta_1\partial\rho_{N_\rho}} \\
\vdots & \ddots & \vdots & \vdots & \ddots & \vdots \\
\frac{\partial^2\mathbf{r}_n}{\partial\theta_{N_\theta}\partial\theta_1} & \cdots & \frac{\partial^2\mathbf{r}_n}{\partial\theta_{N_\theta}\partial\theta_{N_\theta}} & \frac{\partial^2\mathbf{r}_n}{\partial\theta_{N_\theta}\partial\theta_{\rho_1}} & \cdots & \frac{\partial^2\mathbf{r}_n}{\partial\theta_{N_\theta}\partial\rho_{N_\rho}} \\
\frac{\partial^2\mathbf{r}_n}{\partial\rho_1\partial\theta_1} & \cdots & \frac{\partial^2\mathbf{r}_n}{\partial\rho_1\partial\theta_{N_\theta}} & \frac{\partial^2\mathbf{r}_n}{\partial\rho_1\partial\theta_{\rho_1}} & \cdots & \frac{\partial^2\mathbf{r}_n}{\partial\rho_1\partial\rho_{N_\rho}} \\
\vdots & \ddots & \vdots & \vdots & \ddots & \vdots \\
\frac{\partial^2\mathbf{r}_n}{\partial\rho_{N_\rho}\partial\theta_1} & \cdots & \frac{\partial^2\mathbf{r}_n}{\partial\rho_{N_\rho}\theta_{N_\theta}} & \frac{\partial^2\mathbf{r}_n}{\partial\rho_{N_\rho}\partial\theta_{\rho_1}} & \cdots & \frac{\partial^2\mathbf{r}_n}{\partial\rho_{N_\rho}\partial\rho_{N_\rho}}
\end{bmatrix} \tag{4.73}$$

and each element can be obtained as

$$\frac{\partial^2\mathbf{r}_n}{\partial x_p\partial y_q}=\begin{bmatrix}
-\frac{1}{\sqrt{2}}\cdot\frac{\frac{\partial^2\lambda_n(\boldsymbol{\chi})}{\partial x_p\partial y_q}}{\sigma_{\hat{\lambda}_n}} \\
-\frac{1}{4}\alpha_n(\boldsymbol{\chi})^{-3/2}\left(\frac{\partial\alpha_n(\boldsymbol{\chi})}{\partial x_p}\right)\left(\frac{\partial\alpha_n(\boldsymbol{\chi})}{\partial y_q}\right)+\frac{1}{2}\alpha_n(\boldsymbol{\chi})^{-1/2}\left(\frac{\partial^2\alpha_n(\boldsymbol{\chi})}{\partial x_p\partial y_q}\right)
\end{bmatrix}_{2\times 1} \tag{4.74}$$

where

$$\frac{\partial^2 \alpha_n(\boldsymbol{\chi})}{\partial x_p \partial y_q} = \left[\mathbf{L}_0 \frac{\partial \boldsymbol{\phi}_n(\boldsymbol{\chi})}{\partial y_q} \right]^T \mathbf{H}_{\hat{\boldsymbol{\phi}}_n} \mathbf{L}_0 \frac{\partial \boldsymbol{\phi}_n(\boldsymbol{\chi})}{\partial x_p} + \left[\mathbf{L}_0 \boldsymbol{\phi}_n(\boldsymbol{\chi}) - \hat{\boldsymbol{\phi}}_n \right]^T \mathbf{H}_{\hat{\boldsymbol{\phi}}_n} \mathbf{L}_0 \frac{\partial^2 \boldsymbol{\phi}_n(\boldsymbol{\chi})}{\partial x_p \partial y_q} \quad (4.75)$$

Here, x and y represent the corresponding parameters in equations (4.73) and sub-indices p and q correspond to the sub-indices of the associated parameters. For instance, if one needs to evaluate $\partial^2 \mathbf{r}_n / \partial \rho_j \partial \theta_i$ in equation (4.73), x_p should be replaced by ρ_j and y_q should be replaced by θ_i in equations (4.74) and (4.75).

In equation (4.73), $\partial^2 \mathbf{r}_n / \partial \boldsymbol{\chi}^2$ has a size of $2(N_\theta + N_\rho) \times (N_\theta + N_\rho)$ and it cannot be directly multiplied with $\mathbf{r}_n^T$ which has a size of 2×1. Therefore, $\mathbf{r}_n$ is modified as

$$\bar{\mathbf{r}}_n = \begin{bmatrix} \mathbf{r}_n & \mathbf{0}_{2\times 1} & \cdots & \mathbf{0}_{2\times 1} \\ \mathbf{0}_{2\times 1} & \mathbf{r}_n & \cdots & \mathbf{0}_{2\times 1} \\ \vdots & \vdots & \ddots & \vdots \\ \mathbf{0}_{2\times 1} & \mathbf{0}_{2\times 1} & \cdots & \mathbf{r}_n \end{bmatrix}_{2(N_\theta + N_\rho) \times (N_\theta + N_\rho)} \quad (4.76)$$

In equation (4.72), $\partial^2 r_\beta / \partial \boldsymbol{\chi}^2$ and $\partial^2 r_\gamma / \partial \boldsymbol{\chi}^2$ are 2D matrices. $\partial^2 r_\beta / \partial \boldsymbol{\chi}^2$ can be calculated by differentiating equations (4.40) with respect to $\boldsymbol{\chi}$ and it results in the following matrix

$$\frac{\partial^2 r_\beta}{\partial \boldsymbol{\chi}^2} = \begin{bmatrix} \frac{\partial^2 r_\beta}{\partial \theta_1 \partial \theta_1} & \cdots & \frac{\partial^2 r_\beta}{\partial \theta_1 \partial \theta_{N_\theta}} & \\ \vdots & \ddots & \vdots & \mathbf{0}_{N_\theta \times N_\rho} \\ \frac{\partial^2 r_\beta}{\partial \theta_{N_\theta} \partial \theta_1} & \cdots & \frac{\partial^2 r_\beta}{\partial \theta_{N_\theta} \partial \theta_{N_\theta}} & \\ & \mathbf{0}_{N_\rho \times N_\theta} & & \mathbf{0}_{N_\rho \times N_\rho} \end{bmatrix} \quad (4.77)$$

where

$$\frac{\partial^2 r_\beta}{\partial \theta_i \partial \theta_m} = -\frac{1}{4} \beta(\boldsymbol{\theta})^{-3/2} \left(\frac{\partial \beta(\boldsymbol{\theta})}{\partial \theta_i} \right) \left(\frac{\partial \beta(\boldsymbol{\theta})}{\partial \theta_m} \right) + \frac{1}{2} \beta(\boldsymbol{\theta})^{-1/2} \left(\frac{\partial^2 \beta(\boldsymbol{\theta})}{\partial \theta_i \partial \theta_m} \right) \quad (4.78)$$

In equation (4.78), $m = 1, 2, \ldots, N_\theta$ and, $\partial\beta(\boldsymbol{\theta})/\partial\theta_i$ and $\partial\beta(\boldsymbol{\theta})/\partial\theta_m$ are obtained as

$$\frac{\partial\beta(\boldsymbol{\theta})}{\partial\theta_i} = \left(\theta_i - \hat{\theta}_{i0}\right)\Sigma_{\theta_i}^{-1} \tag{4.79}$$

$$\frac{\partial\beta(\boldsymbol{\theta})}{\partial\theta_m} = \left(\theta_m - \hat{\theta}_{m0}\right)\Sigma_{\theta_m}^{-1} \tag{4.80}$$

where θ_{i0} and θ_{m0} denote the prior MPVs of θ_i and θ_m. $\Sigma_{\theta_i}^{-1}$ and Σ_{m}^{-1} represent the i^{th} and m^{th} diagonal element of $\boldsymbol{\Sigma_\theta^{-1}}$, respectively. Further, $\partial^2\beta(\boldsymbol{\theta})/\,\partial\theta_i\,\partial\theta_m$ can be defined as

$$\frac{\partial^2\beta(\boldsymbol{\theta})}{\partial\theta_i\partial\theta_m} = \begin{cases} \Sigma_{\theta_i}^{-1}, \; if \;\; i = m \\ 0 \quad , \; if \; i \neq m \end{cases} \tag{4.81}$$

Similarly, $\partial^2 r_\gamma \,/\, \partial\boldsymbol{\chi}^2$ can be evaluated by differentiating equations (4.42) with respect to $\boldsymbol{\chi}$ and it results in the following matrix

$$\frac{\partial^2 r_\gamma}{\partial\boldsymbol{\chi}^2} = \begin{bmatrix} \mathbf{0}_{N_\theta \times N_\theta} & & \mathbf{0}_{N_\theta \times N_\rho} \\ & \dfrac{\partial^2 r_\gamma}{\partial\rho_1\partial\rho_1} \quad \cdots & \dfrac{\partial^2 r_\gamma}{\partial\rho_1\partial\rho_{N_\rho}} \\ \mathbf{0}_{N_\rho \times N_\theta} & \vdots \quad \ddots & \vdots \\ & \dfrac{\partial^2 r_\gamma}{\partial\rho_{N_\theta}\partial\rho_1} \quad \cdots & \dfrac{\partial^2 r\gamma}{\partial\rho_{N_1}\partial\rho_{N_\rho}} \end{bmatrix} \tag{4.82}$$

where

$$\frac{\partial^2 r_\gamma}{\partial\rho_j\partial\rho_k} = -\frac{1}{4}\gamma(\boldsymbol{\rho})^{-3/2}\left(\frac{\partial\gamma(\boldsymbol{\rho})}{\partial\rho_j}\right)\left(\frac{\partial\gamma(\boldsymbol{\rho})}{\partial\rho_k}\right) + \frac{1}{2}\gamma(\boldsymbol{\rho})^{-1/2}\left(\frac{\partial^2\gamma(\boldsymbol{\rho})}{\partial\rho_j\partial\rho_k}\right) \tag{4.83}$$

In equation (4.83), $k = 1, 2, \ldots, N_\rho$ and, $\partial\gamma(\boldsymbol{\rho})/\partial\rho_j$ and $\partial\gamma(\boldsymbol{\rho})/\partial\rho_s$ are obtained as

$$\frac{\partial\gamma(\boldsymbol{\rho})}{\partial\rho_j} = \left(\rho_j - \hat{\rho}_{j0}\right)\Sigma_{\rho_j}^{-1} \tag{4.84}$$

$$\frac{\partial \gamma(\boldsymbol{\rho})}{\partial \rho_k} = \left(\rho_k - \hat{\rho}_{k0}\right)\Sigma_{\rho_k}^{-1} \tag{4.85}$$

where ρ_{j0} and ρ_{k0} denote the prior MPVs of ρ_j and ρ_k. $\Sigma_{\rho_j}^{-1}$ and $\Sigma_{\rho_s}^{-1}$ represent the j^{th} and k^{th} diagonal element of $\boldsymbol{\Sigma}_{\boldsymbol{\rho}}^{-1}$, respectively. Further, $\partial^2\gamma(\boldsymbol{\rho})/\,\partial\rho_j\,\partial\rho_k$ can be defined as

$$\frac{\partial^2 \gamma(\boldsymbol{\rho})}{\partial \rho_j \partial \rho_k} = \begin{cases} \Sigma_{\rho_j}^{-1}, \; if \;\; j = k \\ 0 \;\;\; , \; if \;\; j \neq k \end{cases} \tag{4.86}$$

To evaluate the Hessian of the objective function, $L(\boldsymbol{\theta})$, it is required to calculate the Hessian of the eigenvalues, $\partial^2\lambda_n(\boldsymbol{\theta})\,/\,\partial\theta_i\,\partial\theta_m$, $\partial^2\lambda_n(\boldsymbol{\theta})\,/\,\partial\theta_i\,\partial\rho_j$ and $\partial^2\lambda_n(\boldsymbol{\theta})\,/\,\partial\rho_j\,\partial\rho_k$ in equation (4.74). Further, Hessian of the eigenvectors, $\partial^2\boldsymbol{\phi}_n(\boldsymbol{\theta})\,/\,\partial\theta_i\,\partial\theta_m$, $\partial^2\boldsymbol{\phi}_n(\boldsymbol{\theta})\,/\,\partial\theta_i\,\partial\rho_j$ and $\partial^2\boldsymbol{\phi}_n(\boldsymbol{\theta})\,/\,\partial\rho_j\,\partial\rho_k$ in equation (4.75). Note that equations (4.74) and (4.75) are generalized by using x_p and y_q to avoid repetition of same equations for different parameters. One should substitute the corresponding parameter and indices into x_p and y_q to obtain the aforementioned Hessian terms.

4.2.4.1. Hessian of Eigenvalues and Eigenvectors

Calculation of the second derivatives of the eigenvalues and eigenvectors is a long procedure when compared to the calculation of their Jacobians. Therefore, final results are provided in this section for the sake of clarity. Detailed derivations can be found in Appendix B.

- **Differentiation with respect to θ_i and θ_m**

After calculations, Hessian of the eigenvalue of the n^{th} mode, $\partial^2\lambda_n(\boldsymbol{\theta})\,/\,\partial\theta_i\,\partial\theta_m$, has been obtained as

$$\frac{\partial^2 \lambda_n(\boldsymbol{\chi})}{\partial \theta_i \partial \theta_m} = \frac{\boldsymbol{\phi}_n^T(\boldsymbol{\chi})\left[\mathbf{K}_i - \frac{\partial \lambda_n(\boldsymbol{\chi})}{\partial \theta_i}\mathbf{M}(\boldsymbol{\rho})\right]\frac{\partial \boldsymbol{\phi}_n(\boldsymbol{\chi})}{\partial \theta_m} + \boldsymbol{\phi}_n^T(\boldsymbol{\chi})\left[\mathbf{K}_m - \frac{\partial \lambda_n(\boldsymbol{\chi})}{\partial \theta_m}\mathbf{M}(\boldsymbol{\rho})\right]\frac{\partial \boldsymbol{\phi}_n(\boldsymbol{\chi})}{\partial \theta_i}}{\boldsymbol{\phi}_n^T(\boldsymbol{\chi})\mathbf{M}(\boldsymbol{\rho})\boldsymbol{\phi}_n(\boldsymbol{\chi})} \tag{4.87}$$

and Hessian of the eigenvector of the n^{th} mode has been obtained as

$$\frac{\partial^2 \boldsymbol{\phi}_n(\boldsymbol{\chi})}{\partial \theta_i \partial \theta_m} = \mathbf{A}_n \frac{\partial^2 \boldsymbol{\phi}_n^-(\boldsymbol{\chi})}{\partial \theta_i \partial \theta_m} \tag{4.88}$$

Here, $\partial^2 \boldsymbol{\phi}_n^-(\boldsymbol{\theta}) \,/\, \partial\theta_i \, \partial\theta_m$ is defined as

$$\frac{\partial^2 \boldsymbol{\phi}_n^-(\boldsymbol{\chi})}{\partial \theta_i \partial \theta_m} = \left(\mathbf{A}_n^T\left[\mathbf{K}(\boldsymbol{\chi}) - \lambda_n(\boldsymbol{\chi})\mathbf{M}\right]\mathbf{A}_n\right)^{-1}\left(\mathbf{A}_n^T \mathbf{d}_{nim}\right) \tag{4.89}$$

where

$$\begin{aligned}\mathbf{d}_{nim} = \frac{\partial^2 \lambda_n(\boldsymbol{\chi})}{\partial \theta_i \partial \theta_m}\mathbf{M}(\boldsymbol{\rho})\boldsymbol{\phi}_n(\boldsymbol{\chi}) - \left[\mathbf{K}_i - \frac{\partial \lambda_n(\boldsymbol{\chi})}{\partial \theta_i}\mathbf{M}(\boldsymbol{\rho})\right]\frac{\partial \boldsymbol{\phi}_n(\boldsymbol{\chi})}{\partial \theta_m} \\ - \left[\mathbf{K}_m - \frac{\partial \lambda_n(\boldsymbol{\chi})}{\partial \theta_m}\mathbf{M}(\boldsymbol{\rho})\right]\frac{\partial \boldsymbol{\phi}_n(\boldsymbol{\chi})}{\partial \theta_i}\end{aligned} \tag{4.90}$$

- **Differentiation with respect to θ_i and ρ_j**

Similarly, Hessian of the eigenvalue of the n^{th} mode, $\partial^2 \lambda_n(\boldsymbol{\theta}) \,/\, \partial\theta_i \, \partial\rho_j$, has been obtained as

$$\frac{\partial^2 \lambda_n(\boldsymbol{\chi})}{\partial \theta_i \partial \rho_j} = \frac{\begin{aligned}&\boldsymbol{\phi}_n^T(\boldsymbol{\chi})\left[\mathbf{K}_i - \frac{\partial \lambda_n(\boldsymbol{\chi})}{\partial \theta_i}\mathbf{M}(\boldsymbol{\rho})\right]\frac{\partial \boldsymbol{\phi}_n(\boldsymbol{\chi})}{\partial \rho_j} \\ &- \boldsymbol{\phi}_n^T(\boldsymbol{\chi})\left[\frac{\partial \lambda_n(\boldsymbol{\chi})}{\partial \rho_j}\mathbf{M}(\boldsymbol{\rho}) + \lambda_n(\boldsymbol{\chi})\mathbf{M}_j\right]\frac{\partial \boldsymbol{\phi}_n(\boldsymbol{\chi})}{\partial \theta_i} - \frac{\partial \lambda_n(\boldsymbol{\chi})}{\partial \theta_i}\boldsymbol{\phi}_n^T(\boldsymbol{\chi})\mathbf{M}_j\boldsymbol{\phi}_n(\boldsymbol{\chi})\end{aligned}}{\boldsymbol{\phi}_n^T(\boldsymbol{\chi})\mathbf{M}(\boldsymbol{\rho})\boldsymbol{\phi}_n(\boldsymbol{\chi})} \tag{4.91}$$

and Hessian of the eigenvector of the n^{th} mode has been obtained as

$$\frac{\partial^2 \boldsymbol{\phi}_n(\boldsymbol{\chi})}{\partial\theta_i \partial\rho_j} = \mathbf{A}_n \frac{\partial^2 \boldsymbol{\phi}_n^-(\boldsymbol{\chi})}{\partial\theta_i \partial\rho_j} \tag{4.92}$$

Here, $\partial^2 \boldsymbol{\phi}_n^-(\boldsymbol{\theta}) \,/\, \partial\theta_i \, \partial\rho_j$ is defined as

$$\frac{\partial^2 \boldsymbol{\phi}_n^-(\boldsymbol{\chi})}{\partial\theta_i \partial\rho_j} = \left(\mathbf{A}_n^T \left[\mathbf{K}(\boldsymbol{\chi}) - \lambda_n(\boldsymbol{\chi})\mathbf{M}\right]\mathbf{A}_n\right)^{-1}\left(\mathbf{A}_n^T \mathbf{d}_{nij}\right) \tag{4.93}$$

where

$$\begin{aligned}\mathbf{d}_{nij} = \left[\frac{\partial^2 \lambda_n(\boldsymbol{\chi})}{\partial\theta_i \partial\rho_j}\mathbf{M}(\boldsymbol{\rho}) + \frac{\partial\lambda_n(\boldsymbol{\chi})}{\partial\theta_i}\mathbf{M}_j\right]\boldsymbol{\phi}_n(\boldsymbol{\chi}) - \left[\mathbf{K}_i - \frac{\partial\lambda_n(\boldsymbol{\chi})}{\partial\theta_i}\mathbf{M}(\boldsymbol{\rho})\right]\frac{\partial\boldsymbol{\phi}_n(\boldsymbol{\chi})}{\partial\rho_j} \\ + \left[\frac{\partial\lambda_n(\boldsymbol{\chi})}{\partial\rho_j}\mathbf{M}(\boldsymbol{\rho}) + \lambda_n(\boldsymbol{\chi})\mathbf{M}_j\right]\frac{\partial\boldsymbol{\phi}_n(\boldsymbol{\chi})}{\partial\theta_i}\end{aligned} \tag{4.94}$$

- **Differentiation with respect to ρ_j and ρ_k**

Similarly, Hessian of the eigenvalue of the n^{th} mode, $\partial^2\lambda_n(\boldsymbol{\theta}) \,/\, \partial\rho_j \, \partial\rho_k$, has been obtained as

$$\begin{aligned}\frac{\partial^2 \lambda_n(\boldsymbol{\chi})}{\partial\rho_j \partial\rho_k} = \frac{\begin{array}{r} -\boldsymbol{\phi}_n^T(\boldsymbol{\chi})\left[\frac{\partial\lambda_n(\boldsymbol{\chi})}{\partial\rho_j}\mathbf{M}_k + \frac{\partial\lambda_n(\boldsymbol{\chi})}{\partial\rho_k}\mathbf{M}_j\right]\boldsymbol{\phi}_n(\boldsymbol{\chi}) \\ -\boldsymbol{\phi}_n^T(\boldsymbol{\chi})\left[\frac{\partial\lambda_n(\boldsymbol{\chi})}{\partial\rho_j}\mathbf{M}(\boldsymbol{\rho}) + \lambda_n(\boldsymbol{\chi})\mathbf{M}_j\right]\frac{\partial\boldsymbol{\phi}_n(\boldsymbol{\chi})}{\partial\rho_k} \\ -\boldsymbol{\phi}_n^T(\boldsymbol{\chi})\left[\frac{\partial\lambda_n(\boldsymbol{\chi})}{\partial\rho_k}\mathbf{M}(\boldsymbol{\rho}) + \lambda_n(\boldsymbol{\chi})\mathbf{M}_k\right]\frac{\partial\boldsymbol{\phi}_n(\boldsymbol{\chi})}{\partial\rho_j}\end{array}}{\boldsymbol{\phi}_n^T(\boldsymbol{\chi})\mathbf{M}(\boldsymbol{\rho})\boldsymbol{\phi}_n(\boldsymbol{\chi})}\end{aligned} \tag{4.95}$$

and Hessian of the eigenvector of the n^{th} mode has been obtained as

$$\frac{\partial^2 \boldsymbol{\phi}_n(\boldsymbol{\chi})}{\partial \rho_j \partial \rho_k} = \mathbf{A}_n \frac{\partial^2 \boldsymbol{\phi}_n^-(\boldsymbol{\chi})}{\partial \rho_j \partial \rho_k} \tag{4.96}$$

Here, $\partial^2 \boldsymbol{\phi}_n^-(\boldsymbol{\theta}) \,/\, \partial \rho_j \, \partial \rho_k$ is defined as

$$\frac{\partial^2 \boldsymbol{\phi}_n^-(\boldsymbol{\chi})}{\partial \rho_j \partial \rho_k} = \left(\mathbf{A}_n^T \left[\mathbf{K}(\boldsymbol{\chi}) - \lambda_n(\boldsymbol{\chi})\mathbf{M}\right]\mathbf{A}_n\right)^{-1}\left(\mathbf{A}_n^T \mathbf{d}_{njk}\right) \tag{4.97}$$

where

$$\begin{aligned}\mathbf{d}_{njk} = &\left[\frac{\partial^2 \lambda_n(\boldsymbol{\chi})}{\partial \rho_j \partial \rho_k}\mathbf{M}(\boldsymbol{\rho}) + \frac{\partial \lambda_n(\boldsymbol{\chi})}{\partial \rho_j}\mathbf{M}_k + \frac{\partial \lambda_n(\boldsymbol{\chi})}{\partial \rho_k}\mathbf{M}_j\right]\boldsymbol{\phi}_n(\boldsymbol{\chi}) \\ &+ \left[\frac{\partial \lambda_n(\boldsymbol{\chi})}{\partial \rho_j}\mathbf{M}(\boldsymbol{\rho}) + \lambda_n(\boldsymbol{\chi})\mathbf{M}_j\right]\frac{\partial \boldsymbol{\phi}_n(\boldsymbol{\chi})}{\partial \rho_k} \\ &+ \left[\frac{\partial \lambda_n(\boldsymbol{\chi})}{\partial \rho_k}\mathbf{M}(\boldsymbol{\rho}) + \lambda_n(\boldsymbol{\chi})\mathbf{M}_k\right]\frac{\partial \boldsymbol{\phi}_n(\boldsymbol{\chi})}{\partial \rho_j}\end{aligned} \tag{4.98}$$

4.2.5. Updating Procedure and Computational Issues

In the presented two-stage sensitivity-based Bayesian model updating procedure, stiffness scaling parameter vector $\boldsymbol{\theta}$ and mass scaling parameter vector $\boldsymbol{\rho}$ are updated by minimizing the objective function $L(\boldsymbol{\chi})$ in equation (4.23) by using "SMU: MATLAB Package for Structural Model Updating" which is shared by Wang et al. (2019). In the SMU package, *fmincon* solver is used with the '*interior-point algorithm*' by employing the analytical Jacobian that is derived in the previous section. The objective function $L(\boldsymbol{\chi})$ is a non-convex function and therefore it may have local minimum points. However, the solvers used in the SMU package may get stuck at the local minimum points and cannot guarantee the global minimum. Therefore, Otsuki et al. (2021) randomly choose initial parameter values of $\boldsymbol{\theta}$ from a uniform distribution defined in the interval of $\mathbf{L}_{\boldsymbol{\theta}} \leq \boldsymbol{\theta} \leq \mathbf{U}_{\boldsymbol{\theta}}$, and initiate the optimization process from each random points to increase the chance of finding global minimum. Similar procedure is followed in this study. Since the prior distribution of the stiffness and mass scaling parameters are

considered to follow a truncated Gaussian distribution, initial parameter values are randomly chosen from a Gaussian distribution truncated by $\mathbf{L}_{\chi}$ and $\mathbf{U}_{\chi}$. It should be noted here that this procedure is only increasing the chance of finding global minimum in the corresponding interval, but it is not guaranteed. SMU MATLAB package in its original form performs the updating of stiffness parameters in a deterministic way by minimizing the objective functions that are constructed with a weighted least squares sense. Therefore, the package is modified to include all derivations presented in the previous sections.

Figure 4.1 shows the flow chart for the presented model updating procedure. The flow chart can be summarized as the following steps

Modal identification stage:

- *Step 1*: By using the BFFTA, estimate the MPVs of the measured eigenvalues as $\hat{\boldsymbol{\lambda}}$ with their corresponding posterior covariance matrix $\boldsymbol{\Sigma}_{\hat{\lambda}}$, and the MPVs of the mode shape matrix $\hat{\boldsymbol{\psi}} = [\hat{\boldsymbol{\psi}}_1 \ \ \hat{\boldsymbol{\psi}}_2 \ \ \hat{\boldsymbol{\psi}}_3 \ . \ . \ . \ \hat{\boldsymbol{\psi}}_{Nm}]$ with the corresponding block diagonal Hessian matrix $\mathbf{H}_{\hat{\psi}}$ whose diagonal elements consist of the set $\{\mathbf{H}_{\hat{\psi}_1}$, $\mathbf{H}_{\hat{\psi}_2}$, $\mathbf{H}_{\hat{\psi}_3}$, . . . , $\mathbf{H}_{\hat{\psi}_{Nm}}\}$.

Model updating stage:

- *Step 2*: Normalize the measured mode shape $\hat{\boldsymbol{\psi}}_n$ as its coordinate (h_n^{th} coordinate) with the largest absolute value to be 1 and it will give the normalized mode shape vector $\hat{\boldsymbol{\phi}}_n$. In addition, obtain $\mathbf{H}_{\hat{\phi}_n}$ by scaling $\mathbf{H}_{\hat{\psi}_n}$ using equation (4.21).
- *Step 3*: Set a prior variance for each stiffness scaling parameter. To do so, first consider the nominal value of $\boldsymbol{\theta}$ by using engineering judgement. Prior estimation of stiffness distribution of physical structures is not precise since the actual distribution is highly uncertain due to the uncertainties in stiffness of joints, real boundary conditions, etc. Therefore, a large prior variance is generally assigned for the stiffness scaling parameters according to their nominal values. By doing so, the posterior distribution is not dominated by the prior distribution of the parameters. The prior covariance matrix of the stiffness parameters, $\boldsymbol{\Sigma}_{\boldsymbol{\theta}}$, is constructed with a diagonal matrix and each diagonal element consists of the calculated variance value.

- *Step 4*: Set a prior variance for each mass scaling parameter. In this study, both mass and stiffness scaling parameters are modeled as the updating parameters. In the literature, it is known that considering both parameters with high prior uncertainties results in an ill-conditioned optimization problem since it may give an infinite number of solutions that minimize the objective function. To overcome this issue, mass parameters are assumed to be well-estimated with small prior uncertainties since the mass is less uncertain than the stiffness in real life. Therefore, a small prior variance is generally assigned for the mass scaling parameters according to their nominal values. The prior covariance matrix of the mass parameters, $\mathbf{\Sigma_\rho}$, is constructed with a diagonal matrix and each diagonal element consists of the calculated variance value.
- *Step 5*: Set number of runs, N_{run} to identify a global minimum. A higher value of N_{run} increases the chance to catch the global minimum while increasing the computational time.
- *Step 6*: Determine the prior value of each stiffness scaling parameter, $\widehat{\boldsymbol{\theta}}_0$. It is extracted from a truncated Gaussian distribution having a prior variance determined in *Step 3*. It is truncated by setting a lower bound, $\mathbf{L_\theta}$, and an upper bound, $\mathbf{U_\theta}$, according to the prior value $\widehat{\boldsymbol{\theta}}_0$.
- *Step 7*: Determine the prior value of each mass scaling parameter, $\widehat{\boldsymbol{\rho}}_0$. It is again extracted from a truncated Gaussian distribution having a prior variance determined in *Step 4*. It is truncated by setting a lower bound, $\mathbf{L_\rho}$, and an upper bound, $\mathbf{U_\rho}$, according to the prior value $\widehat{\boldsymbol{\rho}}_0$.
- *Step 8*: Calculate the prior stiffness matrix $\mathbf{K}(\widehat{\boldsymbol{\theta}}_0)$ and mass matrix $\mathbf{M}(\widehat{\boldsymbol{\rho}}_0)$, and evaluate $\lambda_n(\hat{\boldsymbol{\chi}}_0)$ and $\boldsymbol{\phi}_n(\hat{\boldsymbol{\chi}}_0)$ by the eigenvalue analysis of the current FE model. Note that $\hat{\boldsymbol{\chi}}_0 = \left[\widehat{\boldsymbol{\theta}}_0 \;\; \widehat{\boldsymbol{\rho}}_0\right]^T$.
- *Step 9*: Normalize the mode shape vector $\boldsymbol{\phi}_n(\hat{\boldsymbol{\chi}}_0)$ such that its a_n^{th} coordinate is equal to 1. Note that the a_n^{th} coordinate of the vector $\boldsymbol{\phi}_n(\boldsymbol{\theta})$ with complete DOFs of the FE model corresponds to the h_n^{th} coordinate of the measured mode shape vector $\widehat{\boldsymbol{\phi}}_n$ which includes measured DOFs, only.
- *Step 10*: Use equation (4.29) to construct the residual vector $\mathbf{r}(\boldsymbol{\chi})$ and use equation (4.32) to construct the analytical Jacobian of the objective function, $\partial L(\boldsymbol{\chi})/\partial \boldsymbol{\chi}$.

- *Step 11*: Solve the optimization problem to obtain the MPVs of the updated stiffness and mass scaling parameters. In this study, it is solved by using *fmincon* solver with the '*interior-point algorithm*' in "SMU: MATLAB Package for Structural Model Updating" which is shared by Wang et al. (2019).
- *Step 12*: Repeat *Step 6 – Step 11* to obtain N_{run} solutions for randomly selected initial points. The solution which results in minimum objective function value is selected as the MPV of the updated parameter vector, $\hat{\boldsymbol{\chi}}$. It should be kept in mind that this point is the global minimum among the solutions obtained, and it may not guarantee the actual global minimum of the objective function.
- *Step 13*: Calculate the Hessian matrix of the objective function, $\mathbf{H}_L(\hat{\boldsymbol{\chi}})$, by using equation (4.72). Then, calculate the posterior covariance matrix of the updated parameters. The posterior covariance matrix is calculated by inverse of the Hessian matrix and diagonal elements result in the posterior variance of the updated parameters.

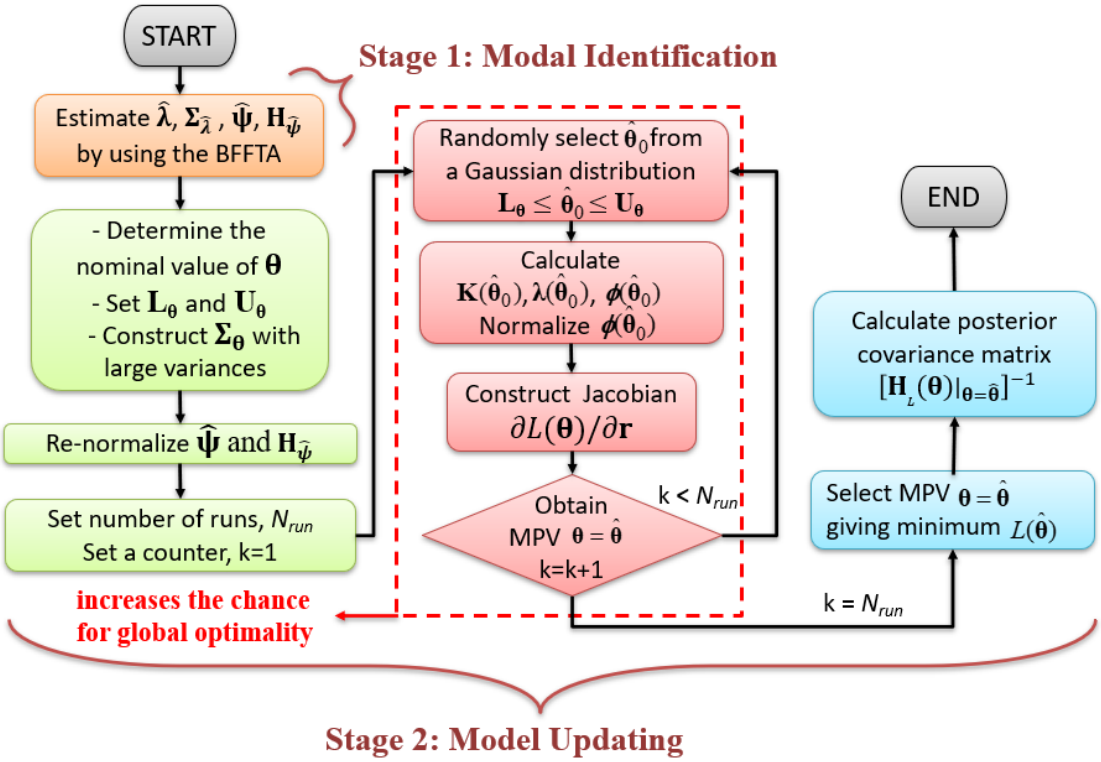

Figure 4.1. Flow chart of the proposed model updating procedure

4.2.6. Numerical and Experimental Studies

In this section, the sensitivity-based Bayesian model updating procedure is investigated by numerical and experimental studies. The results are compared to those of the results obtained in the previous chapter.

4.2.6.1. Numerical Studies

The proposed two-stage sensitivity-based Bayesian model updating method is implemented on the numerical twelve-story shear frame structure that is used in the previous chapter (in the beginning of Section 3.2.6) to compare the model updating results. All measurement process and stiffness parametrization procedure is performed in exactly the same way. Therefore, it is skipped here to avoid repetition.

Square of the actual stiffness value of $K = 202.767 \times 10^3$ kN/m is considered as the variance of each corresponding stiffness parameter to have a non-informative prior distribution. The prior covariance matrix of the stiffness parameters, $\boldsymbol{\Sigma_\theta}$, is constructed as a diagonal matrix and each diagonal element is the calculated variance value. Then, the initial value, $\widehat{\boldsymbol{\theta}}_0$, of the stiffness parameter vector is randomly selected from a Gaussian distribution by setting the mean of the distribution as the value of $\boldsymbol{\theta}$ and setting the variance to be $\boldsymbol{\Sigma_\theta}$. The upper and lower bounds are selected as $L_\theta = 100 \times 10^3$ kN/m and $U_\theta = 1000 \times 10^3$ kN/m. Upper bound is intentionally selected as a high stiffness value to investigate whether the proposed methodology is convergent with high initial parameter values. Then, Gaussian distribution is defined in only these bounds and generated values out of these bounds are discarded. To increase the chance of global optimality in the considered interval, number of runs is set as N_{run}=100. Thus, 100 different optimizations are performed by using 100 different initial models of the structure. In this numerical application, mass is assumed to be well-estimated and it is not considered as an updating parameter so that the results are comparable to those of the previous chapter.

In the numerical study, results of the proposed method (SensBMU) are compared with the results of three different cases that are already investigated in the previous chapter. As a reminder, assumption of each case is defined as follows;

- Case 1: Modelling error variance of each mode is considered to be different for each mode and each is updated as soft constraints. This case is the main focus of the previous chapter.
- Case 2: Modelling error variance is considered to be the same for each mode and updated in each iteration as a soft constraint. This case corresponds to a similar study performed by Hızal and Turan (2020).
- Case 3: Modelling error variance has a prescribed value which is the same for all modes. It is not updated and kept as a rigid constraint. This case corresponds to a similar study performed by Yuen (2010).

As the first application, it is considered that all modes and DOFs of the structure are available and the structure is updated by the complete modal data. Model updating results are provided with the posterior uncertainties for each case in Table 4.1. In the tables of the present study, instead of the MPVs of the updated parameters, relative errors between the actual and MPVs of the updated parameters are provided in percentage and a negative value means the updated parameter has a smaller value than the actual one. According to the results, all the updated stiffness parameters have converged well to their actual values. The posterior c.o.v values for Case 1, 2 and 3 appear to be in the same order of magnitude and they are unrealistically too small. However, it is seen that the methodology presented in the present study results in more realistic values with higher c.o.v values. It should be noted that the present study and Case 3 do not include the norm constraint term for modal shapes. Besides, the present study removes the modelling error term while Case 3 includes it. Therefore, here, one may conclude that the reason of the increase in the posterior uncertainties is most probably the removal of the modelling error term. Of course, it should be kept in mind that the formulations of the present study and Case 3 are different from each other and therefore removing the modelling error term may not be the only reason for the increase in posterior uncertainties of the updated parameters.

Table 4.1. Updated stiffness parameters with complete modal data (× 10^3 kN/m)

	SensBMU		**Case 1**		**Case 2**		**Case 3**	
	Updated (Rel. Err.) (%)	c.o.v (×10^{-4})	Updated (Rel. Err.) (%)	c.o.v (×10^{-11})	Updated (Rel. Err.) (%)	c.o.v (×10^{-11})	Updated (Rel. Err.) (%)	c.o.v (×10^{-11})
θ_1	0.30	9.35	− 0.53	6.18	0.31	36.83	1.35	131.24
θ_2	0.24	7.70	1.25	15.73	0.02	217.47	− 0.38	416.93
θ_3	− 0.01	7.73	0.02	1.79	− 0.03	400.58	0.07	292.15
θ_4	0.13	8.21	− 0.33	5.33	0.11	487.38	0.21	145.62
θ_5	− 0.26	7.97	− 0.28	8.48	0.07	430.31	0.02	90.07
θ_6	− 0.32	8.28	0.76	10.43	0.07	235.75	0.21	122.18
θ_7	0.42	7.62	− 0.13	3.66	0.02	121.20	0.11	17.66
θ_8	0.61	8.34	0.07	2.95	− 0.13	332.10	− 0.62	62.62
θ_9	− 0.24	8.24	0.02	2.92	0.12	444.54	0.21	27.68
θ_{10}	0.03	7.90	0.56	4.00	0.16	417.37	0.46	167.97
θ_{11}	− 0.02	7.58	− 0.33	3.85	0.07	270	0.02	185.36
θ_{12}	− 0.11	7.61	− 0.03	0.35	− 0.08	94.29	− 0.13	54.77

Further, the present study is investigated for incomplete modal data. First, different numbers of measured modes are considered with spatially complete measured mode shapes. For this investigation, it is considered as if the first two, four, seven or ten modes only are measured from the structure and model updating is performed by using these modes only. Updating results are provided in Figure 4.2. Updated values are not as good as the ones obtained for the complete modal data, especially when two and four modes are used only. Since the model is updated with respect to the considered modes only, this is an expected result. According to Table 4.2, posterior c.o.v of the stiffness parameters decrease with the increased number of considered measured modes. This is an expected result since the information used in the probabilistic model is increasing with the increased number of measured modes. Therefore, parameter uncertainty is expected to decrease (Yuen, 2010; Hizal, 2019; Hızal and Turan, 2020). In Table 4.3, results are provided for Case 1 by using the same number of considered modes for comparison purposes. It is seen that the posterior c.o.v values of the parameters are unrealistically too small. Besides, the uncertainties decrease with the increase in the number of considered modes. This result is quite opposite the results obtained in the present study and in the literature. On the other hand, especially for the smaller number of considered modes, the updated stiffness parameter values of the previous study converge to the actual values better than those of the present study. However, it can be observed from the results, for example, when the number of considered modes is two that parameter θ_{12} is the most divergent one from the actual value with a relative error of – 26.02% (corresponds to a stiffness value of 150 × 10^3 kN/m) and its posterior c.o.v

value is also the highest one with a value of 133.15×10^{-4}. It should be noted here that, even though the posterior c.o.v results seem reasonable from this point of view, they are still small numbers since the standard deviation of θ_{12} is about $\sigma_{\theta_{12}} = 2 \times 10^3$ kN/m. Then, 150×10^3 kN/m $\pm \sigma_{\theta_{12}}$ results in the stiffness values far from the actual value of 202.767×10^3 kN/m.

The results are illustratively presented in Figure 4.2 and Figure 4.3. Figure 4.2 is the graphical representation of convergence quality of some stiffness parameters with respect to the number of considered modes. Here, results of the proposed methodology are compared with those of the previous chapter. All the four plots reveal that the proposed method has higher convergence problems when a smaller number of modes are considered. Figure 4.3 shows the graphical representation of the change in the posterior c.o.v with the number of considered modes. Proposed method results in significantly high posterior c.o.v values when compared to the results of the previous chapters. Besides, for Case 1, 2 and 3, the uncertainties are increasing with the increase in the number of considered modes. This result is quite opposite of the results obtained in the proposed method and in the literature. The results of the proposed method are found to be compatible with the literature. However, again the posterior c.o.v values seem small especially for complete modal data.

Table 4.2. Updated stiffness parameters of the proposed method using different number of modes ($\times 10^3$ kN/m)

	Number of considered measured modes							
	2		**4**		**7**		**10**	
	Updated (Rel. Err.) (%)	c.o.v ($\times$**10^{-4}**)	Updated (Rel. Err.) (%)	c.o.v ($\times$**10^{-4}**)	Updated (Rel. Err.) (%)	c.o.v ($\times$**10^{-4}**)	Updated (Rel. Err.) (%)	c.o.v ($\times$**10^{-4}**)
θ_1	4.68	42.48	1.13	22.25	− 1.74	16.40	0.14	12.17
θ_2	− 4.72	61.04	2.75	40.06	1.89	20.70	0.27	8.37
θ_3	3.71	80.96	2.35	49.11	− 1.02	15.06	0.26	9.93
θ_4	− 0.38	98.00	− 2.02	33.57	0.37	16.19	0.29	11.60
θ_5	6.75	84.48	3.67	36.69	0.38	15.06	− 0.30	9.29
θ_6	− 8.47	115.42	− 4.33	35.52	− 0.73	13.45	− 0.63	9.97
θ_7	2.87	80.19	− 2.40	34.69	0.73	18.44	0.02	10.10
θ_8	− 2.29	68.49	2.17	35.31	0.83	14.64	0.45	9.65
θ_9	4.05	71.43	− 4.80	36.22	1.24	15.89	− 0.08	10.33
θ_{10}	− 2.71	73.11	5.02	35.80	− 0.78	14.45	0.27	10.61
θ_{11}	9.97	111.89	− 4.52	31.42	0.86	14.85	0.15	8.32
θ_{12}	− 26.02	133.15	7.09	51.71	0.55	11.85	− 0.08	9.84

Table 4.3. Updated stiffness parameters of Case 1 using different number of modes ($\times 10^3$ kN/m)

	Number of considered measured modes							
	2		**4**		**7**		**10**	
	Updated (Rel. Err.) (%)	c.o.v ($\times\mathbf{10^{-15}}$)	Updated (Rel. Err.) (%)	c.o.v ($\times\mathbf{10^{-14}}$)	Updated (Rel. Err.) (%)	c.o.v ($\times\mathbf{10^{-12}}$)	Updated (Rel. Err.) (%)	c.o.v ($\times\mathbf{10^{-11}}$)
θ_1	− 0.53	1.94	− 0.48	4.61	− 0.48	7.34	− 0.58	6.04
θ_2	1.79	4.49	1.79	7.28	1.74	12.42	1.30	14.61
θ_3	0.51	1.60	0.51	1.55	0.31	1.27	0.07	1.29
θ_4	− 0.38	0.52	− 0.48	3.13	− 0.33	3.12	− 0.33	4.59
θ_5	− 0.48	0.51	− 0.48	2.03	− 0.33	9.75	− 0.33	7.93
θ_6	1.20	0.83	1.05	5.71	0.85	11.57	0.71	9.35
θ_7	0.26	1.06	0.02	2.12	0.02	5.02	− 0.13	3.78
θ_8	0.41	1.97	0.26	2.14	0.07	7.08	0.07	3.01
θ_9	0.07	0.14	0.16	0.11	0.07	4.42	0.07	2.52
θ_{10}	0.51	2.69	0.56	0.13	0.46	3.32	0.56	3.30
θ_{11}	− 1.46	1.64	− 0.67	3.90	− 0.43	3.53	− 0.33	3.31
θ_{12}	2.48	1.40	0.21	0.99	− 0.18	0.67	− 0.08	3.30

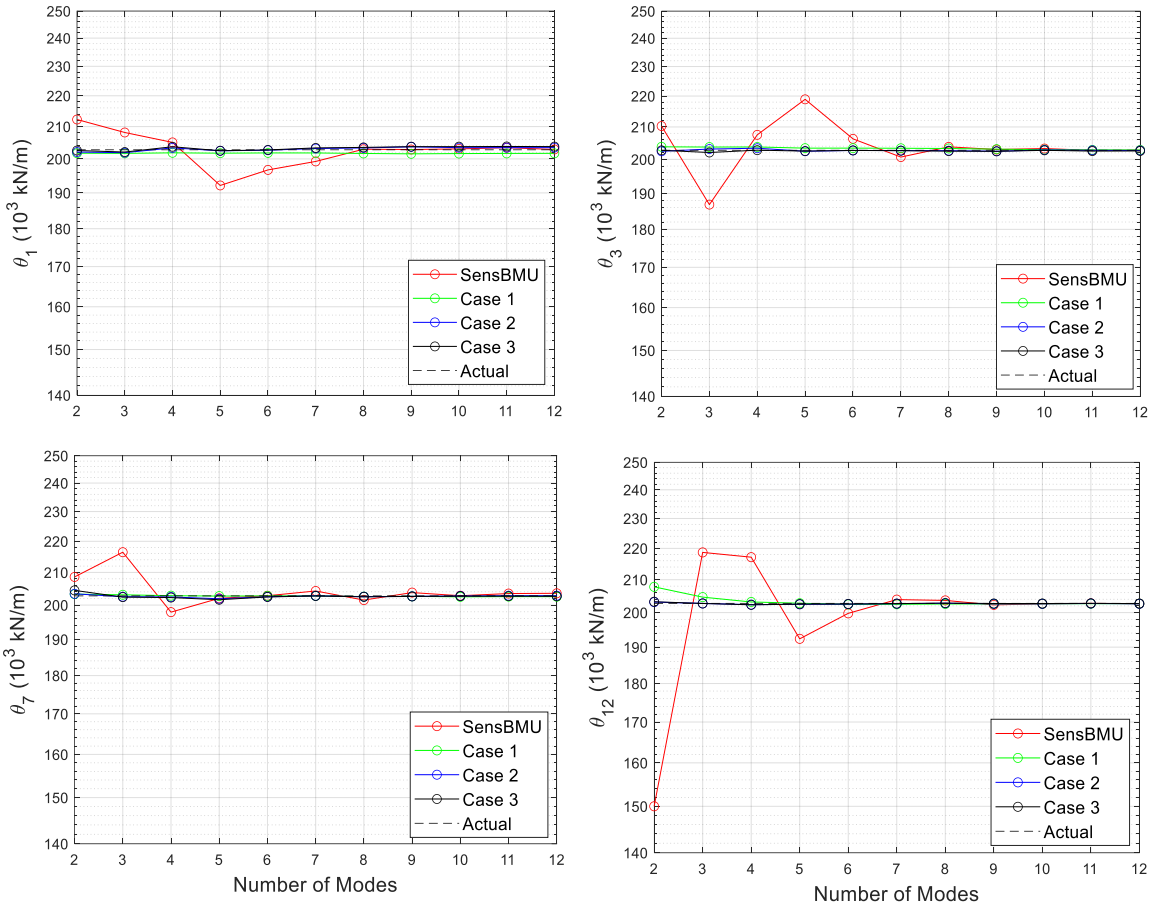

Figure 4.2. Convergence of some updated stiffness parameters with the number of considered modes

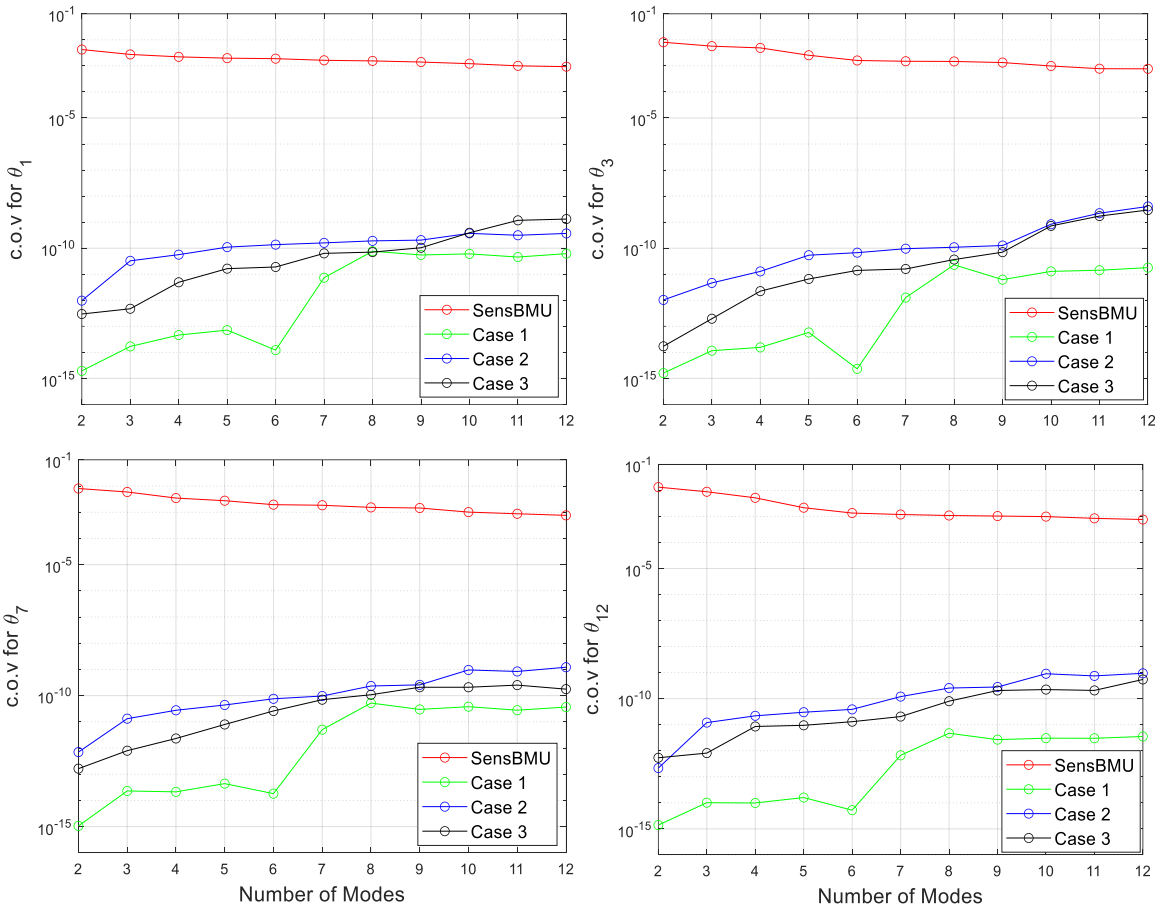

Figure 4.3. Variation of posterior c.o.v values of some stiffness parameters with the number of considered modes

To investigate the reasons of having too small posterior uncertainties, the order of the prior c.o.v values of eigen frequencies that are obtained in the modal identification stage is compared with the order of the posterior c.o.v values of the updated parameters. The comparison is presented in Figure 4.4. It should be noted that modal identification here has been performed by adding a noise level 50% of the RMS value of each noise-free response. As seen from the tables in the figure, they are actually found to be compatible with each other. This may be an answer to the question why such small posterior c.o.v values are encountered for the updated parameters.

	50% noise level			SensBMU		
Mode n	Eigen frequencies $\hat{f}_n$ (Hz)	Prior c.o.v ($\times 10^{-4}$)		Actual	Updated (Rel. Err.) (%)	c.o.v ($\times 10^{-4}$)
1	0.90	7.20	θ_1	202.767	0.30	9.35
2	2.69	9.36	θ_2	202.767	0.24	7.70
3	4.43	11.14	θ_3	202.767	− 0.01	7.73
4	6.11	16.42	θ_4	202.767	0.13	8.21
5	7.68	15.77	θ_5	202.767	− 0.26	7.97
6	9.14	16.95	θ_6	202.767	− 0.32	8.28
7	10.45	20.01	θ_7	202.767	0.42	7.62
8	11.60	23.51	θ_8	202.767	0.61	8.34
9	12.56	19.44	θ_9	202.767	− 0.24	8.24
10	13.33	21.24	θ_{10}	202.767	0.03	7.90
11	13.88	23.80	θ_{11}	202.767	− 0.02	7.58
12	14.23	28.44	θ_{12}	202.767	− 0.11	7.61

Figure 4.4. Comparison of the prior c.o.v levels of eigen frequencies and posterior c.o.v levels of the updated parameters

To question this hypothesis, the prior c.o.v values of the measured modal parameters are considered as in Yuen's study because Yuen defines a prescribed value of 0.01 for the prior c.o.v values (Yuen, 2010). He does not perform a modal identification. Instead, he adds a random noise directly on the actual modal parameter values by using the following relations;

$$\hat{f}_n = f_n(1 + c\,\varepsilon_n)$$
$$\hat{\phi}_{kn} = \phi_{kn}(1 + c\,\varepsilon_{kn}) \tag{4.99}$$

Here, ε_n and ε_{kn} represent the Gaussian random numbers from standard normal distribution and c denotes c.o.v of the noise level. The same procedure is used in the proposed methodology to make a comparison. Further, to investigate whether there is a problem in modal identification stage, modal identification is performed with a noise level of 300% so that the resulting prior c.o.v values are close to 0.01 as seen in Figure 4.5

	Yuen's original study	
Mode n	Eigen frequencies $\hat{f}_n$ (Hz)	Prior c.o.v
1	0.90	0.01
2	2.70	
3	4.41	
4	6.07	
5	7.65	
6	9.11	
7	10.42	
8	11.61	
9	12.55	
10	13.37	

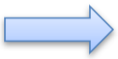

	SensBMU 300% noise level	
Mode n	Eigen frequencies $\hat{f}_n$ (Hz)	Prior c.o.v
1	0.90	0.002
2	2.68	0.003
3	4.43	0.004
4	6.12	0.006
5	7.68	0.008
6	9.14	0.011
7	10.47	0.010
8	11.57	0.016
9	12.59	0.018
10	13.41	0.015

Figure 4.5. Comparison of measured eigenfrequencies and prior c.o.v levels in Yuen's study and those obtained in modal identification stage of the proposed method.

The results are compared in Figure 4.6. Red line shows the model updating results when the prior variances are obtained by 300% noise level from the Bayesian modal identification. Blue line shows the results when the modal identification is not performed, and prior variances are taken directly as 0.01. As seen from the plots, all three cases gives the posterior c.o.v values of the parameters in the similar order and they are higher from the results of previous numerical example. Therefore, the reason of the resulting smaller c.o.v values could be just the low noise level of 50%. These results reveal that modelling error term may not be responsible for too small posterior c.o.v values because Yuen's formulations include the modeling error term.

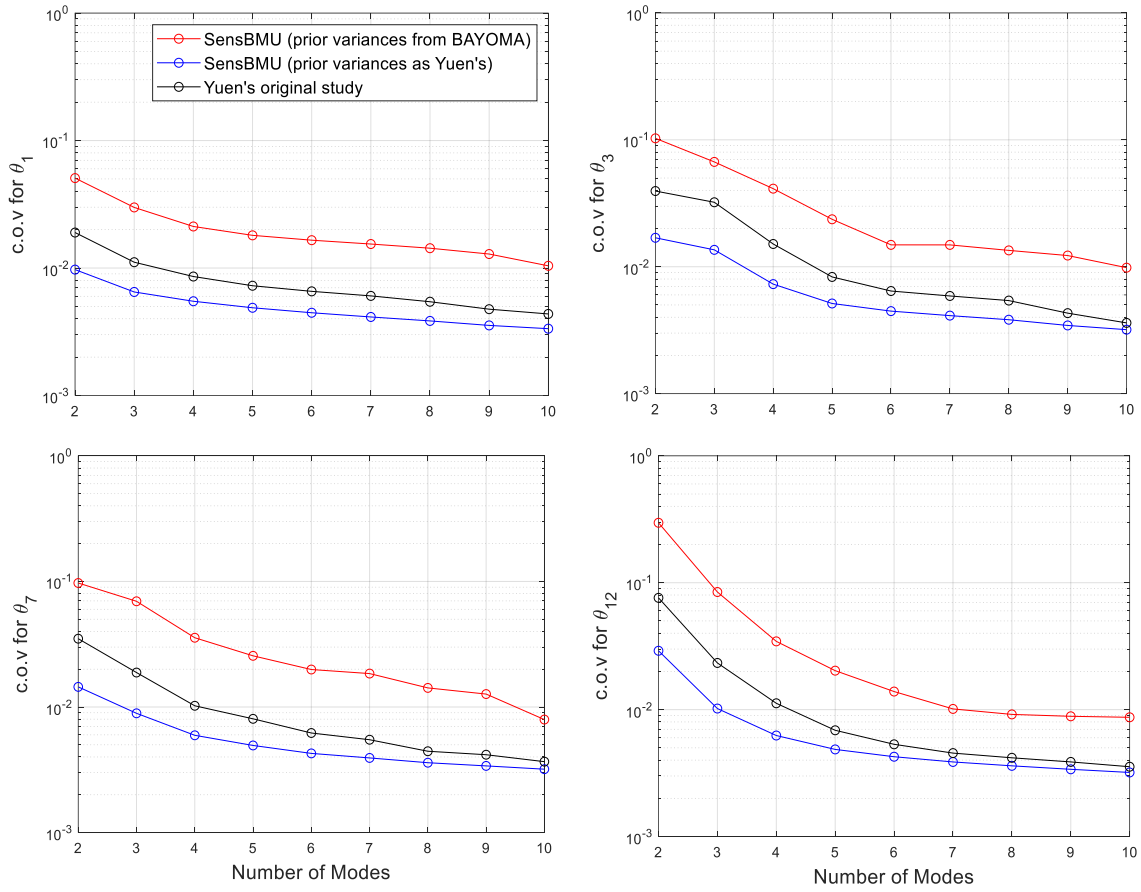

Figure 4.6. Comparison of the results of Yuen's original study and the proposed method (SensBMU)

4.2.6.2. Experimental Study

For the experimental study, presented methodology is applied on a 10-story physical shear frame laboratory model. The model is presented in Figure 4.7. The nominal mass and stiffness values obtained from the geometrical measurements are provided in the figure.

The model is measured by three piezo-electric accelerometers which have a 1000 mV/g sensitivity and 11.4 μg/$\sqrt{Hz}$ spectral noise density. A laptop with a 1.5 GHz CPU and Linux operating system, a 16-channel USB-DUX Sigma data acquisition device with a 24-bit A/D converter, a first-order analog lowpass filter with a cut-off frequency at 120 Hz for each channel have been used to acquire the measurements. The acceleration responses are acquired in five measurement setups with 1000 Hz sampling

frequency for five minutes duration. Then, the multiple setup data is merged with the proposed methodology in the published work by Ceylan et al. (2020) to have a single measurement including 10 DOFs.

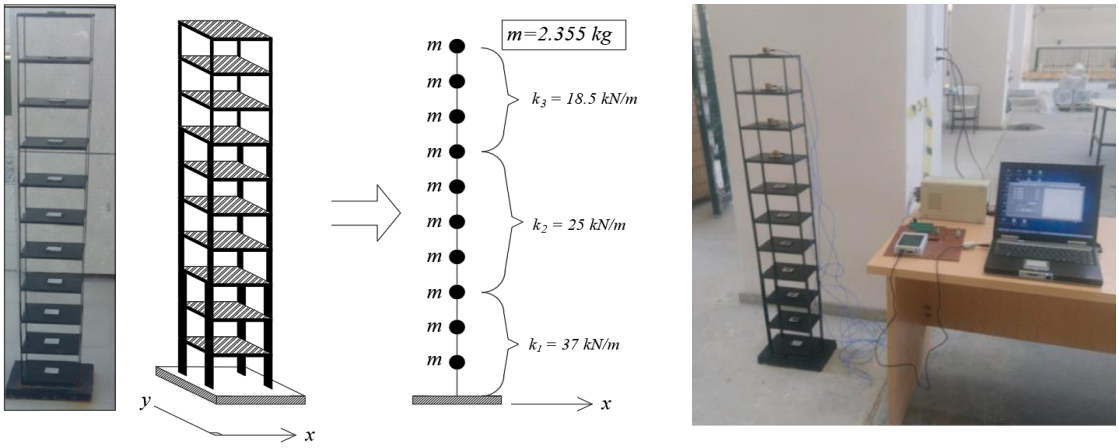

Figure 4.7. 10-story shear frame laboratory model

To construct the multiple initial FE models, a Gaussian distribution is defined for stiffness values with a prior c.o.v level of 50%. The nominal stiffness values are not considered different between stories, and it is selected uniform with a value of 30 kN/m. Lower bound is selected as 10 kN/m and upper bound is selected as 50 kN/m. The mass is also modelled as a Gaussian distribution with a prior c.o.v level of 5%. Lower bound is selected as 2 kg and upper bound is selected as 3 kg. Then, the optimization is repeated for 100 random initial FE models. The stiffness value of each story is selected as an updating parameter which makes as total of 10 stiffness parameters to be updated.

Table 4.4 provides the updating stiffness parameters and their c.o.v values for the 10-story shear frame model. The updating results can be considered to be reasonable when compared to the nominal values even though θ_1 and θ_7 have divergent values from the nominal ones. Besides, posterior c.o.v values are in similar order for all updated parameters.

Table 4.5 provides the eigenfrequencies of the updated FE model. Here, the first five modes are compared with the results in the work published by Hızal (2021) for the

verification purposes. It seems that the eigen frequency of the first mode is sligthly divergent only.

Table 4.4. Updated stiffness parameters and their posterior c.o.v values for the10-story shear frame laboratory model

		SensBMU		**Case 1 Previous Study**		**Case 2**		**Case 3**	
	Nom.	Updated (Rel. Err.) (%)	c.o.v (×10^{-4})	Updated (Rel. Err.) (%)	c.o.v (×10^{-10})	Updated (Rel. Err.) (%)	c.o.v (×10^{-8})	Updated (Rel. Err.) (%)	c.o.v (×10^{-8})
θ_1	37.5	31.2	3.21	15.6	2.13	6.7	16.35	8.2	45.62
θ_2	37.5	4.1	3.43	10.6	5.64	4.2	12.65	6.8	25.32
θ_3	37.5	− 9.2	1.65	2.3	7.96	− 12.3	8.32	12.7	12.69
θ_4	25	− 21.5	1.32	− 11.2	2.65	1.2	5.64	− 7.7	27.67
θ_5	25	9.0	2.60	− 0.2	7.63	5.6	3.69	8.6	31.81
θ_6	25	− 15.6	3.26	5.4	3.45	− 17.4	25.65	14.5	47.98
θ_7	25	− 31.2	1.82	− 12.8	15.46	− 16.8	3.24	− 20.2	17.59
θ_8	18.75	− 0.8	3.37	4.6	32.89	6.3	65.35	10.3	48.63
θ_9	18.75	− 2.3	1.16	− 7.1	6.58	− 10.9	21.27	− 15.7	14.54
θ_{10}	18.75	− 7.4	2.25	2.3	11.12	5.7	3.42	8.3	21.52

Table 4.5. Eigenvalues of the updated FE model of the laboratory frame

# Mode	Nominal	**BFFTA (Hızal, 2021)**	**SensBMU**		
			BFFTA		Upd.
			$\hat{f}_n$	c.o.v (×10^{-3})	
1	2.66	2.61	2.61	1.02	2.65
2	7.37	7.32	7.32	1.97	7.32
3	11.87	11.65	11.64	2.02	11.64
4	16.32	16.99	17.01	2.74	17.01
5	20.21	20.63	20.64	2.60	20.64
6	24.19	-	24.65	3.01	24.66
7	26.52	-	26.94	2.85	26.94
8	29.10	-	29.92	3.13	29.92
9	31.58	-	33.53	2.79	33.53
10	37.01	-	37.58	10.25	37.58

Figure 4.8 presents the updated modal shape vectors and they are compared with the measured ones. It is seen that some modes are not in very well agreement. However, most of the mode shapes are in an acceptable condition.

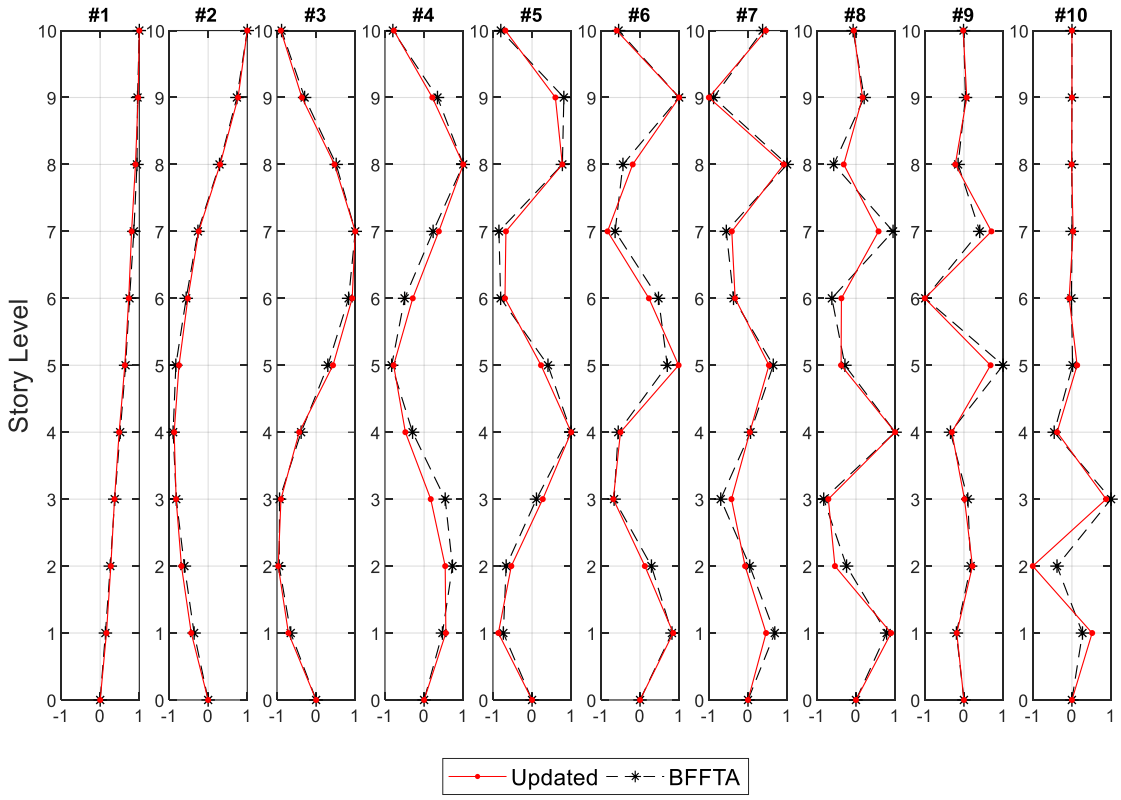

Figure 4.8. Updated mode shape vectors of the laboratory model

4.3. Conclusions

This chapter focuses on the reasons of the unreasonably small posterior uncertainties of the updated parameters that are obtained in the previous chapter. In the previous one, modelling error term is employed to account for the uncertainties in the eigenvalue equation which arise due to using system modes. Formulation has been performed by assuming the modelling error variances of eigenvalue equations to be different for each mode and updated in each iteration. Besides, formulations derived by Hızal (2019) which assumes a single modelling error variance for all modes are investigated as the second assumption. Yuen (2010) considers the modelling error variance as a rigid constraint and assigns a prescribed value for the modelling error variance and does not update it.

Results of the previous chapter have revealed that the formulations with the three modelling error assumptions give unreasonably small posterior c.o.v values. On the other hand, it is realized in the literature that researchers who use a norm constraint

term in the objective function generally face relatively small posterior uncertainties for the updated parameters (Yan and Katafygiotis, 2015; Hızal, 2019; Hızal and Turan, 2020). As a result, it is considered that underlying solution to avoid too small posterior uncertainties may be somehow removing the modelling error and/or the norm constraint terms from the formulations. In this context, in this chapter, Bayesian model updating framework is combined with a sensitivity-based model updating approach. By doing so, modal properties of the FE model are directly employed instead of system modes which are the sources of the modelling errors in the eigenvalue equations. Besides, using the FE model modes automatically removes the need for the norm constraint for the mode shapes since they can be directly obtained from the eigenvalue analysis of the updated system. In this case, eigen frequencies and mode shapes should be dependent on the parameters to be updated. This results in a closed-form non-linear objective function of updating parameters. Optimization of such an objective function has been required numerical optimization algorithms. Therefore, in the present study, sensitivity equations which account for the changes in the parameters have been derived in a probabilistic way by introducing the Bayesian model updating framework and posterior uncertainty analysis are performed by using the derived Hessian matrix of the updated parameters.

The results of the numerical study reveal that the presented two-stage sensitivity-based Bayesian model updating procedure significantly increases the posterior c.o.v values of the updated parameters to more reasonable levels when compared to the results of the previous chapter. Formulation of Case 3 in the previous study does not include the norm constraint term as in the present study and it also gives unreasonably small posterior c.o.v values. Therefore, it is concluded that modelling error term may be responsible for the small uncertainties. Of course, it should be kept in mind that the formulations of the present study and Case 3 are different from each other and therefore removing the modelling error term may not be the only reason for the increase in posterior uncertainties of the updated parameters. Further, it is observed that posterior c.o.v of the updated parameters decrease with the increased number of considered measured modes as expected and stated in the literature. On the other hand, if the updated parameter value is divergent from the actual value, its posterior uncertainty is relatively high when compared to the convergent ones. These may be considered as a proof to interpret the resulting uncertainties as reasonable. Even so, the resulting posterior c.o.v values are still small numbers which may be considered as unrealistic if the updated parameters diverge from the actual values.

CHAPTER 5

PROBABILSTIC DAMAGE DETECTION OF STRUCTURES

5.1. Introduction

Damage detection means identifying the differences between two states of a structure and making comparisons of these two states (Torres, 2017). Generally, the initial state is called “undamaged state” and the other states are called “damaged states”. In order to make a comparison between these two states, it is required to observe a structure for a period of time (i.e., acquisition of measurements from the structure), evaluation of damage-sensitive features and examination of these features. According to Farrar et al. (2001), the damage identification process involves four steps which are operational evaluation, data acquisition, feature extraction and classification. In operational evaluation, implementation of the process, operational and environmental conditions, and limitations are analyzed. In data acquisition, measurement types and its duration, types of sensors and their locations, and type of data which is necessary to extract damage sensitive parameters are determined. In future extraction step, damage sensitive features are evaluated and in classification step, comparison between the initial and current states is performed.

5.1.1. General Description of Dynamics of a Damaged System

The dynamics of a general non-linear, time-varying damaged structure is described by Fritzen and Kraemer (2009) as

$$\mathbf{M}(\theta, E, \mathbf{u}, t)\ddot{\mathbf{u}} + \mathbf{F}(\theta, E, \mathbf{u}, \dot{\mathbf{u}}, t) = \boldsymbol{F}_{op}(t) + \boldsymbol{F}_{test}(t) \tag{5.1}$$

$$\dot{\theta} = \mathbf{g}(\theta, E, \mathbf{u}, \ddot{\mathbf{u}}, t) \tag{5.2}$$

where **M** is the mass matrix, **F** is the force vector of elastic and inelastic forces, damping forces depending on the displacements **u**, the velocities $\dot{\mathbf{u}}$ and the time *t*. θ

represents a damage parameter (such as crack length or loss in stiffness, etc.) and E represents the influence of environmental and operational conditions on the equation of motion (such as temperature, humidity, etc.). The external force vector, $\boldsymbol{F}$ is divided into two parts which are operational loads, $\boldsymbol{F}_{op}$ and test loads, $\boldsymbol{F}_{test}$. For example, there is no test load developing during ambient vibration tests and therefore it is zero in that case. Equation (5.2) represents the fundamentals of the damage detection process. **g** is a non-linear function for the evaluation of the change in damage parameter, θ. Therefore, equation (5.2) projects into the future in each step and give information about the remaining service life. However, due to the statistical variations in measurements, assumptions and uncertainties in the future loads and damage propagation models, the estimation of remaining service life is not an easy task, and it is a probabilistic problem rather than the deterministic one. Further, Fritzen and Kraemer (2009) state that the evaluation of damage and the dynamic response of structures have different time scales. The propagation of damage in structures is a relatively slow process with respect to vibration measurements of structures. Therefore, during a damage detection process, investigated damage parameter θ is assumed to be unchanged.

The damaged dynamic response of the structure, $\mathbf{q}(t)$ can be described as

$$\mathbf{q}(t) = \mathbf{d}(\theta, E, \mathbf{u}, \ddot{\mathbf{u}}, t) \tag{5.3}$$

This equation relates the internal model parameters with the output variables such as measured strains or accelerations, etc. Similarly, transformation of the input signals, $\mathbf{x}(t)$ into the forces can be represented as

$$\boldsymbol{F}_{test}(t) = \mathbf{d}(\theta, E, \mathbf{x}(t)) \tag{5.4}$$

Here, $\mathbf{x}(t)$ may represent the action of ambient excitation, impact hammer and controlled forces. In equations (5.3) and (5.4), damage parameter θ includes any sensor or actuator failure. Although above descriptions seem like a direct solution to obtain the damage parameter θ, this parameter cannot be obtained directly. Instead, changes in the dynamic response are investigated in the damage detection process and the results are linked to the damage parameter. To do so, the damaged dynamic response of the system, $\mathbf{q}(t)$ is compared with an earlier measured baseline response, $\mathbf{q}_0(t)$ which corresponds to the undamaged state of the system. The difference between $\mathbf{q}(t)$ and

$\mathbf{q}_0(t)$ arises due to the parameters of damage, θ and operational and environmental conditions, E. In the literature, this is known as the forward problem and it is described as

$$\Delta\mathbf{q} = \mathbf{q} - \mathbf{q}_0 = \boldsymbol{f}(\theta, E) \tag{5.5}$$

However, in the damage detection process, damaged response, $\mathbf{q}$ and the initial response $\mathbf{q}_0$ are known and damage parameter, θ is tried to be obtained. Therefore, damage detection is an inverse problem and described as

$$\theta = \boldsymbol{f}^{-1}(\Delta\mathbf{q}, E) \tag{5.6}$$

The difficulty in solving this inverse problem arises because the solution is not unique due to the incomplete measurement data or inconsistent solutions because of the measurement noise level. The aim of damage detection is to maximize the correlation between the damage parameter, θ and the selected damage feature. In damage detection process, time responses $\mathbf{q}(t)$ and $\mathbf{q}_0(t)$ are not directly used; instead, dynamic characteristics from frequency domain $\mathbf{q}(\omega)$ or modal domain $\mathbf{q}(\omega_n)$ are extracted to have a lower dimensional parameter space. Minimization of the parameters leads to a linear or non-linear optimization problem to be solved. In addition, selection of the proper damage sensitive features is an important task. However, numerous possible damage patterns may occur in the structures and numerous damage sensitive features are available. Therefore, damage detection is a problem-dependent process and there is no individual methodology to solve all damage detection problems, which makes selection of a proper approach disputable (Fritzen and Kraemer, 2009).

5.1.2. A General Literature Review on the Damage Detection Methods

There are numerous damage detection methods in the literature which have advantages and disadvantages based on the area of their utilization. Therefore, damage detection techniques can be classified from many different points of views, and they have various subbranches. In Table 5.1**,** some of the classifications of these techniques have been presented with their explanations.

Damage detection of structures can be performed in conjunction with on-line and off-line structural health monitoring (SHM) techniques. An on-line SHM technique means the monitoring of structures during operation of the structure and an off-line SHM technique means the monitoring of structures during maintenance. Non-destructive testing methods are the most attractive ones among the damage detection techniques since they can be applied with on-line SHM methods which enables damage assessment of structures under service. At the present time, ongoing developments in technology of sensors, data acquisition systems and the computer processor capacities make it possible to deal with large amount of data, which makes vibration-based damage detection methods very attractive among the non-destructive testing methods. Such statistics based damage detection techniques are preferred over visual inspection and localized experiments (Mahmood et al., 2014).

Table 5.1. Classification of damage detection techniques

Classification	**Types**	**Explanation**	**Reference**
Performance to detect damaged state	Existence	determines whether the damage exists in the structure or not	Rytter, 1993
	Location	determines the location of the damage	
	Type	determines the type of the damage	
	Extension	determines the severity of the damage	
	Prognosis	determines remaining service life of the structure	
Inspection	Local	a local part of the structure is analysed	Fritzen and Kraemer, 2009
	Global	the whole structure is analysed	
Model or non-model based	Model based	results are compared with those obtained from an analytical model	Ooijevaar, 2014
	Non-model based	comparison of damage sensitive parameters obtained from two different measurements of the structure	
Baseline or non-baseline	Baseline	response of the structure measured at earlier stage is used to compare damaged and undamaged states	Worden et al., 2007
	Non-baseline	current response of the structure is compared with the expected behaviour of the structure	

The main idea behind the vibration-based damage detection methods is that the dynamic behavior of a structure changes if the structure experiences any damage (Ooijevaar, 2014). Damage in a structure affects the physical properties of the structure such as mass, stiffness and damping. Any change in these physical properties directly affects the dynamic behavior of the structure which is a function of the mentioned physical properties. The dynamic behavior of a structure gives the information about the damage in a structure. It can be expressed in time, frequency and modal domain. Therefore, vibration-based damage detection techniques also have many subbranches that gather under three main categories which are time, frequency and modal-based methods. The first studies on vibration-based damage detection was on the natural frequency or modal damping change with the structural damage (Cawley and Adams, 1979). This was one of the first modal-based damage detection techniques. Now, researchers also focus on the statistical time series methods such as cross-correlations in time domain, and enhanced signal processing methods such as Wavelet and Hilbert transforms in frequency domain. Different methods are classified based on their approach to the damage detection problem such as detecting changes in modal frequencies, mode shapes or structural flexibility, damage index method, modal residual vectors method, etc. Besides, matrix update methods, nonlinear methods, computational intelligence methods such as neural networks and genetic algorithms are also available in the literature. These methods are also known as data-based damage identification methods. Some of these methods are discussed in the following paragraphs.

The existence of damage in a structure changes its natural frequencies. Since the measurements of frequencies are quick and practical, it is very often used in damage detection of structures. Measured frequencies are compared with those obtained from the undamaged state of the structure or those obtained from the analytical model of the structure.

In the late seventies, Cawley and Adams (1979) presented one of the first types of frequency change methods in damage detection. They compared the ratios of the natural frequencies obtained from response measurements with those obtained from the analytical model. They stated that the existence of damage was revealed immediately by checking the natural frequency changes without any computations. Kim et al. (2003) proposed a method to estimate damage in structures using a few natural frequencies. They state that the frequency change method is preferred due to the simplicity in its measurement. However, the usage of natural frequencies in damage detection is very

limited. Their reason for this is that severe damage may result in significantly low changes in natural frequencies and the errors in ambient measurements can cause significant uncertainty in frequencies. In addition, Farrar and Cone (1994) have observed that a significant change in natural frequencies occurs just after the final stage of the structural damage and they have concluded that it is too late to prevent the structure from failure when the damage is detected by changes in natural frequencies. Therefore, more sensitive methods have been searched in the literature.

After realizing that the natural frequency observations cannot give a detailed and early damage information, researchers have focused on using changes in mode shapes. Modal shapes have found to be much more sensitive to damage. Mode shapes are also found to be sensitive to local damage while frequency change gives a global information. Salawu and William (1995) worked on a reinforced concrete bridge and studied on the damage-detection sensitivity of natural frequencies, damping values, frequency response functions and mode shapes. They used a modal assurance criterion (MAC) to investigate the mode shape quality. They investigated that MAC values obtained from mode shapes showed significant change in case of damage and concluded that investigation of mode shapes is more reliable than investigating the shifts in natural frequencies. Moreover, mode shapes can give information about the location of the damage. However, as Kim et al. (1993) explained, there are some reasons to discuss the feasibility of using mode shapes as damage sensitive parameters. Since the large structures generally faces a local damage rather than a global one, mode shapes of the lower modes may not be affected by the damage. Further, mode shape identification is very sensitive to the random errors induced by measurement noise or human interference. Number of sensors and sensor locations also have an influence on the quality of the identified mode shapes.

Another approach is to use modal shapes curvatures as damage indicators. Mode shape curvature for a beam can be estimated numerically from mode shapes. It is known from the basic engineering knowledge that the curvature is inversely proportional to the flexural stiffness of the beam. The curvature is also the second derivative of the bending deflection. Therefore, any damage affects the flexural stiffness, and so the bending deflection. Reduction in the stiffness increases the curvature of the mode shapes. Change of mode shape curvature gives information about the location of the damage. Further, the extent of the damage can be predicted by investigating the amount of change in the mode shape curvature (Than Soe, 2013). Maeck and De Roeck (2000)

arrived the conclusion in their study that using modal curvatures gives more sensitive results in local damage identification than using the modal displacements.

Damage in a structure can be estimated by observing the change in the flexibility matrix (Jaishi and Ren, 2006). Investigating the difference between the flexibility matrices before and after damage, damage and its location can be estimated by checking the largest value among the columns of the difference matrix. Farrar and Doebling (1999) compared the change in flexibility, mode shape curvature methods and strain energy and reached the conclusion that strain energy-based methods was the most successful ones in detecting damage. As concluded in the natural-frequency-change methods, it is concluded that stiffness and flexibility of the system result in a change in case of severe damage. Further, these methods generally assume that mass matrix of the system is not affected by damage.

Another method is the damage index method which is also known as modal strain energy method. In this method, modal strain energy is compared for undamaged and damaged states. According to Carden and Fanning (2004) and Humar et al. (2006), the modal strain energy, $\mathbf{SE}_i$, in an Euler-Bernoulli beam for a certain mode can be calculated as

$$\mathbf{SE}_i = \frac{1}{2}\int_0^l EI\left(\frac{\partial^2 \phi_i}{\partial x^2}\right)^2 dx \tag{5.7}$$

When the beam is split into the elements, the strain energy in an element for a certain mode is calculated as

$$\mathbf{SE}_{ij} = \frac{1}{2}\int_j^{j+1} EI\left(\frac{\partial^2 \phi_i}{\partial x^2}\right)^2 dx \tag{5.8}$$

where j and j+1 define the limits of element j. Strain energy of each element is related with the strain energy of the whole beam for a certain mode by using the fractional strain energy $\mathbf{FSE}_{ij}$ which is defined as the ratio of the element strain energy $\mathbf{SE}_{ij}$ to the beam strain energy $\mathbf{SE}_i$. Similar expressions can also be defined for damaged case. The comparison of the differences between the fractional strain energies gives information about the location of the possible damage. Farrar and Doebling (1999) used this damage indicator on a bridge and compared it with the other damage detection methods. They revealed that modal strain energy method gives more successful results than the change

in mode shape curvature. They also concluded as the disadvantage of this method that detection of damage would be impossible if the damaged member does not significantly contribute to the strain energy of the estimated modes.

In the literature, there are numerous damage detection methods based on computational intelligence. Torres (2017) has classified these methods in five groups which are neural networks, support vector machine, fuzzy inference, metaheuristic algorithms and hybrid methods. According to Yu and Xu (2011), the computational intelligence methods based on a constrained optimization problem has been considered as the most successful ones.

Chang et al. (2000) employ an iterative neural network to detect various damage scenarios for a clamped-clamped T-beam and successfully identified location and extent of damages in the beam. Chandrashekhar and Ganguli (2009) employed a fuzzy logic system to estimate changes in modal curvatures. Numerical simulations of the finite element model of a cantilever beam showed a good estimation of structural damage. Mares and Surace (1996) detected the location and extent of the damage in beams and trusses using the classical genetic algorithm. Boonlong (2014) used a cooperative coevolutionary genetic algorithm to detect damages in beams by using vibration measurements. Yu and Xu (2011) used an ant colony optimization technique to detect damages of two and three-story building models. Zhu et al. (2017) used a bird mating optimizer algorithm to identify damages in structures. They minimized the differences between the measured and analytical natural frequencies of damaged and undamaged states. Many more researchers have used metaheuristic-based methods in structural damage identification. Swarm intelligence (Yu et al., 2012), Big bang-big crunch (Tabrizian et al., 2013), Global artificial fish swarm algorithm (Yu and Li, 2014) and Firefly algorithm (Pan and Yu, 2015) are some of these techniques studied in the literature. Furthermore, hybrid algorithms which means the usage of a combination of several optimization algorithms have been used by many researchers. Rao and Anandakumar (2007) performed a combination of a particle swarm algorithm and the nelder-mead algorithm to obtain the optimal locations of sensors for SHM. Sandesh and Shankar (2010) used a hybrid of particle swarm algorithm and genetic algorithm on a thin plate to detect multiple crack damages. They used a finite element model for comparison. Identification was performed by minimizing the difference between measured and estimated time-domain acceleration data. Fatahi and Moradi (2018) employed particle swarm algorithm with multi-elitist artificial bee colony to detect

multiple cracks in the frames using a limited number of measured natural frequencies. Torres (2017) proposed some hybrid algorithms to improve the effectiveness of the methods. In his study, multi-particle collision algorithm with Hooke-Jeeves which is already a hybrid algorithm was used with opposition, center-based sampling or rotation-based sampling. He also proposed a hybrid algorithm by combining q-gradient and Hooke-Jeeves algorithms. He verified his proposed damage detection methods on numerical models and different experimental structures, concluding good estimations of location and severity of damage even if some false positive results were obtained.

5.2. Probabilistic Damage Detection Measure

In the literature, only the relative changes in MPVs of the stiffness parameters from the undamaged condition are generally investigated for the purpose of damage detection. However, investigating the relative changes only does not involve the calculated uncertainties for the stiffness parameters. Therefore, a probabilistic damage detection measure, which is already proposed in the literature, has been used in the present study to obtain the relative change in the stiffness parameters in a probabilistic framework.

Vanik et al. (2000) define the probability that the i^{th} parameter of the possibly damaged condition is less the i^{th} parameter of the undamaged condition as

$$\begin{aligned} P_i^{dam}(d_i) &= P(\theta_i^{pd} < (1 - d_i)\theta_i^{ud} \mid \mathbf{D}_{ud}, \mathbf{D}_{pd}) \\ &= \int_{-\infty}^{\infty} P(\theta_i^{pd} < (1 - d_i)\theta_i^{ud} \mid \mathbf{D}_{ud}, \mathbf{D}_{pd}) P(\theta_i^{ud} \mid \mathbf{D}_{ud}, \mathbf{D}_{pd}) d\theta_i^{ud} \end{aligned} \tag{5.9}$$

where d_i is the damage extent defined for the i^{th} parameter in the interval of [0 , 1], θ_i^{ud} and θ_i^{pd} are the stiffness scaling parameters of the undamaged and possibly damaged conditions for the i^{th} parameter, respectively. $\mathbf{D}_{ud}$ and $\mathbf{D}_{pd}$ represent the sets of the measured data obtained from the structure in its undamaged condition and its later condition, which is possibly its damaged condition, respectively. Vanik et al. (2000) have defined $P_i^{dam}(d_i)$ as the probabilistic damage measure and it shows the probability of the decrease in parameter θ_i with the damage extent d_i compared to the undamaged condition.

Calculation of the damage measure defined in equation (5.9) requires the marginal posterior PDF, $p(\theta_i^{ud} \mid \mathbf{D}_{ud})$ (or $p(\theta_i^{pd} \mid \mathbf{D}_{pd})$ for a possibly damage condition), of each updated stiffness parameter θ_i. However, the posterior PDF which is obtained in equation (4.5) is the joint PDF of all the updated parameters in the parameter space. Therefore, $p(\boldsymbol{\theta} \mid \mathbf{D})$ given in equation (4.5) must be integrated over the whole parameter space to obtain the posterior marginal PDF of the individual stiffness parameter θ_i.

For the later definitions, the parameter vector $\boldsymbol{\theta}$ is decomposed as $\boldsymbol{\theta} = [\theta_i \quad \boldsymbol{\theta}^{i-}]^{\mathrm{T}}$ where $\boldsymbol{\theta}^{i-} = [\,\theta_1, \theta_2, \ldots., \theta_{i-1}, \theta_{i+1}, \ldots., \theta_{N_\theta}]$. Then, the PDF $p(\boldsymbol{\theta} \mid \mathbf{D})$ can be written as $p([\theta_i \quad \boldsymbol{\theta}^{i-}]^{\mathrm{T}} \mid \mathbf{D})$. Then, the marginal PDF of the parameter θ_i can be defined as

$$P(\theta_i \mid \mathbf{D}) = \int P(\left[\theta_i \quad \boldsymbol{\theta}^{i-}\right]^T \mid \mathbf{D})\, d\boldsymbol{\theta}^{i-} \tag{5.10}$$

Here, $p([\theta_i \quad \boldsymbol{\theta}^{i-}]^{\mathrm{T}} \mid \mathbf{D})$ is integrated over the parameter space $\boldsymbol{\theta}^{i-}$. However, this integration generally cannot be performed analytically (Vanik et al., 2000). Therefore, various numerical sampling methods are developed in the literature to handle this integration such as Metropolis-Hasting sampler and Gibbs sampler defined under the Markov Chain Monte Carlo samplers (Lye et al., 2021). However, these sampling methods are not introduced in this present study. Instead, the asymptotic expansion that is developed by Papadimitriou et al. (1997) is employed to approximate the integral. They develop this asymptotic approximation for a joint PDF that has a single peak point at the MPVs of the parameters by using Laplace's method. The final form of this approximation is provided as

$$P(\theta_i \mid \mathbf{D}) \approx \varphi\left(\frac{\theta_i - \hat{\theta}_i}{\hat{\sigma}_i}\right) \tag{5.11}$$

where φ represents the standard normal PDF, $\hat{\theta}_i$ is the MPV of the stiffness parameter θ_i and $\hat{\sigma}_i$ is the posterior standard deviation of θ_i.

Vanik et al. (2000) have estimated the integral in equation (5.9) by using the Gaussian asymptotic approximation provided in equation (5.11) as

$$P_i^{dam}(d_i) \approx \Phi\left(\frac{(1-d_i)\hat{\theta}_i^{ud} - \hat{\theta}_i^{pd}}{\sqrt{(1-d_i)^2(\hat{\sigma}_i^{ud})^2 + (\hat{\sigma}_i^{pd})^2}}\right) \quad (5.12)$$

where Φ represents the standard normal cumulative distribution function (CDF).

5.3. Applications on the IASC-ASCE Benchmark Problem

The formulations provided in Chapter 3 and 4 are applied on the FE models which are simple with a low damping ratio and have no modelling error. Therefore, c.o.v. of the updated parameters have still relatively low small values, and it has been concluded that this problem may stem from the FE models used in the numerical applications. Besides, previous chapters just focus on the estimation of most probable values of the parameters and no study is performed for a probabilistic damage identification. Therefore, in this chapter, the algorithms developed in Chapter 3 and 4 are applied on a benchmark problem that is designed by the IASC-ASCE Structural Health Monitoring (SHM) Task Group in the early 2000s. This benchmark problem includes different cases with various damage scenarios, which gives a chance to take the formulations a step further from parameter estimation to a damage detection process. This is one of the main objectives of this chapter.

The benchmark structure is a four-story, two-bay by two-bay quarter-scale steel frame model tested in the Earthquake Engineering Research Laboratory at the University of British Columbia.

The benchmark problem has been designed to be investigated in two phases (Phase-I and Phase-II). Each phase includes numerical models and experimental parts, and the IASC-ASCE SHM Task Group have provided all the analytical models and experimental data on the benchmark website in 2000s. Unfortunately, the benchmark website is not active today. However, FE analysis codes for Phase-I and the experimental data obtained for Phase-II are available on the website of Network for Earthquake Engineering Simulation (NEES) Database for Structural Control and Monitoring Benchmark Problems.

In Phase-I, In Phase-I of the benchmark problem, a 12-DOF shear building model and a 120-DOF model of the structure are constructed by the Task Group. Due to oversimplified assumptions in the analytical models, however, researchers do not

consider the discrepancies between FE models and the experimental structure in this phase (Das and Saha, 2018). Researchers deal with only the simulated data to study on various types of damage, effects of sensor noise, etc. Therefore, this phase is considered just as an analytical study in the literature and the experimental part of Phase-I is used to obtain some preliminary results to set up Phase-II. In Phase-II, the FE model provided by the group is open to modifications, which gives an extra flexibility to the researchers to analyze damage scenarios. Therefore, this phase is considered as the experimental part of the benchmark problem in the literature. Unfortunately, FE analysis codes of this phase are not available.

In the present study, as researchers do in the literature, Phase-I is investigated as a numerical study and Phase-II is investigated as an experimental study. Phase-I includes different cases for simulations and each case includes various damage scenarios. The cases include either a 12-DOF shear building model or a more complex 120-DOF model This gives a chance to analytically investigate the effect of modelling error in the updating process. This compensates another main objective of the present study since no modelling error exists in the previous chapters.

The experimental Phase-II also includes various damage scenarios that are induced on the physical structure. This phase has given a chance to deal with higher modelling error levels since there exists significantly higher uncertainties between the actual structures and their mathematical models.

In this chapter, a comparative study is also performed to investigate the effects of modelling error on the MPVs and the posterior uncertainties of the updated parameters by using the formulations developed in Chapter 3 by using system modes concept, and by using the sensitivity-based Bayesian model updating procedure developed in Chapter 4. The results are also compared with those available in the literature for the same benchmark problem.

The methodologies proposed in the previous two chapters are applied on the benchmark problem. Figure 5.1 shows the benchmark structure, which is a four-story, two-bay by two-bay quarter-scale steel frame model. The structure has a 2.5 m × 2.5 m floor plan with a total height of 3.6 m. All members are made of hot-rolled 300 W grade steel with a nominal yield strength of 300 MPa. All columns are oriented to be stronger in the x direction and all beams are oriented to be stronger in the vertical z direction (Johnson et al., 2004). There are two braces on each outer face of each floor, which

makes a total of eight bracings for each floor as shown in Figure 5.1. Table 5.2 provides section properties of the structural members.

Table 5.2. Properties of Structural Members

(Source: Johnson et al., 2004)

Property	Columns	Beams	Braces
Section type	B100×9	S75×11	L25×25×3
Cross-sectional area, A (m^2)	1.133×10^{-3}	1.43×10^{-3}	0.141×10^{-3}
I_y - strong direction (m^4)	1.97×10^{-6}	1.22×10^{-6}	0
I_x - weak direction (m^4)	0.664×10^{-6}	0.249×10^{-6}	0
Torsion constant, J (m^4)	8.01×10^{-9}	38.2×10^{-9}	0
Young's modulus, E (Pa)	2×10^{11}	2×10^{11}	2×10^{11}
Shear modulus, G (Pa)	0.77×10^{11}	0.77×10^{11}	0.77×10^{11}
Mass per unit volume, ρ (kg/m^3)	7800	7800	7800

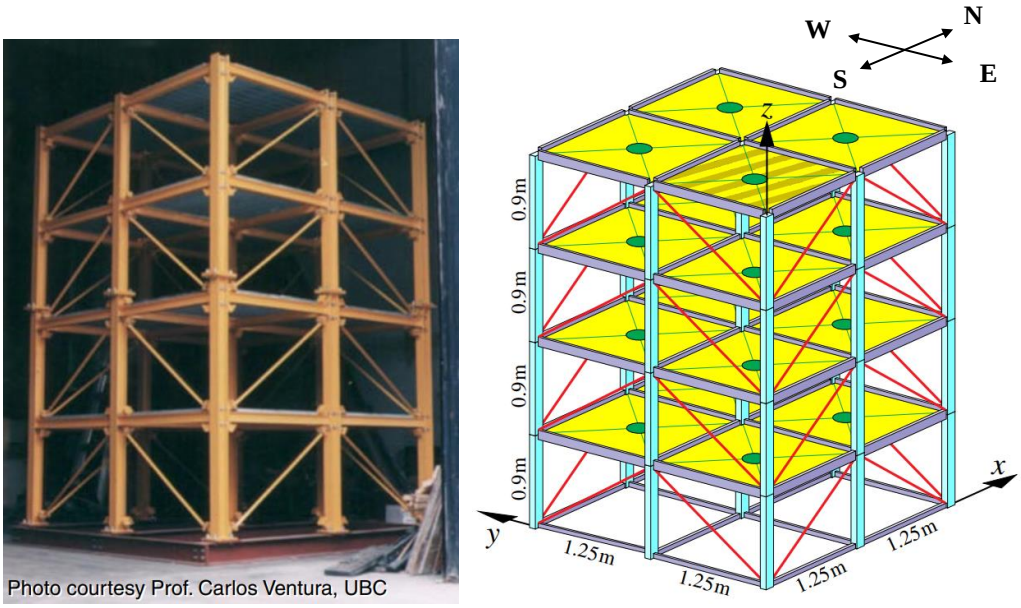

Figure 5.1. IASC-ASCE Benchmark Model Structure

(Source: Johnson et al., 2004)

5.3.1. Numerical Studies: Phase-I of the IASC-ASCE Benchmark Problem

In this section, Phase-I of the IASCASCE Benchmark problem is investigated in detail to introduce the probabilistic damage detection.

5.3.1.1. Description of the Benchmark Problem: Phase-I

Phase-I of the benchmark problem is explained in detail in the paper published by Johnson et al. (2004). In this section, information necessary to describe this phase is extracted from their publication.

In this phase, two FE models are constructed by the task group to simulate the response data and these models with all the FE analysis codes are provided to the researchers in the MATLAB environment. The first one is a 12-DOF model which is constructed by shear building assumptions. The model has two translational DOFs in the *x* and *y* directions assuming the floors move as rigid diaphragms, and one rotational DOF about the center column, which makes a total of 3 DOFs per floor. All other motions are constrained.

The second one is a 120-DOF model that assumes the translations in the *x* and *y* directions, and rotation about the center column for all nodes in each floor to be equal. This makes the floors rigid for the in-plane motions. All the remaining out-of-plane motions (translation in the *z* direction, rotations about *x* and *y* axes) are not constrained, which results in 30 DOFs per floor. This model is more complex than the 12-DOF model. Thus, it gives researchers an opportunity to investigate the modelling error effects between these two models as encountered in real life. To this end, Johnson et al. (2004) recommend that the 120-DOF model should be used to simulate response data as if measuring an actual structure and the12-DOF model can be used as the identification model to account for the modeling error between the analytical models.

Phase-I includes six different cases for simulations. Cases are generated to have either the 12-DOF or 120-DOF model to simulate response data, a different excitation scenario, symmetric or asymmetric mass distribution on the top floor, etc. Table 5.3 defines the properties of each case. For all cases, there are four slabs on each bay of each floor. There are four 800 kg slabs at the first floor, four 600 kg slabs at the second

floor and third floor. For Cases 1, 2 and 3 with a symmetric top floor mass distribution, there are four 400 kg slabs at the fourth (top) floor. For Cases 4, 5 and 6 with asymmetric top floor mass distribution, there are three 400 kg slabs and one 550 kg slab (shaded slab in Figure 5.1) at the fourth (top) floor. In the provided FE analysis codes, mass matrix is modeled with lumped mass assumptions for both 12-DOF and 120-DOF models.

The models in Case 1 and Case 2 are excited with independent loadings on the center column at each floor level in *y* direction only and those in Case 3, 4, 5 and 6 are excited at the center column of the top floor in the *x* and *y* directions. For all cases, excitations are modeled as independent Gaussian white noise processes filtered by a sixth order low-pass filter with a cut-off frequency of 100 Hz.

Measurements are assumed to be acquired as acceleration response data at the middle column of each outer face of each floor, which results in a total of 16 measurement locations. Figure 5.2 illustrates these measurement points on each floor for Cases 1 to 5. In Case 6, the second and fourth floor are assumed to be measured only to simulate incomplete sensor data scenario.

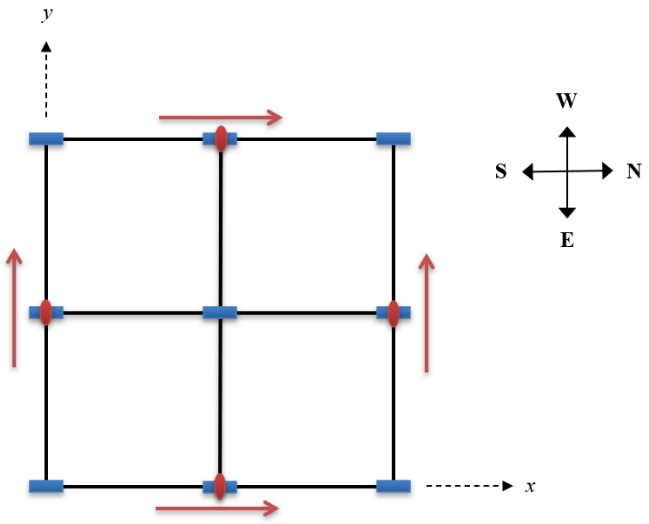

Figure 5.2. Measurement points on each floor for Phase-I of the benchmark problem

Phase-I also includes six different damage scenarios. These damage scenarios are illustrated in Figure 5.3 and explained in Table 5.4.

Table 5.3. Considered Simulation Cases in Phase-I

Case	Data Generation Model	Top Floor Mass Distribution	Excitation Type	Damage Scenario
Case 1	12 DOF	Symmetric	Ambient (at each floor in *y*-dir only)	*i, ii*
Case 2	120 DOF	Symmetric	Ambient (at each floor in *y*-dir only)	*i, ii*
Case 3	12 DOF	Symmetric	Shaker (*x* and *y*-dir on roof only)	*i, ii*
Case 4	12 DOF	Asymmetric	Shaker (*x* and *y*-dir on roof only)	*i, ii, iii, iv, vi*
Case 5	120 DOF	Asymmetric	Shaker (*x* and *y*-dir on roof only)	*i, ii, iii, iv, v, vi*

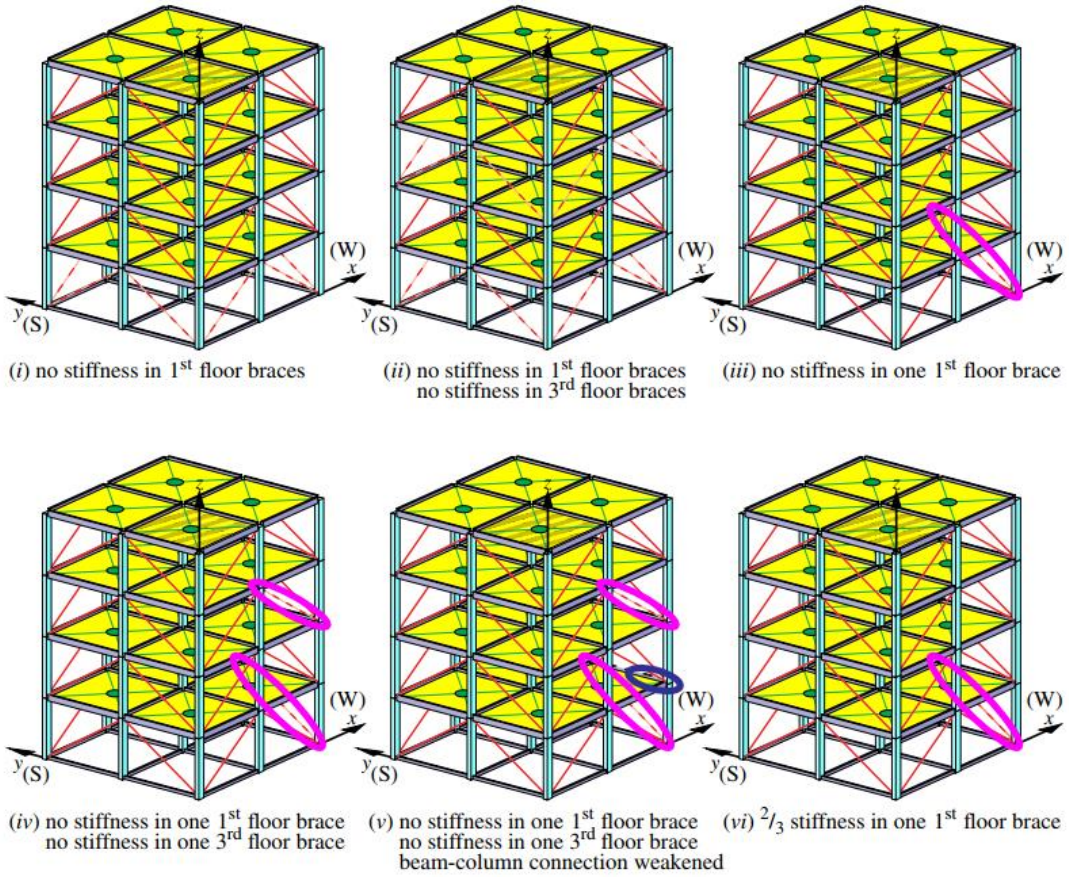

Figure 5.3. Damage scenarios in Phase-I of the Benchmark Problem

(Source: Johnson et al., 2004)

Table 5.4. Descriptions of the damage scenarios in Phase-I of the Benchmark Problem

Damage Scenario	Description
i	There is no stiffness in any of the braces of the first floor
ii	There is no stiffness in any of the braces of the first and third floor
iii	There is no stiffness in one brace of the first floor (brace on the east bay of the north face of the first floor)
iv	There is no stiffness in one brace of the first floor and in one brace of the third floor (brace on the east bay of the north face of the first floor and brace on the north bay of the east face of the third floor)
v	Damage scenario *iv* + beam-column connection on the east bay of the north face weakened
vi	1/3 stiffness loss in one brace of the first story (brace on the east bay of the north face of the first floor)

It should be noted that the last column in Table 5.3 provides the damage scenarios recommended by the task group to be investigated for the corresponding case. Accordingly, only the damage scenarios *i* and *ii* are recommended to be investigated for Cases 1 – 3 and Cases 4 – 6 includes damage scenarios that are relatively harder to detect. Case 4 does not include damage scenario *v* since 12-DOF model assumes perfectly rigid floors which makes weakening in beam-column connection meaningless. Case 5 and 6 includes all the damage scenarios.

The actual stiffness values of the 12-DOF model and percent loss in stiffness values are provided for all damage scenarios in Table 5.5 and Table 5.6, respectively. Table 5.7 provides the natural frequencies of the 12-DOD and 120-DOF models for Case 1 – 3. Eigen frequencies of the 12-DOF model with asymmetric mass defined for Case 4 can be found in Table 5.8 and Table 5.9 provides those of the 120-DOF model with asymmetric mass defined for Case 5.

Table 5.5. Stiffness Values (in MN/m) of 12-DOF Model for Each Story (Source: Johnson et al., 2004)

Story	DOF	Damage scenarios						
		Undamaged	(*i*)	(*ii*)	(*iii*)	(*iv*)	(*v*)	(*vi*)
1	*x*	106.60	58.37	58.37	106.60	106.60	106.60	106.60
	y	67.90	19.67	19.67	55.85	55.85	55.85	63.89
	θ	232.02	81.30	81.30	209.11	209.11	209.11	225.35
2	*x*	106.60	106.60	106.60	106.60	106.60	106.60	106.60
	y	67.90	67.90	67.90	67.90	67.90	67.90	67.90
	θ	232.02	232.02	232.02	232.02	232.02	232.02	232.02
3	*x*	106.60	106.60	58.37	106.60	94.54	94.54	106.60
	y	67.90	67.90	19.67	67.90	67.90	67.90	67.90
	θ	232.02	232.02	81.30	232.02	210.78	210.78	232.02
4	*x*	106.60	106.60	106.60	106.60	106.60	106.60	106.60
	y	67.90	67.90	67.90	67.90	67.90	67.90	67.90
	θ	232.02	232.02	232.02	232.02	232.02	232.02	232.02

Table 5.6. Percent Loss in Stiffness Values of 12-DOF Model for various damage scenarios (Source: Johnson et al., 2004)

Story	DOF	Damage Scenarios					
		(*i*)	(*ii*)	(*iii*)	(*iv*)	(*v*)	(*vi*)
1	*x*	45.24 %	45.24 %	0	0	0	0
	y	71.03 %	71.03 %	17.76%	17.76%	17.76%	5.92%
	θ	64.96%	64.96%	9.87%	9.87%	9.87%	2.88%
2	*x*	0	0	0	0	0	0
	y	0	0	0	0	0	0
	θ	0	0	0	0	0	0
3	*x*	0	45.24 %	0	11.31%	11.31%	0
	y	0	71.03 %	0	0	0	0
	θ	0	64.96%	0	9.16%	9.16%	0
4	*x*	0	0	0	0	0	0
	y	0	0	0	0	0	0
	θ	0	0	0	0	0	0

Table 5.7. Natural Frequencies (Hz) of 12-DOF and 120-DOF models for Case 1 – 3

Undamaged		Damage Scenarios			
		i		*ii*	
12 - DOF	120 - DOF	12 - DOF	120 - DOF	12 - DOF	120 - DOF
9.41 *y*	8.20 *y*	6.24 *y*	4.91 *y*	5.82 *y*	4.36 *y*
11.79 *x*	8.53 *x*	9.91 *x*	6.61 *x*	9.51 *x*	5.77 *x*
16.53 θ	13.95 θ	11.73 θ	8.82 θ	11.01 θ	7.74 θ
25.60 *y*	22.54 *y*	21.53 *y*	18.38 *y*	14.89 *y*	10.26 *y*
32.07 *x*	24.24 *x*	28.92 *x*	21.06 *x*	24.91 *x*	15.22 *x*
38.85 *y*	35.58 *y*	37.37 *y*	32.56 θ	28.41 θ	18.32 θ
45.17 θ	39.05 θ	38.28 θ	33.98 *y*	36.06 *y*	33.80 *y*
48.37 *y*	39.73 *x*	47.34 *x*	38.09 *x*	41.35 *y*	37.47 *y*
48.68 *x*	46.12 *y*	47.83 *y*	45.80 *y*	46.79 *x*	37.83 *x*
60.60 *x*	55.16 *x*	59.99 *x*	54.68 *x*	54.34 *x*	47.81 *x*
68.64 θ	60.75 θ	65.31 θ	58.11 θ	63.64 θ	58.01 θ
85.51 θ	79.46 θ	83.31 θ	78.80 θ	72.61 θ	66.38 θ

Table 5.8. Natural Frequencies (Hz) of 12-DOF Model with Asymmetric Mass Distribution for Case 4

Undamaged	Damage Scenarios					
	(*i*)	(*ii*)	(*iii*)	(*iv*)	(*v*)	(*vi*)
9.29 *y*	6.18 y	5.76 *y*	8.79 y	8.79 y	8.79 y	9.15 y
11.64 *x*	9.80 *x*	9.39 *x*	11.64 *x*	11.50 *x*	11.50 *x*	11.64 *x*
16.19 *θ*	11.63 *θ*	10.90 *θ*	15.80 *θ*	15.68 *θ*	15.68 *θ*	16.07 *θ*
25.27 *y*	21.27 *y*	14.78 *y*	24.37 *y*	24.36 y	24.36 y	24.98 *y*
31.66 *x*	28.59 *x*	24.70 *x*	31.66 *x*	30.82 *x*	30.82 *x*	31.66 *x*
38.26 *y*	36.87 y	28.22 *θ*	37.77 y	37.76 *y*	37.76 y	38.10 *y*
44.20 *θ*	37.93 *θ*	35.97 *y*	43.61 *θ*	42.91 *θ*	42.91 *θ*	43.99 *θ*
44.75 *y*	46.81 *x*	40.60 *y*	47.68 *y*	47.68 y	47.68 y	47.72 *y*
47.97 *x*	47.54 *y*	46.46 *x*	47.96 *x*	47.96 *x*	47.96 *x*	47.97 *x*
59.81 *x*	59.63 *x*	53.68 *x*	59.81 *x*	58.18 x	58.18 *x*	59.81 *x*
66.90 *θ*	64.67 *θ*	63.44 *θ*	66.58 *θ*	66.56 *θ*	66.56 *θ*	66.79 *θ*
83.23 *θ*	82.89 *θ*	71.58 *θ*	83.18 *θ*	81.76 *θ*	81.76 *θ*	83.21 *θ*

Table 5.9. Natural Frequencies (Hz) of 120-DOF Model with Asymmetric Mass Distribution for Case 5

Damage Scenarios						
Undamaged	(*i*)	(*ii*)	(*iii*)	(*iv*)	(*v*)	(*vi*)
8.09 *y*	4.86 *y*	4.30 *y*	7.61 *y*	7.61 *y*	7.59 *y*	7.86 *y*
8.40 *x*	6.53 *x*	5.69 *x*	8.40 *x*	8.13 *x*	8.13 *x*	8.40 *x*
13.78 θ	8.74 θ	7.65 θ	13.38 θ	13.21 θ	13.21 θ	13.58 θ
22.27 *y*	18.12 *y*	10.20 *y*	21.34 *y*	21.30 *y*	21.29 *y*	21.78 *y*
23.92 *x*	20.77 *x*	15.11 *x*	22.95 *x*	22.95 *x*	22.95 *x*	23.92 *x*
35.21 *y*	32.12 θ	18.22 θ	34.49 *y*	34.49 *y*	34.49 *y*	34.87 *y*
38.58 θ	33.62 *y*	33.53 *y*	37.20 θ	37.20 θ	37.20 θ	38.30 θ
39.44 *x*	37.68 *x*	37.00 *y*	39.17 *x*	39.17 *x*	39.17 *x*	39.42 *x*
45.95 *y*	45.60 *y*	37.30 *x*	45.84 *y*	45.84 *y*	45.83 *y*	45.88 *y*
55.02 *x*	54.51 *x*	47.63 *x*	53.16 *x*	53.16 *x*	53.16 *x*	55.02 *x*
60.21 θ	57.51 θ	57.48 θ	59.81 θ	59.81 θ	59.81 θ	59.99 θ
79.22 θ	78.53 θ	65.83 θ	77.50 θ	77.50 θ	77.50 θ	79.16 θ

5.3.1.2. Analyses and Results of Each Simulation Case of Phase-I

In this section, all cases are investigated one by one in detail with the recommended damage scenarios provided in Table 5.3. To do so, FE models are downloaded with all the FE analysis codes in the MATLAB environment from the website of Network for Earthquake Engineering Simulation (NEES) Database for Structural Control and Monitoring Benchmark Problems. Then, the FE model in each case is updated by using the sensitivity-based Bayesian Model Updating methodology presented in the present study. The updating results are compared with those of the previous formulations presented in the previous thesis progress reports. The results are compared to those obtained in the model updating literature, which employ the same benchmark problem.

In this study, independent Gaussian white noise signals are used to excite the structure for all cases to simulate low-amplitude ambient vibrations. All response data are considered as acceleration measurements, and each is contaminated with a Gaussian white noise signal with a 10% of the root mean square (RMS) of the maximum acceleration response to simulate measurement noise (unless otherwise stated). In the published literature, damping ratio of each mode of the physical laboratory structure is

reported to be approximately 1%. Therefore, the damping ratio of each mode is taken to be 1% for all simulation cases in Phase-I.

The Phase-I results of the present study are compared with those of four different studies. First and second ones are the results obtained by the previous formulations presented as “Case 1 and Case 2” in CHAPTER 2. As a reminder of these cases, assumption of each case is defined as follows. In the present study, Case 1 is renamed as Algorithm 2 and Case 2 is renamed as Algorithm 1 since the word “Case” conflicts with the Case definitions in Phase-I of the benchmark problem.

- Algorithm 1: Modelling error variance is considered to be the same for each mode and updated in each iteration as a soft constraint. This case corresponds to a similar study performed by Hızal and Turan (2020). This case is named as Algorithm 1 since Case 2 is formulated before Case 1.
- Algorithm 2: Modelling error variance of each mode is considered to be different for each mode and each is updated as soft constraints.
- Both algorithms employ system modes to account for modelling error.

Third and fourth studies to compare the results are the ones in the literature, which are published by Yuen et al. (2004) and Lam et al. (2004). Both employ a Bayesian model updating technique and implement their methodologies on each simulation case of Phase-I of the IASC-ASCE benchmark problem. Yuen et al. (2004) uses a two-stage updating methodology based on the Bayes’ theorem. In the first stage, they employ a model-based statistical modal identification technique called MODE-ID. In this stage, they construct an objective function by using the prediction error between the time-domain response measurements obtained from the FE model and the actual structure and extract the modal data. In the second stage, they use the obtained modal properties in a Bayesian model updating strategy similar to the one presented in this present study.

Lam et al. (2004) use a one-step statistical model updating methodology based on the Bayes’ theorem. They combine the modal identification and model updating steps and update the modal and model parameters simultaneously in one step.

In this study, for all cases, the prior PDF of each θ_j is set to follow a truncated Gaussian distribution with mean θ_j = 1 for j = 1, 2, 3, 4 and a diagonal covariance

matrix having a prior variance value of 0.25 on each diagonal. This value corresponds to a relatively large c.o.v of 50% to have a non-informative prior distribution. The normal distribution is truncated as $\mathbf{L}_{\boldsymbol{\theta}} \leq \boldsymbol{\theta} \leq \mathbf{U}_{\boldsymbol{\theta}}$ setting $\mathbf{L}_{\boldsymbol{\theta}} = 0$ since negative stiffness value has not a physical meaning and $\mathbf{U}_{\boldsymbol{\theta}} = 2$ since an increase in the stiffness is not expected in case of any damage. Further, mass is considered as well-known and not taken as an updating parameter since the exact mass of the measured model is already known in a numerical study. There is no need to consider the mass with a small prior variance.

5.3.1.2.1. Analyses and Results for Case 1:

This case includes 12-DOF model with symmetrical mass distribution. Four independent Gaussian white noise is used to excite the structure simulating the low-amplitude ambient vibrations. Loadings are applied on the center column at each floor in the *y* direction (weak direction) only. Since the structure is symmetric for the undamaged condition, damage scenarios *i* and *ii*, no translational motion in the *x* direction and no torsional motion are expected for the perfectly ideal world of numerical studies. Therefore, a 4-DOF shear frame model, which is sufficient to represent the *y*-direction dynamics, is employed as the model to be updated instead of the 12-DOF one. The same 4-DOF model is excited to obtain the response data from the structure. A stiffness scaling parameter θ_j is selected to scale the stiffness matrix of the j^{th} story, which makes a total of four scaling parameters to be updated. Each substructure stiffness matrix, $\mathbf{K}_j$, is constructed by using the shear building assumption with a size of 4×4. Each inter-story stiffness is taken to be 67.9 MN/m from Table 5.5.

MPVs of the stiffness scaling parameters and their corresponding uncertainties are obtained by using the sensitivity-based Bayesian model updating approach developed in the present study and by using Algorithm 1 and Algorithm 2 presented in the previous studies. The updating results are provided in Table 5.10 with their posterior c.o.v values (in parentheses) for undamaged condition (UD), damage scenarios *i* and *ii*. The results that are obtained by Lam et al. (2004) and Yuen et al. (2004) are also provided in the table for comparison. The results are also illustrated in Figure 5.4 with the error bars showing ∓ 1 posterior standard deviations ($\mp 1\sigma$). The stiffness loss is provided in Table 5.6 as 71.03% in the *y* direction for all stories in damage scenarios *i*

and *ii*, and it corresponds to an exact value of 0.2897 for the stiffness scaling parameters of the damaged floors. For the undamaged floors, exact value of the parameters is 1.00. The actual values are shown in Figure 5.4 by using black dashed lines for comparison purposes.

Table 5.10. MPVs of stiffness scaling parameters and their posterior c.o.v.'s (%) for Case 1

Damage Scenario	Related Research	θ_1 (c.o.v.)	θ_2 (c.o.v.)	θ_3 (c.o.v.)	θ_4 (c.o.v.)
UD	Actual	1.00	1.00	1.00	1.00
	Present Study	1.00 (3.22)	1.01 (3.24)	1.00 (3.22)	1.00 (3.20)
	Algorithm 1	0.99 (0.14)	1.00 (0.07)	0.99 (0.06)	1.00 (0.05)
	Algorithm 2	0.99 (0.07)	1.01 (0.06)	0.99 (0.05)	1.00 (0.07)
	Yuen et al. (2004)	0.97 (0.50)	0.96 (0.40)	1.01 (0.27)	1.02 (0.32)
	Lam et al. (2004)	0.99 (1.79)	1.00 (2.21)	1.00 (1.68)	1.00 (2.30)
i	Actual	0.29	1.00	1.00	1.00
	Present Study	0.29 (0.51)	1.00 (0.34)	1.00 (0.34)	1.00 (0.24)
	Algorithm 1	0.29 (0.15)	1.00 (0.02)	0.99 (0.02)	1.00 (0.02)
	Algorithm 2	0.29 (0.08)	1.00 (0.03)	0.99 (0.02)	1.00 (0.02)
	Yuen et. al (2004)	0.28 (0.27)	0.98 (0.39)	1.01 (0.36)	1.01 (0.27)
	Lam et al (2004)	0.29 (2.41)	1.00 (2.03)	1.00 (1.40)	1.00 (2.12)
ii	Actual	0.29	1.00	0.29	1.00
	Present Study	0.29 (0.62)	1.00 (0.33)	0.29 (0.47)	1.00 (0.24)
	Algorithm 1	0.30 (0.03)	1.00 (0.004)	0.29 (0.01)	1.00 (0.003)
	Algorithm 2	0.30 (0.003)	1.00 (0.0003)	0.30 (0.003)	0.99 (0.00)
	Yuen et. al (2004)	0.28 (0.32)	0.99 (0.17)	0.29 (0.66)	1.01 (0.18)
	Lam et al (2004)	0.29 (2.74)	1.00 (0.88)	0.29 (2.03)	1.00 (0.76)

According to the results, all five methods can successfully detect the damages introduced in damage scenarios *i* and *ii* without giving any false damage alarm. All the undamaged stiffness parameters give a value close to 1. This is an expected result since there is no modelling error between the updated model and the measured one. Posterior c.o.v values obtained by the present study are found to be compatible with those

obtained in the literature. However, Algorithms 1 and 2 result in smaller c.o.v values as this was the discussion topic of the previous thesis progress reports. In fact, all the posterior c.o.v. values are small numbers in percent since there is no modelling error in the investigated case.

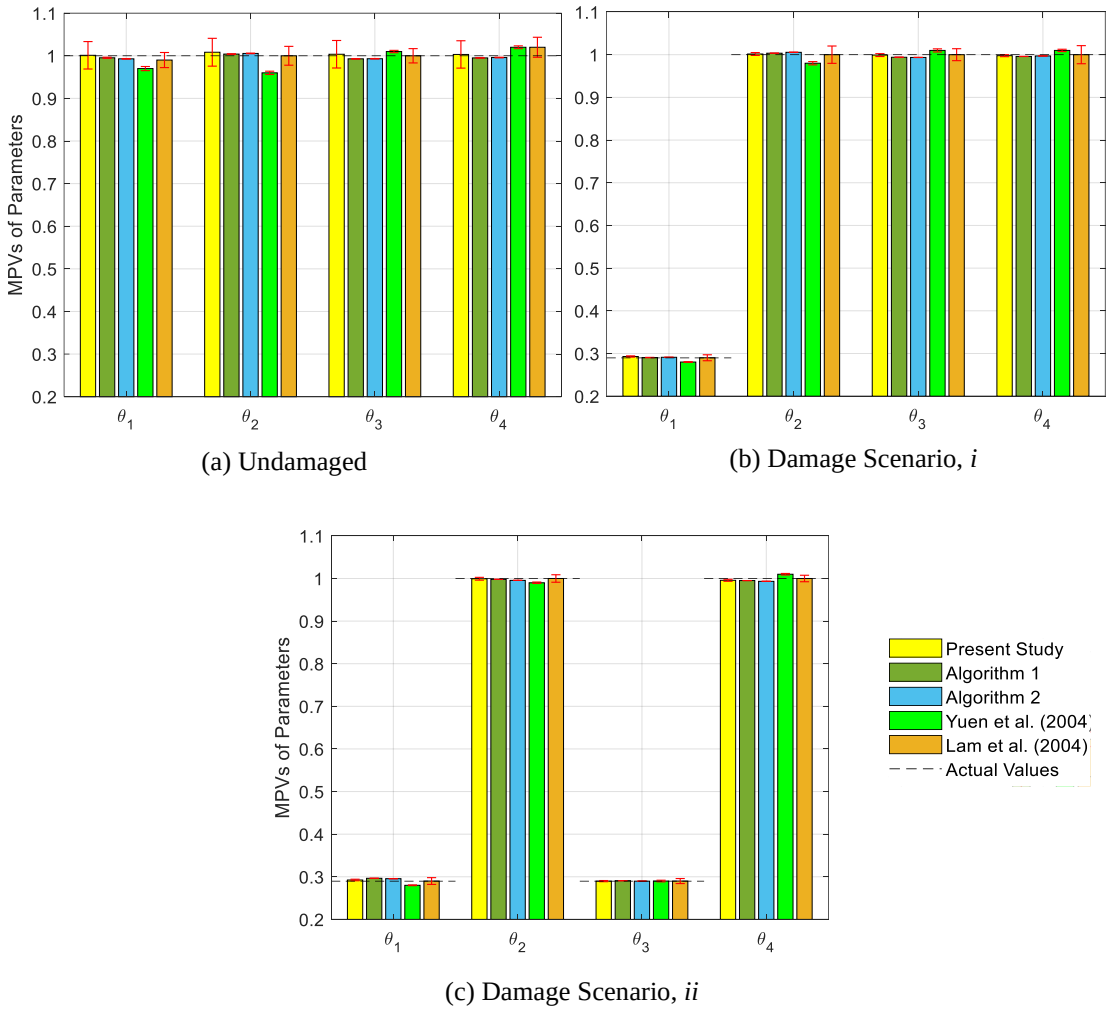

(a) Undamaged

(b) Damage Scenario, *i*

(c) Damage Scenario, *ii*

Figure 5.4. Updated stiffness scaling parameters with $\mp 1\sigma$ for Case 1

In this case, extent and locations of damage are estimated in story level since the excitation type, updated model and symmetry in the measured model allow only the damage identification in story level. Damage extent for each damage scenario is decided by using the probabilistic framework provided in Section 5.2. Figure 5.5 presents the posterior CDF of each damage scenario calculated by using equation (5.9) for the formulations in the present study. In Figure 5.5 (a) for damage scenario *i*, according to the blue curve which represents θ_1, it has the probability that damage is 66.5% or higher

is almost 1 and damage in θ_1 has a probability of 0.025 to exceed 72.5%. Therefore, the mean value of all probabilities is considered to give 70.2% stiffness loss for θ_1 where the actual value is 71.03%. The same interpretation is used for Figure 5.5 (b) and the damage in θ_1 is identified to be 70.3%, and the damage in θ_3 is identified to be 70.7% for damage scenario *ii*. Table 5.11 summarizes the damage detection results for Case 1.

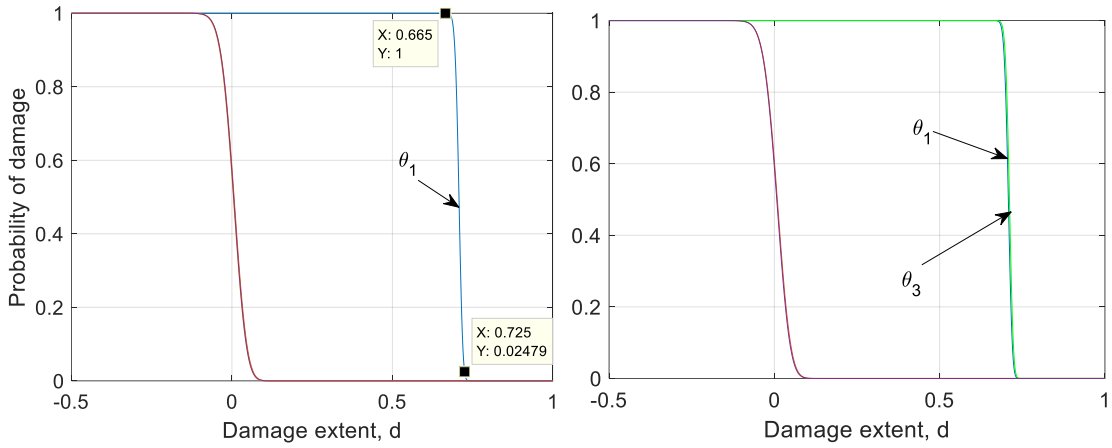

(a) Damage scenario *i* (b) Damage scenario *ii*

Figure 5.5. Probability of damage for the parameters in damage scenarios (a) *i* and (b) *ii* for the present study (Case 1)

Table 5.11. Damage detection results of Case 1 for the present study

	Actual	Present Study
Damage Scenario	Damage Location (Stiffness Loss)	Damage Location (Stiffness Loss)
i	First Floor 71.03 %	First Floor 70.20 %
ii	First Floor 71.03 % Third Floor 71.03 %	First Floor 70.70 % Third Floor 70.03

5.3.1.2.2. Analyses and Results for Case 2:

The only difference between Case 1 and Case 2 is that measured structural model is now the 120-DOF model, and the model to be updated is again the 12-DOF shear frame model. Both models have the symmetric mass distribution. Since 120-DOF model does not have shear building assumptions, the effects of modelling error exist in this case differently from Case 1. Loadings are applied on the center column at each floor in the *y* direction (weak direction) only. Since the 120-DOF structure model is symmetric for the undamaged condition, damage scenarios *i* and *ii*, the motion is restricted as a translational motion in the *y* direction only. Therefore, the 4-DOF shear frame model, which is the same with that used in Case 1 is employed as the model to be updated instead of the 12-DOF one.

Since the 120-DOF model does not constrain out-of-plane DOFs of the floor slabs, it is expected that this model is more flexible than the 12-DOF model which constrains out-of-plane DOFs. Therefore, stiffness scaling parameters of the 12-DOF model which is updated by measuring the 120-DOF model should not be close to 1 and they are expected to be smaller than 1. Therefore, it is hard to obtain the actual stiffness scaling parameters equivalent to those of 12-DOF model for this case. One approach recommended by Johnson et al. (2004) is that the equivalent stiffness can be obtained by using the basic stiffness matrix derivation procedure applying a unit force to each DOF of 120-DOF model that corresponds to DOFs of the 12-DOF model. Another recommended approach is that a least squares approach can be employed to obtain the equivalent model. However, this brings another model updating problem similar to the present one which makes it meaningless. Therefore, in this case, the MPVs of the stiffness scaling parameters are firstly obtained by measuring the undamaged 120-DOF model. Then, the 12-DOF model is updated by measuring the damaged 120-DOF model. The results are provided as the ratio of the MPVs of the stiffness scaling parameters obtained from the damaged structure to those obtained from the undamaged one. It should be noted here that posterior c.o.v.'s for the parameter ratios are obtained by the square root of the sum of the squares (SRSS) of the posterior standard deviations obtained from the undamaged and damaged cases. The reason is to account for the error propagation developed due to the division of the MPVs of the stiffness parameters.

Ratios of the MPVs of the stiffness parameters and their posterior c.o.v.'s (in parentheses) are provided in Table 5.12 for undamaged condition (UD), damage scenarios *i* and *ii*. The results are also illustrated in Figure 5.6 with the error bars showing ∓ 1 posterior standard deviations ($\mp 1\sigma$). The stiffness loss is provided in Table 5.6 as 71.03% in the *y* direction for all stories in damage scenarios *i* and *ii* and it corresponds to an exact value of 0.2897 for the ratio of the stiffness scaling parameters of the damaged floors.

Table 5.12. Ratios of the MPVs of the stiffness parameters and their posterior c.o.v.'s (%) for Case 2

Damage Scenario	Related Research	θ_1 / θ_1^{un} (c.o.v)	θ_2 / θ_2^{un} (c.o.v)	θ_3 / θ_3^{un} (c.o.v)	θ_4 / θ_4^{un} (c.o.v)
i	Actual	0.29	1.00	1.00	1.00
	Present Study	0.20 (1.82)	1.00 (0.38)	0.99 (0.47)	1.00 (0.26)
	Algorithm 1	0.26 (4.72)	1.00 (3.82)	1.00 (3.91)	1.00 (3.48)
	Algorithm 2	0.27 (10.98)	1.00 (1.44)	0.86 (4.66)	0.98 (1.22)
	Yuen et. al (2004)	0.26 (1.62)	0.97 (1.65)	0.93 (1.62)	1.02 (1.63)
	Lam et al (2004)	0.26 (3.24)	1.28 (2.96)	0.77 (2.39)	0.82 (2.17)
ii	Actual	0.29	1.00	0.29	1.00
	Present Study	0.20 (1.75)	1.01 (0.55)	0.13 (2.54)	0.94 (0.41)
	Algorithm 1	0.26 (17.67)	1.00 (3.46)	0.22 (15.26)	0.97 (3.02)
	Algorithm 2	0.33 (0.04)	1.00 (0.005)	0.28 (0.05)	0.96 (0.004)
	Yuen et. al (2004)	0.26 (1.63)	0.99 (1.71)	0.21 (1.64)	1.05 (1.62)
	Lam et al (2004)	0.27 (4.02)	0.90 (2.80)	0.13 (2.80)	1.12 (2.08)

The updating results are not as good as the results obtained in Case 1. This proves that modelling error significantly affects the updating procedures for all investigated five methods. However, the most unsatisfactory results are obtained by the present study with a value of 0.20 for θ_1 for damage scenario *i* and *ii*, which is about 30% smaller than the actual value. Similarly, θ_3 is obtained with a value of 0.13 which is about 55% smaller than the actual value. However, similar results are observed in the studies performed by Yuen et al. (2004) and Lam et al. (2004). Besides, Lam et al. (2004) have

relatively large biased results for undamaged stiffness parameters, which may result in false positive damage alarms. Any of the methods gives false negative results and can locate damage even if the damage extent is somehow biased.

The posterior c.o.v values are obtained with relatively higher values when compared to those of Case 1. This is an expected result since the modelling error induces more uncertainties in the updating procedure and increases the posterior uncertainties. Further, since the ratio of the parameters are considered in this case, the error propagation also results in an increase in the c.o.v values. For direct comparison, the c.o.v of each stiffness scaling parameter itself (without taking ratios) also is also investigated and an increasing trend is observed when compared with those of Case 1.

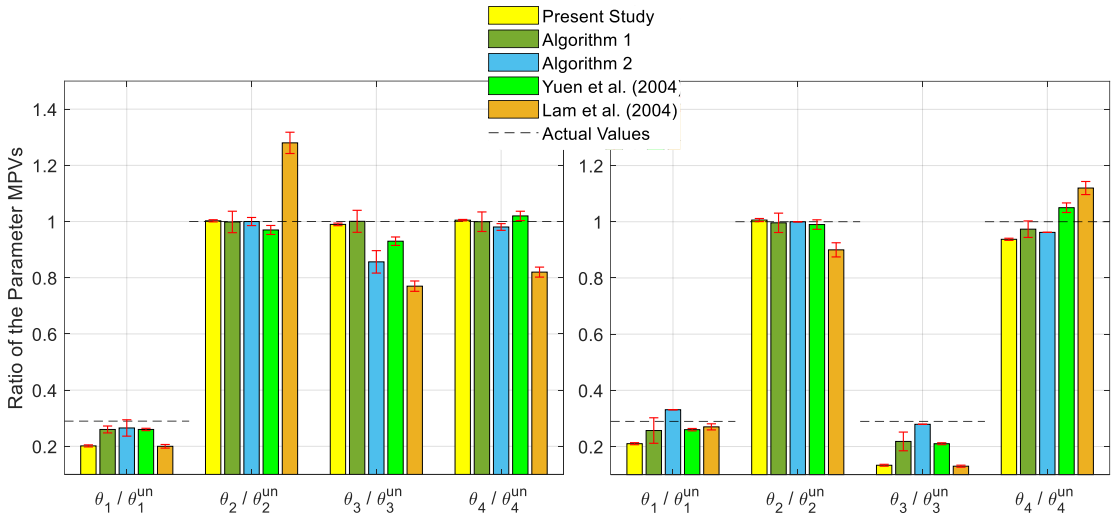

(a) Damage Scenario, *i* (b) Damage Scenario, *ii*

Figure 5.6. Ratios of the stiffness scaling parameters with $\mp 1\sigma$ for Case 2

In this case, as in Case 1, the extent and locations of damage are estimated in story level due to the excitation type, updated model, and symmetry in the measured model. Figure 5.7 presents the posterior CDF of each damage scenario in the present study. By using these curves, damage extents are calculated by the same procedure discussed in Case 1. For the damage scenario *i* and *ii*, damage in θ_1 is identified to be 79.8%, and for the damage scenario *ii*, damage in θ_3 is identified to be 86.60%. Damage detection results are summarized in Table 5.13 for Case 2.

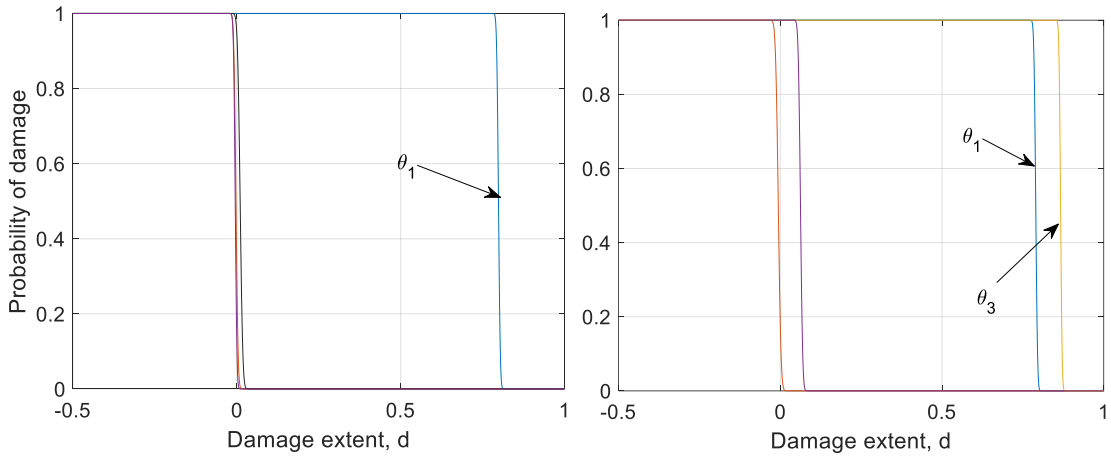

(a) Damage scenario, *i* (b) Damage scenario, *ii*

Figure 5.7. Probability of damage for the parameters in damage scenarios (a) *i* and (b) *ii* for the present study (Case 2)

Table 5.13. Damage detection results of Case 2 for the present study

	Actual	Present Study
Damage Scenario	Damage Location (Stiffness Loss)	Damage Location (Stiffness Loss)
i	First Floor 71.03 %	First Floor 79.80 %
ii	First Floor 71.03 % Third Floor 71.03 %	First Floor 79.80 % Third Floor 86.60 %

5.3.1.2.3. Analyses and Results for Case 3:

The only difference between Case 3 and Case 1 is the excitation type. In Case 3, loadings are applied on the center column at each floor in both *x* and *y* directions. Therefore, as in Case 1, the structure is symmetric for the undamaged condition, damage scenarios *i* and *ii*, and no torsional motion is expected for these damage conditions. This makes these damage scenarios very similar to those in Case 1 since the

same 12-DOF model is used for the identification model and the measured model. For the higher damage scenarios, Case 3 becomes interesting since damage scenarios *iii*, *iv*, *v*, and *vi* makes the structure asymmetric and different modes of the structure are excited for different damage scenarios. However, asymmetric stiffness distribution cannot be modeled by using the 12-DOF model provided by the IASC-ASCE task group since only one stiffness parameter is defined for the *x* direction and the same for the *y* direction. Therefore, in the present study, damage scenarios *iii*, *iv* and *vi* in Case 3 are investigated by constructing a 3D 12-DOF torsional shear building model and this model is used as the one to be updated.

Figure 5.8 shows the floor plan of the r^{th} story of the 3D 12-DOF model. In each story level, a translational DOF in the *x* direction, a translational DOF in the *y* direction and a rotational DOF are defined at the geometrical center of the floor plan. Therefore, these DOFs coincide with the active DOFs in the 12-DOF model that is used to get measurements (the original model recommended for this case). Since the damage scenarios are designed by removing various brace elements on a specific face of a specific floor, a stiffness parameter is defined for each face of each floor, which makes a total of 16 stiffness parameters to be updated. The stiffness values are named as $k_{r,s}$ where the sub-index *r* denotes the story number r = 1, 2, 3 and 4, and *s* represents the direction of the face on which the stiffness value is defined such as $s = +x, +y, -x$ and $-y$.

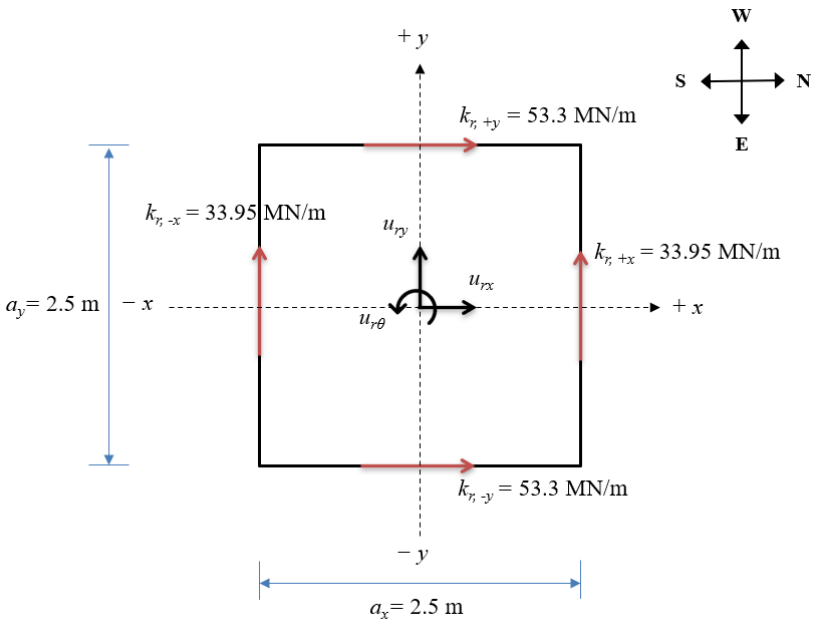

Figure 5.8. Floor plan of the r^{th} story of the 3D 12-DOF torsional shear building model

The parametrization of the FE model is performed as;

$$\mathbf{K}(\boldsymbol{\theta}) = \mathbf{K}_0 + \sum_{r=1}^{4} \theta_{rx}\mathbf{K}_{rx} + \sum_{r=1}^{4} \theta_{ry}\mathbf{K}_{ry} \tag{5.13}$$

where

$$\begin{aligned} \theta_{rx}\mathbf{K}_{rx} &= \theta_{r,+y}\mathbf{K}_{r,+y} + \theta_{r,-y}\mathbf{K}_{r,-y} \\ \theta_{ry}\mathbf{K}_{ry} &= \theta_{r,+x}\mathbf{K}_{r,+x} + \theta_{r,-x}\mathbf{K}_{r,-x} \end{aligned} \tag{5.14}$$

In equation (5.14), $\mathbf{K}_{r,s}$ is the substructural stiffness matrix and $\theta_{r,s}$ is the corresponding stiffness scaling parameter. Each substructural stiffness matrix that represents the contribution of the stiffness of each face to the global stiffness matrix is provided in Figure 5.9.

$$\mathbf{K}_{r,+x} = k_{r,+x}\begin{bmatrix} 0 & 0 & 0 & 0 & 0 & 0 \\ 0 & 1 & a_y/2 & 0 & -1 & -a_y/2 \\ 0 & a_y/2 & a_y^2/4 & 0 & -a_y/2 & -a_y^2/4 \\ 0 & 0 & 0 & 0 & 0 & 0 \\ 0 & -1 & -a_y/2 & 0 & 1 & a_y/2 \\ 0 & -a_y/2 & -a_y^2/4 & 0 & a_y/2 & -a_y^2/4 \end{bmatrix} \quad \mathbf{K}_{r,+y} = k_{r,+y}\begin{bmatrix} 1 & 0 & -a_x/2 & -1 & 0 & a_x/2 \\ 0 & 0 & 0 & 0 & 0 & 0 \\ -a_x/2 & 0 & a_x^2/4 & a_x/2 & 0 & -a_x^2/4 \\ -1 & 0 & a_x/2 & 1 & 0 & -a_x/2 \\ 0 & 0 & 0 & 0 & 0 & 0 \\ a_x/2 & 0 & -a_x^2/4 & -a_x/2 & 0 & a_x^2/4 \end{bmatrix}$$

$$\mathbf{K}_{r,-x} = k_{r,-x}\begin{bmatrix} 0 & 0 & 0 & 0 & 0 & 0 \\ 0 & 1 & -a_y/2 & 0 & -1 & a_y/2 \\ 0 & -a_y/2 & a_y^2/4 & 0 & a_y/2 & -a_y^2/4 \\ 0 & 0 & 0 & 0 & 0 & 0 \\ 0 & -1 & a_y/2 & 0 & 1 & -a_y/2 \\ 0 & a_y/2 & -a_y^2/4 & 0 & -a_y/2 & a_y^2/4 \end{bmatrix} \quad \mathbf{K}_{r,-y} = k_{r,-y}\begin{bmatrix} 1 & 0 & a_x/2 & -1 & 0 & -a_x/2 \\ 0 & 0 & 0 & 0 & 0 & 0 \\ a_x/2 & 0 & a_x^2/4 & -a_x/2 & 0 & -a_x^2/4 \\ -1 & 0 & -a_x/2 & 1 & 0 & a_x/2 \\ 0 & 0 & 0 & 0 & 0 & 0 \\ -a_x/2 & 0 & -a_x^2/4 & a_x/2 & 0 & a_x^2/4 \end{bmatrix}$$

Figure 5.9. Substructural stiffness matrices of 3-D 12-DOF torsional shear frame model

Here, $k_{r,+x}$, $k_{r,+y}$, $k_{r,-x}$ and $k_{r,-y}$ are shown in Figure 5.8 with their nominal values which are obtained as the half of the corresponding values in Table 5.5.

The measured model is the 12-DOF model that is available in FE analysis code provided by the task group. This model is excited by independent white noise signals from all 3 DOFs of each floor. Thus, almost all modes of the structure are excited. However, in the updating process for all the investigated damage scenarios, only the first three translational modes in *x* and *y* directions are employed in the modal identification stage. Torsional modes are not included in model updating process since

the modelling error for the torsional behavior is found to be large between the 12-DOF shear building model provided by the task group and 3D 12-DOF torsional shear frame model, and this causes the updating results to diverge from the reasonable results. It should be noted here that translational modes are coupled with torsional ones in some extent due to the asymmetric stiffness distribution induced in damaged cases. Nevertheless, the induced damages could be successfully obtained with true damage locations and damage extents.

Similar to Case 2, ratios of the stiffness parameters of the damaged scenarios to the undamaged condition are considered and they are provided in Table 5.14, Table 5.15 and Table 5.16 with the obtained c.o.v. values for the damage scenarios *iii*, *iv* and *vi*, respectively.

The results are also illustrated in Figure 5.10 for damage scenarios (a) iii, (b) iv and (c) vi with the error bars showing ∓ 1 posterior standard deviations ($\mp 1\sigma$). It should be noted that, in the literature, it could not be found a similar study that investigates the damage scenarios iii, iv and vi in Case 3, probably since these damage scenarios are not recommended by the task group to be investigated in Case 3. Therefore, the results could not be compared with any studies in the literature.

In Case 3, stiffness loss values are different in percentage scale from those provided in Table 5.6 since the stiffness values are uniformly distributed on two opposing faces in x and y directions and only one face sustains damage. Accordingly, for damage scenario iii, the actual stiffness loss on +x face of the first floor is calculated as 35.49% and it corresponds to an exact value of 0.6451 for the ratio of the corresponding stiffness scaling parameter. Similarly, for damage scenario iv, the actual stiffness loss on +x face of the first floor is the same and the actual stiffness loss on -y face of the third floor is calculated as 22.63% and it corresponds to an exact value of 0.7738 for the ratio of the corresponding stiffness scaling parameter. For damage scenario vi, the actual stiffness loss on +x face of the first floor is calculated as 11.81% and it corresponds to an exact value of 0.8819 for the ratio of the corresponding stiffness scaling parameter.

Table 5.14. Ratios of the MPVs of the stiffness parameters and their posterior c.o.v.'s (%) for Damage Scenario *iii* in Case 3

Parameters	Actual	Present Study	Algorithm 1	Algorithm 2
$\theta_{1,+x}/\theta_{1,+x}^{un}$	0.65	0.62 (1.96)	0.62 (0.39)	0.65 (0.04)
$\theta_{1,+y}/\theta_{1,+y}^{un}$	1.00	1.01 (1.03)	1.00 (0.17)	1.00 (0.01)
$\theta_{1,-x}/\theta_{1,-x}^{un}$	1.00	1.01 (1.35)	1.00 (0.24)	1.00 (0.02)
$\theta_{1,-y}/\theta_{1,-y}^{un}$	1.00	1.00 (1.03)	1.00 (0.17)	1.00 (0.01)
$\theta_{2,+x}/\theta_{2,+x}^{un}$	1.00	1.01 (1.57)	1.00 (0.14)	1.00 (0.02)
$\theta_{2,+y}/\theta_{2,+y}^{un}$	1.00	0.97 (1.50)	0.98 (0.12)	1.00 (0.02)
$\theta_{2,-x}/\theta_{2,-x}^{un}$	1.00	1.02 (1.68)	1.00 (0.14)	1.00 (0.02)
$\theta_{2,-y}/\theta_{2,-y}^{un}$	1.00	0.99 (1.49)	1.00 (0.11)	1.00 (0.02)
$\theta_{3,+x}/\theta_{3,+x}^{un}$	1.00	1.02 (2.09)	1.00 (0.20)	0.98 (0.03)
$\theta_{3,+y}/\theta_{3,+y}^{un}$	1.00	1.01 (0.90)	1.00 (0.07)	1.00 (0.006)
$\theta_{3,-x}/\theta_{3,-x}^{un}$	1.00	0.99 (2.19)	0.97 (0.21)	1.00 (0.03)
$\theta_{3,-y}/\theta_{3,-y}^{un}$	1.00	1.00 (0.90)	1.00 (0.07)	1.00 (0.006)
$\theta_{4,+x}/\theta_{4,+x}^{un}$	1.00	1.01 (1.22)	1.00 (0.13)	1.00 (0.02)
$\theta_{4,+y}/\theta_{4,+y}^{un}$	1.00	0.99 (1.03)	0.98 (0.07)	0.98 (0.00)
$\theta_{4,-x}/\theta_{4,-x}^{un}$	1.00	0.99 (1.21)	0.99 (0.13)	1.00 (0.02)
$\theta_{4,-y}/\theta_{4,-y}^{un}$	1.00	0.98 (1.03)	0.97 (0.07)	0.98 (0.00)

Table 5.15. Ratios of the MPVs of the stiffness parameters and their posterior c.o.v's (%) for Damage Scenario *iv* in Case 3

Parameters	Actual	Present Study	Algorithm 1	Algorithm 2
$\theta_{1,+x}/\theta_{1,+x}^{un}$	0.65	0.61 (1.89)	0.62 (0.40)	0.64 (0.04)
$\theta_{1,+y}/\theta_{1,+y}^{un}$	1.00	1.01 (1.05)	1.00 (0.18)	1.00 (0.01)
$\theta_{1,-x}/\theta_{1,-x}^{un}$	1.00	1.01 (1.29)	1.00 (0.25)	1.00 (0.02)
$\theta_{1,-y}/\theta_{1,-y}^{un}$	1.00	0.99 (1.00)	0.99 (1.18)	1.00 (0.01)
$\theta_{2,+x}/\theta_{2,+x}^{un}$	1.00	1.01 (1.51)	1.00 (0.14)	1.00 (0.02)
$\theta_{2,+y}/\theta_{2,+y}^{un}$	1.00	1.02 (1.52)	1.00 (0.12)	1.00 (0.02)
$\theta_{2,-x}/\theta_{2,-x}^{un}$	1.00	1.02 (1.60)	1.00 (0.14)	1.00 (0.02)
$\theta_{2,-y}/\theta_{2,-y}^{un}$	1.00	0.97 (1.47)	0.97 (0.12)	0.97 (0.02)
$\theta_{3,+x}/\theta_{3,+x}^{un}$	1.00	1.02 (1.82)	1.00 (0.21)	0.99 (0.03)
$\theta_{3,+y}/\theta_{3,+y}^{un}$	1.00	1.00 (0.92)	1.00 (0.07)	1.00 (0.006)
$\theta_{3,-x}/\theta_{3,-x}^{un}$	1.00	0.98 (1.91)	0.97 (0.22)	1.00 (0.03)
$\theta_{3,-y}/\theta_{3,-y}^{un}$	0.77	0.76 (1.10)	0.77 (0.09)	0.78 (0.008)
$\theta_{4,+x}/\theta_{4,+x}^{un}$	1.00	1.01 (1.16)	1.00 (0.13)	1.00 (0.02)
$\theta_{4,+y}/\theta_{4,+y}^{un}$	1.00	1.02 (1.03)	1.00 (0.07)	1.00 (0.00)
$\theta_{4,-x}/\theta_{4,-x}^{un}$	1.00	0.98 (1.15)	1.00 (0.13)	1.00 (0.02)
$\theta_{4,-y}/\theta_{4,-y}^{un}$	1.00	0.97 (1.02)	0.97 (0.08)	0.95 (0.00)

Table 5.16. Ratios of the MPVs of the stiffness parameters and their posterior c.o.v.'s (%) for Damage Scenario *vi* in Case 3

Parameters	Actual	Present Study	Algorithm 1	Algorithm 2
$\theta_{1,+x}/\theta_{1,+x}^{un}$	0.88	0.78 (1.77)	0.78 (1.67)	0.80 (0.03)
$\theta_{1,+y}/\theta_{1,+y}^{un}$	1.00	1.01 (1.02)	1.00 (0.93)	0.99 (0.05)
$\theta_{1,-x}/\theta_{1,-x}^{un}$	1.00	1.01 (1.43)	1.00 (0.37)	1.00 (0.02)
$\theta_{1,-y}/\theta_{1,-y}^{un}$	1.00	1.01 (1.02)	0.99 (0.93)	1.00 (0.05)
$\theta_{2,+x}/\theta_{2,+x}^{un}$	1.00	1.01 (1.65)	1.00 (0.77)	1.00 (0.02)
$\theta_{2,+y}/\theta_{2,+y}^{un}$	1.00	0.97 (1.48)	0.98 (0.63)	1.00 (0.08)
$\theta_{2,-x}/\theta_{2,-x}^{un}$	1.00	1.02 (1.69)	1.00 (0.78)	1.00 (0.02)
$\theta_{2,-y}/\theta_{2,-y}^{un}$	1.00	0.98 (1.47)	1.00 (0.63)	0.99 (0.07)
$\theta_{3,+x}/\theta_{3,+x}^{un}$	1.00	1.02 (2.19)	1.00 (1.17)	0.98 (0.03)
$\theta_{3,+y}/\theta_{3,+y}^{un}$	1.00	1.01 (0.88)	1.00 (0.39)	1.00 (0.04)
$\theta_{3,-x}/\theta_{3,-x}^{un}$	1.00	0.98 (2.28)	0.97 (1.23)	1.00 (0.03)
$\theta_{3,-y}/\theta_{3,-y}^{un}$	1.00	1.00 (0.88)	1.00 (0.40)	1.00 (0.04)
$\theta_{4,+x}/\theta_{4,+x}^{un}$	1.00	1.01 (1.25)	1.00 (0.78)	1.00 (0.02)
$\theta_{4,+y}/\theta_{4,+y}^{un}$	1.00	0.99 (1.01)	0.98 (0.44)	0.99 (0.002)
$\theta_{4,-x}/\theta_{4,-x}^{un}$	1.00	0.99 (1.24)	1.00 (0.77)	0.99 (0.02)
$\theta_{4,-y}/\theta_{4,-y}^{un}$	1.00	0.98 (1.01)	0.97 (0.44)	0.98 (0.002)

The results are also illustrated in Figure 5.10 for damage scenarios (a) *iii*, (b) *iv* and (c) *vi* with the error bars showing ∓ 1 posterior standard deviations ($\mp 1\sigma$). It should be noted that, in the literature, it could not be found a similar study that investigates the damage scenarios *iii*, *iv* and *vi* in Case 3, probably since these damage scenarios are not recommended by the task group to be investigated in Case 3. Therefore, the results could not be compared with any studies in the literature.

In Case 3, stiffness loss values are different in percentage scale from those provided in Table 5.6 since the stiffness values are uniformly distributed on two opposing faces in *x* and *y* directions and only one face sustains damage. Accordingly, for damage scenario *iii*, the actual stiffness loss on +*x* face of the first floor is calculated as 35.49% and it corresponds to an exact value of 0.6451 for the ratio of the corresponding stiffness scaling parameter. For damage scenario *iv*, the actual stiffness loss on +*x* face of the first floor is the same and the actual stiffness loss on -*y* face of the third floor is calculated as 22.63% and it corresponds to an exact value of 0.7738 for the ratio of the corresponding stiffness scaling parameter. For damage scenario *vi*, the actual stiffness loss on +*x* face of the first floor is calculated as 11.81% and it

corresponds to an exact value of 0.8819 for the ratio of the corresponding stiffness scaling parameter.

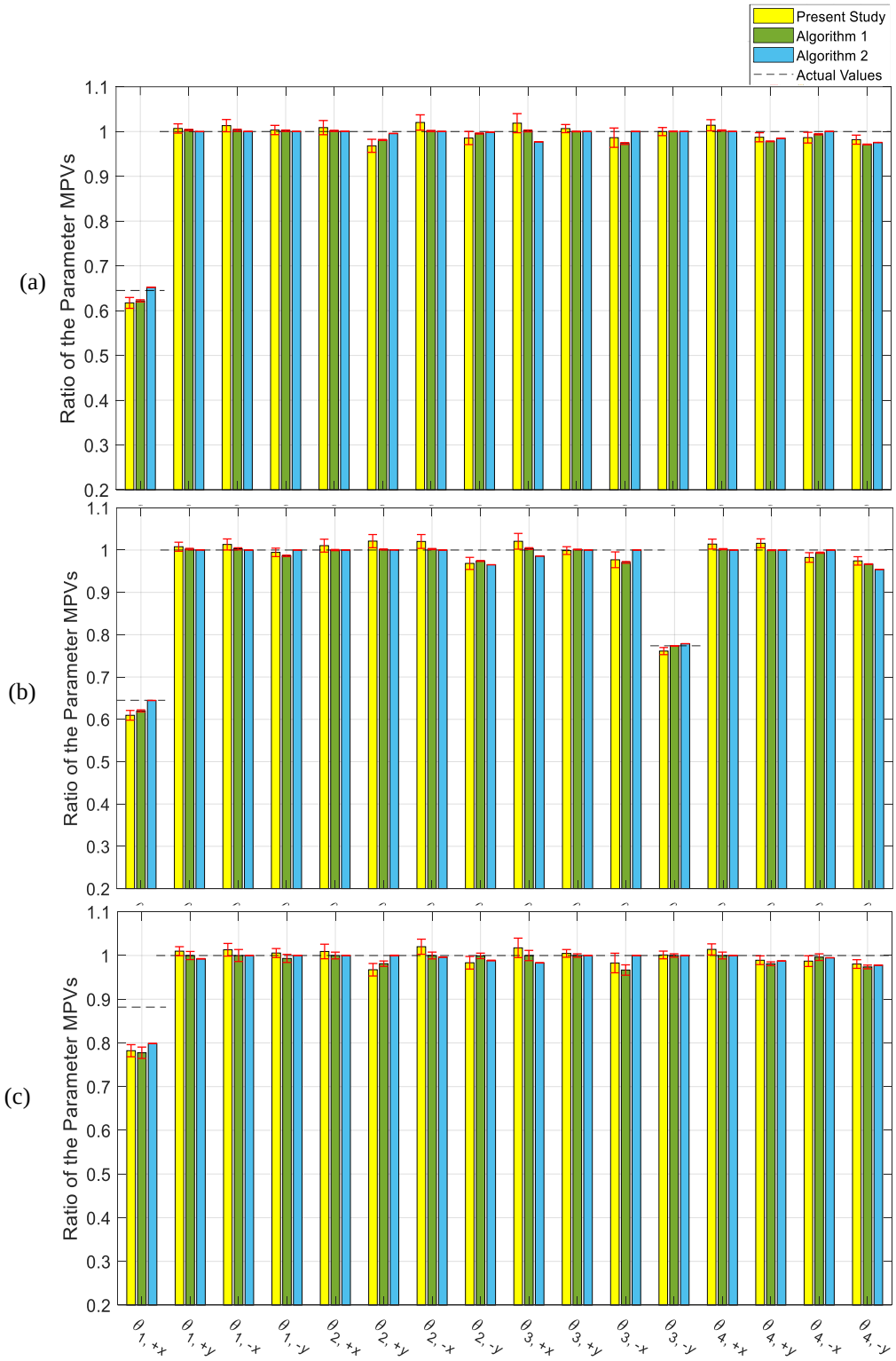

Figure 5.10. Ratios of stiffness scaling parameters with $\mp 1\sigma$ for Damage Scenarios (a) *iii*, (b) *iv* and (c) *vi* in Case 3

Differently from previous cases, in Case 3, damage location could be obtained more precisely by indicating the faces on which the damage is occurred. The provided results reveal that all the three algorithms could successfully detect the location of the induced damages in the investigated damage scenarios. However, identified damage extents are biased from the actual scaling parameters. The reason of the biased results might be that there exists a certain level of modelling error between 12-DOF model provided by the task group and 3D 12-DOF model since the torsional behaviors are differently modeled for these structures. Due to this modelling error, torsional modes are not employed in the model updating stage which may result in biased results. The modelling error effect is not expected to be as large as encountered in Case 2 since Case 2 includes a 120-DOF model which is not constructed with shear building assumptions. However, a simpler 4-DOF model is used as the identification model in Case 2 and all identified modes in the direction of the excitation are employed in the updating procedure, which is not the issue in Case 3. Therefore, it may be meaningless to compare the c.o.v. levels for these two cases.

Figure 5.11 presents the posterior CDF for damage scenarios *iii*, *iv* and *vi* in the present study. By using these curves, damage extents are calculated as follows. For the damage scenario *iii* and *iv*, damage in θ_1 is identified to be 79.8% and for the damage scenario *ii*, damage in θ_3 is identified to be 86.6%. The damage detection results are provided in Table 5.17. The results show that the values of stiffness loss are overestimated when compared with the actual stiffness loss especially for the damage scenario *vi*. This might be due to the modelling error between the measured model and the identification model since the damage in this scenario relatively hard to determine with respect to the other scenario.

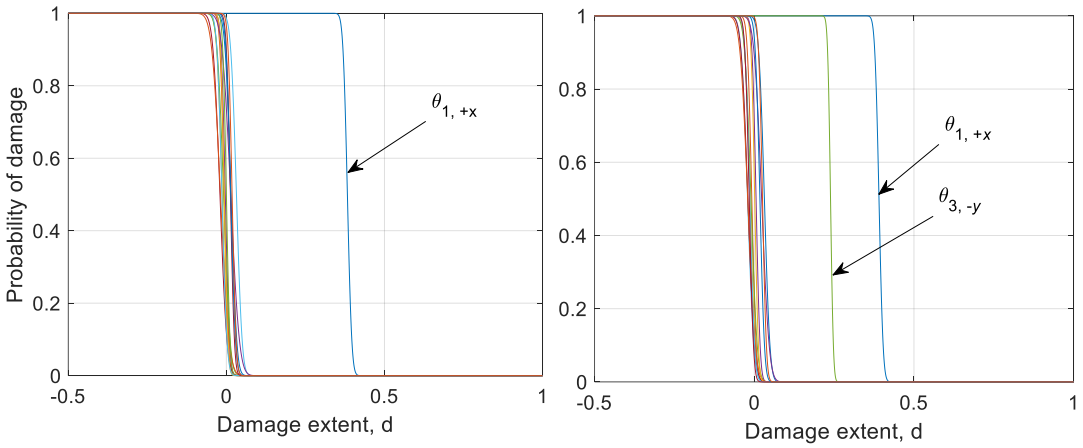

(a) Damage Scenario, *iii*

(b) Damage Scenario, *iv*

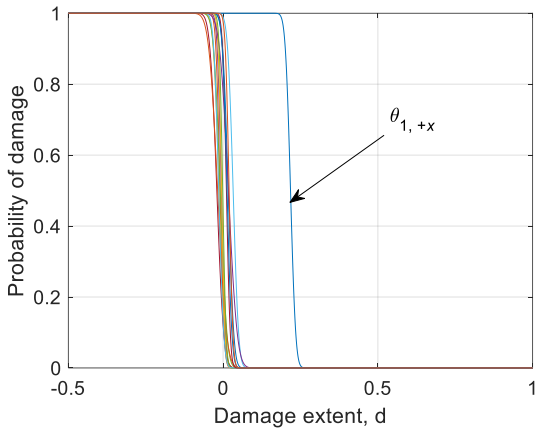

(c)Damage Scenario, *vi*

Figure 5.11. Probability of damage for the parameters in damage scenarios (a) *iii*, (b) *iv* and (c) *vi* for the present study (Case 3)

Table 5.17. Damage detection results of Case 3 for the present study

	Actual	Present Study
Damage Scenario	Damage Location (Stiffness Loss)	Damage Location (Stiffness Loss)
iii	First Floor (+*x* face) 35.49 %	First Floor 38.20 %
iv	First Floor (+*x* face) 35.49 % Third Floor (-*y* face) 22.63 %	First Floor 39.00 % Third Floor 23.80 %
vi	First Floor (+*x* face) 11.81 %	First Floor 21.70 %

5.3.1.2.4. Analyses and Results for Case 4:

The only difference between Case 4 and Case 3 is the mass distribution of the floors. Case 4 has an asymmetric mass on the top floor by changing one of the four 400 kg floor slabs with 550 kg one. Since the mass distribution is also asymmetric with damage cases that also cause an asymmetry in stiffness distribution, vibrational modes are easier to excite in Case 4 when compared with Case 3. For case 4, the same stiffness model of the 3D 12-DOF torsional shear building model is used for the identification model and the 12-DOF shear frame model is used to get measurements. Mass matrix model of these building models is updated to reflect the asymmetrical mass distribution. As in Case 3, ratios of the MPVs of the stiffness parameters are obtained in this case since there exists a certain level of modelling error between the mentioned models. All damage scenarios except damage scenario *v* are investigated in Case 4. Damage scenario *v* includes the weakening of a beam-column connection which cause the rotation of the corresponding slab. This damage case cannot be investigated due to the shear building assumption in the identification model, which restricts the out-of-plan motion. Therefore, damage scenarios *iv* and *v* are identical under this assumption.

The results of all the remaining cases are provided in the following tables and bar graphs illustratively. Whole model updating and damage detection process is performed exactly with the same procedures discussed in Case 3. Therefore, long explanations are skipped here.

The updating results of damage scenarios *i* and *ii* are in very good agreement with the actual stiffness parameters and those obtained by Yuen et al., (2004). The present study gives largest posterior c.o.v values. The reason is thought to be the fact that the formulations in present study does not include modelling error term and directly compares the FE model modes and measured modes. However, the remaining studies includes the modelling error term which results in a decrease in posterior uncertainties.

The present study gives slightly biased results for the damage scenarios *iii* and *iv* and larger biased results are obtained for the damage scenario *vi*. The similar results are also obtained in Case 3. This shows that it is getting hard for the present formulations to detect damage as the damage level decreases under a certain modelling error. However, the Algorithms 1 and 2 give also biased results for the damage scenario *vi*. The summary of the damage detection results can be found in Table 5.23 and Table 5.24.

Table 5.18. Ratios of the MPVs of the stiffness parameters and their posterior c.o.v.'s (%) for Damage Scenario *i* in Case 4

Parameters	Actual	Present Study	Algorithm 1	Algorithm 2	Yuen et. al (2004)
$\theta_{1,+x}/\theta_{1,+x}^{un}$	0.29	0.31 (5.22)	0.30 (4.07)	0.30 (0.001)	0.28 (0.62)
$\theta_{1,+y}/\theta_{1,+y}^{un}$	0.55	0.56 (1.52)	0.58 (1.49)	0.56 (0.00)	0.54 (0.35)
$\theta_{1,-x}/\theta_{1,-x}^{un}$	0.29	0.28 (5.54)	0.29 (4.21)	0.29 (0.001)	0.29 (0.53)
$\theta_{1,-y}/\theta_{1,-y}^{un}$	0.55	0.54 (1.53)	0.55 (1.55)	0.55 (0.00)	0.54 (0.31)
$\theta_{2,+x}/\theta_{2,+x}^{un}$	1.00	1.03 (1.83)	0.99 (0.74)	0.95 (0.002)	1.06 (0.90)
$\theta_{2,+y}/\theta_{2,+y}^{un}$	1.00	1.00 (1.86)	0.99 (0.53)	1.00 (0.00)	0.98 (1.10)
$\theta_{2,-x}/\theta_{2,-x}^{un}$	1.00	0.93 (1.92)	0.99 (0.73)	1.00 (0.002)	0.98 (0.56)
$\theta_{2,-y}/\theta_{2,-y}^{un}$	1.00	1.01 (1.98)	1.00 (0.57)	1.00 (0.00)	1.03 (1.09)
$\theta_{3,+x}/\theta_{3,+x}^{un}$	1.00	0.96 (3.28)	1.00 (1.11)	1.00 (0.00)	1.03 (0.95)
$\theta_{3,+y}/\theta_{3,+y}^{un}$	1.00	1.00 (1.24)	1.00 (0.37)	1.00 (0.00)	0.99 (0.54)
$\theta_{3,-x}/\theta_{3,-x}^{un}$	1.00	1.04 (3.01)	1.00 (1.10)	0.97 (0.00)	1.07 (0.64)
$\theta_{3,-y}/\theta_{3,-y}^{un}$	1.00	0.99 (1.19)	1.00 (0.36)	0.99 (0.00)	0.98 (0.56)
$\theta_{4,+x}/\theta_{4,+x}^{un}$	1.00	0.96 (1.51)	1.00 (0.69)	1.00 (0.002)	1.05 (0.81)
$\theta_{4,+y}/\theta_{4,+y}^{un}$	1.00	1.01 (1.60)	1.01 (0.42)	1.00 (0.00)	0.98 (0.91)
$\theta_{4,-x}/\theta_{4,-x}^{un}$	1.00	1.02 (1.32)	1.00 (0.66)	1.00 (0.002)	0.94 (0.63)
$\theta_{4,-y}/\theta_{4,-y}^{un}$	1.00	1.00 (1.43)	1.00 (0.40)	1.00 (0.00)	1.03 (0.95)

Table 5.19. Ratios of the MPVs of the stiffness parameters and their posterior c.o.v.'s (%) for Damage Scenario *ii* in Case 4

Parameters	Actual	Present Study	Algorithm 1	Algorithm 2	Yuen et. al (2004)
$\theta_{1,+x}/\theta_{1,+x}^{un}$	0.29	0.31 (5.25)	0.31 (3.86)	0.33 (0.00)	0.28 (0.56)
$\theta_{1,+y}/\theta_{1,+y}^{un}$	0.55	0.56 (1.57)	0.57 (1.50)	0.58 (0.00)	0.55 (0.34)
$\theta_{1,-x}/\theta_{1,-x}^{un}$	0.29	0.29 (5.35)	0.27 (4.53)	0.28 (0.00)	0.29 (0.46)
$\theta_{1,-y}/\theta_{1,-y}^{un}$	0.55	0.54 (1.60)	0.55 (1.53)	0.56 (0.00)	0.54 (0.32)
$\theta_{2,+x}/\theta_{2,+x}^{un}$	1.00	0.99 (1.89)	0.98 (0.75)	0.94 (0.00)	1.10 (1.06)
$\theta_{2,+y}/\theta_{2,+y}^{un}$	1.00	1.02 (1.03)	1.01 (0.53)	1.00 (0.00)	0.96 (0.87)
$\theta_{2,-x}/\theta_{2,-x}^{un}$	1.00	0.97 (1.97)	1.00 (0.72)	1.00 (0.00)	0.99 (1.25)
$\theta_{2,-y}/\theta_{2,-y}^{un}$	1.00	0.98 (1.12)	0.98 (0.58)	1.00 (0.00)	1.00 (0.91)
$\theta_{3,+x}/\theta_{3,+x}^{un}$	0.29	0.27 (8.35)	0.29 (3.77)	0.32 (0.00)	0.29 (0.58)
$\theta_{3,+y}/\theta_{3,+y}^{un}$	0.55	0.55 (1.26)	0.55 (0.66)	0.57 (0.00)	0.56 (0.34)
$\theta_{3,-x}/\theta_{3,-x}^{un}$	0.29	0.31 (7.24)	0.29 (3.85)	0.26 (0.00)	0.29 (0.45)
$\theta_{3,-y}/\theta_{3,-y}^{un}$	0.55	0.55 (1.26)	0.54 (0.65)	0.55 (0.00)	0.55 (0.32)
$\theta_{4,+x}/\theta_{4,+x}^{un}$	1.00	1.00 (0.63)	0.99 (0.70)	1.00 (0.00)	0.99 (0.47)
$\theta_{4,+y}/\theta_{4,+y}^{un}$	1.00	1.01 (0.79)	1.01 (0.42)	1.00 (0.00)	0.96 (1.22)
$\theta_{4,-x}/\theta_{4,-x}^{un}$	1.00	1.00 (1.55)	1.01 (0.65)	1.00 (0.00)	0.98 (0.43)
$\theta_{4,-y}/\theta_{4,-y}^{un}$	1.00	1.01 (0.73)	1.00 (0.39)	1.00 (0.00)	0.29 (0.58)

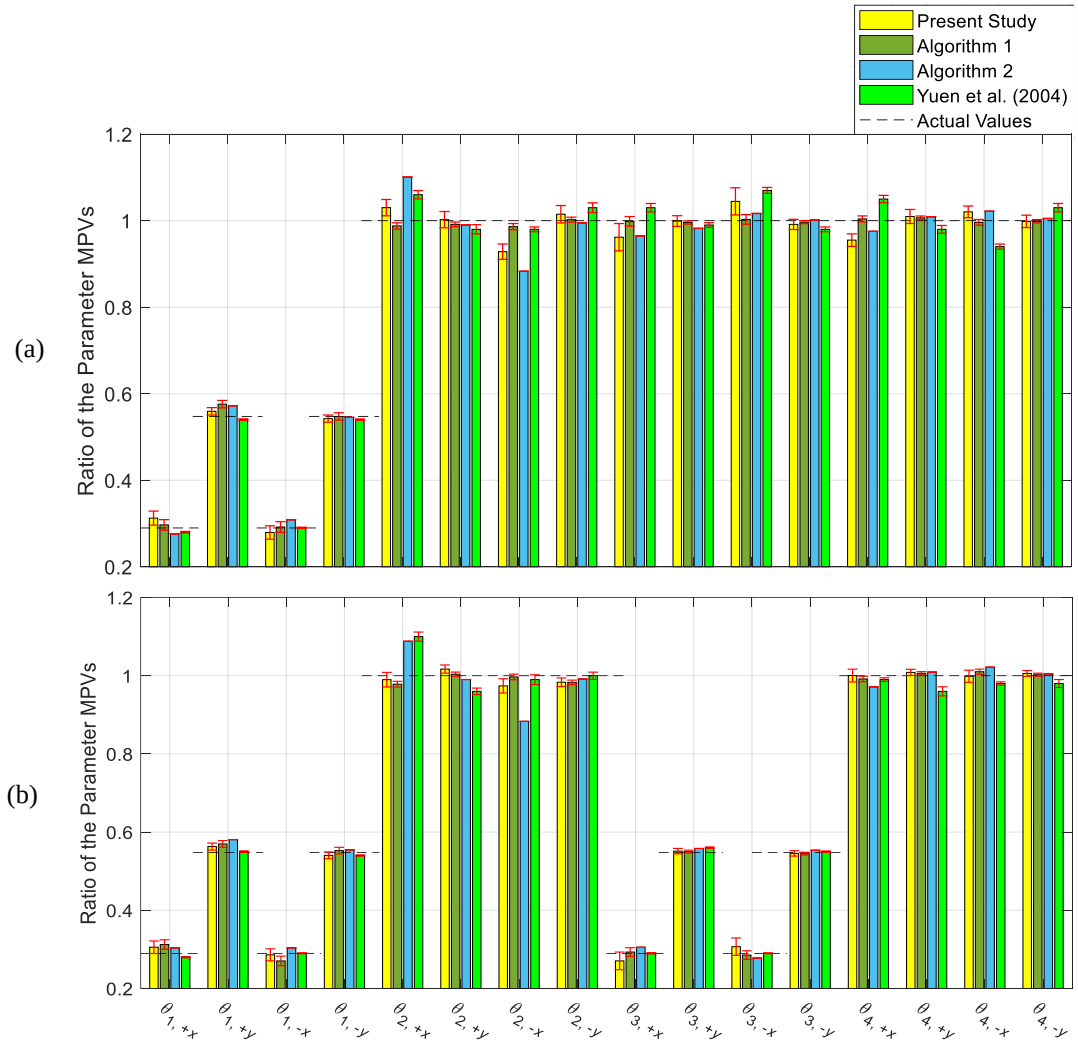

Figure 5.12. Ratios of stiffness scaling parameters with $\mp 1\sigma$ for Damage Scenarios (a) *i*, and (b) *ii* in Case 4

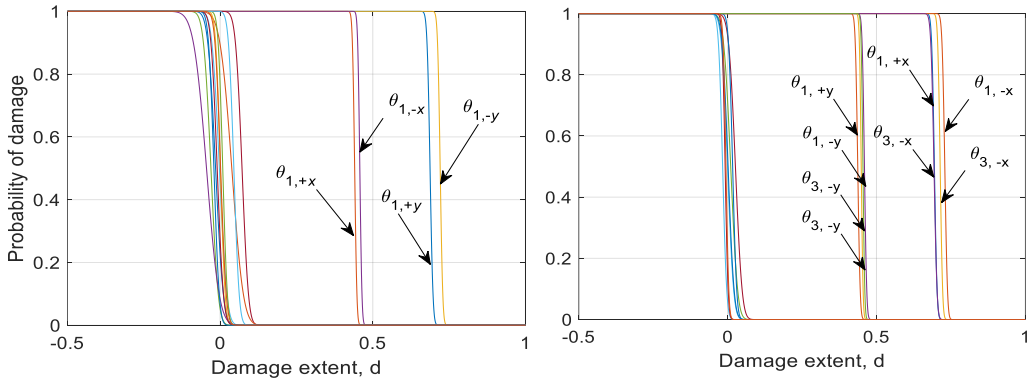

(a) Damage Scenario, *i*

(b) Damage Scenario, *ii*

Figure 5.13. Probability of damage for the parameters in damage scenarios (a) *i* and (b) *ii* for the present study (Case 4)

Table 5.20. Ratios of the MPVs of the stiffness parameters and their posterior c.o.v.'s (%) for Damage Scenario *iii* in Case 4

Parameters	Actual	Present Study	Algorithm 1	Algorithm 2	Yuen et. al (2004)
$\theta_{1,+x}/\theta_{1,+x}^{un}$	0.65	0.62 (2.96)	0.62 (2.12)	0.63 (0.00)	0.64 (0.40)
$\theta_{1,+y}/\theta_{1,+y}^{un}$	1.00	1.00 (1.01)	1.01 (0.94)	1.00 (0.04)	0.99 (0.45)
$\theta_{1,-x}/\theta_{1,-x}^{un}$	1.00	1.03 (1.82)	1.02 (1.34)	1.04 (0.00)	0.97 (0.34)
$\theta_{1,-y}/\theta_{1,-y}^{un}$	1.00	1.01 (0.98)	1.00 (0.93)	0.99 (0.04)	1.00 (0.31)
$\theta_{2,+x}/\theta_{2,+x}^{un}$	1.00	0.96 (2.03)	0.98 (0.81)	1.04 (0.00)	1.04 (0.53)
$\theta_{2,+y}/\theta_{2,+y}^{un}$	1.00	1.00 (1.22)	1.00 (0.58)	0.99 (0.02)	1.01 (0.77)
$\theta_{2,-x}/\theta_{2,-x}^{un}$	1.00	1.02 (1.98)	1.01 (0.78)	0.88 (0.00)	1.00 (0.43)
$\theta_{2,-y}/\theta_{2,-y}^{un}$	1.00	1.00 (1.31)	1.01 (0.63)	1.00 (0.02)	1.01 (0.61)
$\theta_{3,+x}/\theta_{3,+x}^{un}$	1.00	0.97 (2.94)	1.00 (1.21)	0.96 (0.00)	1.00 (0.83)
$\theta_{3,+y}/\theta_{3,+y}^{un}$	1.00	1.00 (0.83)	1.00 (0.40)	0.98 (0.03)	0.98 (0.64)
$\theta_{3,-x}/\theta_{3,-x}^{un}$	1.00	1.04 (2.80)	1.00 (1.22)	1.04 (0.00)	0.99 (0.55)
$\theta_{3,-y}/\theta_{3,-y}^{un}$	1.00	1.00 (0.83)	1.00 (0.39)	1.01 (0.02)	0.98 (0.58)
$\theta_{4,+x}/\theta_{4,+x}^{un}$	1.00	1.02 (1.46)	1.00 (0.77)	0.98 (0.00)	1.01 (0.39)
$\theta_{4,+y}/\theta_{4,+y}^{un}$	1.00	1.00 (0.92)	1.00 (0.46)	1.01 (0.02)	1.09 (1.01)
$\theta_{4,-x}/\theta_{4,-x}^{un}$	1.00	0.97 (1.36)	1.01 (0.71)	1.02 (0.00)	0.99 (0.35)
$\theta_{4,-y}/\theta_{4,-y}^{un}$	1.00	1.00 (0.86)	1.00 (0.43)	1.00 (0.03)	1.00 (0.83)

Table 5.21. Ratios of the MPVs of the stiffness parameters and their posterior c.o.v.'s (%) for Damage Scenario *iv* in Case 4

Parameters	Actual	Present Study	Algorithm 1	Algorithm 2	Yuen et. al (2004)
$\theta_{1,+x}/\theta_{1,+x}^{un}$	0.65	0.60 (2.96)	0.63 (1.91)	0.63 (0.00)	0.63 (0.54)
$\theta_{1,+y}/\theta_{1,+y}^{un}$	1.00	1.01 (1.01)	1.02 (0.84)	1.00 (0.002)	1.00 (0.22)
$\theta_{1,-x}/\theta_{1,-x}^{un}$	1.00	1.03 (1.77)	1.02 (1.21)	1.05 (0.00)	0.98 (0.42)
$\theta_{1,-y}/\theta_{1,-y}^{un}$	1.00	0.98 (0.96)	0.98 (0.86)	0.98 (0.001)	1.00 (0.30)
$\theta_{2,+x}/\theta_{2,+x}^{un}$	1.00	0.97 (1.98)	1.98 (0.75)	1.04 (0.00)	1.01 (0.79)
$\theta_{2,+y}/\theta_{2,+y}^{un}$	1.00	1.02 (1.26)	1.01 (0.52)	0.99 (0.00)	0.99 (0.43)
$\theta_{2,-x}/\theta_{2,-x}^{un}$	1.00	1.03 (1.92)	1.00 (0.72)	0.88 (0.00)	1.03 (0.65)
$\theta_{2,-y}/\theta_{2,-y}^{un}$	1.00	0.99 (1.27)	0.99 (0.58)	0.98 (0.00)	0.99 (0.46)
$\theta_{3,+x}/\theta_{3,+x}^{un}$	1.00	0.99 (2.72)	0.98 (1.12)	0.96 (0.00)	1.02 (0.98)
$\theta_{3,+y}/\theta_{3,+y}^{un}$	1.00	1.00 (0.83)	0.99 (0.37)	0.98 (0.001)	0.98 (0.42)
$\theta_{3,-x}/\theta_{3,-x}^{un}$	1.00	1.02 (2.64)	1.02 (1.08)	1.05 (0.00)	0.97 (0.62)
$\theta_{3,-y}/\theta_{3,-y}^{un}$	0.77	0.76 (0.99)	0.77 (0.46)	0.76 (0.001)	0.77 (0.32)
$\theta_{4,+x}/\theta_{4,+x}^{un}$	1.00	1.02 (1.40)	1.01 (0.68)	0.98 (0.00)	1.00 (0.59)
$\theta_{4,+y}/\theta_{4,+y}^{un}$	1.00	1.01 (0.94)	1.01 (0.42)	1.01 (0.002)	1.03 (0.75)
$\theta_{4,-x}/\theta_{4,-x}^{un}$	1.00	0.97 (1.32)	0.99 (0.66)	1.02 (0.00)	1.02 (0.47)
$\theta_{4,-y}/\theta_{4,-y}^{un}$	1.00	1.00 (0.83)	1.00 (0.40)	0.99 (0.002)	1.02 (0.98)

Table 5.22. Ratios of the MPVs of the stiffness parameters and their posterior c.o.v.'s (%) for Damage Scenario *vi* in Case 4

Parameters	Actual	Present Study	Algorithm 1	Algorithm 2
$\theta_{1,+x}/\theta_{1,+x}^{un}$	0.88	0.79 (2.39)	0.81 (1.50)	0.82(0.00)
$\theta_{1,+y}/\theta_{1,+y}^{un}$	1.00	1.00 (1.02)	1.01 (0.86)	0.99 (0.002)
$\theta_{1,-x}/\theta_{1,-x}^{un}$	1.00	1.02 (1.85)	1.00 (1.24)	1.00 (0.00)
$\theta_{1,-y}/\theta_{1,-y}^{un}$	1.00	1.01 (0.99)	1.00 (0.85)	1.00 (0.002)
$\theta_{2,+x}/\theta_{2,+x}^{un}$	1.00	0.98 (2.03)	0.99 (0.74)	1.00 (0.00)
$\theta_{2,+y}/\theta_{2,+y}^{un}$	1.00	1.00 (1.21)	1.00 (0.53)	1.00 (0.003)
$\theta_{2,-x}/\theta_{2,-x}^{un}$	1.00	1.02 (1.96)	1.01 (0.72)	1.00 (0.00)
$\theta_{2,-y}/\theta_{2,-y}^{un}$	1.00	1.00 (1.30)	1.01 (0.58)	1.00 (0.002)
$\theta_{3,+x}/\theta_{3,+x}^{un}$	1.00	0.97 (3.04)	1.00 (1.11)	0.99 (0.00)
$\theta_{3,+y}/\theta_{3,+y}^{un}$	1.00	1.00 (0.82)	1.00 (0.37)	1.00 (0.001)
$\theta_{3,-x}/\theta_{3,-x}^{un}$	1.00	1.03 (2.89)	0.99 (1.12)	1.00 (0.00)
$\theta_{3,-y}/\theta_{3,-y}^{un}$	1.00	1.00 (0.82)	1.00 (0.36)	1.00 (0.001)
$\theta_{4,+x}/\theta_{4,+x}^{un}$	1.00	1.02 (1.45)	0.98 (0.71)	0.99 (0.00)
$\theta_{4,+y}/\theta_{4,+y}^{un}$	1.00	1.00 (0.91)	1.00 (0.43)	1.00 (0.002)
$\theta_{4,-x}/\theta_{4,-x}^{un}$	1.00	0.98 (1.35)	1.01 (0.65)	1.00 (0.00)
$\theta_{4,-y}/\theta_{4,-y}^{un}$	1.00	1.00 (0.85)	1.00 (0.40)	1.00 (0.002)

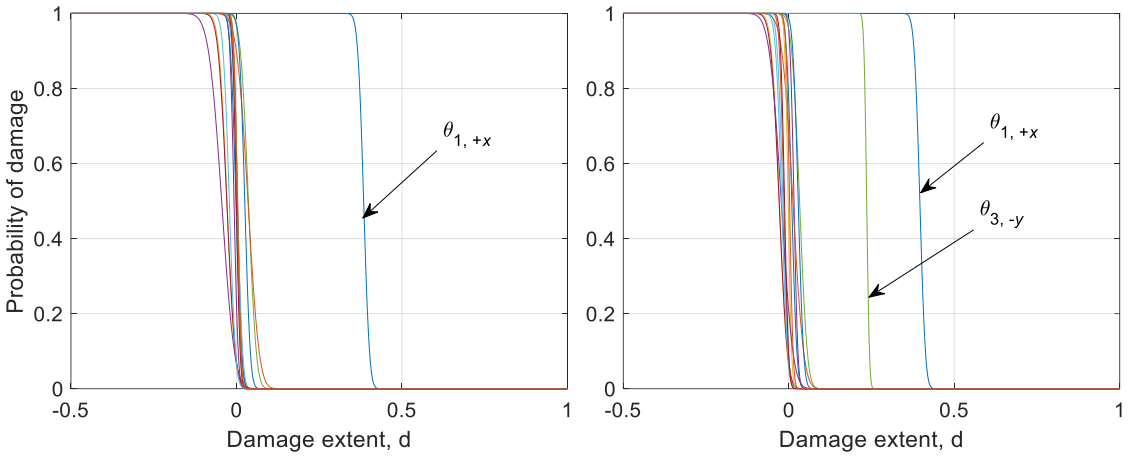

(a) Damage Scenario, *iii*

(b) Damage Scenario, *iv*

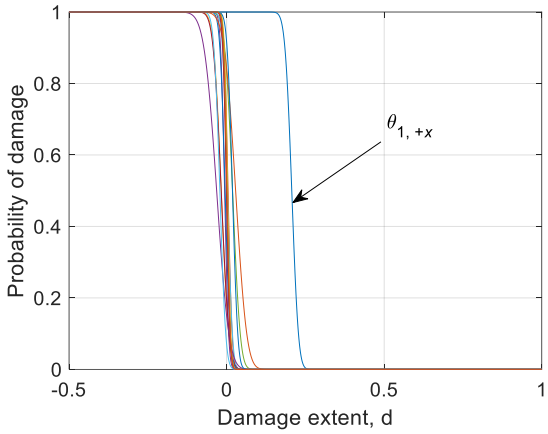

(c) Damage Scenario, *vi*

Figure 5.14. Probability of damage for the parameters in damage scenarios (a) *iii*, (b) *iv* and (c) *vi* for the present study (Case 4)

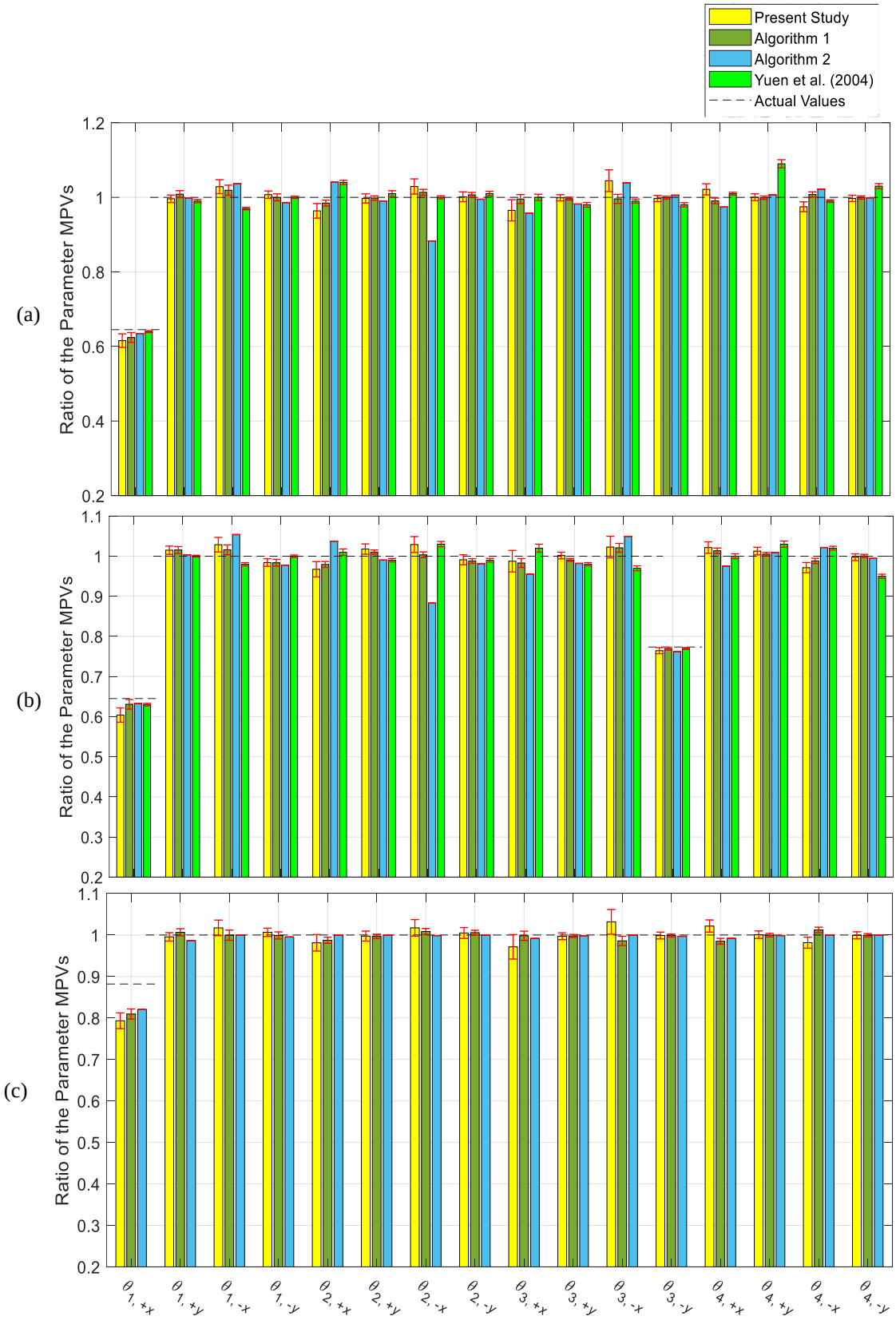

Figure 5.15. Ratios of stiffness scaling parameters with $\mp 1\sigma$ for Damage Scenarios (a) *iii*, (b) *iv* and (c) *vi* in Case 4

Table 5.23. Damage detection results of Case 4 for the present study (for damage scenarios *i* and *ii*)

	Actual	Present Study
Damage Scenario	Damage Location (Stiffness Loss)	Damage Location (Stiffness Loss)
i	First Floor (+*x* face) 71.03 %	First Floor (+*x* face) 68.60 %
	First Floor (-*x* face) 71.03 %	First Floor (-*x* face) 71.95 %
	First Floor (+y face) 45.24 %	First Floor (+y face) 44.00 %
	First Floor (-y face) 45.24 %	First Floor (-y face) 45.70 %
ii	First Floor (+*x* face) 71.03 %	First Floor (+*x* face) 69.30 %
	First Floor (-*x* face) 71.03 %	First Floor (-*x* face) 71.25 %
	First Floor (+y face) 45.24 %	First Floor (+y face) 43.60 %
	First Floor (-y face) 45.24 %	First Floor (-y face) 45.85 %
	Third Floor (+*x* face) 71.03 %	Third Floor (+*x* face) 72.70 %
	Third Floor (-*x* face) 71.03 %	Third Floor (-*x* face) 69.05 %
	Third Floor (+y face) 45.24 %	Third Floor (+y face) 44.80 %
	Third Floor (-y face) 45.24 %	Third Floor (-y face) 45.40 %

Table 5.24. Damage detection results of Case 4 for the present study (for damage scenarios *iii*, *iv* and *vi*)

	Actual	Present Study
Damage Scenario	Damage Location (Stiffness Loss)	Damage Location (Stiffness Loss)
iii	First Floor (+*x* face) 35.49 %	First Floor 38.15 %
iv	First Floor (+*x* face) 35.49 % Third Floor (-*y* face) 22.63 %	First Floor 39.35 % Third Floor 23.45 %
vi	First Floor (+*x* face) 11.81 %	First Floor 20.40 %

5.3.1.2.5. Analyses and Results for Case 5:

The only difference of Case 5 from Case 4 is that the measured model is the 120-DOF model in Case 5. Therefore, this case is known as the most difficult case with asymmetric mass distribution in the literature since a large modelling error exist in the identification model, which is constructed by shear building assumptions. All modes are excited in this case, however, only the first three translational modes in the *x* and *y* directions are employed in the model updating process. As in previous cases, ratios of the MPVs of the stiffness parameters are obtained in this case since there exists a considerable level of modelling error between the models.

The results of the damage scenarios *i*, *ii* and *iii* are provided in the following tables and bar graphs illustratively. The results of the remaining damage scenarios are not provided in this case since the actual damage cannot be distinguished from the many false detections with a similar level of damage extents. In this case, a stiffness parameter ratio with a value of 0.90 or smaller is accepted as a damaged one. Accordingly, the updating results for all the investigated damage scenarios give some false damage detection results for the present study. Besides, there is almost no false detection in the results obtained by the Algorithms 1 and 2. However, the results have

some bias from the actual values for each study. The CDF curves provided in Figure 5.16 (c) reveal that, for the present study, the damaged parameter is not distinguishable from the false detections for the damage scenario *iii*. The summary of the damage detection results can be found in Table 5.28 for the present study in terms of stiffness loses. Further, it is observed that the posterior c.o.v (especially the c.o.v. of the damaged parameters) has the largest values among all the cases. This proves that the largest modelling error exists in this case.

Table 5.25. Ratios of the MPVs of the stiffness parameters and their posterior c.o.v.'s (%) for Damage Scenario *i* in Case 5

Parameters	Actual	Present Study	Algorithm 1	Algorithm 2
$\theta_{1,+x}/\theta_{1,+x}^{un}$	0.29	0.21 (15.60)	0.28 (28.11)	0.28 (2.83)
$\theta_{1,+y}/\theta_{1,+y}^{un}$	0.55	0.51 (0.94)	0.57 (9.90)	0.51 (0.06)
$\theta_{1,-x}/\theta_{1,-x}^{un}$	0.29	0.25 (12.23)	0.24 (30.86)	0.24 (3.20)
$\theta_{1,-y}/\theta_{1,-y}^{un}$	0.55	0.49 (1.42)	0.55 (9.86)	0.53 (0.01)
$\theta_{2,+x}/\theta_{2,+x}^{un}$	1.00	0.88 (3.32)	1.00 (4.89)	1.00 (0.22)
$\theta_{2,+y}/\theta_{2,+y}^{un}$	1.00	1.03 (2.28)	1.00 (1.69)	1.00 (0.02)
$\theta_{2,-x}/\theta_{2,-x}^{un}$	1.00	0.78 (4.28)	1.00 (4.72)	1.00 (0.20)
$\theta_{2,-y}/\theta_{2,-y}^{un}$	1.00	1.03 (1.93)	1.00 (1.58)	1.00 (0.02)
$\theta_{3,+x}/\theta_{3,+x}^{un}$	1.00	0.80 (1.98)	1.00 (6.74)	0.96 (0.52)
$\theta_{3,+y}/\theta_{3,+y}^{un}$	1.00	0.90 (1.65)	0.91 (4.96)	0.97 (0.03)
$\theta_{3,-x}/\theta_{3,-x}^{un}$	1.00	0.87 (1.98)	1.00 (6.96)	0.97 (0.57)
$\theta_{3,-y}/\theta_{3,-y}^{un}$	1.00	0.76 (2.51)	0.91 (4.87)	1.00 (0.004)
$\theta_{4,+x}/\theta_{4,+x}^{un}$	1.00	0.96 (1.40)	1.00 (3.66)	0.92 (0.24)
$\theta_{4,+y}/\theta_{4,+y}^{un}$	1.00	0.95 (1.57)	0.90 (6.13)	0.97 (0.02)
$\theta_{4,-x}/\theta_{4,-x}^{un}$	1.00	0.94 (1.53)	1.00 (3.86)	0.94 (0.26)
$\theta_{4,-y}/\theta_{4,-y}^{un}$	1.00	0.87 (1.71)	0.94 (5.75)	0.93 (0.007)

Table 5.26. Ratios of the MPVs of the stiffness parameters and their posterior c.o.v.'s (%) for Damage Scenario *ii* in Case 5

Parameters	Actual	Present Study	Algorithm 1	Algorithm 2
$\theta_{1,+x}/\theta_{1,+x}^{un}$	0.29	0.23 (15.44)	0.29 (31.20)	0.32 (0.002)
$\theta_{1,+y}/\theta_{1,+y}^{un}$	0.55	0.53 (0.93)	0.47 (12.87)	0.57 (0.00)
$\theta_{1,-x}/\theta_{1,-x}^{un}$	0.29	0.24 (14.20)	0.31 (28.46)	0.25 (0.003)
$\theta_{1,-y}/\theta_{1,-y}^{un}$	0.55	0.51 (1.44)	0.45 (12.49)	0.58 (0.00)
$\theta_{2,+x}/\theta_{2,+x}^{un}$	1.00	0.83 (3.79)	1.00 (4.74)	1.00 (0.00)
$\theta_{2,+y}/\theta_{2,+y}^{un}$	1.00	1.03 (1.34)	0.98 (4.53)	0.99 (0.00)
$\theta_{2,-x}/\theta_{2,-x}^{un}$	1.00	0.85 (4.28)	1.00 (4.52)	0.89 (0.00)
$\theta_{2,-y}/\theta_{2,-y}^{un}$	1.00	1.03 (1.15)	0.95 (4.61)	1.00 (0.00)
$\theta_{3,+x}/\theta_{3,+x}^{un}$	0.29	0.13 (7.42)	0.25 (22.75)	0.26 (0.002)
$\theta_{3,+y}/\theta_{3,+y}^{un}$	0.55	0.31 (3.94)	0.42 (8.90)	0.46 (0.00)
$\theta_{3,-x}/\theta_{3,-x}^{un}$	0.29	0.15 (5.66)	0.25 (23.13)	0.20 (0.003)
$\theta_{3,-y}/\theta_{3,-y}^{un}$	0.55	0.25 (7.03)	0.40 (8.69)	0.49 (0.00)
$\theta_{4,+x}/\theta_{4,+x}^{un}$	1.00	0.87 (1.11)	1.12 (5.56)	0.94 (0.00)
$\theta_{4,+y}/\theta_{4,+y}^{un}$	1.00	1.01 (0.24)	1.02 (2.33)	0.99 (0.00)
$\theta_{4,-x}/\theta_{4,-x}^{un}$	1.00	0.99 (0.88)	1.10 (5.58)	0.93 (0.00)
$\theta_{4,-y}/\theta_{4,-y}^{un}$	1.00	1.01 (0.18)	0.98 (2.42)	0.93 (0.00)

Table 5.27. Ratios of the MPVs of the stiffness parameters and their posterior c.o.v.'s (%) for Damage Scenario *iii* in Case 5

Parameters	Actual	Present Study	Algorithm 1	Algorithm 2
$\theta_{1,+x}/\theta_{1,+x}^{un}$	0.65	0.68 (6.04)	0.65 (8.74)	0.67 (0.001)
$\theta_{1,+y}/\theta_{1,+y}^{un}$	1.00	1.00 (6.04)	1.00 (3.59)	1.00 (0.00)
$\theta_{1,-x}/\theta_{1,-x}^{un}$	1.00	1.09 (3.72)	1.05 (4.84)	1.00 (0.00)
$\theta_{1,-y}/\theta_{1,-y}^{un}$	1.00	0.78 (5.42)	0.97 (3.45)	0.97 (0.00)
$\theta_{2,+x}/\theta_{2,+x}^{un}$	1.00	0.78 (5.42)	1.00 (7.98)	1.00 (0.00)
$\theta_{2,+y}/\theta_{2,+y}^{un}$	1.00	1.03 (1.35)	1.00 (6.76)	1.00 (0.00)
$\theta_{2,-x}/\theta_{2,-x}^{un}$	1.00	0.87 (5.45)	1.00 (6.76)	1.00 (0.00)
$\theta_{2,-y}/\theta_{2,-y}^{un}$	1.00	1.03 (1.26)	1.00 (6.53)	1.00 (0.00)
$\theta_{3,+x}/\theta_{3,+x}^{un}$	1.00	0.87 (1.60)	1.00 (8.81)	1.00 (0.00)
$\theta_{3,+y}/\theta_{3,+y}^{un}$	1.00	1.04 (1.24)	1.00 (7.00)	1.00 (0.00)
$\theta_{3,-x}/\theta_{3,-x}^{un}$	1.00	0.94 (1.53)	1.00 (7.70)	1.00 (0.00)
$\theta_{3,-y}/\theta_{3,-y}^{un}$	1.00	1.05 (1.72)	1.00 (6.55)	1.00 (0.001)
$\theta_{4,+x}/\theta_{4,+x}^{un}$	1.00	1.02 (1.32)	1.00 (10.28)	0.95 (0.00)
$\theta_{4,+y}/\theta_{4,+y}^{un}$	1.00	1.01 (0.54)	1.00 (5.78)	1.00 (0.00)
$\theta_{4,-x}/\theta_{4,-x}^{un}$	1.00	0.88 (1.60)	1.00 (9.28)	0.98 (0.00)
$\theta_{4,-y}/\theta_{4,-y}^{un}$	1.00	0.97 (0.47)	1.00 (6.31)	1.00 (0.00)

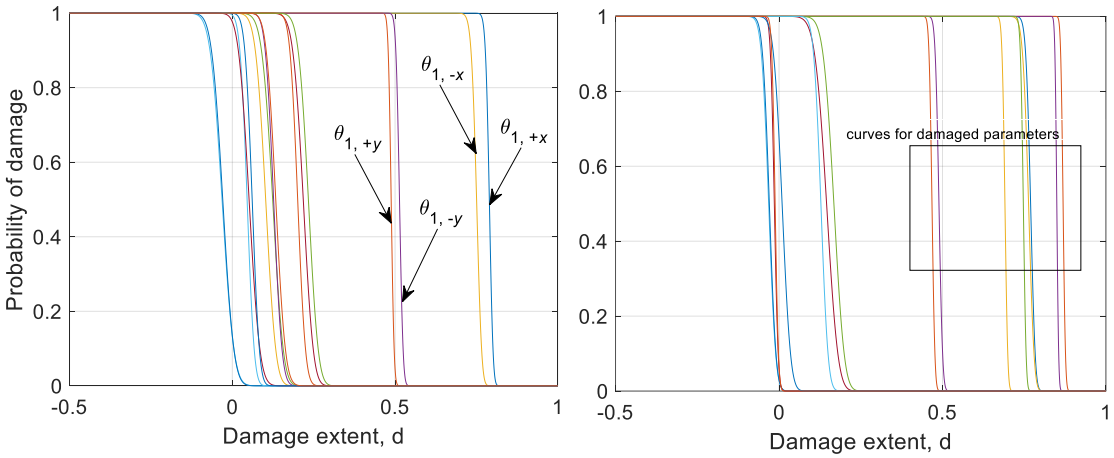

(a) Damage Scenario, *iii*

(b) Damage Scenario, *iv*

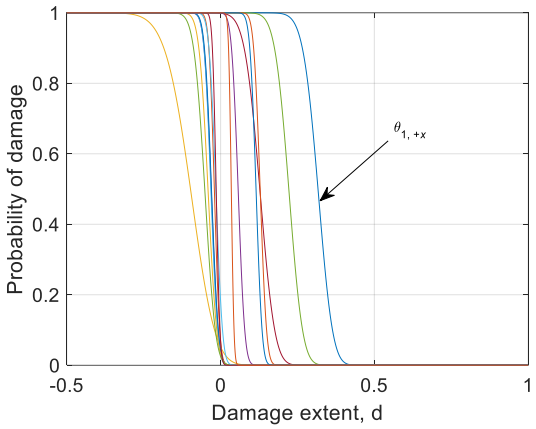

(c) Damage Scenario, *vi*

Figure 5.16. Probability of damage for the parameters in damage scenarios (a) *iii*, (b) *iv* and (c) *vi* for the present study (Case 5)

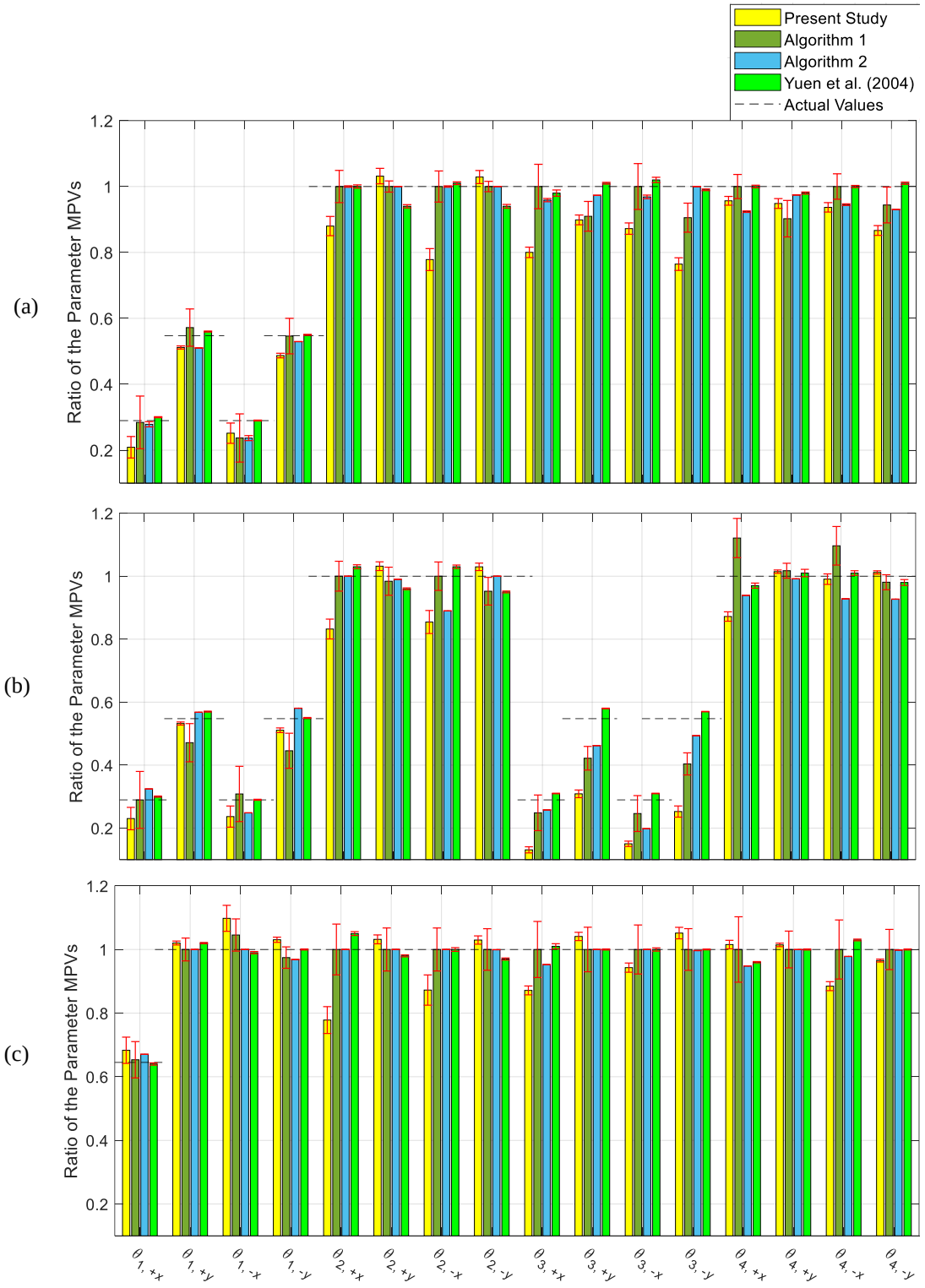

Figure 5.17. Ratios of stiffness scaling parameters with $\mp 1\sigma$ for Damage Scenarios (a) *iii*, (b) *iv* and (c) *vi* in Case 5

Table 5.28. Damage detection results of Case 5 for the present study

Damage Scenario	Actual Damage Location (Stiffness Loss)	Present Study Damage Location (Stiffness Loss)
i	First Floor (+*x* face) 71.03 % First Floor (-*x* face) 71.03 % First Floor (+y face) 45.24 % First Floor (-y face) 45.24 %	First Floor (+*x* face) 78.40 % First Floor (-*x* face) 74.15 % First Floor (+y face) 48.65 % First Floor (-y face) 51.15 % Some minor false damages exist on other faces
ii	First Floor (+*x* face) 71.03 % First Floor (-*x* face) 71.03 % First Floor (+y face) 45.24 % First Floor (-y face) 45.24 % Third Floor (+*x* face) 71.03 % Third Floor (-*x* face) 71.03 % Third Floor (+y face) 45.24 % Third Floor (-y face) 45.24 %	First Floor (+*x* face) 76.35 % First Floor (-*x* face) 75.45 % First Floor (+y face) 46.70 % First Floor (-y face) 48.70 % Third Floor (+*x* face) 86.80 % Third Floor (-*x* face) 84.90 % Third Floor (+y face) 68.85 % Third Floor (-y face) 74.45 % Some minor false damages exist on other faces
iii	First Floor (+*x* face) 35.49 %	First Floor 30.20 % Some major false damages exist on other faces

5.4. Conclusions

It is observed from the results of the previous chapters that the problem of having unreasonably small posterior c.o.v values of the MPVs of the stiffness parameters may stem from the FE models used in the numerical applications. The reason of this problem is linked to the fact that the previous models have no modelling errors. Therefore, in this chapter, a benchmark problem which includes modelling error in its analytical FE models is investigated to see the effects of modelling error on the updating results. Besides, previous chapters just focus on the estimation of MPVs of the parameters and no study is performed for a probabilistic damage identification. Therefore, in this chapter, the algorithms developed previously are applied on the benchmark problem since it includes different cases with various damage scenarios, which gives a chance to take the formulations a step further from parameter estimation to a damage detection process.

In the investigated benchmark problem, Case 1 includes no modelling error as in the previous chapters. However, the resulting posterior c.o.v levels in Case 1 are not as small as those encountered in the previous studies which have an order of 10^{-11}. Besides, the noise level is 10% in the present study while it is 20% in the previous studies. Therefore, it is concluded that damping ratio of the structure may be the parameter that is responsible for the posterior c.o.v. levels to be significantly small. The damping ratio is taken as 1% for all modes in the present study while it is taken as 0.1% in the previous studies. To this end, Case 1 is investigated under the same conditions with 20% noise level, 0.1% damping ratios for all modes and with the same duration of measurements. The results show that the c.o.v values decrease approximately from 3% to 0.05% for the present study. The same trend is observed for Algorithm 1 and 2. This result reveals that damping ratio is not only the parameter that is responsible for an order of 10^{-11} c.o.v values, but the posterior c.o.v values directly depend on the FE model itself.

The other conclusion is that modelling error affects all the investigated studies together with those in the literature. However, it is found that the results of the sensitivity-based Bayesian model updating procedure which is proposed in Chapter 4 are more prone to the modelling error when compared with the algorithms discussed in Chapter 3. This result is obtained by comparing the results of Case 2 and 5, which have

relatively larger modelling errors, with those of other cases that have no modelling error or relatively smaller one. It is observed that the present study gives relatively larger biased estimates of the MPVs of the stiffness parameters. This results in false detections of damage levels. Thus, the present study identifies false damage locations while the other algorithms can successfully identify the damage locations despite the biased results.

In the context of this study, the experimental Phase-II of the benchmark problem is also investigated with the same strategies followed in Phase-I. To do so, ambient acceleration measurements are used to obtain the experimental modal frequencies and mode shapes of the physical structure. The mass distribution of the physical structure is designed so that the mass center of each floor is shifted with a considerable amount from the geometrical center, and the amount of shift is also different for each floor. Therefore, even in the undamaged condition, the identified vibrational modes are found to be highly coupled. Therefore, the same 3-D 12-DOF torsional shear building model that is introduced in Case 3 is used as the identification model. However, any reasonable stiffness parameter values could not be obtained by using the two-stage sensitivity-based Bayesian model updating strategy when the mass is not considered as an updating variable. Then, the methodology is reformulated to include the mass as the parameter to be updated and it is already presented in Chapter 4. This significantly improves the updating results in a reasonable way. Besides, the Algorithms 1 and 2 give relatively reasonable updating results. However, identified damage extents and locations have various false detections. As a conclusion, it is thought that the modelling error between the physical structure and the analytical model is significantly high since the physical one is a moment-resisting frame and model is constructed by shear frame assumptions. It is already found in the numerical studies that all algorithms are affected by the modelling error, but the two-stage sensitivity-based Bayesian model updating method is more prone to this.

CHAPTER 6

CONCLUSIONS

Conclusions of each study have been already provided at the end of each chapter. In this section, a brief summary of remarkable findings and general concluding remarks are presented.

- In Chapter 2, the problems encountered in FE model updating are addressed when the single objective function is set as the weighted sums of the error functions. The literature has still no rational ways to assign weighing factors in such objective functions. To this end, a Bayesian inference method which already exists in the literature is investigated in detail. Further, the results are compared with those obtained from the frequentist approach. It is observed that the Bayesian inference method requires a large number of modal data set to give reasonable optimal weighting values. Frequentist approach also requires large number of samples. Therefore, the investigated method is not found to be practical.
- In Chapter 3, a two-stage Bayesian model updating technique is reformulated to make comparisons between three different modelling error assumptions. It is found that all investigated assumptions result in too small posterior c.o.v values. Besides, the presented Bayesian model updating strategy gives the smallest values among three of them. Having small posterior c.o.v is found to be unrealistic since there might be no need to make probabilistic analysis to get such small uncertainties. As the reason of this outcome, modelling error term and norm constraint terms in the objective function are blamed. Therefore, if these terms are omitted from the objective function, the resulting posterior c.o.v values should increase. This idea brings the development of the sensitivity-based Bayesian model updating method that is proposed in Chapter 4.
- In Chapter 4, a two-stage sensitivity-based Bayesian model updating method is proposed to bring the posterior c.o.v values to reasonable levels. For this purpose, a deterministic sensitivity-based approach which already exists in

the literature is modified to have a probabilistic Bayesian-based model updating procedure. To this end, the Hessian matrix is derived for the posterior uncertainty analysis of the updated parameters. Further, mass is included as the parameter to be updated to increase the robustness of the methodology. The results of the proposed method are compared to those obtained in Chapter 3. Comparisons reveal that the proposed methodology is successful to give posterior c.o.v values in reasonable levels when compared to the results of Chapter 3. One drawback of the proposed method is that the mode matching problem inevitably exists since the objective function is set by using the modes of the FE model instead of system modes.

- In Chapter 5, the two-stage sensitivity-based Bayesian model updating method proposed in Chapter 4 and the presented methods in Chapter 3 are implemented on a benchmark problem that has numerical and experimental phases. This benchmark problem also includes different damage scenarios. Therefore, in this chapter, probabilistic damage identification is also performed by using the investigated model updating techniques. The results reveal that the posterior c.o.v values are increased for all updating methods when compared to the results provided in previous chapters. Therefore, it is concluded that the posterior c.o.v levels are the modelling error level between FE model and measured structure. However, as in the previous comparisons, the proposed sensitivity-based Bayesian model updating method has resulted in the highest posterior c.o.v values which fulfills one of the main research objectives of this thesis.

APPENDIX A

DERIVATION OF HESSIAN MATRIX FOR THE BAYESIAN MODEL UPDATING METHOD UTILIZING THE CONCEPT OF SYSTEM MODES

Derivation of the the Hessian matrix in equation (3.58);

- Derivation of $\mathbf{J}^{(\boldsymbol{\lambda},\boldsymbol{\lambda})}$:

$\mathbf{J}^{(\boldsymbol{\lambda},\boldsymbol{\lambda})} = diag(\ J^{(\lambda_n,\lambda_n)}\ )$ is a diagonal matrix with a size of $N_m \times N_m$ and the n^{th} diagonal element is obtained as

$$\begin{aligned} J^{(\lambda_n,\lambda_n)} &= \left.\frac{\partial^2 J}{\partial \lambda_n^2}\right|_{\lambda_n=\lambda_n^*,\phi_n=\phi_n^*,\theta=\theta^*,S_{eq,n}=S_{eq,n}^*} \\ &= S_{eq,n}^{*-1}\boldsymbol{\phi}_n^{*T}\mathbf{M}^T\mathbf{M}\boldsymbol{\phi}_n^* + S_{\hat{\lambda}_n}^{-1} \\ &= S_{eq,n}^{*-1}G_{\lambda_n} + S_{\hat{\lambda}_n}^{-1} \end{aligned} \tag{A.1}$$

- Derivation of $\mathbf{J}^{(\boldsymbol{\lambda},\boldsymbol{\Phi})}$:

$$\frac{\partial J}{\partial \lambda_n} = -S_{eq,n}^{-1}\boldsymbol{\phi}_n^T\mathbf{K}(\boldsymbol{\theta})^T\mathbf{M}\boldsymbol{\phi}_n + S_{eq,n}^{-1}\boldsymbol{\phi}_n^T\mathbf{M}^T\mathbf{M}\boldsymbol{\phi}_n\lambda_n - S_{\hat{\lambda}_n}^{-1}\hat{\lambda}_n + S_{\hat{\lambda}_n}^{-1}\lambda_n$$

$\mathbf{J}^{(\boldsymbol{\lambda},\boldsymbol{\Phi})} = diag(\ \mathbf{J}^{(\lambda_n,\boldsymbol{\phi}_n)}\ )$ is a block diagonal matrix with a size of $N_m \times N_d N_m$ and the n^{th} row vector is obtained as

$$\begin{aligned} \mathbf{J}^{(\lambda_n,\boldsymbol{\phi}_n)} &= \left.\frac{\partial^2 J}{\partial \lambda_n \partial \boldsymbol{\phi}_n}\right|_{\lambda_n=\lambda_n^*,\boldsymbol{\phi}_n=\boldsymbol{\phi}_n^*,\theta=\theta^*,S_{eq,n}=S_{eq,n}^*} \\ &= -2S_{eq,n}^{*-1}\boldsymbol{\phi}_n^{*T}\left[\mathbf{K}(\boldsymbol{\theta}^*) - \lambda_n^*\mathbf{M}\right]^T\mathbf{M} \end{aligned} \tag{A.2}$$

- Derivation of $\mathbf{J}^{(\boldsymbol{\theta},\boldsymbol{\lambda})}$:

$$\mathbf{J}^{(\boldsymbol{\theta},\lambda)} = \left[\mathbf{J}^{(\boldsymbol{\theta},\lambda_1)} \quad \cdots \quad \mathbf{J}^{(\boldsymbol{\theta},\lambda_n)} \quad \cdots \quad \mathbf{J}^{(\boldsymbol{\theta},\lambda_{N_m})} \right]_{N_\theta \times N_m}$$

where the n^{th} column vector is obtained as

$$\begin{aligned} \mathbf{J}^{(\boldsymbol{\theta},\lambda_n)} &= \left. \frac{\partial^2 J}{\partial \boldsymbol{\theta} \partial \lambda_n} \right|_{\lambda_n=\lambda_n^*, \boldsymbol{\phi}=\boldsymbol{\phi}_n^*, \theta=\theta^*, S_{eq,n}=S_{eq,n}^*} \\ &= -\sum_{i=1}^{N_\theta} S_{eq,n}^{*-1} (\mathbf{K}_i \boldsymbol{\phi}_n^*)^T \mathbf{M} \boldsymbol{\phi}_n^* \\ &= -S_{eq,n}^{*-1} \mathbf{G}_{K_n}^T \mathbf{M} \boldsymbol{\phi}_n^* \end{aligned} \tag{A.3}$$

- Derivation of $\mathbf{J}^{(\boldsymbol{\Phi},\boldsymbol{\Phi})}$:

$\mathbf{J}^{(\boldsymbol{\Phi},\boldsymbol{\Phi})} = diag(\ \mathbf{J}^{(\boldsymbol{\phi}_n,\boldsymbol{\phi}_n)}\ )$ is a block diagonal matrix with a size of $N_d N_m \times N_d N_m$ and the n^{th} block matrix is evaluated as

$$\begin{aligned} \mathbf{J}^{(\boldsymbol{\phi}_n,\boldsymbol{\phi}_n)} &= \left. \frac{\partial^2 J}{\partial \boldsymbol{\phi}_n^2} \right|_{\lambda=\lambda_n^*, \boldsymbol{\phi}_n=\boldsymbol{\phi}_n^*, \boldsymbol{\theta}=\boldsymbol{\theta}^*, S_{eq,n}=S_{eq,n}^*} \\ &= S_{eq,n}^{*-1} \boldsymbol{\Gamma}_n^{*T} \boldsymbol{\Gamma}_n^* + \eta_n^{*-2} \mathbf{L}_0^T \mathbf{H}_{\hat{\phi}_n} \mathbf{L}_0 + 2\alpha_n^* \mathbf{L}_0^T \mathbf{L}_0 - 2\beta_n^* \mathbf{I}_{N_d} \\ &= 2\mathbf{A}_n^* - 2\beta_n^* \mathbf{I}_{N_d} \end{aligned} \tag{A.4}$$

- Derivation of $\mathbf{J}^{(\boldsymbol{\theta},\boldsymbol{\Phi})}$:

$$\mathbf{J}^{(\boldsymbol{\theta},\boldsymbol{\Phi})} = \left[\mathbf{J}^{(\boldsymbol{\theta},\boldsymbol{\phi}_1)} \quad \cdots \quad \mathbf{J}^{(\boldsymbol{\theta},\boldsymbol{\phi}_n)} \quad \cdots \quad \mathbf{J}^{(\boldsymbol{\theta},\boldsymbol{\phi}_{N_m})} \right]_{N_\theta \times N_d N_m}$$

where the n^{th} block matrix is obtained as

$$\mathbf{J}^{(\boldsymbol{\theta},\boldsymbol{\phi}_n)} = \begin{bmatrix} \mathbf{J}^{(\boldsymbol{\phi}_1,\boldsymbol{\phi}_n)} \\ \mathbf{J}^{(\boldsymbol{\phi}_i,\boldsymbol{\phi}_n)} \\ \mathbf{J}^{(\boldsymbol{\phi}_{N_\theta},\boldsymbol{\phi}_n)} \end{bmatrix}$$

and the i^{th} row vector is calculated as

$$\begin{aligned} \mathbf{J}^{(\theta_i,\boldsymbol{\phi}_n)} &= \left.\frac{\partial^2 J}{\partial\theta_i\partial\boldsymbol{\phi}_n}\right|_{\lambda_n=\lambda_n^*,\boldsymbol{\phi}_n=\boldsymbol{\phi}_n^*,\boldsymbol{\theta}=\boldsymbol{\theta}^*,S_{eq,n}=S^*_{eq,n}} \\ &= 2S_{eq,n}^{*-1}\boldsymbol{\phi}_n^{*T}(\mathbf{K}_0^T + \sum_{i=1}^{N_\theta}\mathbf{K}_i^T\theta_i^{*T} - \lambda_n^*\mathbf{M}^T)\mathbf{K}_i \\ &= 2S_{eq}^{*-1}\boldsymbol{\phi}_n^{*T}\boldsymbol{\Gamma}_n^{*T}\mathbf{K}_i \end{aligned} \tag{A.5}$$

- Derivation of $\mathbf{J}^{(\boldsymbol{\theta},\boldsymbol{\theta})}$:

$$\begin{aligned} J^{(\boldsymbol{\theta},\boldsymbol{\theta})} &= \left.\frac{\partial^2 J}{\partial\boldsymbol{\theta}^2}\right|_{\lambda=\lambda^*,\boldsymbol{\phi}_n=\boldsymbol{\phi}_n^*,\boldsymbol{\theta}=\boldsymbol{\theta}^*,S_{eq,n}=S^*_{eq,n}} \\ &= \Sigma_{\boldsymbol{\theta}}^{-1} + \sum_{n=1}^{N_m} S_{eq,n}^{*-1}\mathbf{G}_{K_n}^T\mathbf{G}_{K_n} \end{aligned} \tag{A.6}$$

- Derivation of $\mathbf{J}^{(\boldsymbol{\lambda},\mathbf{S_{eq}})}$:

$\mathbf{J}^{(\boldsymbol{\lambda},\mathbf{S_{eq}})} = diag(\ J^{(\lambda_n,\,S_{eq,n})}\ )$ is a diagonal matrix with a size of $N_m \times N_m$ and the n^{th} diagonal element is obtained as

$$J^{(\lambda_n, S_{eq,n})} = \left.\frac{\partial^2 J}{\partial \lambda_n \partial S_{eq,n}}\right|_{\lambda_n=\lambda_n^*, \boldsymbol{\phi}_n=\boldsymbol{\phi}_n^*, \boldsymbol{\theta}=\boldsymbol{\theta}^*, S_{eq,n}=S_{eq,n}^*}$$
$$= \underbrace{\boldsymbol{\phi}_n^T \mathbf{K}^T \mathbf{M} \boldsymbol{\phi}_n}_{g_{\lambda_n}} S_{eq,n}^{-2} - \underbrace{\boldsymbol{\phi}_n^T \mathbf{M}^T \mathbf{M} \boldsymbol{\phi}_n}_{G_{\lambda_n}} S_{eq,n}^{-2} \lambda_n \tag{A.7}$$
$$= S_{eq,n}^{*-2} (g_{\lambda_n} - G_{\lambda_n} \lambda_n^*)$$

- Derivation of $\mathbf{J}^{(\boldsymbol{\Phi}, \mathbf{S_{eq}})}$:

$\mathbf{J}^{(\boldsymbol{\Phi}, \mathbf{S_{eq}})} = diag(\ \mathbf{J}^{(\boldsymbol{\phi}_n, S_{eq,n})}\ )$ is a block diagonal matrix with a size of $N_d N_m \times N_m$ and the n^{th} block vector is obtained as

$$\mathbf{J}^{(\boldsymbol{\phi}_n, S_{eq,n})} = \left.\frac{\partial^2 J}{\partial \boldsymbol{\phi}_n \partial S_{eq,n}}\right|_{\lambda_n=\lambda_n^*, \boldsymbol{\phi}_n=\boldsymbol{\phi}_n^*, \boldsymbol{\theta}=\boldsymbol{\theta}^*, S_{eq,n}=S_{eq,n}^*} \tag{A.8}$$
$$= -S_{eq,n}^{*-2} \boldsymbol{\Gamma}_n^{*T} \boldsymbol{\Gamma}_n^* \boldsymbol{\phi}_n^*$$

- Derivation of $\mathbf{J}^{(\boldsymbol{\theta}, \mathbf{S_{eq}})}$:

$$\mathbf{J}^{(\boldsymbol{\theta}, \mathbf{S_{eq}})} = \left[\ \mathbf{J}^{(\boldsymbol{\theta}, S_{eq,1})} \quad \cdots \quad \mathbf{J}^{(\boldsymbol{\theta}, S_{eq,n})} \quad \cdots \quad \mathbf{J}^{(\boldsymbol{\theta}, S_{eq,N_m})}\ \right]_{N_\theta \times N_m}$$

where the n^{th} column vector is obtained as

$$\mathbf{J}^{(\boldsymbol{\theta}, S_{eq,n})} = \left.\frac{\partial^2 J}{\partial \boldsymbol{\theta} \partial S_{eq,n}}\right|_{\lambda_n=\lambda_n^*, \boldsymbol{\phi}_n=\boldsymbol{\phi}_n^*, \boldsymbol{\theta}=\boldsymbol{\theta}^*, S_{eq,n}=S_{eq,n}^*} \tag{A.9}$$
$$= -S_{eq,n}^{*-2} \mathbf{G}_{K_n}^T \mathbf{G}_{K_n} \boldsymbol{\theta}^* + S_{eq,n}^{*-2} \mathbf{G}_{K_n}^T \mathbf{g}_{K_n}$$

- Derivation of $\mathbf{J}^{(\mathbf{S_{eq}}, \mathbf{S_{eq}})}$:

$\mathbf{J}^{(\mathbf{S_{eq}}, \mathbf{S_{eq}})} = diag(\ J^{(S_{eq,n}, S_{eq,n})}\ )$ is a diagonal matrix with a size of $N_m \times N_m$ and the n^{th} diagonal element is obtained as

$$
\begin{aligned}
J\left(S_{eq,n}\ ,\ S_{eq,n}\right) &= \left.\frac{\partial^2 J}{\partial S_{eq,n}^2}\right|_{\lambda_n=\lambda_n^*,\boldsymbol{\phi}_n=\boldsymbol{\phi}_n^*,\boldsymbol{\theta}=\boldsymbol{\theta}^*,S_{eq,n}=S^*_{eq,n}} \\
&= -\frac{1}{2}N_d S_{eq,n}^{*-2} + S_{eq,n}^{*-3}\boldsymbol{\phi}_n^{*T}\boldsymbol{\Gamma}_n^{*T}\boldsymbol{\Gamma}_n^*\boldsymbol{\phi}_n^* \\
&= -\frac{1}{2}N_d S_{eq,n}^{*-2} + S_{eq,n}^{*-3}\left\|\boldsymbol{\Gamma}_n^*\boldsymbol{\phi}_n^*\right\|^2
\end{aligned}
\tag{A.10}
$$

APPENDIX B

DERIVATION OF HESSIAN OF EIGENVALUES AND EIGENVECTORS FOR THE SENSITIVITY-BASED BAYESIAN MODEL UPDATING METHOD

This Appendix provides the derivations of Hessian of eigenvalues and eigenvectors with respect to the stiffness and mass parameters for the sensitivity-based Bayesian model updating method proposed in Chapter 4.

Defining the eigenvalue equation for the n^{th} mode

$$\left[\mathbf{K}(\boldsymbol{\theta}) - \lambda_n(\boldsymbol{\chi})\mathbf{M}(\boldsymbol{\rho})\right]\boldsymbol{\phi}_n(\boldsymbol{\chi}) = \mathbf{0} \tag{B.1}$$

- **Differentiation with respect to θ_i and θ_m**

Differentiating equation (B.1) with respect to θ_i gives the following expression

$$\left[\mathbf{K}_i - \frac{\partial\lambda_n(\boldsymbol{\chi})}{\partial\theta_i}\mathbf{M}(\boldsymbol{\rho})\right]\boldsymbol{\phi}_n(\boldsymbol{\chi}) + \left[\mathbf{K}(\boldsymbol{\theta}) - \lambda_n(\boldsymbol{\chi})\mathbf{M}(\boldsymbol{\rho})\right]\frac{\partial\boldsymbol{\phi}_n(\boldsymbol{\chi})}{\partial\theta_i} = \mathbf{0} \tag{B.2}$$

Then, differentiating equation (B.2) with respect to θ_m gives the following expression

$$\begin{aligned}\left[-\frac{\partial^2\lambda_n(\boldsymbol{\chi})}{\partial\theta_i\partial\theta_m}\mathbf{M}(\boldsymbol{\rho})\right]\boldsymbol{\phi}_n(\boldsymbol{\theta}) + \left[\mathbf{K}_i - \frac{\partial\lambda_n(\boldsymbol{\chi})}{\partial\theta_i}\mathbf{M}(\boldsymbol{\rho})\right]\frac{\partial\boldsymbol{\phi}_n(\boldsymbol{\chi})}{\partial\theta_m} \\ + \left[\frac{\partial\mathbf{K}(\boldsymbol{\theta})}{\partial\theta_m} - \frac{\partial\lambda_n(\boldsymbol{\chi})}{\partial\theta_m}\mathbf{M}(\boldsymbol{\rho})\right]\frac{\partial\boldsymbol{\phi}_n(\boldsymbol{\chi})}{\partial\theta_i} + \left[\mathbf{K}(\boldsymbol{\theta}) - \lambda_n(\boldsymbol{\chi})\mathbf{M}(\boldsymbol{\rho})\right]\frac{\partial^2\boldsymbol{\phi}_n(\boldsymbol{\chi})}{\partial\theta_i\partial\theta_m} = \mathbf{0}\end{aligned} \tag{B.3}$$

Pre-multiplying equation (B.3) by $\boldsymbol{\phi}_n^T(\boldsymbol{\chi})$;

$$\begin{aligned}\boldsymbol{\phi}_n^T(\boldsymbol{\chi})\left[-\frac{\partial^2\lambda_n(\boldsymbol{\chi})}{\partial\theta_i\partial\theta_m}\mathbf{M}(\boldsymbol{\rho})\right]\boldsymbol{\phi}_n(\boldsymbol{\chi})+\boldsymbol{\phi}_n^T(\boldsymbol{\chi})\left[\mathbf{K}_i-\frac{\partial\lambda_n(\boldsymbol{\chi})}{\partial\theta_i}\mathbf{M}(\boldsymbol{\rho})\right]\frac{\partial\boldsymbol{\phi}_n(\boldsymbol{\chi})}{\partial\theta_m}\\ +\boldsymbol{\phi}_n^T(\boldsymbol{\chi})\left[\frac{\partial\mathbf{K}(\boldsymbol{\theta})}{\partial\theta_m}-\frac{\partial\lambda_n(\boldsymbol{\chi})}{\partial\theta_m}\mathbf{M}(\boldsymbol{\rho})\right]\frac{\partial\boldsymbol{\phi}_n(\boldsymbol{\chi})}{\partial\theta_i}\\ +\boldsymbol{\phi}_n^T(\boldsymbol{\chi})\left[\mathbf{K}(\boldsymbol{\theta})-\lambda_n(\boldsymbol{\chi})\mathbf{M}(\boldsymbol{\rho})\right]\frac{\partial^2\boldsymbol{\phi}_n(\boldsymbol{\chi})}{\partial\theta_i\partial\theta_m}=\mathbf{0}\end{aligned} \tag{B.4}$$

Since $\boldsymbol{\phi}_n^T(\boldsymbol{\chi})$ is the left eigenvector of the matrix $\mathbf{K}(\boldsymbol{\theta})-\lambda_n(\boldsymbol{\chi})\mathbf{M}(\boldsymbol{\rho})$ in equation (B.4), last term of the left side of the equation is zero. Then, rearranging equation (B.4);

$$\begin{aligned}-\frac{\partial^2\lambda_n(\boldsymbol{\chi})}{\partial\theta_i\partial\theta_m}\boldsymbol{\phi}_n^T(\boldsymbol{\chi})\mathbf{M}(\boldsymbol{\rho})\boldsymbol{\phi}_n(\boldsymbol{\chi})+\boldsymbol{\phi}_n^T(\boldsymbol{\chi})\left[\mathbf{K}_i-\frac{\partial\lambda_n(\boldsymbol{\chi})}{\partial\theta_i}\mathbf{M}(\boldsymbol{\rho})\right]\frac{\partial\boldsymbol{\phi}_n(\boldsymbol{\chi})}{\partial\theta_m}\\ +\boldsymbol{\phi}_n^T(\boldsymbol{\chi})\left[\mathbf{K}_m-\frac{\partial\lambda_n(\boldsymbol{\chi})}{\partial\theta_m}\mathbf{M}(\boldsymbol{\rho})\right]\frac{\partial\boldsymbol{\phi}_n(\boldsymbol{\chi})}{\partial\theta_i}=\mathbf{0}\end{aligned} \tag{B.5}$$

By rearranging equation (B.5), Hessian of the eigenvalue of the n^{th} mode can be obtained as

$$\frac{\partial^2\lambda_n(\boldsymbol{\chi})}{\partial\theta_i\partial\theta_m}=\frac{\boldsymbol{\phi}_n^T(\boldsymbol{\chi})\left[\mathbf{K}_i-\frac{\partial\lambda_n(\boldsymbol{\chi})}{\partial\theta_i}\mathbf{M}(\boldsymbol{\rho})\right]\frac{\partial\boldsymbol{\phi}_n(\boldsymbol{\chi})}{\partial\theta_m}+\boldsymbol{\phi}_n^T(\boldsymbol{\chi})\left[\mathbf{K}_m-\frac{\partial\lambda_n(\boldsymbol{\chi})}{\partial\theta_m}\mathbf{M}(\boldsymbol{\rho})\right]\frac{\partial\boldsymbol{\phi}_n(\boldsymbol{\chi})}{\partial\theta_i}}{\boldsymbol{\phi}_n^T(\boldsymbol{\chi})\mathbf{M}(\boldsymbol{\rho})\boldsymbol{\phi}_n(\boldsymbol{\chi})} \tag{B.6}$$

Equation (B.3) is rearranged to solve for the Hessian of the eigenvector of the n^{th} mode as

$$\begin{aligned}\left[\mathbf{K}(\boldsymbol{\theta})-\lambda_n(\boldsymbol{\chi})\mathbf{M}(\boldsymbol{\rho})\right]&\frac{\partial^2\boldsymbol{\phi}_n(\boldsymbol{\chi})}{\partial\theta_i\partial\theta_m}\\ &=\frac{\partial^2\lambda_n(\boldsymbol{\chi})}{\partial\theta_i\partial\theta_m}\mathbf{M}(\boldsymbol{\rho})\boldsymbol{\phi}_n(\boldsymbol{\chi})-\left[\mathbf{K}_i-\frac{\partial\lambda_n(\boldsymbol{\chi})}{\partial\theta_i}\mathbf{M}(\boldsymbol{\rho})\right]\frac{\partial\boldsymbol{\phi}_n(\boldsymbol{\chi})}{\partial\theta_m}\\ &\quad-\left[\mathbf{K}_m-\frac{\partial\lambda_n(\boldsymbol{\chi})}{\partial\theta_m}\mathbf{M}(\boldsymbol{\rho})\right]\frac{\partial\boldsymbol{\phi}_n(\boldsymbol{\chi})}{\partial\theta_i}\end{aligned} \tag{B.7}$$

However, Hessian of the eigenvectors cannot be obtained by using equation (B.7) since the matrix $\mathbf{K}(\boldsymbol{\theta})-\lambda_n(\boldsymbol{\chi})\mathbf{M}(\boldsymbol{\rho})$ on the left-hand side is a rank deficient one. Therefore, rank deficiency problem is solved by the same procedure that is performed for the calculation of the Jacobian of eigenvectors in Section 4.2.3.2. Accordingly, since the Jacobian of the h_n^{th} coordinate of $\bar{\boldsymbol{\phi}}_n(\boldsymbol{\chi})$ and since the Jacobian of the a_n^{th} coordinate of $\boldsymbol{\phi}_n(\boldsymbol{\theta})$ are zeros (See equation (4.49)), the Hessian of these coordinates are also zeros. Then,

$$\frac{\partial^2\bar{\boldsymbol{\phi}}_{h_n,n}(\boldsymbol{\chi})}{\partial\theta_i\partial\theta_m}=0 \quad\text{and}\quad \frac{\partial^2\boldsymbol{\phi}_{a_n,n}(\boldsymbol{\chi})}{\partial\theta_i\partial\theta_m}=0 \tag{B.8}$$

The transformation in equation (4.50) is substituted into the left-hand side of equation (B.7). Further, $\partial^2\tilde{\mathbf{1}}\,/\,\partial\theta_i\,\partial\theta_m$ is a zero vector, and the following equation is obtained as

$$\left[\mathbf{K}(\boldsymbol{\theta})-\lambda_n(\boldsymbol{\chi})\mathbf{M}(\boldsymbol{\rho})\right]\mathbf{A}_n\frac{\partial^2\bar{\boldsymbol{\phi}}_n(\boldsymbol{\chi})}{\partial\theta_i\partial\theta_m}=\mathbf{d}_{nim} \tag{B.9}$$

where $\mathbf{d}_{nim}$ represents the right-hand side of equation (B.7) as

$$\begin{aligned}\mathbf{d}_{nim}=\frac{\partial^2\lambda_n(\boldsymbol{\chi})}{\partial\theta_i\partial\theta_m}\mathbf{M}(\boldsymbol{\rho})\boldsymbol{\phi}_n(\boldsymbol{\chi})&-\left[\mathbf{K}_i-\frac{\partial\lambda_n(\boldsymbol{\chi})}{\partial\theta_i}\mathbf{M}(\boldsymbol{\rho})\right]\frac{\partial\boldsymbol{\phi}_n(\boldsymbol{\chi})}{\partial\theta_m}\\ &-\left[\mathbf{K}_m-\frac{\partial\lambda_n(\boldsymbol{\chi})}{\partial\theta_m}\mathbf{M}(\boldsymbol{\rho})\right]\frac{\partial\boldsymbol{\phi}_n(\boldsymbol{\chi})}{\partial\theta_i}\end{aligned} \tag{B.10}$$

Similar to Section 4.2.3.2, equation (B.9) is pre-multiplied by $\mathbf{A}_n^T$ as

$$\mathbf{A}_n^T\left[\mathbf{K}(\boldsymbol{\theta})-\lambda_n(\boldsymbol{\chi})\mathbf{M}(\boldsymbol{\rho})\right]\mathbf{A}_n\frac{\partial^2\boldsymbol{\phi}_n^-(\boldsymbol{\chi})}{\partial\theta_i\partial\theta_m}=\mathbf{A}_n^T\mathbf{d}_{nim} \tag{B.11}$$

and one can obtain $\partial^2\boldsymbol{\phi}_n^-(\boldsymbol{\chi})\,/\,\partial\theta_i\,\partial\theta_m$ as

$$\frac{\partial^2\boldsymbol{\phi}_n^-(\boldsymbol{\chi})}{\partial\theta_i\partial\theta_m}=\left(\mathbf{A}_n^T\left[\mathbf{K}(\boldsymbol{\theta})-\lambda_n(\boldsymbol{\chi})\mathbf{M}(\boldsymbol{\rho})\right]\mathbf{A}_n\right)^{-1}\left(\mathbf{A}_n^T\mathbf{d}_{nim}\right) \tag{B.12}$$

Then, Hessian of the n^{th} mode shape vector, $\partial^2\boldsymbol{\phi}_n(\boldsymbol{\chi})\,/\,\partial\theta_i\,\partial\theta_m$, can be obtained as

$$\frac{\partial^2\boldsymbol{\phi}_n(\boldsymbol{\chi})}{\partial\theta_i\partial\theta_m}=\mathbf{A}_n\frac{\partial^2\boldsymbol{\phi}_n^-(\boldsymbol{\chi})}{\partial\theta_i\partial\theta_m} \tag{B.13}$$

- **Differentiation with respect to θ_i and ρ_j**

  Differentiating equation (B.2) with respect to ρ_j gives the following expression

$$\begin{aligned}\left[-\frac{\partial^2\lambda_n(\boldsymbol{\chi})}{\partial\theta_i\partial\rho_j}\mathbf{M}(\boldsymbol{\rho})-\frac{\partial\lambda_n(\boldsymbol{\chi})}{\partial\theta_i}\mathbf{M}_j\right]\boldsymbol{\phi}_n(\boldsymbol{\chi})&\\ +\left[\mathbf{K}_i-\frac{\partial\lambda_n(\boldsymbol{\chi})}{\partial\theta_i}\mathbf{M}(\boldsymbol{\rho})\right]\frac{\partial\boldsymbol{\phi}_n(\boldsymbol{\chi})}{\partial\rho_j}&\\ -\left[\frac{\partial\lambda_n(\boldsymbol{\chi})}{\partial\rho_j}\mathbf{M}(\boldsymbol{\rho})+\lambda_n(\boldsymbol{\chi})\mathbf{M}_j\right]\frac{\partial\boldsymbol{\phi}_n(\boldsymbol{\chi})}{\partial\theta_i}&\\ +\left[\mathbf{K}(\boldsymbol{\theta})-\lambda_n(\boldsymbol{\chi})\mathbf{M}(\boldsymbol{\rho})\right]\frac{\partial^2\boldsymbol{\phi}_n(\boldsymbol{\chi})}{\partial\theta_i\partial\rho_j}=\mathbf{0}&\end{aligned} \tag{B.14}$$

Pre-multiplying equation (B.14) by $\boldsymbol{\phi}_n^T(\boldsymbol{\chi})$;

$$
\begin{aligned}
&-\frac{\partial^2\lambda_n(\boldsymbol{\chi})}{\partial\theta_i\partial\rho_j}\boldsymbol{\phi}_n^T(\boldsymbol{\chi})\mathbf{M}(\boldsymbol{\rho})\boldsymbol{\phi}_n(\boldsymbol{\chi})-\frac{\partial\lambda_n(\boldsymbol{\chi})}{\partial\theta_i}\boldsymbol{\phi}_n^T(\boldsymbol{\chi})\mathbf{M}_j\boldsymbol{\phi}_n(\boldsymbol{\chi}) \\
&\qquad+\boldsymbol{\phi}_n^T(\boldsymbol{\chi})\left[\mathbf{K}_i-\frac{\partial\lambda_n(\boldsymbol{\chi})}{\partial\theta_i}\mathbf{M}(\boldsymbol{\rho})\right]\frac{\partial\boldsymbol{\phi}_n(\boldsymbol{\chi})}{\partial\rho_j} \\
&\qquad-\boldsymbol{\phi}_n^T(\boldsymbol{\chi})\left[\frac{\partial\lambda_n(\boldsymbol{\chi})}{\partial\rho_j}\mathbf{M}(\boldsymbol{\rho})+\lambda_n(\boldsymbol{\chi})\mathbf{M}_j\right]\frac{\partial\boldsymbol{\phi}_n(\boldsymbol{\chi})}{\partial\theta_i} \\
&\qquad+\boldsymbol{\phi}_n^T(\boldsymbol{\chi})\left[\mathbf{K}(\boldsymbol{\theta})-\lambda_n(\boldsymbol{\chi})\mathbf{M}(\boldsymbol{\rho})\right]\frac{\partial^2\boldsymbol{\phi}_n(\boldsymbol{\chi})}{\partial\theta_i\partial\rho_j}=\mathbf{0}
\end{aligned}
\tag{B.15}
$$

Since $\boldsymbol{\phi}_n^T(\boldsymbol{\chi})$ is the left eigenvector of the matrix $\mathbf{K}(\boldsymbol{\theta})-\lambda_n(\boldsymbol{\chi})\mathbf{M}(\boldsymbol{\rho})$ in equation (B.15), last term of the left side of the equation is zero. Then, rearranging equation (B.15), Hessian of the eigenvalue of the n^{th} mode can be obtained as

$$
\begin{aligned}
\frac{\partial^2\lambda_n(\boldsymbol{\chi})}{\partial\theta_i\partial\rho_j}=\frac{\begin{aligned}
&-\frac{\partial\lambda_n(\boldsymbol{\chi})}{\partial\theta_i}\boldsymbol{\phi}_n^T(\boldsymbol{\chi})\mathbf{M}_j\boldsymbol{\phi}_n(\boldsymbol{\chi}) \\
&\qquad+\boldsymbol{\phi}_n^T(\boldsymbol{\chi})\left[\mathbf{K}_i-\frac{\partial\lambda_n(\boldsymbol{\chi})}{\partial\theta_i}\mathbf{M}(\boldsymbol{\rho})\right]\frac{\partial\boldsymbol{\phi}_n(\boldsymbol{\chi})}{\partial\rho_j} \\
&\qquad-\boldsymbol{\phi}_n^T(\boldsymbol{\chi})\left[\frac{\partial\lambda_n(\boldsymbol{\chi})}{\partial\rho_j}\mathbf{M}(\boldsymbol{\rho})+\lambda_n(\boldsymbol{\chi})\mathbf{M}_j\right]\frac{\partial\boldsymbol{\phi}_n(\boldsymbol{\chi})}{\partial\theta_i}
\end{aligned}}{\boldsymbol{\phi}_n^T(\boldsymbol{\chi})\mathbf{M}(\boldsymbol{\rho})\boldsymbol{\phi}_n(\boldsymbol{\chi})}
\end{aligned}
\tag{B.16}
$$

Equation (B.14) is rearranged to solve for the Hessian of the eigenvector of the n^{th} mode as

$$\left[\mathbf{K}(\boldsymbol{\theta})-\lambda_n(\boldsymbol{\chi})\mathbf{M}(\boldsymbol{\rho})\right]\frac{\partial^2\boldsymbol{\phi}_n(\boldsymbol{\chi})}{\partial\theta_i\partial\rho_j}=\left[\frac{\partial^2\lambda_n(\boldsymbol{\chi})}{\partial\theta_i\partial\rho_j}\mathbf{M}(\boldsymbol{\rho})+\frac{\partial\lambda_n(\boldsymbol{\chi})}{\partial\theta_i}\mathbf{M}_j\right]\boldsymbol{\phi}_n(\boldsymbol{\chi}) - \left[\mathbf{K}_i-\frac{\partial\lambda_n(\boldsymbol{\chi})}{\partial\theta_i}\mathbf{M}(\boldsymbol{\rho})\right]\frac{\partial\boldsymbol{\phi}_n(\boldsymbol{\chi})}{\partial\rho_j} + \left[\frac{\partial\lambda_n(\boldsymbol{\chi})}{\partial\rho_j}\mathbf{M}(\boldsymbol{\rho})+\lambda_n(\boldsymbol{\chi})\mathbf{M}_j\right]\frac{\partial\boldsymbol{\phi}_n(\boldsymbol{\chi})}{\partial\theta_i} \tag{B.17}$$

However, Hessian of the eigenvectors cannot be obtained by using equation (B.17) since the matrix $\mathbf{K}(\boldsymbol{\theta})-\lambda_n(\boldsymbol{\chi})\mathbf{M}(\boldsymbol{\rho})$ on the left-hand side is a rank deficient one. Therefore, rank deficiency problem is solved by the same procedure that is performed for the calculation of the Jacobian of eigenvectors in Section 4.2.3.2. Accordingly, since the Jacobian of the h_n^{th} coordinate of $\bar{\boldsymbol{\phi}}_n(\boldsymbol{\chi})$ and since the Jacobian of the a_n^{th} coordinate of $\boldsymbol{\phi}_n(\boldsymbol{\theta})$ are zeros (See equation (4.49)), the Hessian of these coordinates are also zeros. Then,

$$\frac{\partial^2\bar{\boldsymbol{\phi}}_{h_n,n}(\boldsymbol{\chi})}{\partial\theta_i\partial\rho_j}=0 \quad \text{and} \quad \frac{\partial^2\boldsymbol{\phi}_{a_n,n}(\boldsymbol{\chi})}{\partial\partial\theta_i\partial\rho_j}=0 \tag{B.18}$$

The transformation in equation (4.50) is substituted into the left-hand side of equation (B.17). Further, $\partial^2\tilde{\mathbf{1}}\,/\,\partial\theta_i\,\partial\rho_j$ is a zero vector, and the following equation is obtained as

$$\left[\mathbf{K}(\boldsymbol{\theta})-\lambda_n(\boldsymbol{\chi})\mathbf{M}(\boldsymbol{\rho})\right]\mathbf{A}_n\frac{\partial^2\boldsymbol{\phi}_n^-(\boldsymbol{\chi})}{\partial\theta_i\partial\rho_j}=\mathbf{d}_{nij} \tag{B.19}$$

where $\mathbf{d}_{nij}$ represents the right-hand side of equation (B.17) as

$$\mathbf{d}_{nim} = \frac{\partial^2 \lambda_n(\boldsymbol{\chi})}{\partial\theta_i \partial\theta_m}\mathbf{M}(\boldsymbol{\rho})\boldsymbol{\phi}_n(\boldsymbol{\chi}) - \left[\mathbf{K}_i - \frac{\partial\lambda_n(\boldsymbol{\chi})}{\partial\theta_i}\mathbf{M}(\boldsymbol{\rho})\right]\frac{\partial\boldsymbol{\phi}_n(\boldsymbol{\chi})}{\partial\theta_m} - \left[\mathbf{K}_m - \frac{\partial\lambda_n(\boldsymbol{\chi})}{\partial\theta_m}\mathbf{M}(\boldsymbol{\rho})\right]\frac{\partial\boldsymbol{\phi}_n(\boldsymbol{\chi})}{\partial\theta_i} \tag{B.20}$$

Equation (B.19) is pre-multiplied by $\mathbf{A}_n^T$ as

$$\mathbf{A}_n^T\left[\mathbf{K}(\boldsymbol{\theta}) - \lambda_n(\boldsymbol{\chi})\mathbf{M}(\boldsymbol{\rho})\right]\mathbf{A}_n\frac{\partial^2\boldsymbol{\phi}_n^-(\boldsymbol{\chi})}{\partial\theta_i\partial\theta_m} = \mathbf{A}_n^T\mathbf{d}_{nim} \tag{B.21}$$

and one can obtain $\partial^2\boldsymbol{\phi}_n^-(\boldsymbol{\chi}) \,/\, \partial\theta_i\,\partial\rho_j$ as

$$\frac{\partial^2\boldsymbol{\phi}_n^-(\boldsymbol{\chi})}{\partial\theta_i\partial\rho_j} = \left(\mathbf{A}_n^T\left[\mathbf{K}(\boldsymbol{\theta}) - \lambda_n(\boldsymbol{\chi})\mathbf{M}(\boldsymbol{\rho})\right]\mathbf{A}_n\right)^{-1}\left(\mathbf{A}_n^T\mathbf{d}_{nij}\right) \tag{B.22}$$

Then, Hessian of the n^{th} mode shape vector, $\partial^2\boldsymbol{\phi}_n(\boldsymbol{\chi}) \,/\, \partial\theta_i\,\partial\rho_j$, can be obtained as

$$\frac{\partial^2\boldsymbol{\phi}_n(\boldsymbol{\chi})}{\partial\theta_i\partial\rho_j} = \mathbf{A}_n\frac{\partial^2\boldsymbol{\phi}_n^-(\boldsymbol{\chi})}{\partial\theta_i\partial\rho_j} \tag{B.23}$$

- **Differentiation with respect to ρ_j and ρ_k**

Differentiating equation (B.1) with respect to ρ_j gives the following expression

$$\left[-\frac{\partial\lambda_n(\boldsymbol{\chi})}{\partial\rho_j}\mathbf{M}(\boldsymbol{\rho}) - \lambda_n(\boldsymbol{\chi})\mathbf{M}_j\right]\boldsymbol{\phi}_n(\boldsymbol{\chi}) + \left[\mathbf{K}(\boldsymbol{\theta}) - \lambda_n(\boldsymbol{\chi})\mathbf{M}(\boldsymbol{\rho})\right]\frac{\partial\boldsymbol{\phi}_n(\boldsymbol{\chi})}{\partial\rho_j} = \mathbf{0} \tag{B.24}$$

Then, differentiating equation (B.24) with respect to ρ_k gives the following expression

$$\left[-\frac{\partial^2\lambda_n(\boldsymbol{\chi})}{\partial\rho_j\partial\rho_k}\mathbf{M}(\boldsymbol{\rho})-\frac{\partial\lambda_n(\boldsymbol{\chi})}{\partial\rho_j}\mathbf{M}_k-\frac{\partial\lambda_n(\boldsymbol{\chi})}{\partial\rho_k}\mathbf{M}_j\right]\boldsymbol{\phi}_n(\boldsymbol{\chi})$$
$$-\left[\frac{\partial\lambda_n(\boldsymbol{\chi})}{\partial\rho_j}\mathbf{M}(\boldsymbol{\rho})+\lambda_n(\boldsymbol{\chi})\mathbf{M}_j\right]\frac{\partial\boldsymbol{\phi}_n(\boldsymbol{\chi})}{\partial\rho_k} \tag{B.25}$$
$$-\left[\frac{\partial\lambda_n(\boldsymbol{\chi})}{\partial\rho_k}\mathbf{M}(\boldsymbol{\rho})+\lambda_n(\boldsymbol{\chi})\mathbf{M}_k\right]\frac{\partial\boldsymbol{\phi}_n(\boldsymbol{\chi})}{\partial\rho_j}$$
$$+\left[\mathbf{K}(\boldsymbol{\theta})-\lambda_n(\boldsymbol{\chi})\mathbf{M}(\boldsymbol{\rho})\right]\frac{\partial^2\boldsymbol{\phi}_n(\boldsymbol{\chi})}{\partial\rho_i\partial\rho_k}=\mathbf{0}$$

Pre-multiplying equation (B.25) by $\boldsymbol{\phi}_n^T(\boldsymbol{\chi})$;

$$-\frac{\partial^2\lambda_n(\boldsymbol{\chi})}{\partial\rho_j\partial\rho_k}\boldsymbol{\phi}_n^T(\boldsymbol{\chi})\mathbf{M}(\boldsymbol{\rho})\boldsymbol{\phi}_n(\boldsymbol{\chi})-\frac{\partial^2\lambda_n(\boldsymbol{\chi})}{\partial\rho_j}\boldsymbol{\phi}_n^T(\boldsymbol{\chi})\mathbf{M}_k\boldsymbol{\phi}_n(\boldsymbol{\chi})$$
$$-\frac{\partial^2\lambda_n(\boldsymbol{\chi})}{\partial\rho_k}\boldsymbol{\phi}_n^T(\boldsymbol{\chi})\mathbf{M}_j\boldsymbol{\phi}_n(\boldsymbol{\chi})$$
$$-\boldsymbol{\phi}_n^T(\boldsymbol{\chi})\left[\frac{\partial\lambda_n(\boldsymbol{\chi})}{\partial\rho_j}\mathbf{M}(\boldsymbol{\rho})+\lambda_n(\boldsymbol{\chi})\mathbf{M}_j\right]\frac{\partial\boldsymbol{\phi}_n(\boldsymbol{\chi})}{\partial\rho_k} \tag{B.26}$$
$$-\boldsymbol{\phi}_n^T(\boldsymbol{\chi})\left[\frac{\partial\lambda_n(\boldsymbol{\chi})}{\partial\rho_k}\mathbf{M}(\boldsymbol{\rho})+\lambda_n(\boldsymbol{\chi})\mathbf{M}_k\right]\frac{\partial\boldsymbol{\phi}_n(\boldsymbol{\chi})}{\partial\rho_j}$$
$$+\boldsymbol{\phi}_n^T(\boldsymbol{\chi})\left[\mathbf{K}(\boldsymbol{\theta})-\lambda_n(\boldsymbol{\chi})\mathbf{M}(\boldsymbol{\rho})\right]\frac{\partial^2\boldsymbol{\phi}_n(\boldsymbol{\chi})}{\partial\rho_j\partial\rho_k}=\mathbf{0}$$

Since $\boldsymbol{\phi}_n^T(\boldsymbol{\chi})$ is the left eigenvector of the matrix $\mathbf{K}(\boldsymbol{\theta})-\lambda_n(\boldsymbol{\chi})\mathbf{M}(\boldsymbol{\rho})$ in equation (B.26), last term of the left side of the equation is zero. Then, rearranging equation (B.26), Hessian of the eigenvalue of the n^{th} mode can be obtained as

$$\frac{\partial^2\lambda_n(\boldsymbol{\chi})}{\partial\rho_j\partial\rho_k}=\frac{\begin{aligned}&\left[-\frac{\partial^2\lambda_n(\boldsymbol{\chi})}{\partial\rho_j}\boldsymbol{\phi}_n^T(\boldsymbol{\chi})\mathbf{M}_k-\frac{\partial^2\lambda_n(\boldsymbol{\chi})}{\partial\rho_k}\boldsymbol{\phi}_n^T(\boldsymbol{\chi})\mathbf{M}_j\right]\boldsymbol{\phi}_n(\boldsymbol{\chi})\\&-\boldsymbol{\phi}_n^T(\boldsymbol{\chi})\left[\frac{\partial\lambda_n(\boldsymbol{\chi})}{\partial\rho_j}\mathbf{M}(\boldsymbol{\rho})+\lambda_n(\boldsymbol{\chi})\mathbf{M}_j\right]\frac{\partial\boldsymbol{\phi}_n(\boldsymbol{\chi})}{\partial\rho_k}\\&-\boldsymbol{\phi}_n^T(\boldsymbol{\chi})\left[\frac{\partial\lambda_n(\boldsymbol{\chi})}{\partial\rho_k}\mathbf{M}(\boldsymbol{\rho})+\lambda_n(\boldsymbol{\chi})\mathbf{M}_k\right]\frac{\partial\boldsymbol{\phi}_n(\boldsymbol{\chi})}{\partial\rho_j}\end{aligned}}{\boldsymbol{\phi}_n^T(\boldsymbol{\chi})\mathbf{M}(\boldsymbol{\rho})\boldsymbol{\phi}_n(\boldsymbol{\chi})} \tag{B.27}$$

Equation (B.25) is rearranged to solve for the Hessian of the eigenvector of the n^{th} mode as

$$\begin{aligned}&\left[\mathbf{K}(\boldsymbol{\theta})-\lambda_n(\boldsymbol{\chi})\mathbf{M}(\boldsymbol{\rho})\right]\frac{\partial^2\boldsymbol{\phi}_n(\boldsymbol{\chi})}{\partial\rho_i\partial\rho_k}\\&=\left[\frac{\partial^2\lambda_n(\boldsymbol{\chi})}{\partial\rho_j\partial\rho_k}\mathbf{M}(\boldsymbol{\rho})+\frac{\partial\lambda_n(\boldsymbol{\chi})}{\partial\rho_j}\mathbf{M}_k+\frac{\partial\lambda_n(\boldsymbol{\chi})}{\partial\rho_k}\mathbf{M}_j\right]\boldsymbol{\phi}_n(\boldsymbol{\chi})\\&\quad+\left[\frac{\partial\lambda_n(\boldsymbol{\chi})}{\partial\rho_j}\mathbf{M}(\boldsymbol{\rho})+\lambda_n(\boldsymbol{\chi})\mathbf{M}_j\right]\frac{\partial\boldsymbol{\phi}_n(\boldsymbol{\chi})}{\partial\rho_k}\\&\quad+\left[\frac{\partial\lambda_n(\boldsymbol{\chi})}{\partial\rho_k}\mathbf{M}(\boldsymbol{\rho})+\lambda_n(\boldsymbol{\chi})\mathbf{M}_k\right]\frac{\partial\boldsymbol{\phi}_n(\boldsymbol{\chi})}{\partial\rho_j}\end{aligned} \tag{B.28}$$

However, Hessian of the eigenvectors cannot be obtained by using equation (B.28) since the matrix $\mathbf{K}(\boldsymbol{\theta})-\lambda_n(\boldsymbol{\chi})\mathbf{M}(\boldsymbol{\rho})$ on the left-hand side is a rank deficient one. Therefore, rank deficiency problem is solved by the same procedure that is performed for the calculation of the Jacobian of eigenvectors. Accordingly, since the Jacobian of the h_n^{th} coordinate of $\bar{\boldsymbol{\phi}}_n(\boldsymbol{\chi})$ and since the Jacobian of the a_n^{th} coordinate of $\boldsymbol{\phi}_n(\boldsymbol{\theta})$ are zeros (See equation (4.49)), the Hessian of these coordinates are again zeros. Then,

$$\frac{\partial^2\bar{\boldsymbol{\phi}}_{h_n,n}(\boldsymbol{\chi})}{\partial\rho_j\partial\rho_k}=0 \quad\text{and}\quad \frac{\partial^2\boldsymbol{\phi}_{a_n,n}(\boldsymbol{\chi})}{\partial\rho_j\partial\rho_k}=0 \tag{B.29}$$

The transformation in equation (4.50) is substituted into the left-hand side of equation (B.28). Further, $\partial^2\widetilde{\mathbf{1}} / \partial\rho_j\,\partial\rho_k$ is a zero vector, and the following equation is obtained as

$$\left[\mathbf{K}(\boldsymbol{\theta}) - \lambda_n(\boldsymbol{\chi})\mathbf{M}(\boldsymbol{\rho})\right]\mathbf{A}_n \frac{\partial^2 \boldsymbol{\phi}_n^-(\boldsymbol{\chi})}{\partial\rho_j\partial\rho_k} = \mathbf{d}_{njk} \tag{B.30}$$

where $\mathbf{d}_{njk}$ represents the right-hand side of equation (B.28) as

$$\begin{aligned}\mathbf{d}_{njk} = &\left[\frac{\partial^2\lambda_n(\boldsymbol{\chi})}{\partial\rho_j\partial\rho_k}\mathbf{M}(\boldsymbol{\rho}) + \frac{\partial\lambda_n(\boldsymbol{\chi})}{\partial\rho_j}\mathbf{M}_k + \frac{\partial\lambda_n(\boldsymbol{\chi})}{\partial\rho_k}\mathbf{M}_j\right]\boldsymbol{\phi}_n(\boldsymbol{\chi}) \\ &+\left[\frac{\partial\lambda_n(\boldsymbol{\chi})}{\partial\rho_j}\mathbf{M}(\boldsymbol{\rho}) + \lambda_n(\boldsymbol{\chi})\mathbf{M}_j\right]\frac{\partial\boldsymbol{\phi}_n(\boldsymbol{\chi})}{\partial\rho_k} \\ &+\left[\frac{\partial\lambda_n(\boldsymbol{\chi})}{\partial\rho_k}\mathbf{M}(\boldsymbol{\rho}) + \lambda_n(\boldsymbol{\chi})\mathbf{M}_k\right]\frac{\partial\boldsymbol{\phi}_n(\boldsymbol{\chi})}{\partial\rho_j}\end{aligned} \tag{B.31}$$

Equation (B.30) is pre-multiplied by $\mathbf{A}_n^T$ as

$$\mathbf{A}_n^T\left[\mathbf{K}(\boldsymbol{\theta}) - \lambda_n(\boldsymbol{\chi})\mathbf{M}(\boldsymbol{\rho})\right]\mathbf{A}_n \frac{\partial^2 \boldsymbol{\phi}_n^-(\boldsymbol{\chi})}{\partial\rho_j\partial\rho_k} = \mathbf{A}_n^T\mathbf{d}_{njk} \tag{B.32}$$

and one can obtain $\partial^2\boldsymbol{\phi}_n^-(\boldsymbol{\chi}) / \partial\rho_j\,\partial\rho_k$ as

$$\frac{\partial^2 \boldsymbol{\phi}_n^-(\boldsymbol{\chi})}{\partial\rho_j\partial\rho_k} = \left(\mathbf{A}_n^T\left[\mathbf{K}(\boldsymbol{\theta}) - \lambda_n(\boldsymbol{\chi})\mathbf{M}(\boldsymbol{\rho})\right]\mathbf{A}_n\right)^{-1}\left(\mathbf{A}_n^T\mathbf{d}_{njk}\right) \tag{B.33}$$

Then, Hessian of the n^{th} mode shape vector, $\partial^2\boldsymbol{\phi}_n(\boldsymbol{\chi}) / \partial\rho_j\,\partial\rho_k$, can be obtained as

$$\frac{\partial^2 \boldsymbol{\phi}_n(\boldsymbol{\chi})}{\partial\rho_j\partial\rho_k} = \mathbf{A}_n\frac{\partial^2 \boldsymbol{\phi}_n^-(\boldsymbol{\chi})}{\partial\rho_j\partial\rho_k} \tag{B.34}$$

REFERENCES

Abdullah, N.A.Z., Sani, M.S.M., Rahman, M.M., Zaman, I. (2015). A review on model updating in structural dynamics. *IOP Conference Series: Materials Science and Engineering*. 100, 012015.

Alkayem, N.F., Cao, M., Zhang, Y., Bayat, M., Su, Z. (2018). Structural damage detection using finite element model updating with evolutionary algorithms: a survey. *Neural Computing and Applications*. 30, 389–411.

Au, S. K. (2011). Fast Bayesian FFT Method for Ambient Modal Identification with Separated Modes. *Journal of Engineering Mechanics*. 137(3), 214–226.

Au, S. K. (2012). Connecting Bayesian and frequentist quantification of parameter uncertainty in system identification. *Mechanical Systems and Signal Processing*. 29, 328–342.

Au, S. K., Zhang, F.L. (2016). Fundamental two-stage formulation for Bayesian system identification, Part I: General theory. *Mechanical Systems and Signal Processing*. 66–67, 31–42.

Bakir, P.G., Reynders, E., De Roeck, G. (2007). Sensitivity-based finite element model updating using constrained optimization with a trust region algorithm. *Journal of Sound and Vibration*. 305, 211–225.

Beck, J.L., Au, S.-K., Vanik, M.W. (2001). Monitoring Structural Health Using a Probabilistic Measure. *Computer-Aided Civil and Infrastructure Eng*ineering. 16, 1–11.

Beck, J.L., Au, S.K., Vanik, M.W. (1999). A Bayesian probabilistic approach to structural health monitoring, *Proceedings of the 1999 American Control Conference* (Cat. No. 99CH36251). IEEE, San Diego, CA, USA, pp. 1119–1123 vol.2.

Behmanesh, I., Moaveni, B. (2016). Accounting for environmental variability, modeling errors, and parameter estimation uncertainties in structural identification. *Journal of Sound and Vibration*. 374, 92–110.

Behmanesh, I., Moaveni, B. (2015). Probabilistic identification of simulated damage on the Dowling Hall footbridge through Bayesian finite element model updating. *Structural Control and Health Monitoring*. 22, 463–483.

Berman, A. (1995). Multiple acceptable solutions in structural model improvement. *AIAA Journal*. 33, 924–927.

Bicanic, N., Chen, H. (2010). Identification of structural damage in buildings using iterative procedure and regularisation method. *Engineering Computations*. 27, 930–950.

Boonlong, K. (2014). Vibration-Based Damage Detection in Beams by Cooperative Coevolutionary Genetic Algorithm. *Advances in Mechanical Engineering*. 6, 624949.

Caesar, B., Peter, J. (1987). Direct update of dynamic mathematical models from modal test data. *AIAA Journal*. 25, 1494–1499.

Carden, E.P., Fanning, P. (2004). Vibration Based Condition Monitoring: A Review. *Structural Health Monitoring: An International Journal*. 3, 355–377.

Carvalho, J., Datta, B.N., Gupta, A., Lagadapati, M. (2007). A direct method for model updating with incomplete measured data and without spurious modes. *Mechanical Systems and Signal Processing*. 21, 2715–2731.

Cawley, P., Adams, R. (1979). The Location of Defects in Structures From Measurements of Natural Frequencies. *Journal of Strain Analysis for Engineering Design*. 14, 49–57.

Ceylan, H., Turan, G., Hızal, Ç. (2020). Pre-Identification Data Merging for Multiple Setup Measurements with Roving References. *Experimental Techniques*. 44, 435–456.

Chandrashekhar, M., Ganguli, R. (2009). Structural Damage Detection Using Modal Curvature and Fuzzy Logic. *Structural Health Monitoring: An International Journal*. 8, 267–282.

Chang, C.C., Chang, T.Y.P., Xu, Y.G., Wang, M.L. (2000). Structural Damage Detection Using an Iterative Neural Network. *Journal of Intelligent Material Systems and Structures*. 11, 32–42.

Christodoulou, K., Ntotsios, E., Papadimitriou, C., Panetsos, P. (2008). Structural model updating and prediction variability using Pareto optimal models. *Computer Methods in Applied Mechanics and Engineering*. 198, 138–149.

Christodoulou, K., Papadimitriou, C. (2007). Structural identification based on optimally weighted modal residuals. *Mechanical Systems and Signal Processing*. 21, 4–23.

Das, S., Saha, P. (2018). Structural health monitoring techniques implemented on IASC-ASCE benchmark problem: a review. *Journal of Civil Structural Health Monitoring*. 8, 689–718.

Esfandiari, A., Bakhtiari-Nejad, F., Sanayei, M., Rahai, A. (2010). Structural finite element model updating using transfer function data. *Computers & Structures*. 88, 54–64.

Fang, S.-E., Ren, W.-X., Perera, R. (2012). A stochastic model updating method for parameter variability quantification based on response surface models and Monte Carlo simulation. *Mechanical Systems and Signal Processing*. 33, 83–96.

Farhat, C., Hemez, F.M. (1993). Updating finite element dynamic models using an element-by-element sensitivity methodology. *AIAA Journal*. 31, 1702–1711.

Farrar, C., Angel, M., Bement, M., Salvino, L. (2009). Structural health monitoring for ship structures. *Conference: International Workshop on Structural Health Monitoring*, September 9, 2009 ; Palo Alto, CA .

Farrar, C., Cone, K.M. (1994). Vibration testing of the I-40 bridge before and after the introduction of damage. *Conference: International modal analysis conference*, Nashville, TN (United States),13-16 Feb 1995

Farrar, C.R., Doebling, S.W., Nix, D.A. (2001). Vibration–based structural damage identification. *Philosophical Transactions of the Royal Society of London A: Mathematical, Physical and Engineering Sciences.* 359, 131–149.

Farrar, C.R., Doebling, W., (1999). Damage Detection II: Field applications to large structures, in: Modal Analysis and Testing. *Nato Science Series*. Kluwer Academic Publishers.

Fatahi, L., Moradi, S. (2018). Multiple crack identification in frame structures using a hybrid Bayesian model class selection and swarm-based optimization methods. *Structural Health Monitoring: An International Journal*. 17, 39–58.

Fritzen, C.-P., Kraemer, P. (2009). Self-diagnosis of smart structures based on dynamical properties. *Mechanical Systems and Signal Processing*. 23, 1830–1845.

Govers, Y., Link, M. (2010). Stochastic model updating - Covariance matrix adjustment from uncertain experimental modal data. *Mechanical Systems and Signal Processing*. 24, 696–706.

Haralampidis, Y., Papadimitriou, C., Pavlidou, M. (2005). Multi-objective framework for structural model identification. *Earthquake Engineering and Structural Dynamics*. 34, 665–685.

Hızal, Ç. (2021). Frequency domain data merging in operational modal analysis based on least squares approach. *Measurement*. 170, 108742.

Hızal, Ç. (2019). Modal Identification of Structures by Using Bayesian Statistics. *Doctor of Philosophy*. Izmir Institute of Technology, Izmir, Turkey..

Hızal, Ç., Turan, G. (2020). A two-stage Bayesian algorithm for finite element model updating by using ambient response data from multiple measurement setups. *Journal of Sound and Vibration*, 469:115139.

Humar, J., Bagchi, A., Xu, H. (2006). Performance of Vibration-based Techniques for the Identification of Structural Damage. *Structural Health Monitoring: An International Journal*. 5, 215–241.

Jaishi, B., Ren, W.-X. (2006). Ren, W.X.: Damage detection by finite element model updating using modal flexibility residual. *Journal of Sound and Vibration* 290, 369–387.

Jin, S.-S., Cho, S., Jung, H.-J., Lee, J.-J., Yun, C.-B. (2014). A new multi-objective approach to finite element model updating. *Journal of Sound and Vibration*. 333, 2323–2338.

Johnson, E.A., Lam, H.F., Katafygiotis, L.S., Beck, J.L. (2004). Phase I IASC-ASCE Structural Health Monitoring Benchmark Problem Using Simulated Data. *Journal of Engineering Mechanics*. 130(1), 3–15.

Jung, D.-S., Kim, C.-Y. (2013). Finite element model updating on small-scale bridge model using the hybrid genetic algorithm. *Structure and Infrastructure Engineering*. 9, 481–495.

Katafygiotis, L.S., Yuen, K.-V. (2001). Bayesian spectral density approach for modal updating using ambient data. *Earthquake Engineering & Structural Dynamics*. 30, 1103–1123.

Khoshnoudian, F., Esfandiari, A. (2011). Structural damage diagnosis using modal data. *Scientia Iranica*. 18, 853–860.

Kim, I.Y., de Weck, O.L. (2005). Adaptive weighted-sum method for bi-objective optimization: Pareto front generation. *Structural and Multidisciplinary Optimization*. 29, 149–158.

Kim, J.-T., Ryu, Y.-S., Cho, H.-M., Stubbs, N. (2003). Damage identification in beam-type structures: Frequency-based method vs mode-shape-based method. *Engineering Structures*. 57–67.

Lam, H.F., Katafygiotis, L.S., Mickleborough, N.C. (2004). Application of a Statistical Model Updating Approach on Phase I of the IASC-ASCE Structural Health Monitoring Benchmark Study. *Journal of Engineering Mechanics*. 130, 34–48.

Lye, A., Cicirello, A., Patelli, E. (2021). Sampling methods for solving Bayesian model updating problems: A tutorial. *Mechanical Systems and Signal Processing*. 159, 107760.

Maeck, J., De Roeck, G. (2000). Damage Detection on a Prestressed Concrete Bridge and RC Beams Using Dynamic System Identification. *Key Engineering Materials*. 167–168.

Mahmood, S.M.F., Haritos, N., Gad, E., Zhang, L. (2014). A multi-reference-based mode selection approach for the implementation of NExT–ERA in modal-based damage detection. *Structural Control & Health Monitoring*. 21(8), 1137.

Mares, C., Surace, C. (1996). An Application of Genetic Algorithms To Identify Damage In Elastic Structures. *Journal of Sound and Vibration*. 195, 195–215.

Marwala, T., Sibisi, S. (2005). Finite element model updating using bayesian framework and modal properties. *Journal of Aircraft*. 42(1)

Modak, S.V., Kundra, T.K., Nakra, B.C. (2002). Comparative study of model updating methods using simulated experimental data. *Computers & Structures*. 80, 437–447.

Montalvão, D., M. M. Maia, N., Ribeiro, A. (2006). A Review of Vibration-based Structural Health Monitoring with Special Emphasis on Composite Materials. *The Shock and Vibration Digest*. 38, 295.

Mottershead, J.E., Friswell, M.I. (1993). Model Updating In Structural Dynamics: A Survey. *Journal of Sound and Vibration*. 167, 347–375.

Mottershead, J.E., Link, M., Friswell, M.I. (2011). The sensitivity method in finite element model updating: A tutorial. *Mechanical Systems and Signal Processing*. 25, 2275–2296.

Mthembu, L.S. (2012). Finite element model updating. *Doctor of Philosophy*. University of the Witwatersrand, Johannesburg,

Mustafa S., Matsumoto Y. (2017). Bayesian Model Updating and Its Limitations for Detecting Local Damage of an Existing Truss Bridge. *Journal of Bridge Engineering*. 22, 04017019.

Oh, B.K., Kim, M.S., Kim, Y., Cho, T., Park, H.S. (2015). Model Updating Technique Based on Modal Participation Factors for Beam Structures. *Computer-Aided Civil and Infrastructure Engineering*. 30, 733–747.

Ooijevaar, T.H. (2014). Vibration based structural health monitoring of composite skin-stiffener structures. *Doctor of Philosophy*. University of Twente, Enschede, The Netherlands.

Otsuki, Y., Lander, P., Dong, X., Wang, Y. (2021). Formulation and Application of SMU – an Open-Source MATLAB Package for Structural Model Updating. *Advances in Structural Engineering*. 25(4), 698–715.

Pan, C., Yu, L. (2015). Structural Damage Detection and Moving Force Identification Based on Firefly Algorithm. *Advances in Swarm and Computational Intelligence*, Lecture Notes in Computer Science. Springer International Publishing, pp. 57–64.

Papadimitriou, C., Beck, J.L., Katafygiotis, L.S. (1997). Asymptotic Expansions for Reliability and Moments of Uncertain Systems. *Journal of Engineering Mechanics*. 123, 1219–1229.

Perera, R., Marin, R., Ruiz, A. (2013). Static–dynamic multi-scale structural damage identification in a multi-objective framework. *Journal of Sound and Vibration*. 332, 1484–1500.

Rao, A.R.M., Anandakumar, G. (2007). Optimal placement of sensors for structural system identification and health monitoring using a hybrid swarm intelligence technique. *Smart Materials and Structures*. 16, 2658–2672.

Rytter, A. (1993). Vibrational Based Inspection of Civil Engineering Structures. *Doctor of Philosophy.* Aalborg University, Denmark

Salawu O. S., Williams C. (1995). Bridge Assessment Using Forced-Vibration Testing. *Journal of Structural Engineering*. 121, 161–173.

Sandesh, S., Shankar, K. (2010). Application of a hybrid of particle swarm and genetic algorithm for structural damage detection. *Inverse Problems in Science and Engineering*. 18, 997–1021.

Sedehi, O. (2019). Data-driven Uncertainty Quantification and Propagation in Structural Dynamics Inverse Problems. *Doctor of Philosophy.* The Hong Kong University of Science and Technology, Hong Kong

Song, M., Behmanesh, I., Moaveni, B., Papadimitriou, (2020). Accounting for Modeling Errors and Inherent Structural Variability through a Hierarchical Bayesian Model Updating Approach: An Overview. *Sensors.* 20, 3874.

Tabrizian, Z., Afshari, E., Amiri, G.G., Beigy, A., Hossein, M., Nejad, S.M.P. (2013). A New Damage Detection Method: Big Bang-Big Crunch (BB-BC) Algorithm. *Shock and Vibration.*

Than Soe, M. (2013). Vibration-based finite element model updating and structural damage identification. *Doctor of Philosophy.* University of Greenwich, England

Torres, R.H. (2017). Vibration-Based Damage Identification Using Hybrid Optimization Algorithms. *Doctor of Philosophy.* São José dos Campos, Brasil

Vanik, M.W., Beck, J.L., Au, S.K. (2000). Bayesian Probabilistic Approach to Structural Health Monitoring. *Journal of Engineering Mechanics*. 126, 738–745.

Wang, Y., Dong, X., Li, D., Otsuki, Y. (2019.) SMU: MATLAB Package for Structural Model Updating, version 1.2.

Worden, K., Farrar, C.R., Manson, G., Park, G. (2007). The fundamental axioms of structural health monitoring. *Proceedings of the Royal Society of London A: Mathematical, Physical and Engineering Sciences.* 463, 1639–1664.

Yan, W.-J., Katafygiotis, L.S. (2015). A novel Bayesian approach for structural model updating utilizing statistical modal information from multiple setups. *Structural Safety.* 52, 260–271.

Yu, L., Li, C. (2014). A Global Artificial Fish Swarm Algorithm for Structural Damage Detection. *Advances in Structural Engineering*. 17, 331–346.

Yu, L., Xu, P. (2011). Structural health monitoring based on continuous ACO method. *Microelectronics Reliability.* 51, 270–278.

Yu, L., Xu, P., Chen, X. (2012). A SI-Based Algorithm for Structural Damage Detection, *Advances in Swarm Intelligence*, Lecture Notes in Computer Science. Springer Berlin Heidelberg, pp. 21–28.

Yuen, K.-V. (2010). Bayesian Methods for Structural Dynamics and Civil Engineering, 1st edition. ed. Wiley, Singapore ; Hoboken, NJ.

Yuen, K.-V., Au, S.K., Beck, J.L. (2004). Two-Stage Structural Health Monitoring Approach for Phase I Benchmark Studies. Journal of Engineering Mechanics. 130, 16–33.

Yuen, K.-V., Beck, J.L., Katafygiotis, L.S. (2006). Efficient model updating and health monitoring methodology using incomplete modal data without mode matching. *Structural Control and Health Monitoring*. 13, 91–107.

Yuen, K.-V., Katafygiotis, L.S. (2003). Bayesian Fast Fourier Transform Approach for Modal Updating Using Ambient Data. *Advances in Structural Engineering*. 6, 81–95.

Yuen, K.-V., Katafygiotis, L.S. (2001). Bayesian time–domain approach for modal updating using ambient data. *Probabilistic Engineering Mechanics.* 16, 219–231.

Yuen, K.-V., Kuok, S.-C. (2011). Bayesian Methods for Updating Dynamic Models. *Applied Mechanics Reviews*. 64, 010802.

Zapico-Valle, J.L., Abad-Blasco, J., González-Martínez, M.P., Franco-Gimeno, J.M., García-Diéguez, M. (2012). Modelling and calibration of a beam-column joint based on modal data. *Computer and Structures.* 108–109, 31–41.

Zhu, J.J., Huang, M., Lu, Z.R. (2017). Bird mating optimizer for structural damage detection using a hybrid objective function. *Swarm and Evolutionary Computation*. 35, 41–52.

VITA

Name – Surname: Hasan CEYLAN

Educational Information:

Graduation Degree	Institution	Graduation Year
BSc.	Muğla Sıtkı Koçman University	2012
MSc.	Izmir Institute of Technology	2015
PhD.	Izmir Institute of Technology	2022

Awards:

Best Student Paper Award for the following conference paper:

Ceylan, H. and Turan, G. (2016). Modal Parameter Identification of a Continuous Beam Bridge by Using Grouped Response Measurements. *Istanbul Bridge Conference*. 8-10 August. Istanbul, Turkey.

Publications:

Ceylan, H., Turan, G., Hızal, Ç. (2020). Pre-Identification Data Merging for Multiple Setup Measurements with Roving References. *Experimental Techniques*. 44, 435–456.

Hızal, Ç., Turan, G., Aktaş, E., Ceylan, H. (2019). A mode shape assembly algorithm by using two stage Bayesian Fast Fourier Transform Approach. *Mechanical Systems and Signal Processing*. 134, 106328.